Hierarchically Structured Poly(*p*-xylylene)*s*: From Molecular Architecture to Macroscopic Foams

Dissertation
zur
Erlangung des Doktorgrades
der Naturwissenschaften
(Dr. rer. nat.)

dem
Fachbereich Chemie der
Philipps-Universität Marburg
vorgelegt von

Dipl.-Chem. Ilka Elisabeth Paulus

aus
Battenberg-Laisa

Marburg (Lahn) 2013

Hierarchically Structured Poly(*p*-xylylene)s:
From Molecular Architecture to Macroscopic Foams

Dissertation zur Erlangung des Doktorgrades
der Naturwissenschaften (Dr. rer. nat.)

dem Fachbereich Chemie der Philipps-Universität Marburg
vorgelegt am 17. Dezember 2013
von

Dipl.-Chem. Ilka Elisabeth Paulus
(geb. 29.07.1984)

aus Battenberg-Laisa

Marburg (Lahn) 2013

Hochschulkennziffer: 1180

Erstgutachter: Prof. Dr. Andreas Greiner

Zweitgutachter: Prof. Dr. Joachim H. Wendorff

Tag der mündlichen Prüfung:17. Januar 2014

One never notices what has been done; one can only see what remains to be done.

Marie Curie (1876-1934)

Die vorliegende Arbeit wurde in der Zeit von Januar 2010 bis September 2012 am Fachbereich Chemie der Philipps Universität Marburg am Institut für Physikalische Chemie, Kernchemie und Makromolekulare Chemie und von Oktober 2012 bis Dezember 2013 am Lehrstuhl für Makromolekulare Chemie II der Universität Bayreuth angefertigt.

Table of Contents

Abbreviations

°C	degree **C**elsius
2D	**two d**imensional
3D	**three d**imensional
4-VB	**4-v**inyl**b**iphenyl
4VP	**4-v**inyl**p**yridine
9-VA	**9-v**inyl**a**nthracene
AIBN	α,α’-**a**zo**i**so**b**utyro**n**itrile
alkyl-PPX	**p**oly(*n*-**alkyl**-***p***-**x**ylylene)
ATRP	**a**tom **t**ransfer **r**adical **p**olymerization
c	**c**enti, 10^{-2}
CP	**c**hloro**p**rene
CTAB	**c**etyl**t**rimethyl**a**mmonium **b**romide
CVD	**c**hemical **v**apor **d**eposition
Da	**Da**lton
DB-M	**d**ouble **b**ond containing **m**onomer
DFT	**d**ensity **f**unctional **t**heory
DPX	[2.2]paracyclophane, **d**i-***p***-**x**ylene (general, no regard to substituents)
DSC	**d**ifferential **s**canning **c**alorimetry
e.g.	**e**xepli **g**ratia, for example
EDX	**e**nergy **d**ispersive **x**-ray spectroscopy
EPR	**e**lectron **p**aramagnetic **r**esoncance
et al.	**et al**ii, and others
G	**g**iga, 10^{9}
GMA	**g**lycidyl **m**eth**a**crylat
GPC	**g**el **p**ermeation **c**hromatography
HEMA	2-**h**ydroxy**e**thyl **m**eth**a**crylate
iCVD	**i**nitiated **c**hemical **v**apor **d**eposition
IR	**i**nfra **r**ed
IR	**i**nfra **r**ed
k	**k**ilo, 10^{3}
LCST	**l**ower **c**ritical **s**olution **t**emperature
m	**m**eter
m	as suffix: **m**ili, 10^{-3}
MA	**m**aleic **a**nhydride
MA	**m**aleic **a**nhydride
mbar	**mili b**ar
MEMS	**m**icro-**e**lectronic **m**echanical **s**ystems
MMA	**m**ethyl **m**eth**a**crylat
n	**n**ano
n. a.	**n**o **a**nalysis performed
$Ni(dppp)Cl_2$	[1,3-bis(**d**i**p**henyl**p**hos**p**hino)propane]di**c**h**l**oro**ni**ckel(II)
NiPAAm	***N***-**i**so**p**orpyl **a**cryl**am**ide

NPMI	***N*-p**henyl **m**ale**i**mide
N-VP	***N*-v**inyl**p**yrrolidone
OAD	**o**blique **a**ngle **d**eposition
oCVD	**o**xidative **c**hemical **v**apor **d**eposition
p_b	**b**ase **p**ressure (in CVD reactor)
p	**p**ressure
PECVD	**p**lasma **e**nhanced **c**hemical **v**apor **d**eposition
PFOMA	**p**er**f**luoro**o**ctyl **m**eth**a**crylate
PGMA	**p**oly(**g**lycidyl **m**eth**a**crylat)
PHEMA	**p**oly(2- **h**ydroxy**e**thyl **m**eth**a**crylate)
PMDETA	*N,N,N',N'',N''*-**p**enta**m**ethyl**d**i**e**thylene**t**ri**a**mine
PMMA	**p**oly(**m**ethyl **m**eth**a**crylat)
PNiPAAm	**p**oly(***N*-i**so**p**ropyl **a**cryl**am**ide)
PPE	**p**oly(oxy-2,6-dimethyl-1,4-**p**henyl)
ppm	**p**arts **p**er **m**illion
PPX	**p**oly(***p*-x**ylylene) (general, no regard to substituents)
PPX-butyl	**p**oly(*n*-**butyl**-***p*-x**ylylene)
PPX-C	**p**oly(**c**hloro-*p*-**x**ylylene)
PPX-D	**p**oly(**d**i-chloro-***p*-x**ylylene)
PPX-heptyl	**p**oly(*n*-**heptyl**-***p*-x**ylylene)
PPX-HT	**p**oly(α,α,α'α'-tetra-fluoro-***p*-x**ylylene)
PPX-N	**p**oly(***p*-x**ylylene)
PPX-propyl	**p**oly(*n*-**propyl**-***p*-x**ylylene)
PS	**p**olystyrene
*p*X	***p*-x**ylylene
ref.	**ref**erence
RH	**r**elative **h**umidity
r_{xx}	**r**-parameer (reactiviy ratio in radical copolymerizations)
S	**S**iemens
SEM	**s**canning **e**lectron **m**icroscopy
T	**t**emperature
T_{dep}	**dep**osition **t**emperature
T_g	**g**lass transition **t**emperature
TGA	**t**hermo**g**ravimetric **a**nalysis
T_p	**p**yrolysis **t**emperature
T_{sub}	**sub**limation **t**emperature
TUFT	**tu**bes by **f**iber **t**emplates
T_{vap}	e**vap**oration **t**emperature
V	**v**inylic comonomer
VDP	**v**apor **d**eposition **p**olymerization
wt%	**w**eigh**t %**
X-ray	**R**oentgen ray
µ	micro, 10^{-6}
µ-CT	**m**icro **c**omputed **t**omography

Important Monomers and Polymers

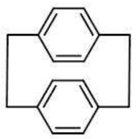

[2.2]paracyclophane, DPX-N

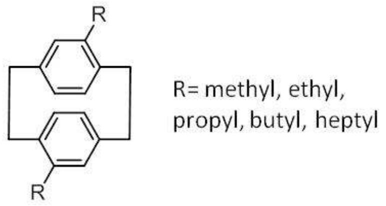

4,12-di-alkyl-[2.2]paracyclophane, alkyl-DPX

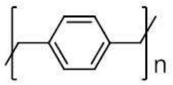

poly(*p*-xylylene), PPX-N

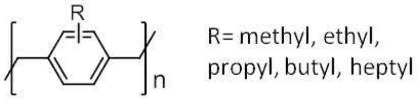

poly(alkyl-*p*-xylylene), alkyl-PPX

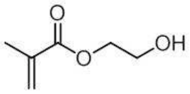

2-hydroxyethyl methacrylate, HEMA

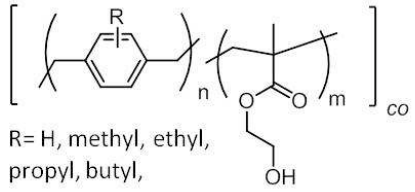

poly(*p*-xylylene-*co*-2-hydroxyethyl methacrylate), P(PX-*co*-HEMA)

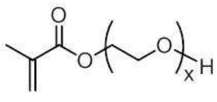

oligo(ethylene glycol) methacrylate, OEGMA

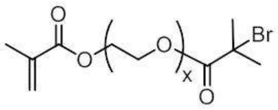

2-isobutyryloxy oligo(ethylene glycol) methacrylate, OEGMA-Br

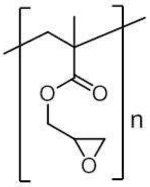

poly(glycidyl methacrylate), PGMA

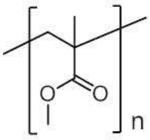

poly(methyl methacrylate), PMMA

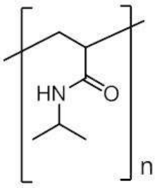

poly(*N*-isopropyl acrylamide), PNiPAAm

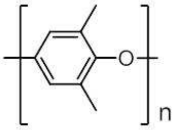

poly(oxy-2,6-dimethyl-1,4-phenylen), PPE

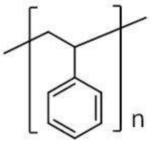

polystyrol, PS

1 Introduction

Poly(*p*-xylylene) (PPX) polymers posses many useful properties and distinguish as protective coatings.[1-3] Among them are extraordinary resistance to chemicals, as well as good mechanical, excellent barrier and electrical insulation performance. The technical synthesis route via chemical vapor deposition (CVD) further contributes to the uniqueness of this material class.[4] CVD is a coating technique that enables highly substrate conformal coatings down to the micrometer range, which are not achievable by solution based methods.[2] In 1966 W. F. GORHAM significantly improved the PPX synthesis procedure by establishing the use of [2.2]paracyclophane instead of *p*-xylene as precursor.[4] This led to quantitative yields of PPX free of any side products. Te industrial application and commercialization of PPX, also known as Parylene, was established by Union Carbide Corporation in the 1970s and is used until today. The transparent coatings of easily controllable thickness find wide application in electronic industry[1] and micro-electronic mechanical systems[5-7] (MEMS), but also in biological and medical applications,[8] since PPX is a biocompatible[9] material. As an example, in the medical field PPX coatings help to prevent platelet adhesion and enable drug release from implants like coronary stents,[10, 11] or serve to protect electronic implants from body fluids.[12] Though only few PPX derivates are used in industrial coating applications (Figure 1), a considerable number of substituted [2.2]paracyclophanes are subject to intense current research and available on laboratory scale. The latest invention in the field of PPX coatings are antimicrobial Parylene coatings available from Speciality Coatings Systems (SCS).[13]

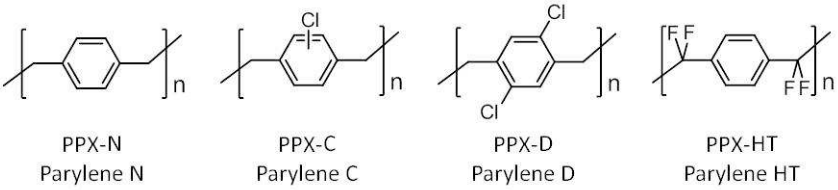

Figure 1 Most common commercially available PPX, or Parylene, derivates.

The aim of this work is to demonstrate possibilities for PPX modification, functionalization and structuring in different orders of magnitude, leading from modifications in molecular architecture to three dimensional structure formation on macroscopic scale.

2 Overall Motivation and Aim

The PPX polymers are already well established as protective coatings due to the remarkable inertness of derivates like PPX-N and PPX-C in combination with the special synthesis approach via CVD. However, this inertness and intractability becomes a problem when thinking of further uses of this interesting polymer class beyond the already existing.

In polymer science there are several approaches to influence the properties of a material, influencing the given polymer on different structural levels. On the one hand it is straight forward modification of the intrinsic properties by chemical modification of the monomer's molecular structure or alteration of the macromolecule architecture by copolymerization. On the other hand there is polymer processing. This can be mixing with other polymers or materials in order to obtain blends or composites, or alterations in shape to influence the macroscopic behavior of the material.

The present thesis is divided in four parts, each addressing a different approach to influence and modify PPX polymers with the aim of improving and simplifying known methods and exploring new techniques in order to broaden the application spectrum of PPX polymers.

In the following a short introduction into the motivation and aim of the chosen approaches is given, a detailed presentation of the concepts and strategies pursued in this thesis can be found in the respective chapters (Section 4). An overview of the already established PPX synthesis and modification techniques can be found in Section 3.

The use of new [2.2]paracyclophanes carrying functional groups opened the way to so called “reactive coatings”, that attract more and more attention. [14, 15] Especially in the biomedical field, where PPX-C is already widely used, the patterning of reactive surfaces is of great interest. The modification of bulk instead of surface properties of PPX was also enabled by modification of the [2.2]paracyclophane precursors. The introduction of bulky substituents lead to highly flexible and soluble PPX derivates accessible via the CVD synthesis method.[16, 17]

However, precursor substitution and functionalization often requires multi step synthesis to obtain the desired products. This is not only time consuming but also expensive, especially when thinking about coating applications on larger industrial scale. The CVD technology, which is not limited to the deposition of PPX polymers but also available for other monomers,[18] shows the possibility for an alternative approach to modify and functionalize PPX coatings, which is the copolymerization of [2.2]paracyclophanes with conventional double bound containing monomers like methacrylates. The general feasibility was already demonstrated in early times of PPX chemistry[19, 20] and later in the 1990s.[21-26] However, due to several challenges like product purity and homogeneity of the copolymers, this very promising method did not receive much attention.

The first chapters deals with the reactivation of the copolymerization approach, where the use of new easily accessible precursors together with changes in CVD reactor design are explored in order to influence the macromolecular architecture of PPX polymers. In the second part of this thesis different methods for the surface modification of PPX film are investigated with the objective to obtain reactive surfaces without the use of functionalized [2.2]paracyclophanes.

Because of its stability and inertness common PPX does not offer many easy possibilities to be processed or combined with other materials after the deposition process. However, literature offers some examples where shape changes and the basis for interaction with other materials is already introduced during the CVD procedure. One example is the TUFT[27] (tubes by fiber templates) process. Here template fibers, obtained e.g. via electrospinning, are coated with PPX in a conventional CVD process, leading to PPX tubes after removal of the template fibers. By variations of this method PPX tubes can be used as carrier for catalysts[28] or even living organisms.[29]

Electrospinning itself is a powerful technique to process polymer solutions into fibers,[30, 31] but was not accessible for CVD PPX due to the insolubility of this polymers until recently. The third chapter will deal with the electrospinning of soluble PPX and explore this processing technique in order to achieve macroscopic property modifications with a microstructured material.

The forth part of this work is dedicated to the application oriented use of PPX in combination with other materials. The purpose is to point out the possibilities of bulk property changes in PPX without the need of chemical modification, the use of PPX in composite materials and generation macroscopic PPX structures inspired by the TUFT process.

3 Theoretical Background and Literature Overview

3.1 Chemical Vapor Deposition (CVD)

Chemical vapor deposition (CVD) is known as a powerful tool for surface engineering and preparation of thin and highly substrate conformal films. A general description of the process is given by JASINSKI *et al.* and says *"CVD is a process whereby gas phase molecules are decomposed in some manner to leave behind solid material"*.[32] The source of the gas phase molecules can be either organic or inorganic precursors and the resulting films are metals,[33] semi-conductors[32] or organic polymers.[18] Though the deposition of metals and semi-conductors is of great interest for all types of (micro) electronic devices,[34, 35] the focus of this brief introduction will be on the generation of polymer films. In the case of polymer CVD the term VDP (vapor deposition polymerization) is also used in literature. However, the key steps of the process, shown in Figure 2, are valid for the CVD of inorganic and organic films. In the CVD process the precursor is sublimated or evaporated (1) and reacts in the gas phase (2) to give an activated (or reactive) species. The type of this reaction depends on the specific CVD method and precursor, but is generally initiated by elevated temperatures. The adsorption/desorption (3) of the activated species on/from the substrate surface is an equilibrium controlled by CVD conditions like pressure and substrate temperature. The adsorbed species diffuse (4) along the surface and finally form a film (5). The film formation can take place by nucleation and growth or reaction of the activated species with each other. In an ideal case all precursor is consumed by the film growth, but in realistic scenarios a certain amount passes the substrate without reacting. Since CVD is usually carried out under reduced pressure, the process has to be executed in special reactors.

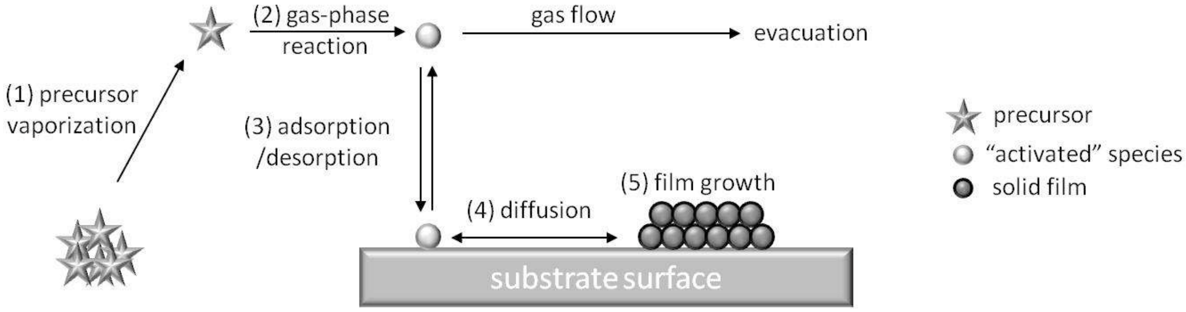

Figure 2 Schematic illustration of the chemical vapor deposition (CVD) process.[33, 35-37] Key steps for the film formation are (1) precursor vaporization, (2) precursor activation in the gas phase, (3) adsorption onto the substrate, (4) diffusion on the surface and (5) film growth.

PPX can be considered as the classic CVD polymer and will be dealt with in more detail in the following Sections of this work. In recent years the CVD of polymeric films other than PPX have gained increasing attention for coating applications, as reviewed by GLEASON and coworkers.[18, 38] The great advantages of polymer coatings from the gas phase are the absence of solvents, no need for solubility of precursor or final polymer and high substrate conformity. Especially in the micrometer range conformal and uniform coating of complex surface structures like trenches and tubes cannot be achieved from solutions. The ability to penetrate into such small confinements is unique for the CVD approach due to the gaseous monomer, which deposits onto the substrate prior to polymerization. A great number of conventional homo and copolymers[39, 40], like functional poly acrylates[41] and methacrylates[42-44], fluorinated polymers[45, 46], or polythiophenes[47], are available as thin coatings via the CVD approach, and lead the way to functional, responsive, or conductive polymer surface coatings.

Depending on the monomer used in CVD, different strategies have to be applied in order to start the polymerization on the substrate surface.[36] The most common ones are initiated CVD (iCVD), using an initiator like *tert*-benzoyl peroxide, oxidative CVD (oCVD), using an oxidizing agent or plasma-enhanced CVD (PECVD), using plasma to start polymerization. In the case of iCVD, which is used for methcrylate polymerizations, the peroxide bond of the imitator is cleaved by passing through a hot filament. The “activated” initiator deposits together with the monomer onto the substrate surface and initiates the polymerization. Further details of the different CVD techniques and examples for adequate monomers and initiators are given in the cited literature.

3.2 Poly(*p*-xylylene)s: Synthesis via CVD and Properties/Applications

As already mentioned PPX polymers are widely applied as protective coatings via the GORHAM-CVD process. Nevertheless, the polymer can be obtained by alternative synthesis routes. These are CVD from alternative precursors, like *p*-xylene (via SZWARC-route[48] or plasma assisted CVD[49, 50]) or α,α’-substituted *p*-xylenes[51] and different solution polymerization methods,[51] of which the GILCH polymerization[52] is the most important. However, since the present work focuses on PPX obtained via GORHAM-CVD, alternative synthesis approaches will not be explained further.

The synthesis of PPX by chemical vapor deposition is a special case of CVD polymerization. Nevertheless, the key steps described in Figure 2 are valid. First, the precursor is sublimated and in the gas phase, pyrolyzed to give the reactive monomer species, the *p*-xylylene (*p*X). The *p*X deposites on the substrate surface and polymerizes to give the final polymer. When the polymer was first synthesized by SZWARC in 1947 *p*-xylene was used as precursor.[48] Later, in 1966 GORHAM found [2.2]paracyclophane (also di-*p*-xylylene, DPX) to be a more suitable precursor and established the so-called GORHAM-process for PPX synthesis, which in contrast to the SZWARC-route, leads to side product free PPX films in high yields, consisting of linear polymer chains.[4]

The CVD process is carried out under reduced pressure and requires a special reactor in order to achieve the temperatures needed for sublimation and pyrolysis of the precursor molecule (Figure 3). The reactor is divided in three compartments, sublimation chamber, pyrolysis chamber and deposition chamber, which are heated to the respective temperatures.

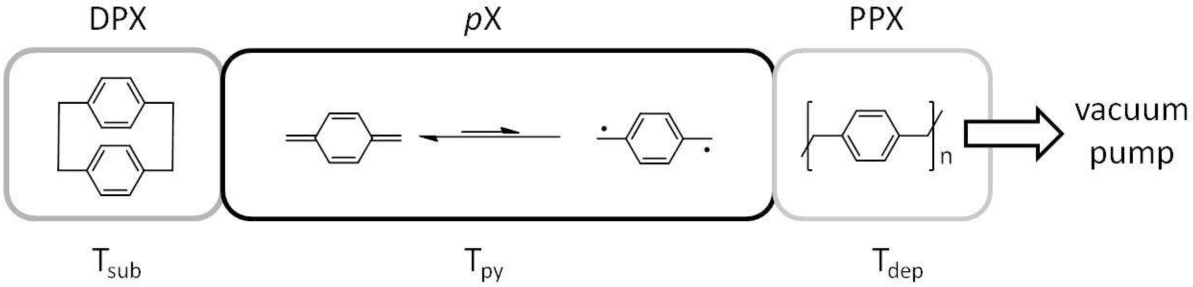

Figure 3 Schematic illustration of the CVD reactor used for the polymerization of PPX. The reactor is divided in three compartments, which are heated to different temperatures for precursor sublimation (T_{sub}), precursor pyrolysis (T_{py}) and deposition onto the substrate (T_{dep}).

The PPX polymer is formed not only without any solvent or catalyst, but also without the assistance of an extra initiator, since the *p*X is a radical itself. The polymerization mechanism of PPX consists of three steps, same as common polymerizations: initiation, propagation and termination. Due to the special monomer formation via pyrolysis and monomer deposition from the gas phase, each step comprises special characteristics which will be explained in the following in form of a brief literature review.

Prior to the initiation is the pyrolysis reaction of [2.2]paracyclophane (Figure 4). Experimental studies[4, 53, 54] and theoretic calculations[55] showed that the two ethylene bridges of the [2.2]paracyclophane do not break simultaneously, but an intermediate biradical is formed. The pyrolytical decomposition takes place at relatively low temperatures, due to the ring strain caused by the two connecting ethylene bridges, which bend the aromatic rings.[56] Quantummechanical calculations showed, that the *p*X exists in two states, the singlet ground state (chinoidal form) and the trpilet excited state (benzoidal form), which are relatively close in energy (12 kcal mol^{-1}).[1]

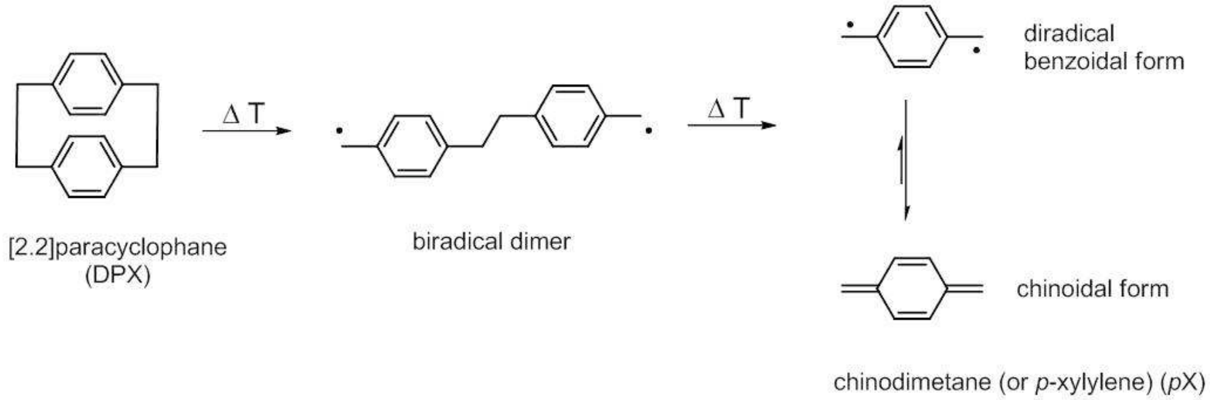

Figure 4 Generation of the reactive monomer species from [2.2]paracyclophane by pyrolysis.

The monomer vapor enters the deposition chamber and adsorbs on the chamber walls. Here the monomer can either stay or desorb, depending on local energy conditions. In literature the term "condensation" is often used to describe the deposition of *p*X on the chamber walls, but no perceptible liquid phase is formed.[57] If sufficient monomer is present on the surface the polymerization is initiated spontaneously. Since CVD takes place at low pressures (few mbar or less) and more than one monomer is needed to initiate polymerization (see below) there is no polymerization in the gas phase, but only on the surface of the deposition chamber walls and substrates.

Considering the initiation reaction of PPX polymerization there are two different opinions. In recent literature the formation of the biradical dimer from two *p*X monomers is described as the initiation of the polymerization With different approaches of semi empirical methods and density functional theory calculations, SMALARA *et al.*[55] showed that the dimer formation is an exothermic reaction resulting in a product of lower energy compared to the two monomers. The addition of further monomer to the growing chain (the propagation reaction) is also exothermic and comprises considerably lower activation energy. The authors also reported no significant differences in calculations for the mono and dichloro substitutes derivates PPX-C and PPX-D.[55] The assumption of the biradical dimer to be the initiating species was also expressed by SZWARC, for example in his review from 1976.[58]

In earlier PPX literature the formation of the biradical trimer is considered to be the critical step in initiation. BEACH[57] proposed a kinetic model of one-dimensional growth of the PPX-film on a substrate surface. Considering the activation energies determined from PPX polymerization in solution by ERREDE[59] and calculations made by KUBO[60] he concluded, that not the dimer but the trimer biradical formation gives a product lower in energy than the uncombined number of monomers. Later, GAYNOR *et al.*[25, 26] extended the assumptions of BEACH to a two-dimensional model considering also the film thickness in dependence of the position in the deposition chamber. In comparison with experimental data they also conclude that the biradical trimer is the initiating species for PPX-C. They propose the biradical tetramer to be the initiating species in PPX-D polymerization, since the electron withdrawing chlorine substituens deactivate the *p*X monomer.

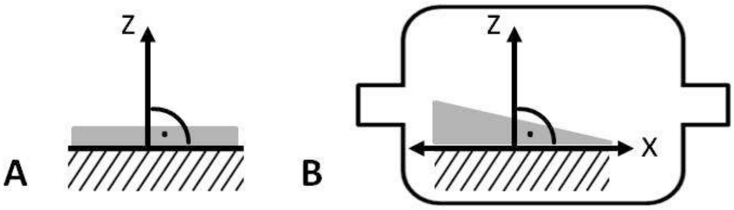

Figure 5 Illustration of the film growth direction considered in the kinetic model to determine the order of initiation reaction a) one-dimensional model: growth from the surface in z direction (BEACH[57]) b) two-dimensional model: growth in z direction and pressure gradient resulting in a film thickness gradient in x direction.

The *p*X monomers hit the surface 100-1000 times before sticking and taking part in initiation or propagation reactions,[57] for this reason the monomer gas is able to penetrate very well into confined structures[61] and achieve highly substrate conformal coatings. As already mentioned, polymerization occurs spontaneously after adsorption on the chamber walls. For differently substituted *p*X monomer species there is a threshold adsorption temperature, above which no polymerization will take place on the surface. The growth rate of the PPX chains increase with decreasing substrate temperature (due to negative activation energy) and is proportional to the square of partial monomer pressure.[57, 62] The deposition temperature is not only important for the film growth rate but also influences the PPX quality. PPX-N is a semi crystalline polymer with rather complicated thermal behaviour due to polymorphism. Polymer deposited at temperatures between room temperature and -17 °C is obtained with around 60% crystallinity in α-modification.[60, 63] Despite the high crystallinity the polymer is transparent, due to micro crystalls dispersed in the amorphous fraction. The glass transition is broad and difficult to observe in differential scanning calorimetry (DSC) though reported to be at 13 °C by KIRKPATRICK and WUNDERLICH[63] in 1985. Earlier publications by GORHAM[4] in 1966 gave a value of 80°C. Upon heating (220-260 °C) the α modification transforms into the β-polymorph, which undergoes an β_1 into β_2 polymorphic transition (260-290 °C). At higher temperatures, the β-modification melts (320-450 °C) and the polymer decomposes. Because of the irreversibility of the α to β transition upon simple cooling, the first heating curve of PPX-N differs substantially from subsequent ones. However, additional to the reversible and sharp β_1 to β_2 transition, a small annealing peak (around 200 °C) and small amount of α to β_1 transition can be observed in the second heating cycle.[63]

In PPX polymerization the activation energy for chain propagation is less than for the initiation reaction, therefore the monomer consumption in chain growth is higher and high molecular weight polymers are achieved.[2] For insoluble PPX derivatives the molecular weights were estimated by electron paramagnetic resonance (EPR) measurements of living radicals in freshly deposited films and esimated to be more than 1 million.[64] According to GORHAM typical PPX chains consist of 2000-3000 monomer units,[4] which is a about 200,000-300,000 Da. With the availability of soluble PPX derivatives, the molecular weights could be analyzed by conventional gel permeation chromatoraphy and were determined to be 60,000-600,000 Da for alkyl-substituted PPX[16] and 200,000-800,000 Da for siloxane-substituted PPX[17] (compared to polystyrene standards).

In PPX polymerization there is no real termination reaction. Since the growing chain is a biradical, recombination reactions are no termination. The chain growth stops, when the chain end radical is buried in the growing film an cannot be reached by new monomer any longer. Upon ventilation of the CVD reactor after the deposition process, oxygen diffuses into the films and reacts with the remaining radicals, as shown by EPR studies.[64]

3.3 Modification of Poly(*p*-xylylene)s

For the modification of PPX polymers, there are several possible strategies. The first and most explored method is the pre-deposition modification of the [2.2]paracyclophane precursor. This strategy is well established in industrial applications by the use of chlorinated precursors, but there is also a large number of functionalized and substituted precursors accessible at least on laboratory scale. Depending on the nature and size of the substituent on the aromatic ring substantial property changes can be achieved, as will be pointed out in Section 3.3.1. A different approach, where the bulk properties of the PPX are preserved, is the surface modification after deposition of the PPX films. This can be done for example by substitution of aromatic hydrogen or by modification of already existing functional groups on the PPX polymers (see Section 3.3.2). In the latter case pre- and post-modification complement each other. A third and completely different method is *in-situ* copolymerization of the [2.2]paracyclophane precursor with "vinyl-like", double bond containing comonomers or reactive gases during the CVD process. With this approach, which will be explained further in Section 3.3.3, bulk and surface modifications are possible. A fourth strategy is processing the PPX polymers during or after CVD to achieve composite-like or structured materials (see Section 3.3.4).

3.3.1 Pre-deposition: Modification of [2.2]Paracyclophane

Organic paracyclophane chemistry delivers access to a great number of substituted [2.2]paracyclophanes with up to four substituents per aromatic ring.[65-68] However, an important prerequisite for the successful PPX synthesis via CVD is the thermal stability of the substituent. As an example, BIER reported, that the pyrolysis of 4-carbamido[2.2]paracyclophane resulted in unfunctionalized PPX-N polymer due to thermal instability of the functional group during the CVD process.[69]

The CVD of neat [2.2]paracyclophane results in a highly crystalline, insoluble and chemically inert polymer. Depending on the substituent on the aromatic rings of the [2.2]paracyclophane either the intrinsic properties of the polymer (like solubility) or the surface properties of the still insoluble PPX film are changed, for the latter case the term reactive surface coatings has been established. Both modifications are of academic as well as industrial interest, since the CVD of PPX is an already widely used process.

Figure 6 shows a selection of available mono-substituted [2.2]paracyclophane precursors. In CVD reactions, this precursors yield PPX polymers with a statistical 1:1 ratio of non-functionalized to functionalized *p*-xylylene units, and are therefore often described as copolymers. Anyhow, in this work the term copolymer will exclusively refer to copolymers of

[2.2]paracyclophane with "vinyl-type" monomers and molecules that are no *p*-xylene derivates, as described in Section 3.3.3.

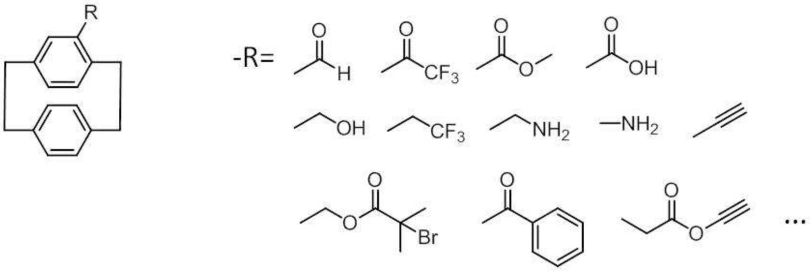

Figure 6 Selection of mono-substituted [2.2]paracyclophane precursors for PPX synthesis via CVD.[14, 69, 70]

The introduction of functional groups, like alkynes or amines, into the PPX allow direct surface modification via click-reactions or protein binding and enable precise engineering of biological microenvironments. Blood compatibility of medical implants, such as metallic coronary stents is a mayor issue, since blood plasma coagulation can cause thrombosis.[71] PPX coatings on such implants can prevent platelet adhesion. LAHANN *et al.*[70] showed that protein immobilization on poly(amino-*p*-xylylene-*co*-*p*-xylylene) and poly(hydroxy methyl-*p*-xlylene-*co*-*p*-xylylene) coated surfaces significantly improve the blood compatibility. Even more straight forward, considering immobilization of proteins or other molecules, are alkyne functionalized surfaces available from 4-ethinyl-[2.2]paracyclophane, that undergo click-reactions.[14] By using masks to cover certain substrate areas during CVD or a two furnace CVD setup combining differently substituted [2.2]paracyclophanes, LAHANN and coworkers also generate patterned and gradient PPX surfaces (Figure 7). The gradient surfaces give spatial control over the surface functionalization, as an example two differently functionalized precursor were used to generate a surface with two reactive gradients to engineer an environment for cellular signal transduction gradients[72] and controlled biomolecule immobilization.[73] The patterned PPX surfaces were generated using an 2-bromo-isobutyryl functionalized [2.2]paracyclophane, which is an initiator for atom radical transfer polymerization (ATRP) for further grafting reactions in post-deposition modifications[74] and 4-benzoyl[2.2]paracyclophane as a photodefinable coating for further surface reactions.[75]

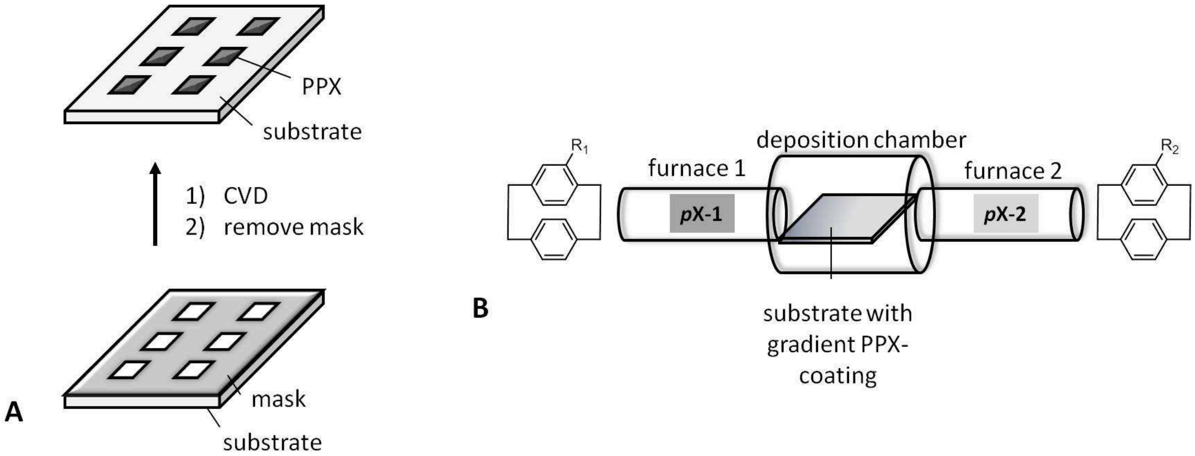

Figure 7 Scheme of surface patterning technique and gradient deposition for PPX synthesis via CVD. Applying a surface mask allows to deposit PPX on selected areas on the substrate[74] (A) and introducing precursor *p*X-1 and *p*X-2 from of two different sources into the deposition chamber leads to gradient PPX-films[72, 73] (B).

The use of bi-substituted precursors doubles the amount of functional groups available on the surface of the PPX films. However, the synthesis of such [2.2]paracyclophanes can be more difficult, because of the electronic effects governing aromatic substitutions in paracyclophanes. A selection of CVD suitable precursors is shown in Figure 8.

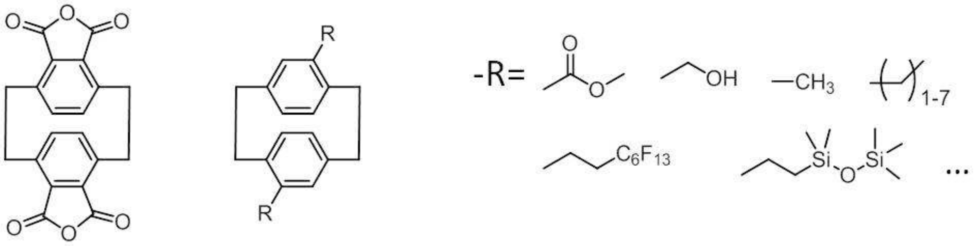

Figure 8 Selection of [2.2]paracyclophane precursors with substituents on both aromatic rings for PPX synthesis via CVD.[14, 16, 17, 69, 70]

PPX with small substituents, like hydroxy methyl are, due to the high crystallinity of the polymer, still insoluble in common organic solvents. The synthesis of [2.2]paracyclophanes with bulky substituents like alkyl chains[16] longer than propyl and siloxanes[17] led to soluble PPX derivates with substantially changed mechanical properties (Table 1). Additionally the substitution provided access to soluble PPX derivates, synthesized via CVD, which gave new insight into the polymer microstructure and enabled direct analysis of the molecular weights.

Table 1 Solubility and mechanical properties of some PPX derivates.

PPX derivate	**Solubility**	**T_g/ °C**	**E-Modulus/ GPa**	**Elongation at break/ %**
PPX-N	chlorinated biphenyls, benzyl benzoate at T> 200 °C[4], T≈ 300°C[59]	80[4] 13[63]	2.4[4, 76]	up to 250[76], 10-15[4]
PPX-C	α-chlornaphthalene at 150 °C[4]	80[4]	2.7[76] 3.17[4]	up to 200[76] 220[4]
PPX-propyl[16]	e.g. THF, chloroform at RT	2	0.31-0.42	380
PPX-butyl[16]	e.g. THF, chloroform at RT	-4	0.16	220
PPX-heptyl[16]	e.g. THF, chloroform at RT	-29	0.04	230
PPX-siloxane[17]	e.g. chloroform at RT	-10	0.02	469

T_g = glass transition temperature

3.3.2 Post-deposition: Modification of PPX-Surfaces

To modify or functionalize the surfaces of PPX-N films harsh methods have to be applied in order to introduce functional groups. This can either be done by dry methods, that involve discharge or microwave plasma treatments in the presence of e.g. ammonia or disodium sulfide, by several wet chemical methods via electrophilic aromatic substitution[77], with aggressive oxidizing agents, or by photooxidation.[78] For ultrathin PPX-N and PPX-C films SENKEVICH *et al.* reported a treatment with ammonium sulfide directly after deposition to quench remaining surface radicals and convert them into hydroxy groups.[79]

In case of PPX-C the chlorine atom, that can be used for further reactions and functionalizations. WAHJUDI *et al.*[80] demonstrated a number of ways to surface modify PPX-C films by different chemical reactions (Figure 9). Of special interest are PPX films which comprise hydroxy or sulfur groups on their surface, in order to improve adhesion to metals and allow further reactions with biomolecules. The authors further reported successful grafting of thermoresponsive Poly(*N*-isoproyl acrylamide) (PNiPAAM) via ATRP on the PPX-C surfaces which were functionalized with an 2-chloro-propionyl substituent. The attachment of PNiPAAm is of particular interest for cell culturing[81] and protein adhesion,[82] since the polymer changes from hyrophilic to hydrophobic at its lower critical solution temperature (LCST) of about 32 °C.

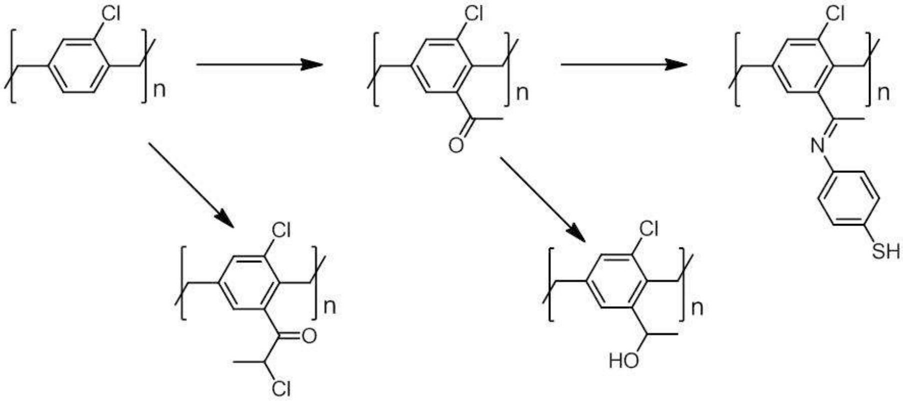

Figure 9 Examples of post-deposition functionalization of PPX-C as described by WHAJUDI *et al.*[80]

Similar *grafting from* approaches utilizing PPX functionalized with other initiators were reported by JIANG *et al.*, ZHENG and ZHANG *et al.* JIANG *et al.*[74] used an 2-bromo-isobutyryl functionalized [2.2]paracyclophane precursor (see also Section 3.3.1, Figure 6) and deposit on masked substrates to achieve a patterned PPX-initiator surface. After the surface initiated grafting with oligo(ethylene glycol) methyl ether methacrylate the substrates show non-fouling behavior. ZENG[83] reported the use of α,α'-dibromo-*p*-xylene as precursor for the CVD of poly(α-bromo-*p*-xylyene), that was applied directly to initiate ATRP grafting reactions with methyl methacrylate. Grafting reactions with *N*-isopropyl acrylamide (NiPAAm) for cell adhesion tests were performed by ZHANG *et al.*[84] Therefore the authors functionalized PPX-C with chloropropionyl substituents by FRIEDEL-CRAFTS acylation.

3.3.3 *In-situ*: Modification by Copolymerization

As mentioned before, in the present work the term "copolymer" will refer to polymers composed of *p*-xylylene units and "vinyl-like" monomers or other molecules that are no derivates of *p*-xylene.

The synthesis of such copolymers was already subject to research at the beginnings of PPX chemistry. One synthesis route explored by ERREDE *et al.*[85] describes the copolymerization in solution with olefinic comonomers and other molecules. The author reported successful copolymerization reactions with maleic anhydride, diethyl maleate, dimethyl fumarate, acrylnitrile, *n*-butyl acrylate and styrene as well as chinones. For this reactions the reactive *p*X was obtained by pyrolysis of *p*-xylene, trapped in cooled solvent (e.g. toluene at -78 °C) and added slowly to the comonomer or comonomer solution that was maintained at temperatures at about 100 °C. The obtained products were reported to show thermoplastic behavior and, at least in the case of poly(*p*-xylylene-*co*-maleic anhydride) to dissolve slowly in warm 10% KOH solution. Reactions carried out at different conditions, like mixing the monomer and heating of the reaction mixture, did not result in copolyermization but unmodified PPX, due to the high reactivity of the *p*X monomer. IWATSUKI *et al.*[86] reported, the copolymerization in solution at 50 °C for different chlorine substituted *p*-xylylenes (e.g. α,α,α',α'-tetrachloro-*p*-xylen (and α,α,α',α'-2,5-hexachloro-*p*-xylene), and demonstrated by this means that electron withdrawing substitutens on the aromatic ring and the methylene groups of the *p*-xylylene reduce their reactivity and allow copolymerization with vinyl-type comonomers.

In a similar procedure a polymeric products were obtained from warming up a solution of *p*X and phosphorus trichloride in hexane from -78 °C to room temperature.[87] The obtained polymer poly(*p*-xylylenephosphinic chloride) was reported to be esterified with methanol to give a partially soluble product, converted to polymeric phosphonic acid upon treatment with aqueous sodium hydroxide solution and react with amines. Similarily *p*X reacted with other phosphorous trihalides and dichlorophenylphosphine. ERREDE *et al.* furthermore described polymerization reactions of *p*X in solution with SO_2, mercaptanes, nitroso compunds, and the gaseous radicals NO_2, NO and O_2[85, 88] They also reported that *p*X does not react readily with most chain transfer agents like carbon tetrachloride, toluene, benzochinone and others. An overview of the successfully obtained copolymers from *p*X solutions is given in Table 2.

Of particular interest from the above mentioned copolymers are the PPX-peroxides.[88, 89] At ideal conditions an alternating copolymer of *p*-xylene units and O_2-moieties was prepared. The PPX-peroxides were reported to be insoluble at room temperature and to decompose explosively at temperatures about 100 °C. By controlled decomposition studies was found, that peroxide moieties are not statistically distributed in the copolymer but rather pure PPX-N blocks exist. As decomposition products crystalline PPX-N was found together with the aromatic, oxygen containing decomposition products terephthalaldehyde, *p*-hydroxymethyl benzaldehyde and *p*-xylene glycole.

After the thermal cleavage of the peroxide bond of PPX-peroxides, ERREDE reports fast decomposition in either two aldehyds and hydrogen or one aldehyde and one alcohol. The decomposition product ratio showed a certain dependence on the decomposition temperature chosen.

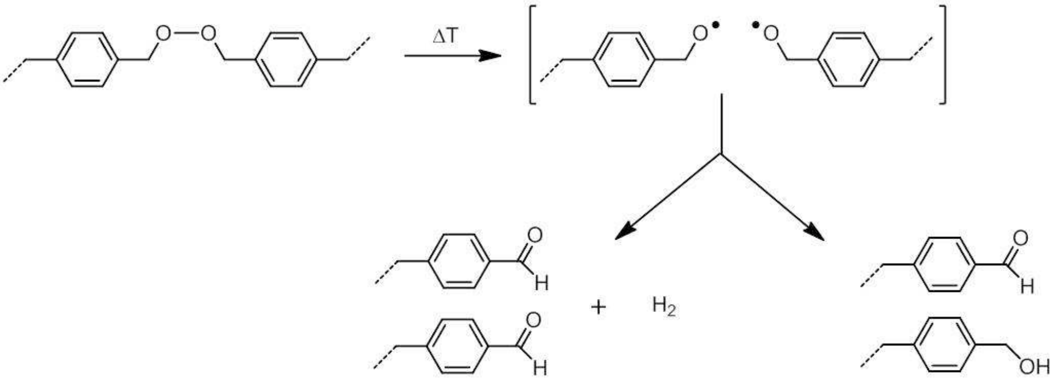

Figure 10 Thermal cleavage of peroxide bond in PPX-peroxide suspended in water as described by ERREDE.[88] After the homolytic cleavage of the peroxide bond the alkoxy radicals undergo fast reactions resulting in either two aldehyds or one alcohol and one aldehyde.

However, copolymers obtained by this method are not suitable for conformal coatings as known for PPX via CVD. Therefore the approach of the *in situ* copolymerization during the CVD process received more attention and was investigated by different groups. In this case the reactive *p*X monomer is mixed with comonomer vapor behind the pyrolysis furnace, requiring a modified CVD setup (see also Section 5.3.1). First copolymers with maleic anhydride (MA) and chloroprene (CP) were reported by SCHAEFGEN *et al.*[19, 20] in 1955 using the SZWARC route. At the same time copolymerization attempts with styrene,[20, 90] butadiene[20] and acrylonitrile[20] were reported to be not successful. Further investigations were carried out in 1991 by SOCHILIN *et al.*[21] who for the first time varied deposition temperatures systematically. By this means copolymers of [2.2]paracyclophane with maleic anhydride (T_{dep}= RT), 4-vinylpyridine (4-VP) (T_{dep}= -80 °C), *N*-vinylpyrrolidone (N-VP) (T_{dep}= -30 °C) and styrene (S) (T_{dep}= -80 °C) were obtained. The deposition of the comonomer was carried out on a target placed perpendicular to the monomer flow. A few years later second group around GAYNOR, SENKEVICH and DESU described further successful copolymer synthesis. The copolymer synthesis were carried out with unsubstituted or chloro-substituted [2.2]paracyclophane and 9-vinylanthracene (9-VA),[23] 4-vinylbiphenyl (4-VB),[23] perfluorooctyl methacrylate (PFOMA)[23-25] and *N*-phenyl maleimide (NPMI)[26] as comonomers. All reported copolymers were insoluble and copolymer analysis was accomplished by IR-spectroscopy, elemental analysis and wavelength dispersive x-ray analysis. The copolymers were deposited parallel to the monomer flow direction and the composition varied with the position in the deposition chamber. The authors reported furthermore property changes of the copolymers with respect to the PPX homopolmyers, like lower refractive index for poly(chloro-*p*-xylylene-*co*-perfluorooctyl methacrylate).[24] More details of this copolymers are collected in Table 3.

Table 2 Overview of PPX-copolymers and telechels obtained from solution polymerization of *p*-xylylene.

Comonomer	Ref.	Properties of the resulting polymer
SO_2	[85]	insoluble with composition equal to monomer ratio in solution, soften at 200°C (0.5 mbar).
NO and NO_2	[85]	telechels with less than 10 *p*X units
O_2	[85, 88, 89]	insoluble polymer peroxide, *p*X to peroxide ratio up to 1:1
PCl_3	[87]	polymeric product poly(*p*-xylylenephosphinic chlride), and derivates after polymer analogous reactions
PX_3 X=H, I, Br	[87]	low molecular weight products, telechels, *p*-xylyle dihalide as byproducts
p-nitroso-*N*,*N*-dimethylaniline 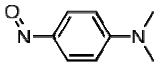	[85]	soluble in concentrated HCl, precipitates in water
α-nitroso-β-naphthol 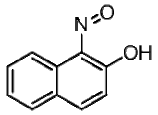	[85]	soluble in organic solvents, softens around 200 °C
nitrosobenzene 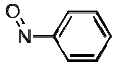	[85]	soluible in organic solvents, softens around 200 °C
thiophenol 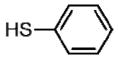	[85]	insoluble polymer, *p*X to thiopenol ratio 21:1
n-octyl mercaptan 	[85]	insoluble polymer
chloranil 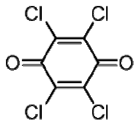	[85]	gelatineous polymer, *p*X to chloranil ratio 1.8:1
dichlorophenyl-phosphine 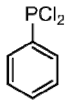	[87]	high molecular weight polymer, hydrolizable to poly(*p*-xylylenephenylphosphine oxide) soluble in actic acid

Despite the successful copolymerization and the high potential of PPX-copolymers, all copolymers reported by Sochilin and Gaynor *et al.* contained unreacted comonomer and needed further purification before analysis. Composition gradients were reported for all copolymers obtained by Gaynor *et al.*, who deposited parallel to the monomer flow. Sochilin *et al.*, who deposited on a target perpendicular to the monomer flow, report a gradient for poly(*p*-xylylene-*co*-*N*-vinylpyrrolidone) with respect to the center and the edges of the deposition target. Similar oberservations were also reported by Bier for PPX polymer deposited from mono functionalized [2.2]paracyclophanes in both deposition directions, [69] and Lahann coworkers who use this characteristic of mono functionalized precursor to generate gradient films (see Section 3.3.1). In all cases the gradient copolymers were deposited in CVD setups with static sample holder.

More copolymers were synthesized by Stumpe and reported in the context of a diploma thesis in 2003.[91] Here [2.2]paracyclophane and 4-chloro[2.2]paracyclophane were successfully copolymerized with different methacrylate comonomers, like 2-hydroxyethl methacrylate (HEMA) and maleic acid derivates, like dimethyl maleate. For poly(*p*-xylylene-*co*-HEMA) maximum HEMA contents of 24% and water contact angles of 45° were reported.

Table 3 Overview of PPX-copolymers reported in literature, synthesized via CVD.

Comonomer	Ref.	Pre-cursor	Conditions	Comments
PFOMA 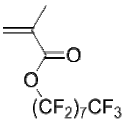	[25]	DPX-C	T_{vap}= 54 °C, T_{subl}=115 °C, p≈ 0.37 mbar T_{dep}=20-28 °C	parallel deposition
	[23]	(DPX-N) DPX-C	T_{vap}= 64-66°C, T_{subl}=128 °C, p≈ 0.37 mbar T_{dep}=15-20 °C	parallel deposition, max (T_{vap}66°C, T_{dep}15°C)≈ 35%, max (T_{vap}64°C, T_{dep}20°C)≈ 7-20% depending on position in deposition chamber, lower refractive index than PPX-C
	[24]	DPX-C	T_{vap}= 54°C, T_{subl}=95 °C, p≈ 0.37 mbar T_{dep}=18 °C	parallel deposition, thickness gradient depending on position in deposition chamber

max = maximum comonomer content, T_{vap}= comonomer vaporization temperature, p= base pressure

Table 3 continued Overview of PPX-copolymers reported in literature, synthesized via CVD.

Comonomer	Ref.	Precursor	Conditions	Comments
maleic anhydride 	[19]	*p*-xylene	p= 1.3-6.7 mbar T_{dep}=RT	-
	[20]	*p*-xylene	feed ratio *p*X/MA 1.2:1	yield 10%, swelling in acetone and chloroform, *p*X/MA 2-14:1 depending on position in deposition chamber
	[21]	DPX-N	T_{dep}=RT and -30 °C	max= 35% (T_{dep}= RT), MA content at T_{dep}=RT > T_{dep}=-30 °C, T_g= 98 °C, perpendicular deposition
4-vinyl-pyridine 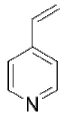	[21]	DPX-N	T_{dep}= -80 °C and lower	good optical and mechanical properties, amorphous, T_g= 145 °C
styrene 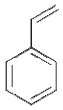	[21]	DPX-N	T_{dep}= -80 °C and lower	not transparent, brittle, amorphous
chloroprene 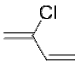	[20]	*p*-xylene	feed CP/*p*X 3.1-4.4:1	swells in boiling tetralin, CP content *p*X/CP 8:1, 38:1
	[19]	*p*-xylene	p= 1.3-6.7 mbar, T_{dep}= RT and -80 °C	-
9-VA 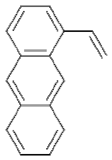	[23]	DPX-N DPX-C	T_{vap}= 165°C, T_{subl}=128 °C, p≈ 0.13 mbar T_{dep}=20-23 °C	-
4-VB 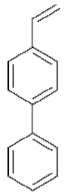	[23]	DPX-N DPX-C	T_{vap}= 160°C, T_{subl}=128 °C, p≈ 0.13 mbar T_{dep}=20-23 °C	parallel deposition, increased thermal stability

max = maximum comonomer content, T_{vap}= comonomer vaporization temperature, p= base pressure

A different strategy, that yields surface functionalized films by copolymerization with double bond containing molecules is based on the SOLID technique. This is a special CVD approach, where the activated precursor is deposited onto a liquid surface where it forms a film. If *p*X is deposited onto a suitable liquid, the radicals of the growing PPX chain can react with present double bonds and bind these molecules covalently to the PPX chain.

BOLOGNESI *et al.* reported the incorporation of different unsaturated flourenes into PPX-C, achieving by this means surface functionalized PPX-C films.[92] NADDAKA *et al.* later describe the reaction of different halogenated acrylates and methacrylates with PPX-C via the SOLID method. The amount of incorporated comonomer was found to be in accordance with their predicted reactivity. Furthermore they report the subsequent reactions of the ester groups with amines, to demonstrate the possibility of further functionalization of the obtained PPX films.[93]

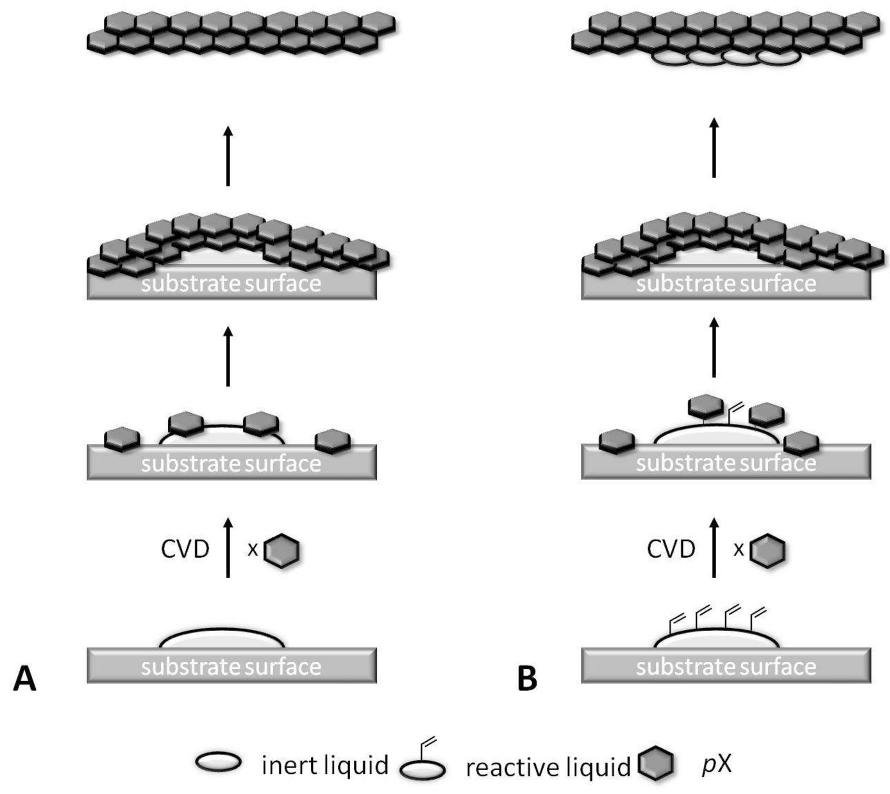

Figure 11 Schematic representation of the SOLID-process on an inert liquid (A) and a reactive liquid (B) for PPX polymers. PPX deposits onto the liquid during CVD, in case of an reactive liquid, these molecules are incorporated into the PPX film.

3.3.3.1 Copolymerization Mechanism

In addition to the experimental work on PPX copolymers summarized in Section 3.3.3, theoretical studies on the copolymerization mechanism and monomer reactiviy were reported by BOBROWSKI, FREZA and SKURSKI. Recently they provided theoretical calculations for the reactivity of *p*-xylylene[94] and *p*-xylylene dimer[95] for the reaction with vinylic molecules

($CH_2=CHY$, $CH_2=CY_2$). Activation barriers for the reaction with vinylic monomers were generally smaller considering *p*-xylylene dimer, while for both *p*-xylylene species the activation barrier decreased with increasing electronegativity of the substituent Y on the vinylic monomer (e.g. Y= H, Cl, $COOC_6F_5$, NO_2, C_6F_5, CF_3, C_6H_5, CN). For molecules with strong electronegative substituents, like $CH_2=C(CN)_2$ the activation barrier for the reaction with *p*-xylylene is competitive to the activation barrier for the formation of a *p*-xylylene biradical dimer, and inititation with *p*-xylylene can be considered an alternative mechanism for copolymerization. However, for the reaction with most vinylic monomers, the polymerization is considered to be initiated via the *p*-xylylene biradical dimer.

A smilar mechanism is described by GAYNOR et al.[25] who mention the necessity of biradical trimers in case of PPX-N and PPX-C and biradical tetramers in case of PPX-D to initiate either homo or copolymerizations with vinylic monomers.

Considering the copolymerization mechanism NADDAKA et al.[93] describe together with BOBROWSKI two alternative pathways with different kinetic barriers for the reaction of *p*-xylylene dimers with (meth)acryl monomers (Figure 12). According to the authors the kinetic energy barrier on pathway A for direct attack of the DPX on the vinylic carbon $\mathit{C}H_2=CR^1COOR^2$ is considerably less than for the hydrogen abstraction described in pathways B. Furthermore it is similar to kinetic barriers in PPX homopolymer propagation, wherefore pathway A is a competitive mechanism for chain growth. However, the kinetic barriers for all pathways decrease with increasing electronegativity of the substituent on the double bond.[95]

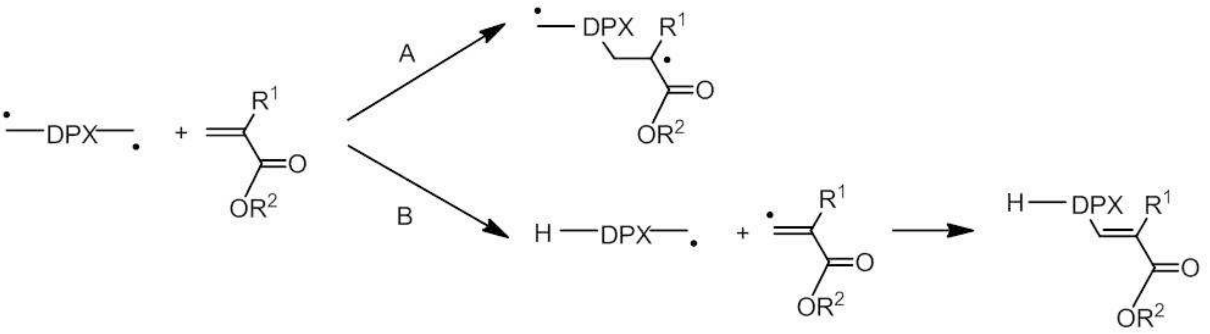

Figure 12 Possible reaction pathways for copolymerization of *p*-xylylene biradical dimer (DPX) with (meth)acrylic monomers as described by BOBROWSKI *et al.* and NADAKKA *et al.* Pathway A describes direct electrophilic attack of the *p*-xylylene biradical dimer (DPX) on the vinyl carbon atom leading to a biradical species that is able to continue polymerization. Pathways B comprises a larger kinetic barrier than A for the hydrogen abstraction and will not lead to further chain growth.[93, 96]

In further studies BOBROWSKI et al. calculate energy barriers and rate constants for chain growth in copolymerization of *p*-xylylene (*p*X) with vinylic comonomers (V) $CH_2=CHY$ (with Y= H, Cl, $COOC_6F_5$, NO_2, C_6F_5, CF_3, C_6H_5, CN) and $CH_2=C(CN)_2$.[96] BOBROWSKI et al. found, that regardless of the last units in the growing polymer chain (*p*X or V), the attachment of *p*X was energetically favorable (lower activation energy and lower potential energy of the product) and proceeds with a substantially higher rate constant (2 to 6 magnitudes higher). This means that even in the presence of both monomers the chain will most likely grow by the attachment of *p*X monomers. Only in the cases of Y=NO_2, $COOC_6F_5$ and CH_2=C(CN)$_2$ the attachment of the V comonomer is competitive or equally likely. From the obtained rate constants the authors also calculated the reactivity ratios r_{pX} and r_V for the addition of *p*X and V to any possible chain sequence (Table 4). As expected from the rate constants, the r parameters show that the addition of *p*X is strongly favored, as long as it is available. The resulting polymer therefore will be rich in *p*X and comprised of longer *p*X blocks. However, all calculations are based on ideal situations concerning monomer distribution in the reaction chamber. The authors underline, that the conclusions on copolymer composition derived from their calculations cannot be used to completely explain the compositions of real copolymers. When copolymerization takes place after introduction of both monomer in gaseous state into the reaction chamber, the chains are likely to be composed predominantly of *p*X units and larg *p*X blocks. In case of copolymer obtained via the SOLID method, where PPX is deposited onto a reactive liquid, the chains will be composed or more vinylic comonomer as they grow further into the droplet.

Table 4 Reactivity ratios r_{pX} and r_V calculated by BOBROWSKI et al.[96] (p= 1013hPa*, T=298.15K)

Vinyl substituent Y	r_{pX}	r_V
H	$2.57 \cdot 10^7$	$3.88 \cdot 10^{-6}$
Cl	$3.13 \cdot 10^5$	$1.98 \cdot 10^{-4}$
CF_3	$2.12 \cdot 10^5$	$3.39 \cdot 10^{-6}$
C_6H_5	$1.28 \cdot 10^5$	$1.62 \cdot 10^{-5}$
CN	$2.92 \cdot 10^3$	$1.41 \cdot 10^{-5}$
$COOC_6F_5$	326.29	$2.50 \cdot 10^{-9}$
NO_2	234.67	$2.54 \cdot 10^{-5}$
=C(CN)$_2$	4.96	$4.29 \cdot 10^{-9}$

* CVD polymerization typically takes place at p<< 1013hPa, BOBROWSKI et al. also calculated rate constants for p=10 Pa, but gave no r parameter

Considerable differences in reactivity ratios for *p*X and several comonomers ($r_{pX} >> r_{co}$) were also estimated by GAYNOR et al. using their two dimensional kinetic model based on BEACH's assumptions (see Section 3.2).[25] To overcome this problem and grow PPX copolymer films rich in comonomer they proposed to grow films at deposition temperatures where the *p*X component reaches its threshold adsorption temperature while the comonomer still condenses on the substrate.[26] Availability of comonomers suitable for this model is limited because they need to have extremely low vapor pressures.

3.3.4 *In-situ*: Modification by Structuring and Shaping

The methods for PPX modification presented so far were chemical modification of the [2.2]paracyclophane precursor, modification of the polymer structure by copolymerization or are a combination of both. However, many of the PPX derivates or copolymers are still insoluble and infusible. The special synthesis from the gas phase via CVD offers the possibility to shape and structure the PPX during its formation. Applying special techniques, namely oblique angle deposition (OAD), template coating and gradient coating, PPX can be modified in order to adapt a special structure, shape or surface functionalization. One example for template coatings applying as substrate mask was already given in Figure 7, together with the reactive gradient approach.

In the OAD method (Figure 13), the substrate is tilted in a special angle, e.g α= 10°, with respect to the monomer flow. As a consequence the growing chains on the substrate surface exert some shielding effects, leading to a spatially inhomogeneous film growth. Unstructured, planar films in standard PPX coatings are carried out at an angle of 90°, that is a monomer flow perpendicular to the deposition target. DEMIREL *et al.* reported that by controlling the rotation of the substrate holder further control of the film morphology was achieved.[97] As a result columnar, helical or chevron-like wires were grown from the substrate surface with 100-150 nm diameter and an aspect ratio up to 1:1000. Due to this morphology the PPX films show higher surface area, porosity and increased water contact angles than films of the same PPX derivate with smooth surfaces. The author report furthermore, that depositing PPX via OAD on porous templates the diameter of the grown PPX structures is well controllable.[98]

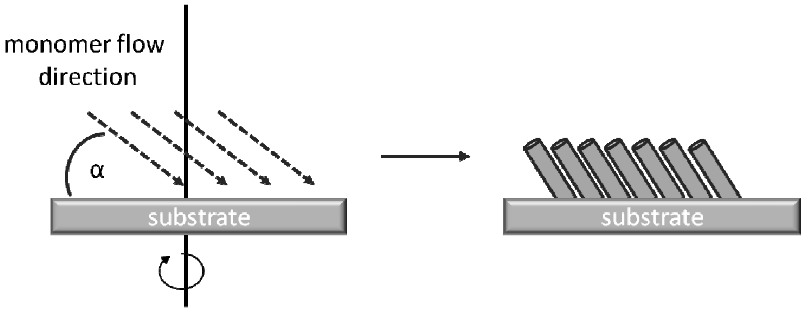

Figure 13 Schematic representation of the oblique angle deposition technique (OAD). If the monomer flow hits the surface in a certain angle α= 5-15°, the PPX wires grow in form of helices, columns or chevron (depending on substrate rotation), giving the film a special morphology and surface structure.[97, 99]

A widely applied technique for the generation of nano and micro tubes is the TUFT (tubes by fiber templates) process. Here polymer fibers, e.g. obtained by electrospinning (Section 3.4) are coated with PPX via CVD and after removal of the template fiber, generally by extraction, a hollow PPX tube is obtained.[100] This concept is applicable to a great variety of polymer fibers and different PPX derivates.[30, 101] Examples are the immobilization of catalysts inside the PPX tube, as shown by MITSCHANG et al.[28].

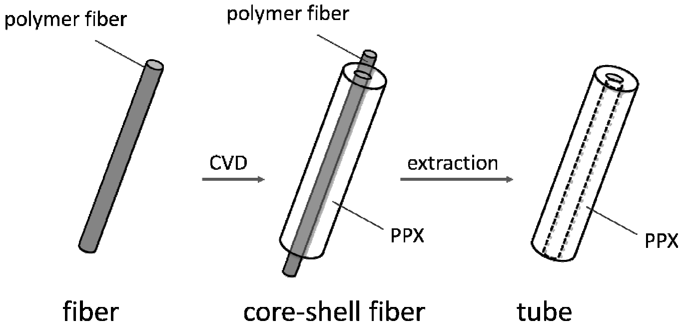

Figure 14 Schematic illustration of the TUFT (tubes by fiber templates) process. A template fiber is coated with PPX by CVD, after template extraction a PPX tube remains.[100]

The preparation of free standing micro channels for microfluidic and *lab on a chip* approaches can be prepared with template trenches (Figure 15). In this concept a substrate with trenches with high aspect ratios are coated with PPX. In general, PPX gives highly conformal coatings of such surface geometries and is famous for its high penetration depth. Anyhow, above a certain thickness the trench is closed and a micro channel on the bottom of the trench remains. By this means either substrate embedded[102] or, after removal from the template, free standing micro channels[103] are obtained.

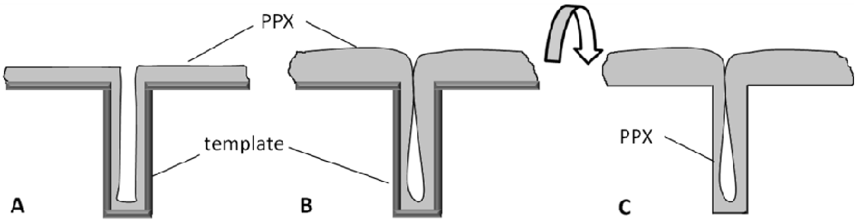

Figure 15 Schematic representation of the template method to generate micro-fluidic channels. If template trenches with a suitable aspect ratio (A) are coated with a certain amount of PPX the trench is closed on the top (B) leaving behind a micro-channel after removing the PPX film from the template trench (C).

3.4 Electrospinning

Electrospinning is an elegant and highly versatile processing technique for polymer solutions. In this physical process, mentioned for the first time in a patent by FORMHALS[104] in 1934, polymer fibers with diameters in the range of micrometer or even a few nanometer can be obtained. Theory and applications of electrospinning were broadly investigated and reviewed,[30, 31, 105, 106] but are nevertheless still a field of extremely fast development. This is due to the broad range of potential applications and numerous possibilities to vary processing parameter as well as spinning techniques which influence fiber formation and morphology. In this work, only the basic principle of electrospinning will be explained, detailed information can be found in literature references.

In electrospinning a strong electric field is applied to a droplet of polymer solution (or melt) formed on the tip of a needle. This leads to the formation of a cone (TAYLOR cone[105]) from which, if the electrical charges overcome the surface tension of the liquid, a jet emerges (Figure 16). Due to bending instabilities introduced by the electrical field the charged jet moves towards the counter electrode in a helical motion.[107] During this motion the solvent evaporates and the polymer fiber is stretched until it finally deposits as a thin and solid polymer fiber on the counter electrode.

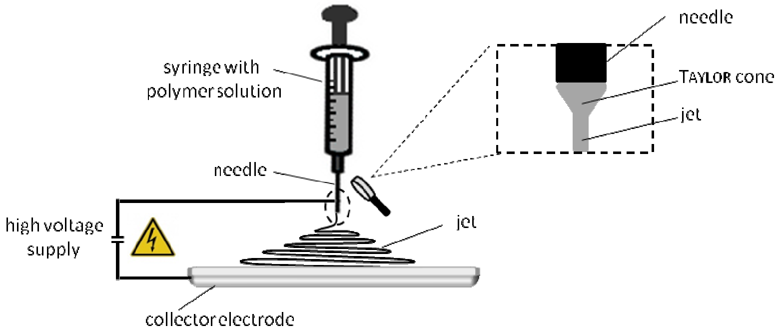

Figure 16 Schematic illustration of an electrospinning setup, showing the polymer solution in a syringe, the electrospinning jet and the counter electrode. On the tip of the needle the solution forms the TAYLOR cone, from which the jet emerges (magnification).

Among the parameter influencing the electrospinning process are viscosity, surface tension and electric conductivity of the solution, as well as strength of the applied electric field and distance between needle and counter electrode. The surface tension of a solution tries to maintain the surface area per unit mass as small as possible and therefore favors a spherical shape (RAYLEIGH instability[108]). The repulsion of excess charges imposed by the external electric filed, on the other hand, drive the system towards the opposite and favor an increase in surface area. Viscoelastic forces resist rapid shape changes, and therefore favor formation of smooth fibers.[109] The complicated interplay of this parameter decides whether small droplets of polymer solution move towards the collector electrode (electrospraying) or a continuous polymer jet is formed and a fiber mat is collected (electrospinning). In an “intermediate” state fibers with spherical or spindle-shaped thickenings (beads or bead-on-string fibers) are observed. In this case the polymer solution is of sufficient molecular weight and viscosity, so that the entanglement of the polymer molecules prevents the breakup of the jet and therefore the spraying. In general, beads are formed on electrospun fibers when the spinning solution is of low polymer concentration, and therefore of low viscosity, possesses low charge density and high surface tension.[109]

Considering fiber morphology solvent evaporation[110] and relative humidity[111] are crucial factors. Humidity has an influence on the charge density of the jet, since water vapor molecules in the air lead to charge dissipation. Therefore, at low humidity the charge on the jet is higher.[112] For the same reason fiber thickness increases with increasing humidity, since the charge repulsions are responsible for thinning the jet on its way to the counter electrode.

The generation of porous fibers can be achieved with appropriate solvents and polymer concentrations,[113, 114] by spinning of polymer blends and selectively removing one of the polymer components[115] and by controlling relative humidity.[111]

The generation of micro- and nano fiber networks is interesting for applications in filter technology, for membranes, as catalyst supports and special textiles where a high surface to volume ration is required. An additional surface topology, like pores or beads on electrospun fibers will increase this ratio, influence the wetting behavior and might play an important role in specific adsorption processes.

A different approach to increase the surface are and diminish the pore size of a nonwoven, is the formation of nano nets during electrospinning. This phenomenon is known for polyamides,[116, 117] polyacrylic acid,[118] polyurethane[119] and gelatin.[120] According to DING et al.[118] and WANG et al.[119] the nano nets are formed when charged droplets, emerging from the needle during the electrospinning process, are forced to phase separate by solvent evaporation in the electric field. Figure 17 shows a schematic representation of the “electronetting” as described by DING Et al. and WANG et al. Different forces act simultaneously on the droplet: while the electric force and gravity accelerate the droplet towards the counter electrode, air resistance is deforming it. Coulomb forces, caused by repelling charges, try to expand the droplet and are counteracted by the surface tension of the solution and viscoelastic forces. The morphology and area density are reported to be strongly dependent on the voltage, humidity, solvent, salt concentration and distance from needle to collector.

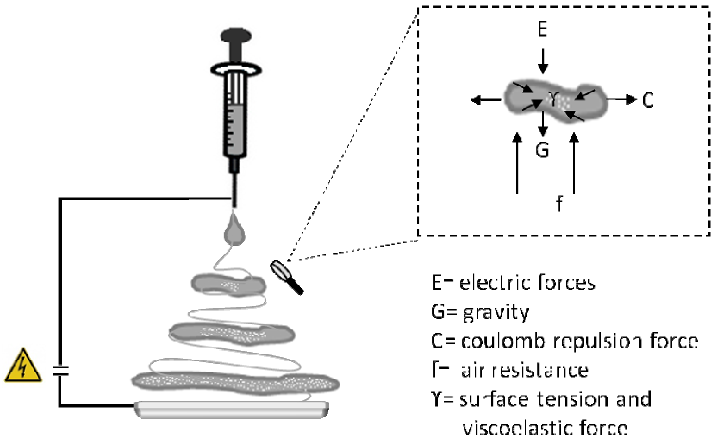

Figure 17 Schematic illustration of the formation of nano nets by electrospinning as described by Ding et al.[118] and Wang et al.[119] The forces acting on the droplet are: electric force and gravity, that carry the droplet from the needle to the collector; repulsive forces (coulomb forces) of the charges expand the droplet, while air resistance is deforming it. Surface tension and viscoelastic forces counteract and try to contract the droplet. Evaporating solvent leads to phase separation and net formation from the droplet.

3.5 Water Contact Angle, Superhydrophobicity and Self-cleaning Surfaces

Tuning the wetting behavior of surfaces is a topic of great interest in terms of basic scientific as well as application oriented research. Of mayor importance are superhydrophobic and self-cleaning surfaces obtained by micro and/or nano structuring of materials, commonly known as the “Lotus effect”.[121] On a self-cleaning surface an impacting water droplet rolls off and is able to remove dirt from the surface during its rolling motion. Superhydrophobicity and self-cleaning ability are useful for textiles, windows and paints, but also as non-fouling and non-icing surfaces.[122]

In the following the basic concept of water contact angle θ (CA) determination and superhydrophobic surfaces will be explained qualitatively. Detailed information can be found in the review by Roach et al.[122] and other cited literature.

The hydrophobicity or hydrophilicity of a surface is determined by the angle between a water droplet that contacts a surface and the surface itself (Figure 18 A) (Young-model[123]). The contact angle depends on the surface energy of both solid and liquid, and the interfacial forces (Υ) between air/gaseous phase (G), solid (S) and liquid (L).

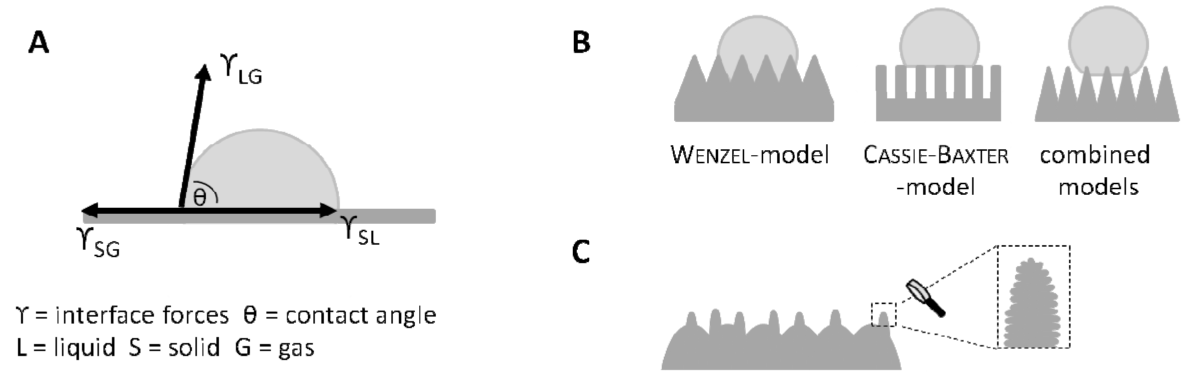

Figure 18 Schematic representation of contact angle determination and influencing parameter[124] (A), different models for real surfaces as described by and Roach et al.[122] (B) and a surface with multi scale roughness (C).

Important for the description of the wetting or non-wetting behavior of a surface are also the contact angle hysteresis, which is the difference in CA between a droplet of increasing or decreasing volume (advancing and receding contact angle), and the roll-off angle (RA) (angle to which a surface needs to be tilted before a water droplet rolls off). If CA hysteresis and RA are low, droplets roll off the surface easily.

Real surfaces display a certain roughness, which has to be taken into account for CA calculations. Different models (Figure 18 B) can be used to describe the behavior of a droplet on a real surface. The Wenzel-model[125] refers to a droplet wetting the surface, while the Cassie-Baxter-model[126] describes a droplet resting on top of the surface features. In the Cassie-Baxter-model air is entrapped between the surface and the droplet leading to an increased liquid/air interface. If the Wenzel, the Cassie-Baxter-model or a combination of both is suitable to describe the wetting or non-wetting on a specific surface depends on its intrinsic hydrophobicity as well as the geometry and positioning of its surface features.

In general, surfaces with water CA <90° are described as hydrophilic, since the water droplets spread and wet the surface. Is the CA >90° the surface is considered hydrophobic. At CA >150° the term superhydrophobic is used. If superhydrophobicity is observed, as for example on the lotus leaf, the surfaces often display roughness on different length scales (Figure 18 C). This multi scale roughness facilitates furthermore that droplets roll off the surfaces. The combination of high CA and small CA hysteresis or low RA leads to self-cleaning surfaces, where impacting water droplets clean the surface easily.

3.6 Polymer Foams

Polymer foams can be prepared from most thermoplastic polymers and by several methods. They do generally consist of a solid polymer matrix and a gaseous phase. The polymer matrix can be composed of a single polymer or a mixture of polymers (e.g. in form of a blend or interpenetrating network) and may contain additives or fillers. Though there are different ways of foam generation, common to all approaches is the fundamental process of gas bubble formation in a liquid system, the growth and stabilization of the bubbles, and finally the solidification of the polymer matrix. The gas needed for foam production can either be generated *in situ* by a gas generating reaction (chemical foaming, like CO_2 formation in PU and PUR foams) or is added as so called blowing agent (physical foaming, as e.g. in PS foams). Anyway, the gas is first dissolved in the liquid matrix until a supersaturated state is reached and bubbles form. The formation of a second phase requires nucleation and nucleation agents can help to accelerate this process. Bubble growth and stabilization has to be controlled with additives and/or foaming parameter (e.g. temperature, time) are crucial for the internal structure of a foam.

In an initial state the gas bubbles are isolated and spherical, when they grow to a certain point they touch each other, distort, and form the so called cells, with flat faces due to the touching of adjacent cells. These foams are called closed-cell foams (see Figure 19), because the faces act as physical barrier between the cells. This foam type is used in packaging and thermal insultiaon. If the faces collapse, only the edges and vertexes remain. Such foams are called open-cell foams (Figure 20) and comprise interconnected cells, where matter exchange between the cells can take place easily. Typical open-cell foams are sponges and cushions.

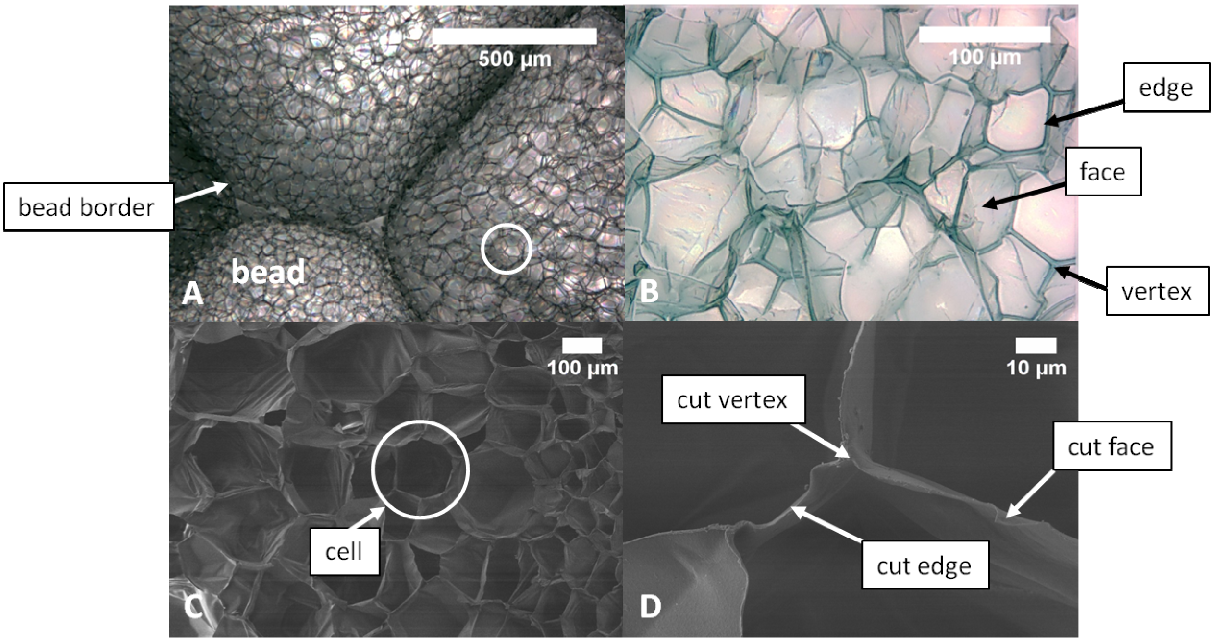

Figure 19 Closed-cell foams. Microscope images (A,B) and SEM micrographs (C,D) of different EPS foams.

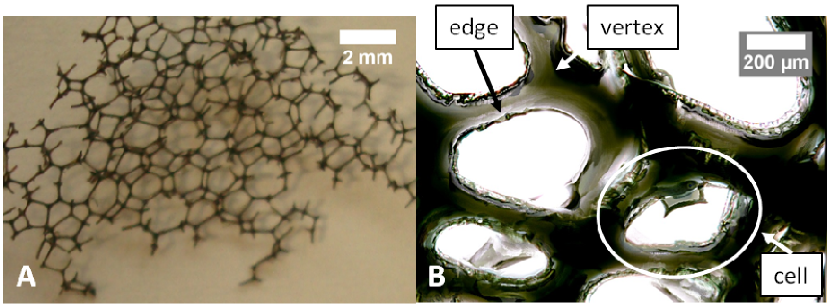

Figure 20 Photograph (A) and microscope image (B) of an open cell foam.

The mechanical properties of polymer foams depend to a great extend on the intrinsic properties of the polymer material it is composed of. However, due to the cellular microstructure, their properties differ from the solid material. The cell structure (open or closed) is less important, since most man-made foams behave like open-cell foams, because during the manufacturing process most of the material is concentrated in the cell edges.[127] Another crucial factor is relative density, which correlates to the cell size. The performance of a polymer foam upon compression and its impact strength are important for their area of application and classify them as elastic, plastic or brittle foams. More specifically, this means which load a foam is able to bear before compression and before collapsing, and its ability to recover from a load. The behavior upon stretching, elongation and bending is equally important. A detailed description of the mechanical behavior of cellular solids is given by ASHBY and MEHL MEDALIST.[127]

A special type of closed-cell foams are bead foams, like expanded polystyrene foam (EPS, trade name e.g. Styropor® from BASF). As show schematically in Figure 21, the production of EPS can be divided in two mayor steps, first symmetrical polystyrene beads, containing a blowing agent such as pentane, are exposed to heat and expand. This pre-expanded beads are filled into a mold and further expanded with steam. Since the second expansion takes place in a confinement the beads fuse and glue together. Figure 19 A shows a low magnification image of EPS, where four beads, each formed of multiple small foam cells, are visible. Bead size, final density of the EPS and the amount of "free space" between the beads are controlled by foaming parameter like time and temperature.[128] This "free space" is connected, forming an air channel within the foam and is the inverse structure of an open-cell foam. The internal structure of a bead foam is a two scale microstructure, comprised of the beads and air channels on the one hand, and on the closed-cell foam forming each bead on the other hand. Therefore the mechanical behavior of EPS foams depends also on the quality of the bead junctions.

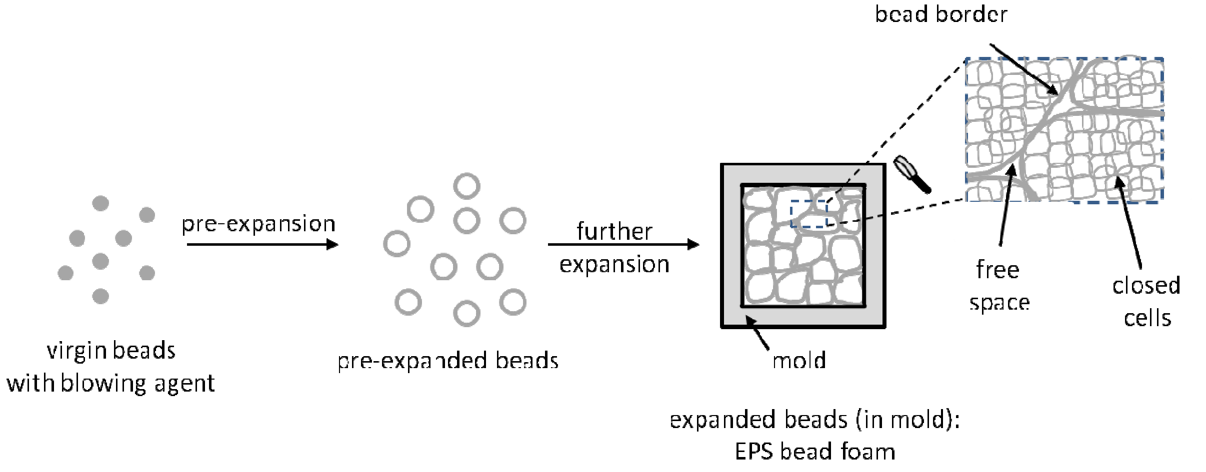

Figure 21 Schematic representation of the production process of expanded polystyrene foam (EPS), as described by LANDROCK.[129] In the final EPS the beads are deformed and fused, but, depending on the production parameter, there still is free space in between.

4 Results and Discussion

4.1 Molecular Architecture of PPX-Homo and Copolymers

4.1.1 Motivation, Hypothesis and Concept

The properties of commercially available PPX derivatives are governed by their high crystallinity, which results from the interactions of the aromatic units in the backbone. As presented in Section 3.3 modifications of the intrinsic properties can be achieved by introducing bulky substituents on the aromatic ring or via copolymerization with “vinyl-like” comonomers and reactive gases.

Substituted PPX are subject of current investigation and a great variety is available at least on laboratory scale (see Sections 1 and 3.3.1). The development of soluble CVD-PPX by substitution on the aromatic ring with alkyl or siloxane substituents by BIER *et al.* opened new possibilities for the analysis of PPX polymers.[16, 17] Though the alkyl-PPX polymers showed substantially improved mechanical behavior compared to PPX-N and PPX-C, they face problems of impurities, especially for longer alkyl substituents.

Despite the fact that the copolymerization with “vinyl-like” comonomer is a cost effective and fast alternative to [2.2]paracyclophane modifications, only a few publications exist on PPX copolymers with “vinyl-like” comonomers.[21, 23, 26] The authors report significant property changes compared to PPX homopolymers but also several difficulties in copolymer synthesis, analysis and their direct application as coating material (see Section 3.3.3). All reported copolymers were obtained with precursors known to give insoluble PPX homopolymers and were, even as copolymer, insoluble. This insolubility limits the methods available for copolymer characterization. The synthesis were carried out in CVD reactors with static sample holders and all the products contained unreacted comonomer. Consequently they could not be applied as polymer coatings via CVD, since the unreacted comonomer had to be removed by post deposition treatment.

Copolymerization of PPX with reactive gases like O_2, NO and NO_2 in solution were reported to give insoluble polymeric and telechelic products.[85, 89, 130] This PPX derivates are of particular interest, since polymeric peroxide and telechels are potential building blocks for copolymerizations.

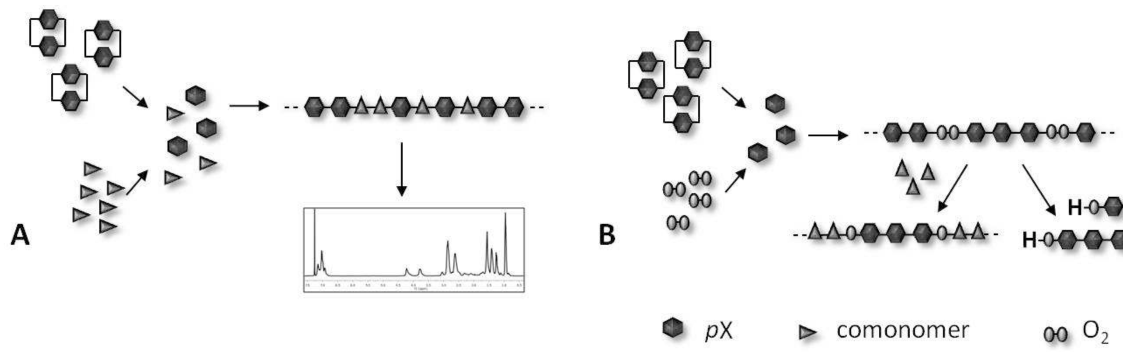

Figure 22 Illustration of the concept for the copolymerization of alkyl substituted [2.2]paracyclophanes with double bond containing comonomers and oxygen. The soluble copolymers can be analyzed by in solution, e.g. by NMR spectroscopy (A). Soluble alkyl-PPX peroxides will be available for further use as macroinitiators or telechels (B).

The working hypothesis for the results presented in this chapter was based on the assumption, that using alkylated precursors as described by BIER *et al.* for copolymerizations with "vinyl-like" monomers and oxygen would lead to soluble copolymers. These copolymers will be available for conventional, solution based polymer analysis methods like nuclear magnetic resonance spectroscopy (NMR) and gel permeation chromatography (GPC) which will provide further insight into their microstructure and might provide valuable information on the polymerization mechanism. This kind of molecular characterization could not be performed with the insoluble PPX-copolymers reported in literature. Furthermore, the solubility of alkyl-PPX peroxides would allow their use as macroinitiators or telechels for subsequent block-copolymerizations in solution.

Furthermore it was assumed that varying the CVD process parameter like the comonomer's partial pressure will influence the comonomer content in the copolymers. By this means copolymers with different compositions and alkyl-PPX peroxides with PPX blocks of different length would be available.

The combination of CVD for copolymer synthesis and solution polymerization methods for the further use of PPX building blocks, should allow the use of the entire spectrum of copolymer architecture for PPX polymers. However, besides the academic interest in copolymer synthesis and analysis, the possibility to influence the bulk and surface properties of PPX polymers in a controlled manner will open new fields of applications.

For coating applications impurities like unreacted precursor or comonomer are undesirable in homo as well as in copolymers, because a post treatment for purification is often not possible. It is known that reactor and sample holder geometry and orientation influence the deposition behavior of PPX homopolymers and film quality.[131, 132] Therefore it was assumed that the geometry of the deposition chamber and location of the substrates inside have crucial influence on the quality of the obtained homo and copolymer coatings.

The copolymerization concept was first tried with 2-hydroxyethyl methacrylate (HEMA) as comonomer, since the homopolymer poly(2-hydroxyethyl methacrylate) (PHEMA) is, just as PPX-N and PPX-C, well established in medical and biological applications.[133, 134] Furthermore successful copolymerization with neat [2.2]paracyclophane was already reported.[91] The copolymers from alkyl-substituted [2.2]paracyclophanes were expected to be soluble, therefore suitable for copolymer analysis and furthermore biocompatible.

4.1.2 Copolymers of Different [2.2]Paracyclophanes with HEMA

4.1.2.1 Soluble and Insoluble Copolymers - Copolymer Analysis

Copolymers of differently substituted [2.2]paracyclophane precursors with 2-hydroxyethyl methacrylate (HEMA) were successfully synthesized (Figure 23). The alkyl-substituted [2.2]paracyclophane precursor were obtained by KUMADA coupling reactions as reported by BIER *et al.*[16]

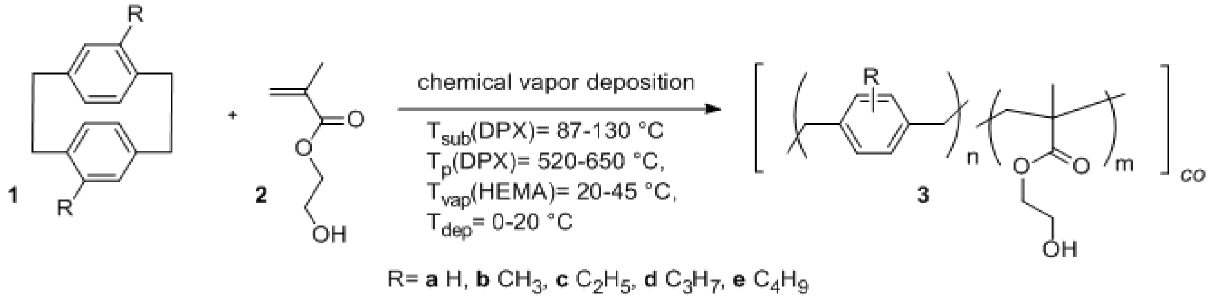

Figure 23 Reaction scheme of different [2.2]paracyclophanes (DPX) with 2-hydroxyethyl methacrylate (HEMA) to give P(PX-*co*-HEMA) copolymers via chemical vapor deposition (CVD). In order to find appropriate copolymerization conditions and depending on the respective precursor, different precursor sublimation (T_{sub}) and pyrolysis temerpatures (T_p), HEMA evaporation temperature (T_{vap}) and deposition temperature (T_{dep}) were used.

Same as the PPX homopolymers, copolmyers of P(PX-pr-*co*-HEMA) and P(PX-bu-*co*-HEMA) were soluble in THF and chloroform. All obtained copolymers of P(PX-N-*co*-HEMA), P(PX-me-*co*-HEMA) and P(PX-et-*co*-HEMA) were insoluble in common solvents.

IR spectroscopic analysis after purification of the films confirmed the presence of both monomer units in all obtained copolymers. The carbonyl ester group stretching vibration around 1720 cm^{-1} confirmed the presence of HEMA units in the copolymer and the broad absorption around 3700-3100 cm^{-1} was attributed to hydroxy stretching vibrations and confirmed the retention of the hydroxy groups during the CVD copolymerization process. The strong absorption around 820 cm^{-1} is characteristic for the aromatic C-H vibrations of the PX unit.

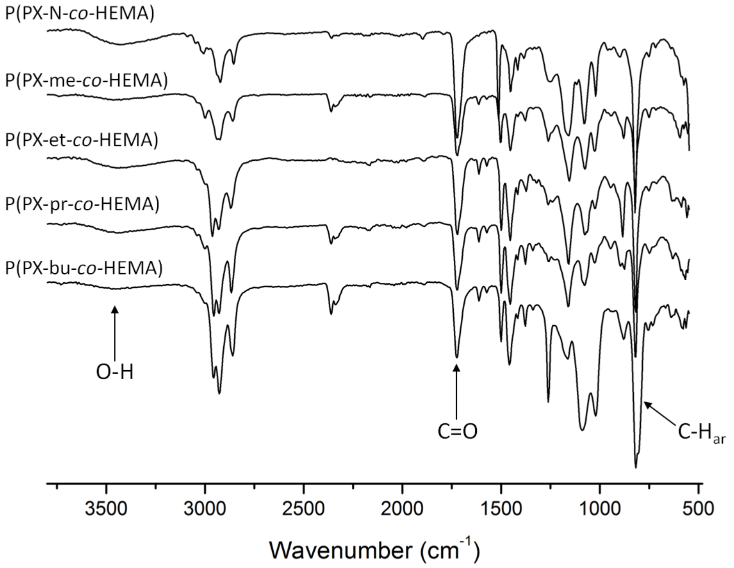

Figure 24 ATR-IR transmission spectra of P(PX-*co*-HEMA) copolymer with differently substituted [2.2]paracyclophanes. The hydroxy and carboxy vibrations confirm the presence of HEMA units in the copolymer, aromatic C-H vibrations account for PX units. The integral ratio of the carboxy and CH$_{ar}$ vibrations can be used to measure the relative HEMA content in the sample (absorptions at 2350 cm^{-1} are caused by ambient CO$_2$, weak absorptions of the ATR crystal are present in the region of 2250-2000 cm^{-1}).

Same as in ATR-IR spectra both monomer units can be identified in the solid state NMR (SS-NMR) of the insoluble copolymers P(PX-N-*co*-HEMA), P(PX-me-*co*-HEMA) and P(PX-et-*co*-HEMA) (Figure 25). For P(PX-N-*co*-HEMA) the interpretation is straight forward, since only three resonances are expected for pure PPX-N at 140 ppm (C$_a$), 129 ppm (C$_b$) and 39 ppm (C$_c$). The signals are reported to shift slightly or split depending on the crystalline modification of the PPX-N.[135] The remaining resonances were assigned to HEMA units with carbonyl carbon C$_g$ at 178 ppm, ethyl group from the hydroxy ester C$_h$ at 67 ppm and C$_i$ at 61 ppm and the quarternary carbon C$_f$ at 45 ppm. The methyl carbon C$_e$ and the backbone carbon C$_d$ show broad signals, which accounts for the different environments of the carbons due to radical polymerization leading to atactic polymers. This effect is expected to be enhanced by the copolymerization with *p*X-N. The same accounts for the backbone methylene carbons of *p*X-N C$_c$, which show a broad resonance with a small shoulder in high field compared to the signals reported for PPX-N homopolymers.[135] The additional resonance in the aromatic region was also attributed to changes in chemical shift originated by the attachment to HEMA comonomer. The interpretation of the spectra of P(PX-me-*co*-HEMA) and P(PX-et-*co*-HEMA) led to the same conclusions. Here, due to the substitution on the aromatic with a methyl or ethyl group, additional signals are present in the aromatic region.[69, 136] The resonance of the methyl substituent in P(PX-me-*co*-HEMA) overlaps with C$_e$, but for P(PX-et-*co*-HEMA) an additional resonance at 25 ppm, attributed to the methylene carbon of the ethyl substituent is visible.

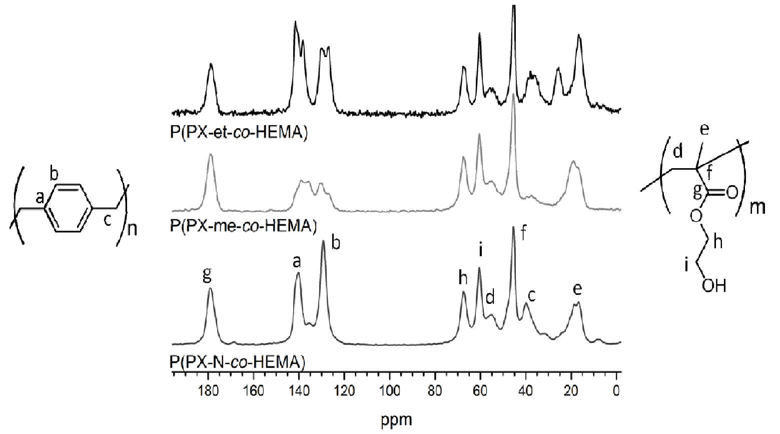

Figure 25 SS-NMR of P(PX-N-*co*-HEMA), P(PX-me-*co*-HEMA) and P(PX-et-*co*-HEMA).

However, both ATR-IR and SS-NMR only confirmed the presence of both components in the investigated material but not their junction. For proof of copolymerization and structural characterization 2D-NMR spectroscopic analysis of the soluble copolymers were performed.

The identification of characteristic proton signals of HEMA and PX-butyl in ^{1}H spectrum was straight forward by comparison with the homopolymers as shown in Figure 26. Additional resonance signals at 6.94 ppm and 3.05 ppm (marked with dashed arrows), were attributed to *p*X units directly bound to HEMA units and will be discussed in the following.

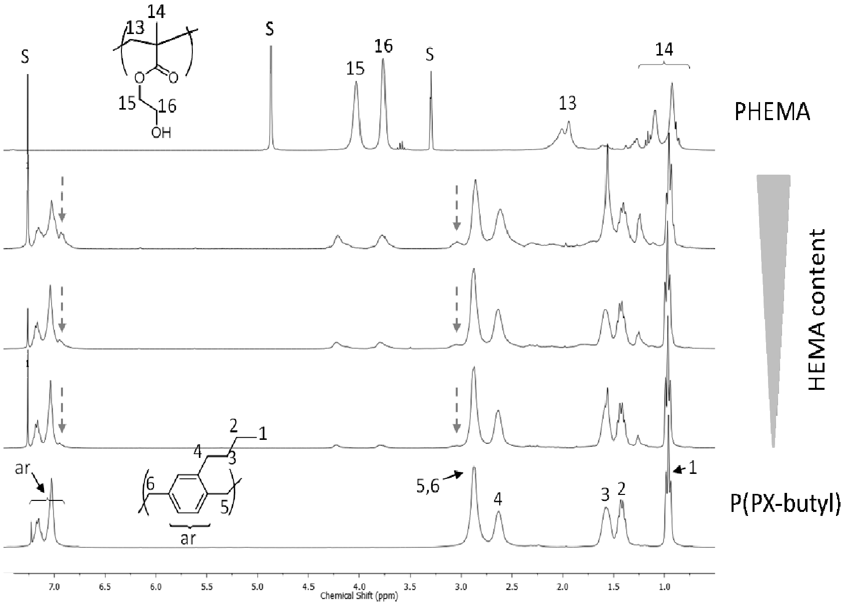

Figure 26 ^{1}H-NMR spectra of PHEMA and P(PX-butyl) homopolymers and P(PX-bu-*co*-HEMA) copolymers. With increasing HEMA content (from bottom to top) additional resonance signals appear (marked with dashed arrow), which can be assigned to the PX-butyl units adjacent to HEMA units by 2D-NMR spectra. “S” marks solvent signals for $CDCl_3$ (PPX-butyl and copolymers) and MeOH-d_4 (PHEMA).

The same accounts for ^{13}C-NMR spectra (Figure 27), which showed the typical PPX-butyl and PHEMA signals, and additional resonances at 45.5 ppm and in the aromatic region (marked with dashed arrows). Furthermore the signals for all carbons except the methyl carbon of the butyl chain (C_1) were split in multiple signals. This was already observed for alkyl-PPX homopolymers and attributed to slightly different magnetic environments of the respective carbons due to head-to-tail isomerism in the homopolymer.[16] By copolymerization the number of possible environments for each backbone carbon is further increased and differences in chemical shifts were expected.

$^1H,^{13}C$-HSQC and $^1H,^{13}C$-HMBC were used for proton and carbon peak assignments. Besides the known cross-peaks for *p*X-butyl and HEMA units, the carbon resonance around 45.5 ppm was assigned to the proton resonance from 3.05 ppm and a second resonance which overlaped with the signals of $H_{5,6}$ and H_4 (Figure 28). HMBC spectra (Figure 29 and Figure 30) clearly showed couplings of this protons with C_{14} and C_{18} from HEMA and the aromatic carbons from PX. Furthermore this signal (45.5 ppm) was correlated to protons H_{14}.

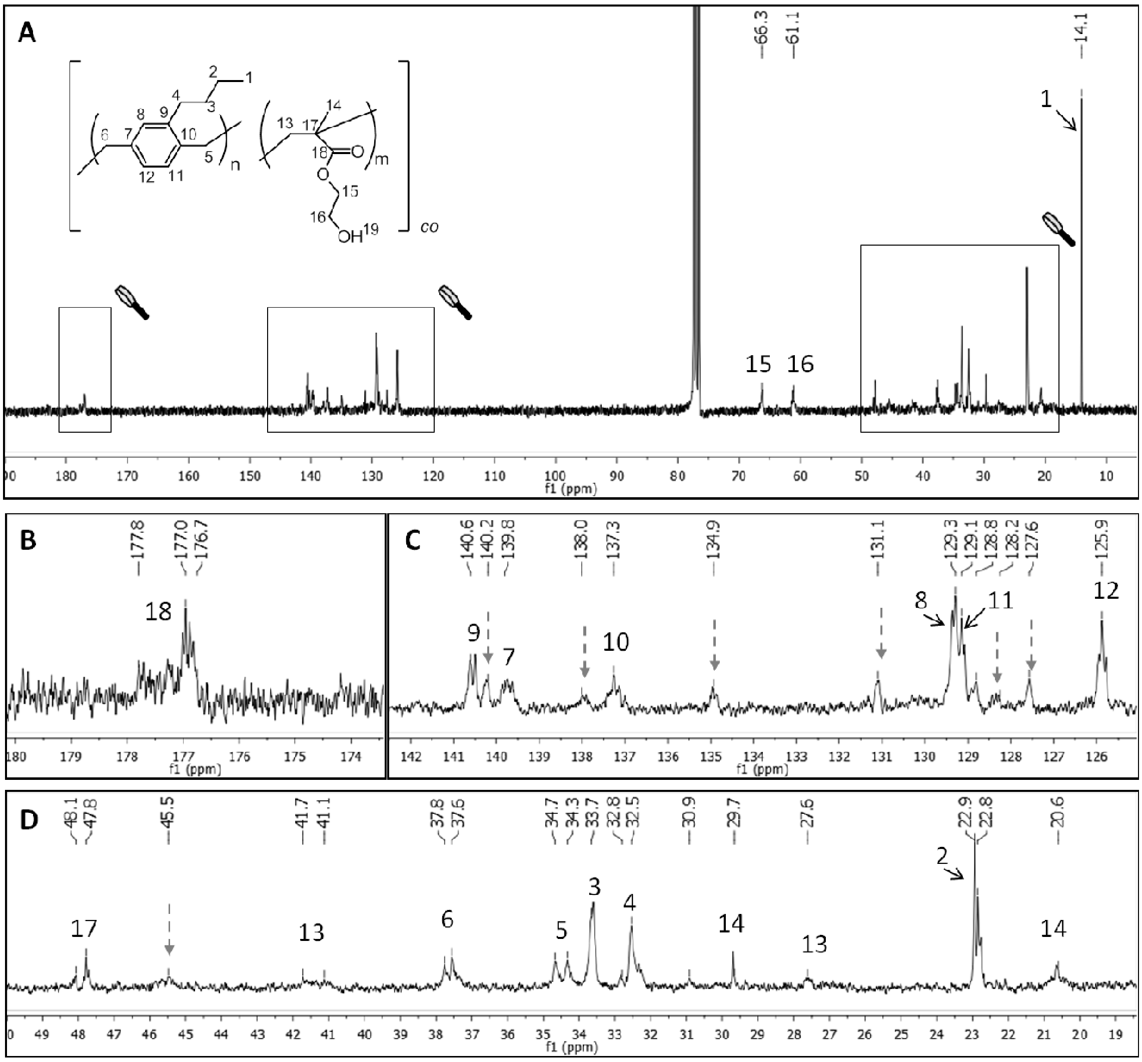

Figure 27 Complete ^{13}C-NMR spectrum of P(PX-bu-*co*-HEMA) in $CDCl_3$ (A) and magnifications of the regions of special interest 180-173 ppm (B), 142-126 ppm (C) and 49-19 ppm (D). The spectra show, same as ^1H spectra, resonance signals (marked by dashed arrow) which are caused by PX units directly bound to HEMA in the copolymer.

Therefore, the carbon signal around 45.5 ppm and respective proton signal were assigned to the methylene carbons ($C_{5'}$, $C_{6'}$) and protons ($H_{5'}$, $H_{6'}$) of PX-butyl backbone which are bound directly to HEMA units. Further evidence of direct vicinitiy of the *p*X-butyl and HEMA units is found by the coupling of C_{17} with $H_{5'}$,$H_{6'}$ (Figure 29) and aromatic carbons with H_{13} (Figure 30).

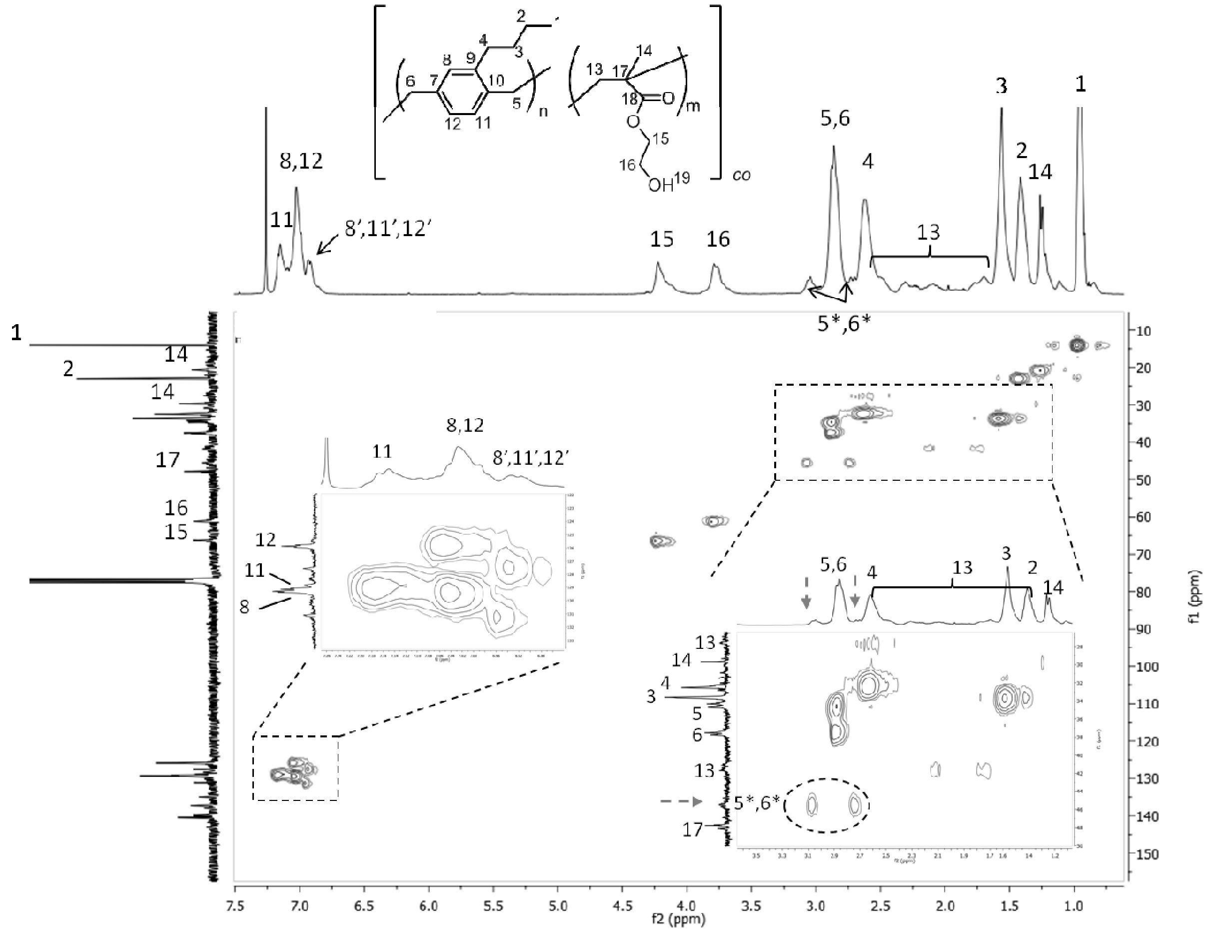

Figure 28 ^{1}H,^{13}C -HSQC spectrum of P(PX-butyl-*co*-HEMA) in $CDCl_3$, resonance signals were assigned with the help of HMBC spectra.

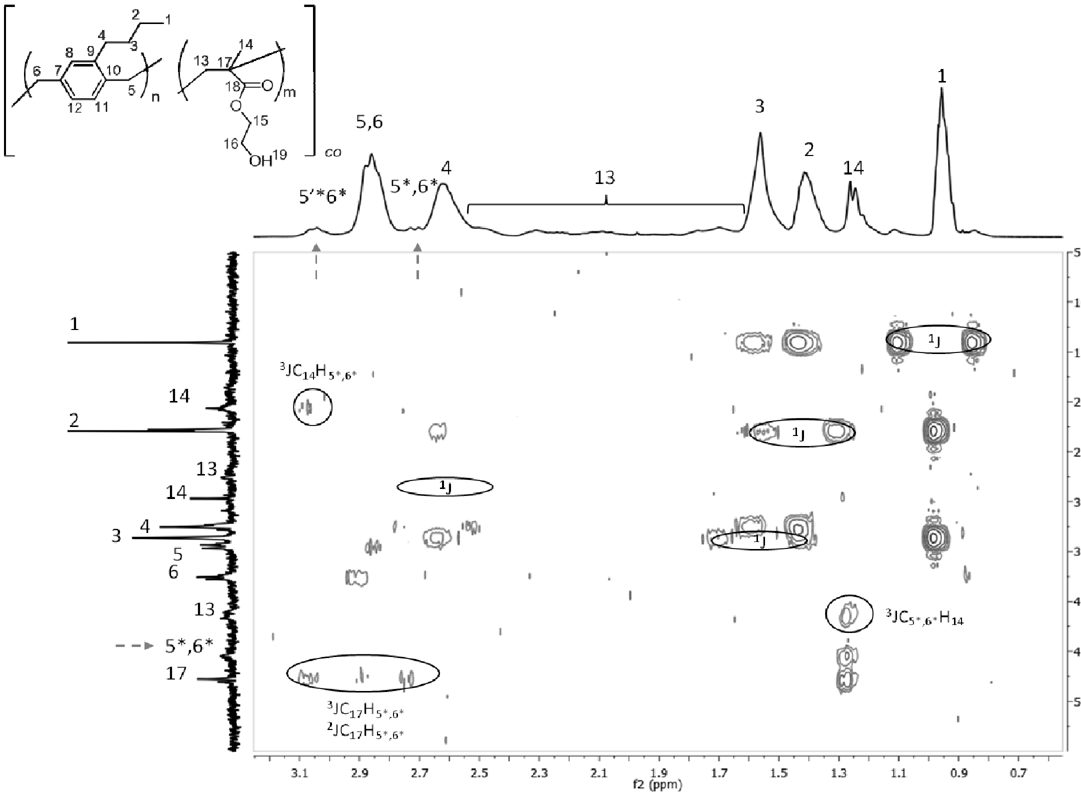

Figure 29 Part of the ^{1}H,^{13}C-HMBC spectrum of P(PX-butyl-*co*-HEMA) in $CDCl_3$ showing the region of 3.2-0.5 ppm and 55-8 ppm with aliphatic couplings. Resonance signals proving the coupling of PX-butyl and HEMA units are assigned.

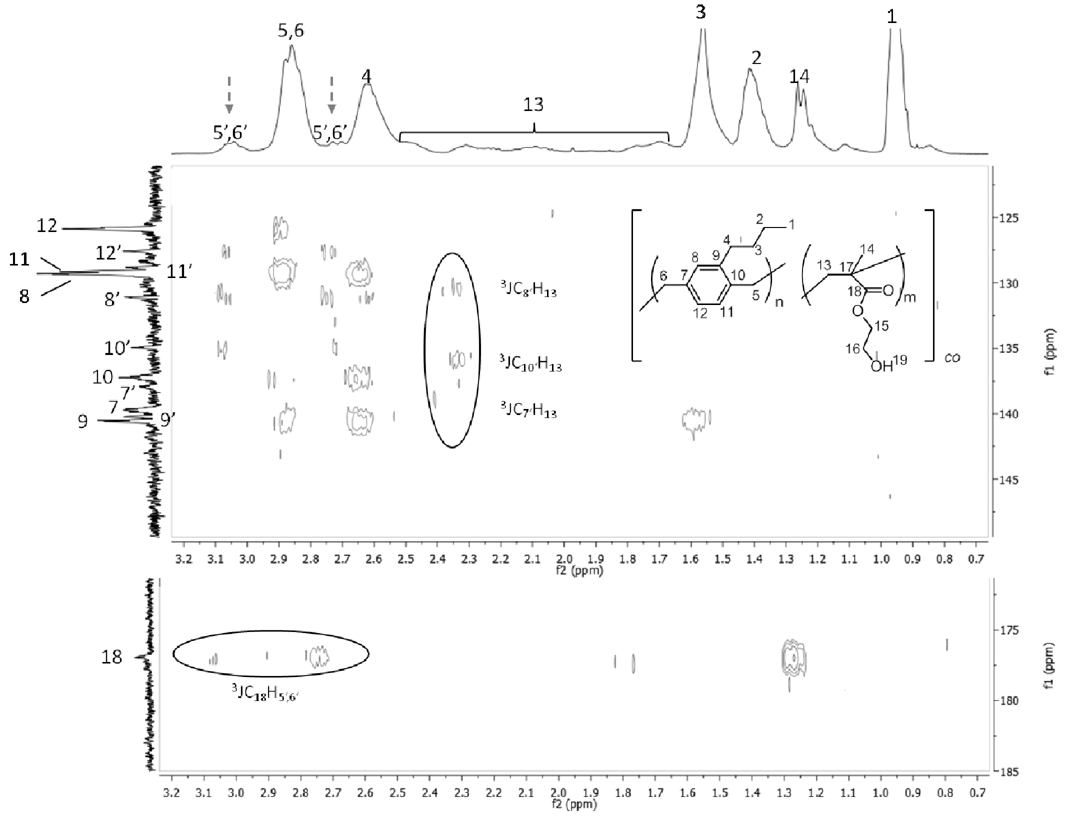

Figure 30 Part of the ^{1}H,^{13}C-HMBC spectrum of P(PX-butyl-*co*-HEMA) in $CDCl_3$ showing the regions of 3.2-0.7 ppm and 150-122 ppm or 185-172 ppm. Resonance signals proving the coupling of PX-butyl and HEMA units are assigned.

Molecular weight of P(PX-butyl-*co*-HEMA) copolymers was lower than generally obtained for PPX-butyl homopolymers. Trends for molecular weight variation with increasing comonomer content could not be observed (Table 5). This is most likely due to the setup used, where the comonomer content varied with position of the chamber (see Section 4.1.2.2). Samples for GPC analysis were taken after purification of the polymers, therefore the molecular weights resemble the average of the overall sample obtained in the respective run. Elugrams of the GPC analysis showed identical curves for refractive index (RI) and ultraviolet (UV) detectors, as shown in Figure 31 for run 2d.

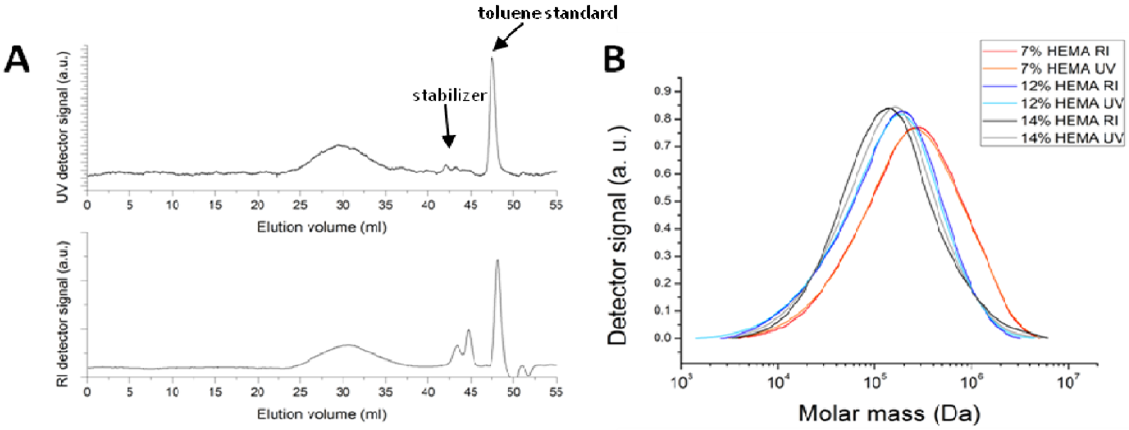

Figure 31 Molecular weight analysis of P(PX-bu-*co*-HEMA) by THF-GPC, refractive index (RI) and ultraviolett (UV) detectors show the same results. Elugramm of run 2d (A) and molecular weight analysis of runs 2c, 2e and 2f (B).

Table 5 Molecular weights determined by THF-GPC (relative to PS standards) of P(PX-butyl-*co*-HEMA), after purification.

Run	**% HEMA**	**THF-GPC (RI detector)**		
		10^5 M_n/ Da	**10^5 M_w/ Da**	**PDI**
2a	6	-	-	-
2b	7	0.64	1.82	2.84
2c	8	1.01	4.37	3.97
2d	12	0.94	2.23	2.37
2e	13	0.67	2.54	3.81
2f	15	0.69	2.56	3.69
2g	24	-	-	-
2h	27	0.75	1.59	2.11

Copolymerization of HEMA with different paracyclophanes is expected to increase the thermal stability compared to HEMA homopolymer. Figure 32 A shows the thermogravimetric analysis of P(PX-N-*co*-HEMA) with 55-65% HEMA content compared to the homopolymers. The temperatures of maximum thermal degradation, determined as the minimum of the first deviation of the degradation curve, for P(PX-bu-*co*-HEMA) are shown in Figure 32 B. In the investigated range a linear decrease with increasing HEMA content in the copolymer was observed.

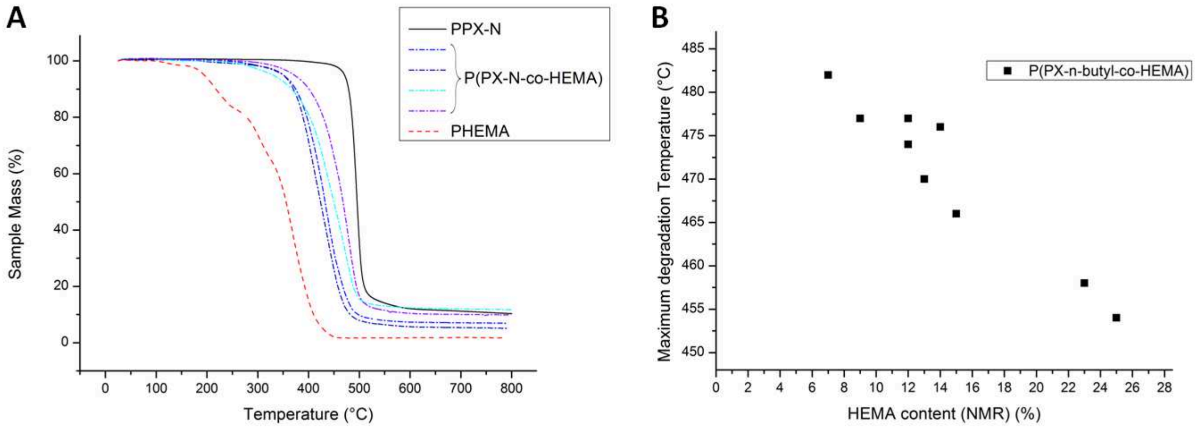

Figure 32 A Thermals stability of P(PX-N-*co*-HEMA) copolymers compared to the homopolymers. **B** Maximum degradation temperature with HEMA content for P(PX-butyl-*co*-HEMA).

PPX-N is a semi crystalline polymer with rather complicated thermal behavior due to polymorphism as described in Section 3.2. Figure 33 compares the second heating cycle of PPX-N with three P(PX-N-*co*-HEMA) copolymers (all deposited at 20 °C). PPX-N shows a broad endothermal transition around 200 °C, which is supposed to be an annealing peak or remaining α to β_1 transition, and a sharp endothermal signal at 295 °C which can be attributed to the β_1 to β_2 transition. Some P(PX-N-*co*-HEMA) copolymers already start to decompose in the interesting region of 300 °C, but the stable sample did not show any relevant endothermal effect in this region. All copolymer samples show a small broad exothermal signal in the region of 250 °C and a baseline shift around 100 °C. The latter is supposed to be the glass transition of the polymer, since a similar shift can be observed in the respective cooling curves. The copolymerization of DPX-N with HEMA, as expected, strongly affected the "in situ" crystallinity and polymorphism of the polymer.

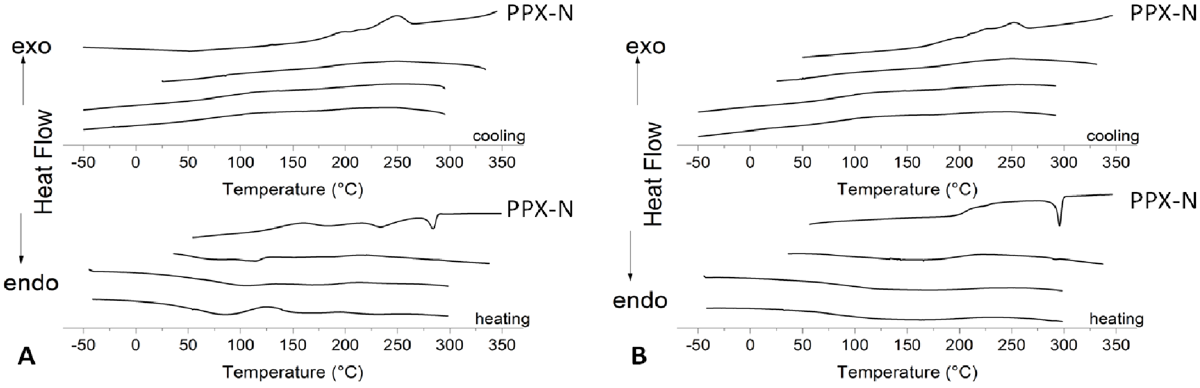

Figure 33 DSC analysis PPX-N-co-HEMA copolymers in comparison with PPX-N, A: first heating and cooling, B second heating and cooling cycles. See text for interpretation.

The thermal behavior of PPX-alkyls is not studied as extensively as for PPX-N. For PPX-butyl Bier et al.[16] reported a glass transitions of -4 °C and an endothermal transition at 118 °C. In P(PX-*n*-butyl-*co*-HEMA) copolymers these transitions are affected by the copolymerization. As shown in Figure 34 A, the glass transition increases with increasing HEMA content and the exothermal and endothermal transitions of the PPX-butyl homopolymer (62°C and 116 °C) are no longer visible. However, in some copolymers more than a single glass transition effect was observed. The DSC thermogramm of the P(PX-*n*-butyl-*co*-HEMA) copolymer in Figure 34 B shows a glass transition at -6 °C, typical for PPX-n-butyl homopolymer, and a subsequent second glass transition at 15 °C, attributed to the copolymer. In addition, upon further heating a very broad exothermal transition (65 °C) and subsequent endothermal effect (115°C) were visible. This indicates the presence of longer PPX-*n*-butyl blocks in the copolymer which are able to behave in DSC like homopolymer.

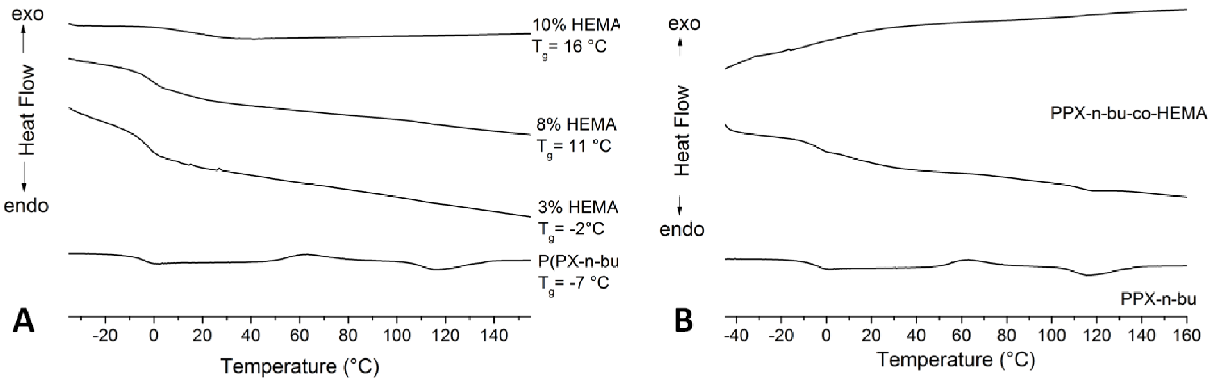

Figure 34 DSC thermograms of P(PX-*n*-butyl-*co*-HEMA) compared to P(PX-*n*-butyl) homopolymer.

P(PX-*co*-HEMA) copolymers with longer alkyl substituent on the *p*X unit showed a lower maximum HEMA content in the copolymer. Since parameter scans were not performed for all copolymers and no further studies on the reactivity ratios of the alkyl-DPX with other comonomers were performed, it is difficult to evaluate if this trend is reproducible for comonomers with similar electronic structure to HEMA. For electron withdrawing substituents on the aromatic rings and methylene groups of *p*-xylylenes, a decrease in reactivity is known.[86] However, the alkyl substituens should not exert such an effect, since they are not electronegative substituents. Furthermore, a deactivating effect on the highly reactive *p*X radial should favor the copolymerization with vinyl-type comonomers. Another influence factor in case of the alkyl substituents can be steric effects. Though an influence on alkyl-PPX homopolymerization was not found,[16] this influence was not investigated for other comonomers.

Table 6 Maximum HEMA contents obtained for different P(PX-*co*-HEMA) copolymers.

Polymer	Maximum HEMA content / mol%	Analysis method
P(PX-N-*co*-HEMA)	66	elemental analysis
P(PX-methyl-*co*-HEMA)*	60	elemental analysis
P(PX-ethyl-*co*-HEMA)*	50	elemental analysis
P(PX-propyl-*co*-HEMA)	37	^{1}H-NMR
P(PX-butyl-*co*-HEMA)	29	^{1}H-NMR

* no parameter screening

Since both PPX and HEMA are non-cytotoxic and established in biomedical applications, copolymers composed of their monomer units are expected to be equally applicable. For this reason first qualitative tests to estimate the biocompatibility P(PX-N-*co*-HEMA) were carried out. Mouse fibroblast cells (L929) were seeded on copolymer coated well plates and compared to PPX-N and a PS blank sample (neatwell plate). The cells were not affected negatively in their growth by the copolymer.

4.1.2.2 Influence of CVD Parameters and Reactor Design in Copolymerization

PPX via CVD is generally synthesized for coating purposes, in other words, directly deposited onto the final substrate. Typically, CVD reactors with large deposition chambers are used and the polymer deposits as a thin film (hundreds of nanometers to several micrometers) onto the desired substrates and the chamber walls. For the investigation of new copolymers it was more suitable to limit the deposition area to be able to work with smaller amounts of precursor, recover all obtained product from the deposition chamber to avoid material loss as well as contamination of the deposition chamber for further batches. For this reason homemade CVD reactors with relatively small volumes were used for PPX copolymer investigations (see Section 5.3). The copolymers were deposited in different deposition chamber models, where the gaseous monomer deposited parallel and perpendicular to the monomer flow direction (Figure 118). All copolymers obtained in the homemade CVD reactor, regardless of the deposition chamber model, contained unreacted HEMA comonomer after the deposition and needed purification before further analysis. This was also the case for low HEMA evaporation temperatures and copolymers with low HEMA content.

In accordance with results from GAYNOR et al. copolymers obtained from deposition parallel to the monomer flow direction showed strong spatial inhomogenity considering film thickness and comonomer content.[25, 26] Gradient films with increasing relative HEMA content with increasing distance from the chamber inlet were obtained for P(PX-pr-*co*-HEMA) and P(PX-bu-*co*-HEMA) copolymers.

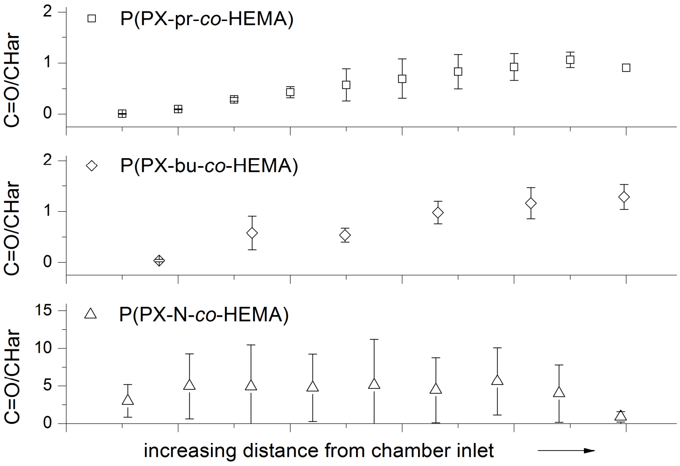

Figure 35 Composition changes for different P(PX-*co*-HEMA) copolymers with increasing distance from chamber inlet. For P(PX-pr-*co*-HEMA) (□) and P(PX-bu-*co*-HEMA) (◇) a gradient with increasing HEMA content towards the chamber end could be observed, while inhomogenities within the sample were more pronounced for P(PX-N-*co*-HEMA) (△).

In P(PX-N-*co*-HEMA) copolymers such a clear trend could not be found. Most films showed more pronounced differences in composition comparing the bottom (the film side adhering to the chamber wall) and top of the film at the same position (with regard to distance from chamber inlet) than comparing different positions. Examples of the parameter screening (Table 15, Section 5.5.2) are shown in Figure 36.

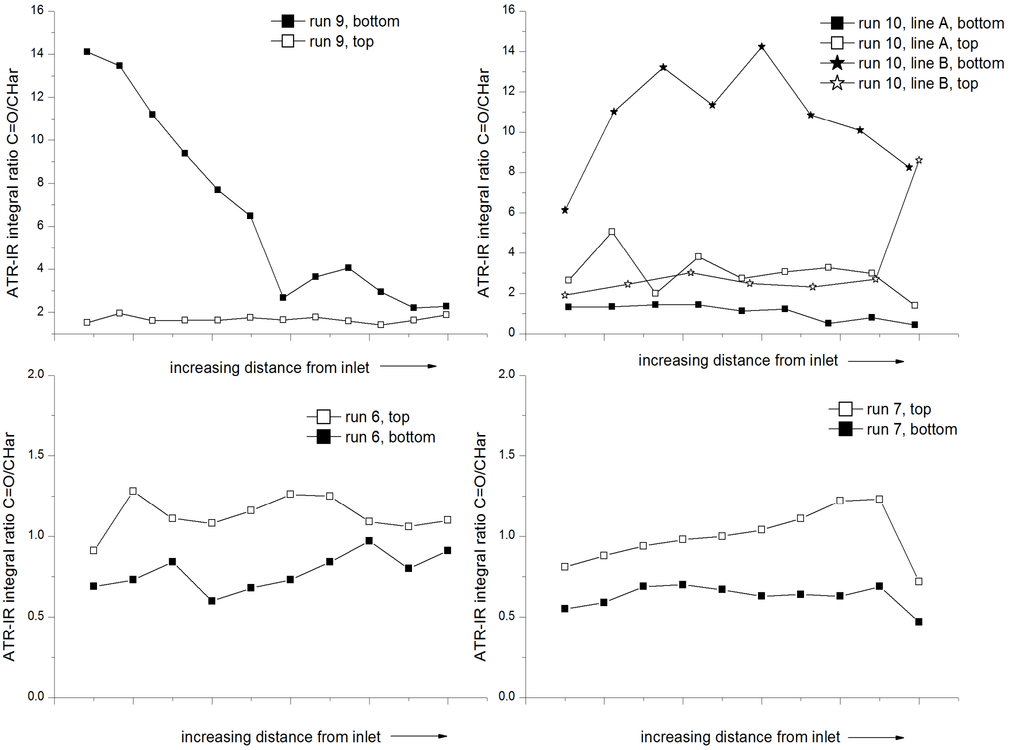

Figure 36 Relative HEMA content determined via ATR-IR signal integration ratios for different P(PX-N-*co*-HEMA) copolymers at different distances from the deposition chamber inlet. Inhomogenity in film composition was found comparing the film's top (empty symbols) and bottom (filled symbols) sides at the same position rather than comparing the position with regard to the inlet of the deposition chamber (details of parameter screening see Table 15 in Section 5.5.2)

Due to the spatial inhomogenity the parameter screenings for P(PX-*co*-HEMA) copolymers deposited parallel to the monomer flow direction did not show any relation between the HEMA content and HEMA evaporation temperature.

Deposition perpendicular to the monomer flow direction and analysis of the sample recovered from a limited part of the deposition target showed the dependence of HEMA content in the copolymer with HEMA evaporation temperature in the investigated range (Figure 37).

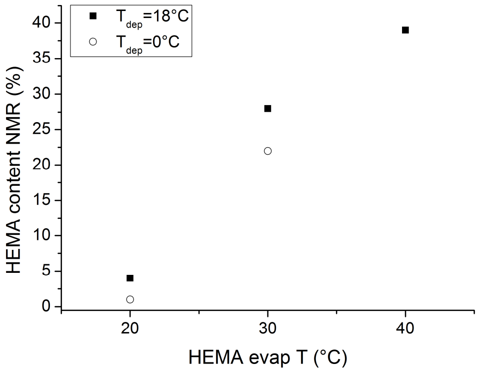

Figure 37 HEMA content (mol%) in dependence of HEMA evaportion temperature in P(PX-pr-*co*-HEMA) copolymers deposited perpendicular to monomer flow (chamber model B).

Copolymer synthesis of P(PX-N-*co*-HEMA) in the commercially available SCS Labcoater modified with an additional comonomer inlet led to transparent and more homogeneous films considering film thickness and composition. The relative HEMA content of the films was monitored with ATR-IR and increases with increasing HEMA evaporation temperature as shown in Figure 38 A. At the same time water contact angle was found to decrease with increasing HEMA evaporation temperature (Figure 38 B). This not only confirms the incorporation of HEMA units in the copolymer but also their availability on the surface.

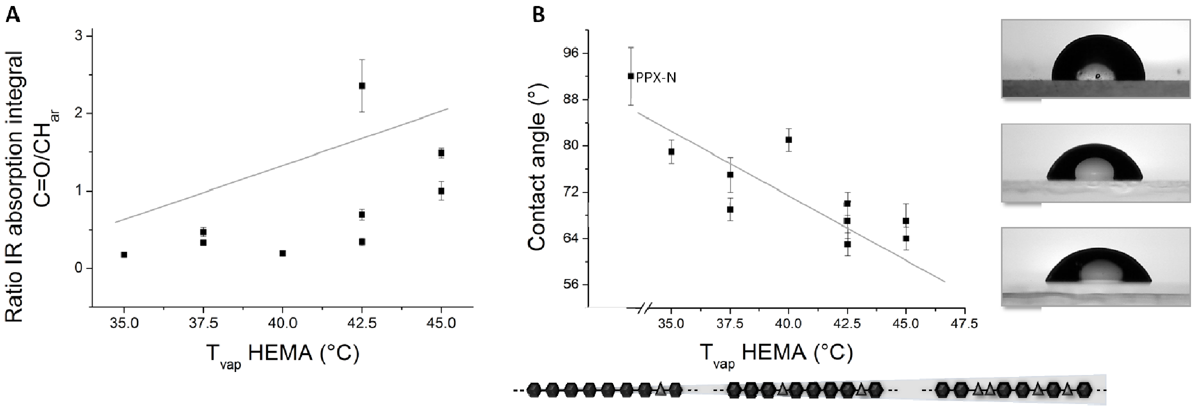

Figure 38 P(PX-N-*co*-HEMA) synthesized in SCS Labcoater modified for copolymerization. A: Relative HEMA content in the copolymer (determined by ATR-IR) increases with increasing HEMA evaporation temperature. B: Water contact angle decreases with increasing HEMA evaporation temperature.

Figure 39 P(PX-N-*co*-HEMA) film synthesized in the modified Labcoater on glass slide. The films are completely transparent. In the marked area the film was scratched to show that there is polymer film on the slide.

Table 7 P(PX-N-*co*-HEMA) films prepared in SCS Labcoater.

Run	T_{vap}(HEMA) / °C	C=O/CH_{ar}	Thickness/ nm	Contact Angle/ °
1	35	0.17 ± 0.01	432 ± 13	79 ± 2
2	37.5	0.47 ± 0.06	174 ± 4	69 ± 2
3	37.5	0.33 ± 0.04	339 ± 2	75 ± 2
4	40	0.30 ± 0.02	171 ± 16	80 ± 1
5	40	0.19 ± 0.01	750 ± 12	81 ± 2
6	42.5	0.69 ± 0.07	550 ± 11	60 ± 2
7	42.5	2.36 ± 0.34	575 ± 6	67 ± 3
8	42.5	0.34 ± 0.05	621 ± 4	70 ± 2
9	45	1.49 ± 0.06	259 ± 5	64 ± 2
10	45	1.00 ± 0.12	185 ± 10	67 ± 3
11*	40	0.35 ± 0.02	604 ± 25	59 ± 2

*sample is not transparent but opaque

PPX is known to form smooth and uniform surfaces with low surface roughness. However, AFM investigations on thin films (2 nm up to several hundred nm thickness) are known to show certain surface roughness. The size of the surface features, described as globular structures or mounds, depends on deposition rate and time.[137] Similar surface features are also described for iCVD synthesis of e.g. poly(glycicyl methacrylate) (PGMA) films. With increasing partial pressure of the reactive species, increases the deposition rate. Film deposited at higher rates show increased surface structure in form of mounds.[138]

PPX-N as well as P(PX-N-*co*-HEMA) films deposited in the homemade CVD reactor showed a rough surface as shown in Figure 40 A-F. In this setup (see 5.4.1 and 5.4.3) the films were deposited parallel to the monomer flow in a small deposition chamber, and a thickness gradient was found. At the entrance of the deposition chamber the films were thicker than in the back of the chamber. Consequently, the deposition rate at the entrance was higher. Images E and F of Figure 40 show the surface of a P(PX-N-*co*-HEMA) film. Compared to the images from PPX-N (Images A and B) there surface was rougher and showed more and smaller globular surface features. In the Labcoater much thinner homo and copolymer films of homogeneous thickness and composition could be synthesized (300-700 nm for P(PX-N-*co*-HEMA)), which did show almost no surface features (Image G and I). If P(PX-N-*co*-HEMA) was synthesized in the Labcoater with higher deposition rates (achieved by higher precursor evaporation temperature), the films were turbid same as the copolymers from the homemade setup and showed globular surface features (Image H).

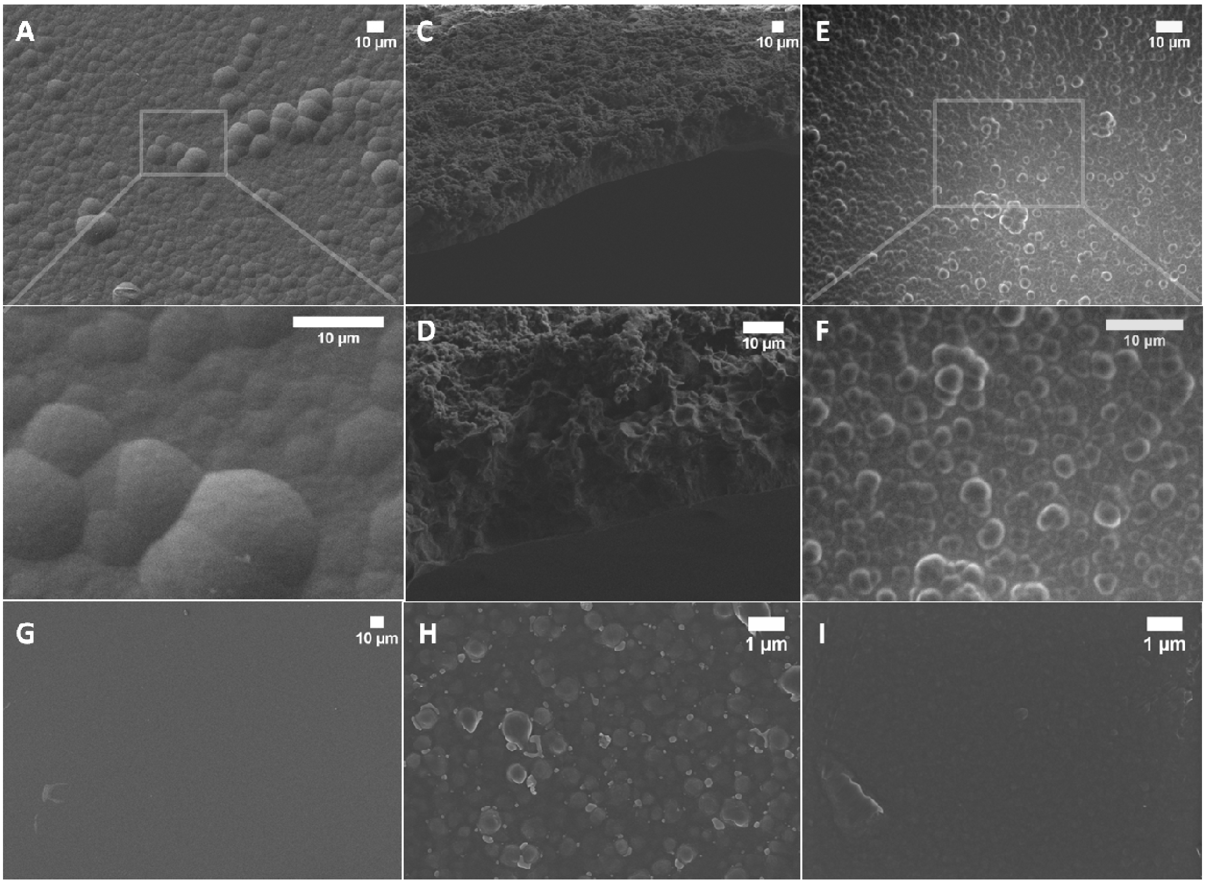

Figure 40 SEM micrographs of different CVD polymer films prepared in homemade reactor (A-F) and Labcoater (G-I). The surface of PPX-N (A,B) homopolymer comprises mounds (Hügel). Even more surface roughness is observed for copolymers PPX-N-co-HEMA (C-E). Polymer films prepared in Labcoater (at higher pressures and presumed lower growth rates, overall: much thinner films) show a more even surface. PPX-N (G) shows only occasional mounds. The copolymers PPX-N-co-HEMA (H and I) show surface structure - H was turbid, I was transparent.

4.1.3 Alkyl-PPX Peroxides

In contrast to the PPX peroxides reported in literature by Errede *et al.*[85, 88, 89] the alkyl-PPX peroxides were synthesized by introducing ambient air into the CVD reactor (see Section 5.3.1). Same as in the reported solution polymerization, the oxygen biradicals reacted with *p*X monomers and were incorporated as comonomer into the growing polymer chain.

The amount of oxygen incorporated was monitored by proton NMR spectroscopy (Figure 41). The main chain methylene protons next to the oxygen atoms ($H_{5*/6*}$) appeared as a doublet at 5.01 ppm. Their integral added to the regular main chain methylene protons ($H_{5/6}$, 2.88 ppm) was four, which is the expected value per *p*X unit in the polymer.

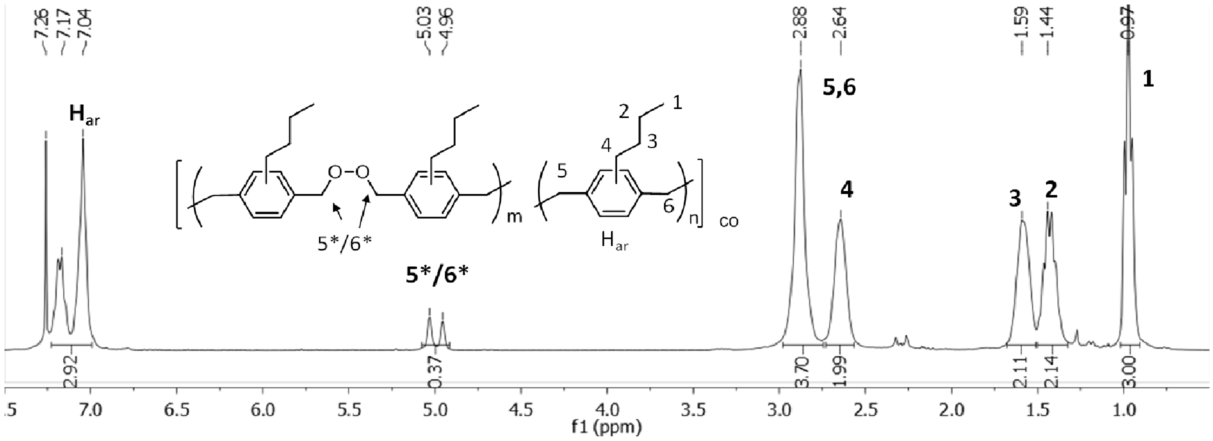

Figure 41 ^{1}H-NMR of PPX-butyl peroxide (purified by precipitation). Integrals of 5*/6* and 5/6 add up to four, which is the expected value for methylene groups from the main chain per *p*X unit in the molecule.

By 2D ^{1}H-^{13}C correlation spectrum HMQC the methoxy protons (5*/6*) were assigned to carbons around 76 ppm and at 74.4-74.2 ppm (Figure 42). The carbon around 76 ppm overlaped with the solvent signal of deuterated chloroform. The connection of the methoxy protons (5*/6*) to the *p*X aromat was proved by HMBC (Figure 43), which shows the correlations and therefore confirms the PPX-butyl peroxide structure.

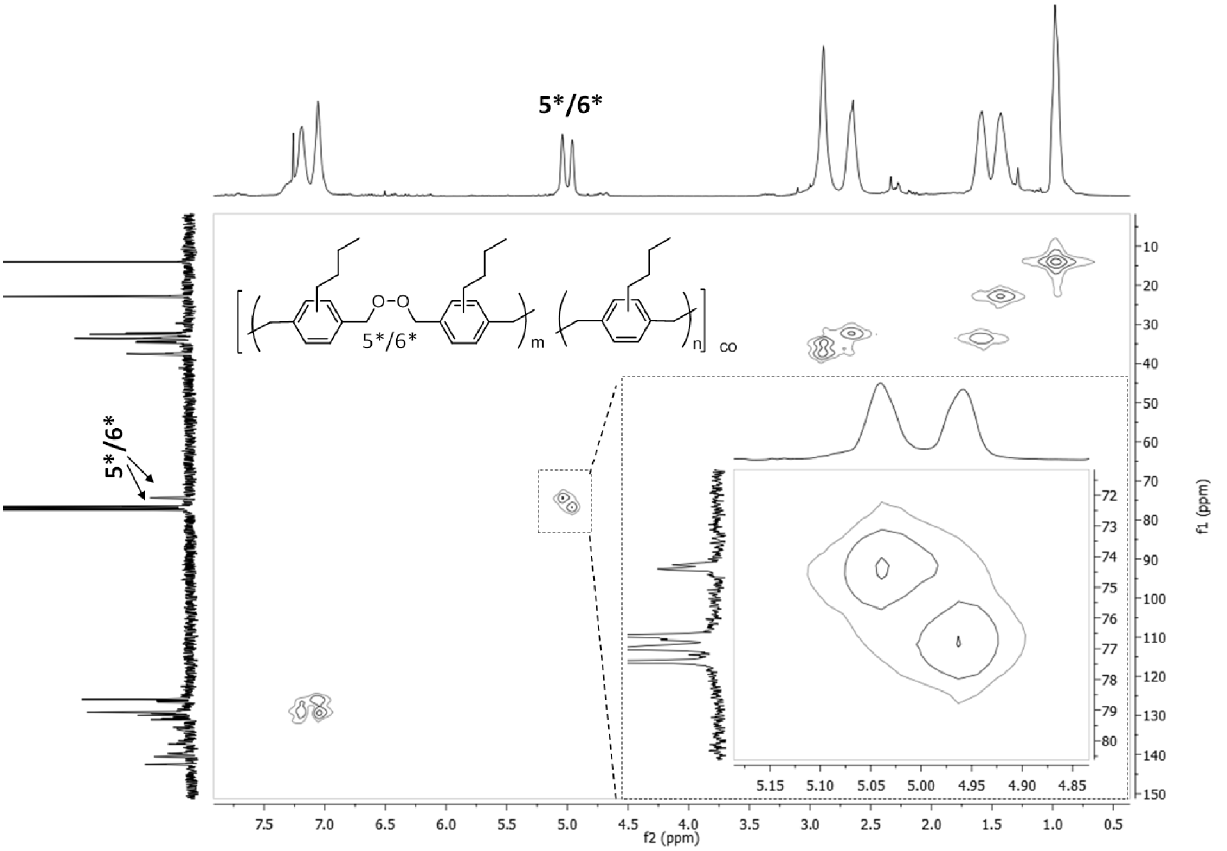

Figure 42 HMQC NMR spectrum of PPX-butyl peroxide (in $CDCl_3$) allows the proton/carbon assignation of 5*/6*. One of this carbons overlaps with the solvent signal of $CDCl_3$.

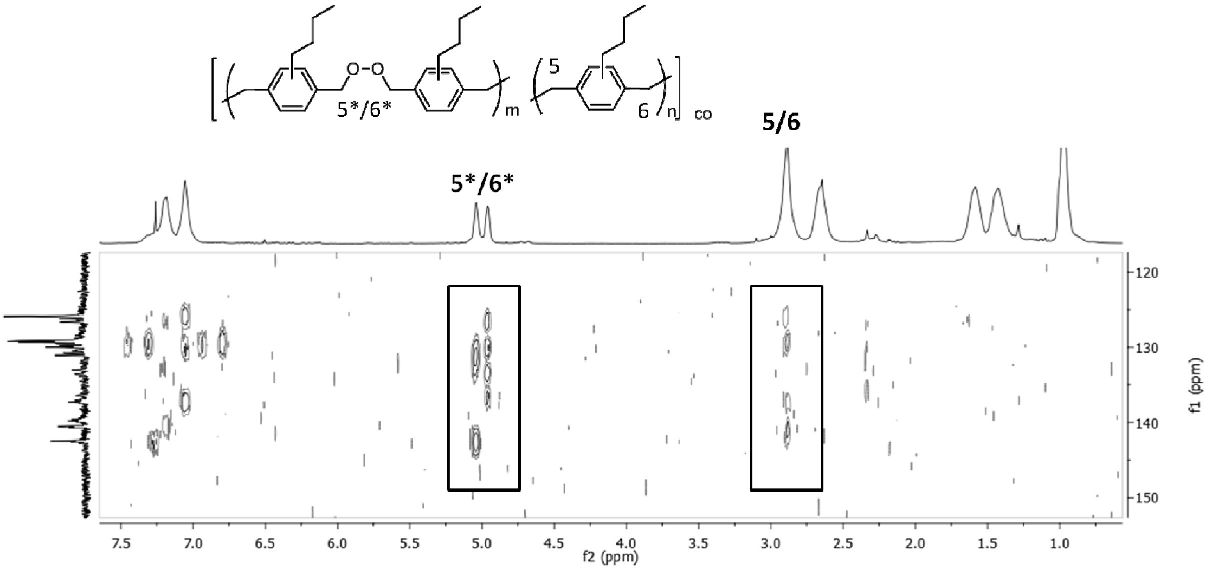

Figure 43 HMBC NMR spectrum of PPX-butyl peroxide (in $CDCl_3$) confirms the vicinity of protons 5*/6* to the aromatic rings, same as 5/6 and therefore confirms the structure of the PPX-butyl peroxides.

The amount of oxygen incorporated was controlled by the process pressure (Figure 44), by this means up to 20 mol % peroxide units were incorporated into the copolymer.

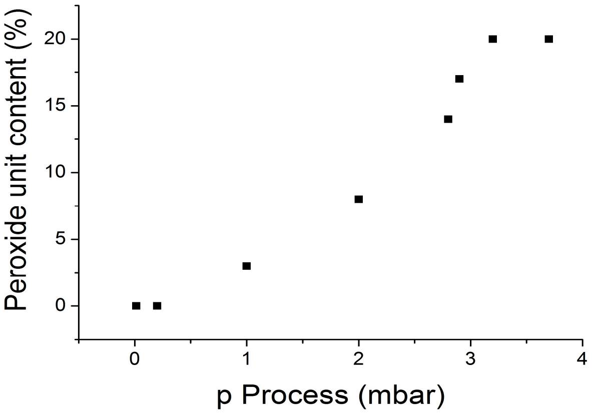

Figure 44 PPX-butyl peroxides, peroxide unit content can be controlled by process pressure.

In order to use the PPX-butyl peroxides as macronitiators for PPX-block copolymers the thermal stability of the peroxide bond was investigated. Thermogravimetric analysis of the PPX-butyl peroxides with different peroxide content are shown in Figure 45. The as deposited samples contained a low molecular weight fraction resulting in a two step degradation, same as PPX-butyl homopolymers (see Secion 4.1.4 for discussion). However, with increasing peroxide content the thermal stability decreased, which was attributed to the rupture of the peroxide bonds and faster thermal degradation of the lower molecular weight cleavage products.

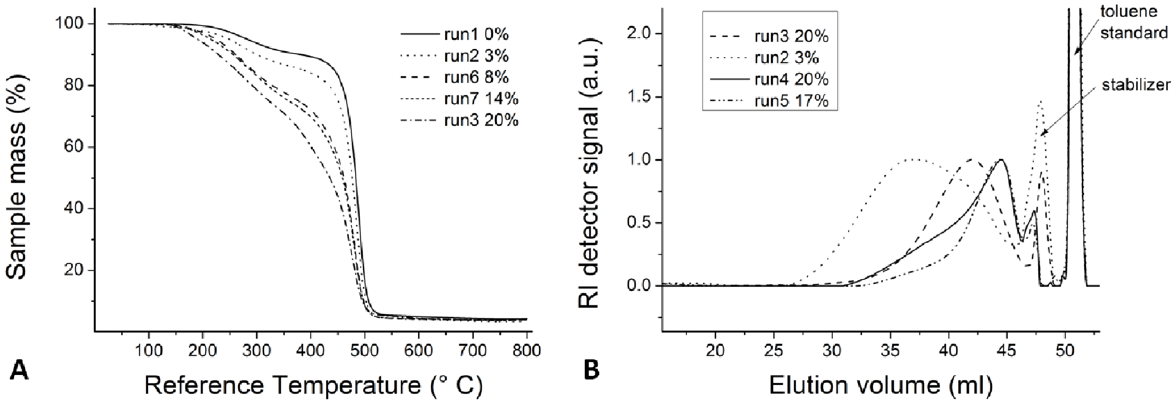

Figure 45 Thermal degradation curves of the PPX-butyl peroxides show weight starting below 150 °C (A). PPX-butyl peroxides show broad molecular weight distributions and are partially eluted in the low molecular weight exclusion volume (B).

The molecular weight distributions for different PPX-butyl peroxides are shown in Figure 45 B. The molecular weights of the PPX-butyl peroxides ranged between 4,300 and 46,000 (compared to PS standard) with polydispersities in the range of 2 to 4. The exact determination of the molecular weights was not performed, since the lower molecular weight fraction was eluted together with the THF stabilizing agent in the exclusion volume. Anyway, the molecular weights were lower than for PPX-butyl homopolymers.

The cleavage of the peroxide bond is expected to result in benzylalcohole and benzaldehyde end groups as reported by ERREDE. The expected structure for PPX-butyl peroxide and their expected chemical shifts in proton NMR are shown in Figure 46.

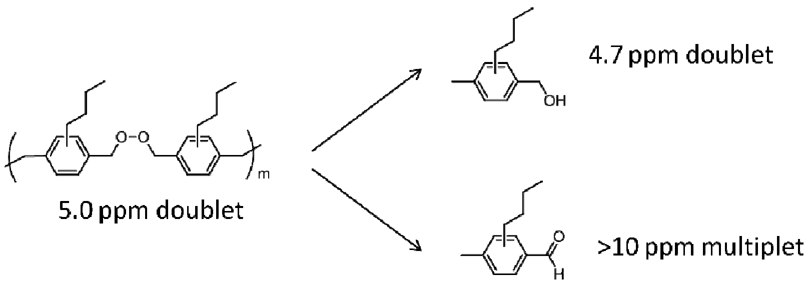

Figure 46 Products of peroxide bond cleavage and their chemical shift in ^{1}H-NMR.

Samples of PPX-butyl peroxide (run 7, Table 25 in Section 5.5.8) were heated for one hour to different temperatures and subsequently analyzed by NMR and GPC in order to determine the rupture of the peroxide bond and the obtained cleavage products. Figure 47 shows relevant excerpts of ^{1}H-NMR spectra recorded before and after the thermal treatment. Before the treatment only small amounts of aldehyds (resonances > 10 ppm and shift of aromatic protons to > 7.5 ppm) and alcohols (doublet at 4.7 ppm) are present. After 1 h at 50 °C or 100 °C the major amount of peroxide bonds is still unimpaired. Even heating up to 145 °C for a short period did not cleave all peroxide bonds. Complete rupture of the peroxide units was observed for 1 h at 130 °C.

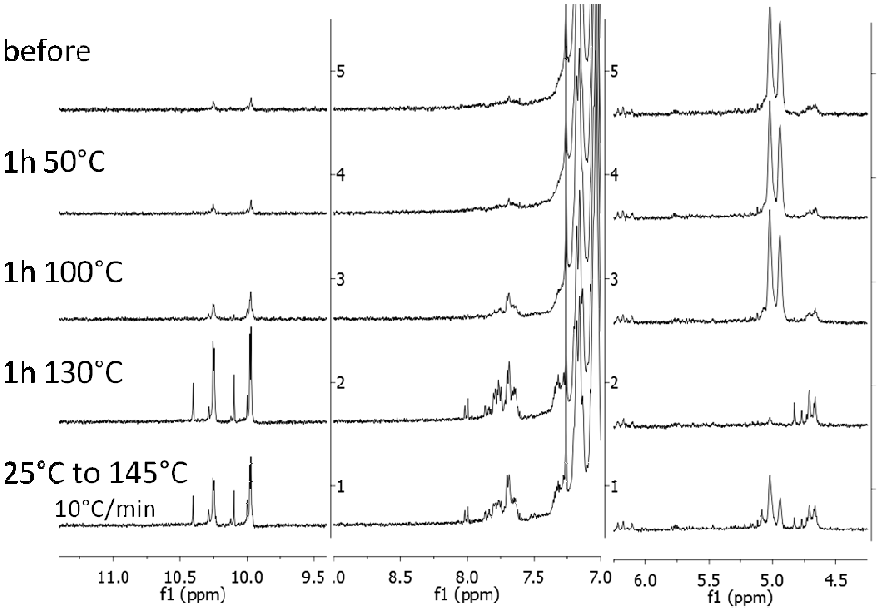

Figure 47 ^{1}H-NMR spectra of PPX-butyl peroxide (run7) before and after thermal treatment. Complete rupture of the peroxide bonds was observed at 1 h at 130 °C.

GPC analysis of the samples before and after thermal treatment confirmed the rupture of the peroxide bonds. With increasing temperature of the thermal treatment the samples were eluted at higher elution volumes, what accounts for lower molecular weights (Figure 48). Same as explained before, exact molecular weights were not determined

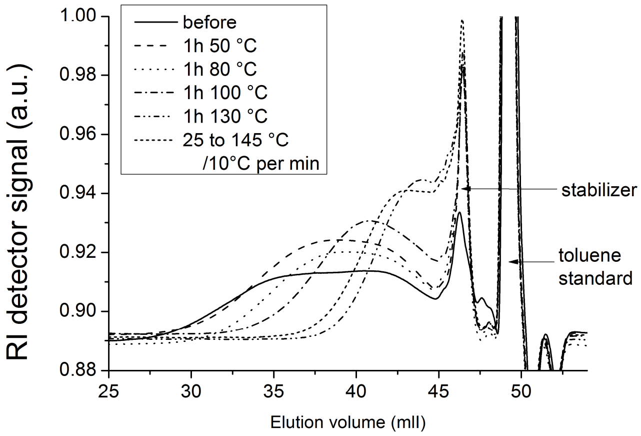

Figure 48 Molecular weight distributions of PPX-butyl peroxide (run7) before and after thermal treatment (THF-GPC). Molecular weights of the samples decreased with increasing temperature of the thermal treatment.

However, since temperatures above 100 °C at longer time intervals are needed to cleave the peroxide bond, PPX-butyl is not suitable as macroniniator for block-copolymerization with common acrylate and methyacrylate monomers. Methyl methacrylate, as an example, is thermally initiated at temperatures below 100 °C.[139, 140] An alternative to thermal cleavage of the peroxide bond in polymeric macroinitiators was reported by MUKUDAN *et al.* The authors described the initiation of vinyl polymerization by polystyrene-peroxide macronitiators at room temperature with the assistance of amines (like ethyl diamine or dimethylaniline).[141]

An alternative to block-copolymerization by the use of macronitiators is the formation of telechels from the PPX-butyl peroxides. For this purpose a reductive cleavage of the peroxide bond generating alcohol end groups is considered feasible. α,ω-Hydroxy terminated PPX-butyl can be used in polycondensation or addition reactions to give polyesters or polyurethanes.

However, yields of the PPX-butyl peroxide synthesis were, with average values around 20%, low. Synthesis optimization in form of reactor design and the use of pure oxygen instead of air in order to obtain same oxygen incorporation at lower process pressures will facilitate further investigations in this field.

4.1.4 Alkyl-PPX Homopolymer Film Quality

Alkyl-PPX homopolymers were reported to contain low molecular weight impurities, especially for alkyl substituents longer than propyl.[16] The oligomers show different solubility behavior, have the consistency of a viscous oil and affect the thermal stability of the material. Due to the excellent solubility of the affected alkyl-PPX the oligomers can be removed by extraction or precipitation. However, for the use of PPX as coating material via CVD additional purification steps like extraction or precipitation are not possible.

The low molecular weight impurities were detected by NMR and TGA analysis. In proton resonance spectra the presence of low molecular weight impurities was confirmed by comparing the resonance signals of as deposited polymer with the respective paracyclophane precursor and purified polymer as shown in Figure 49 for PPX-butyl. The resonances from spectrum B for the as deposited polymer coincided with the purified polymer (spectrum C) but showed additional signals in the regions of 6.8-5.0 ppm, 2.4-2.2 ppm and small resonances around 1.1 ppm that did not entirely correspond to unreacted paracyclophane signals shown in spectrum A.

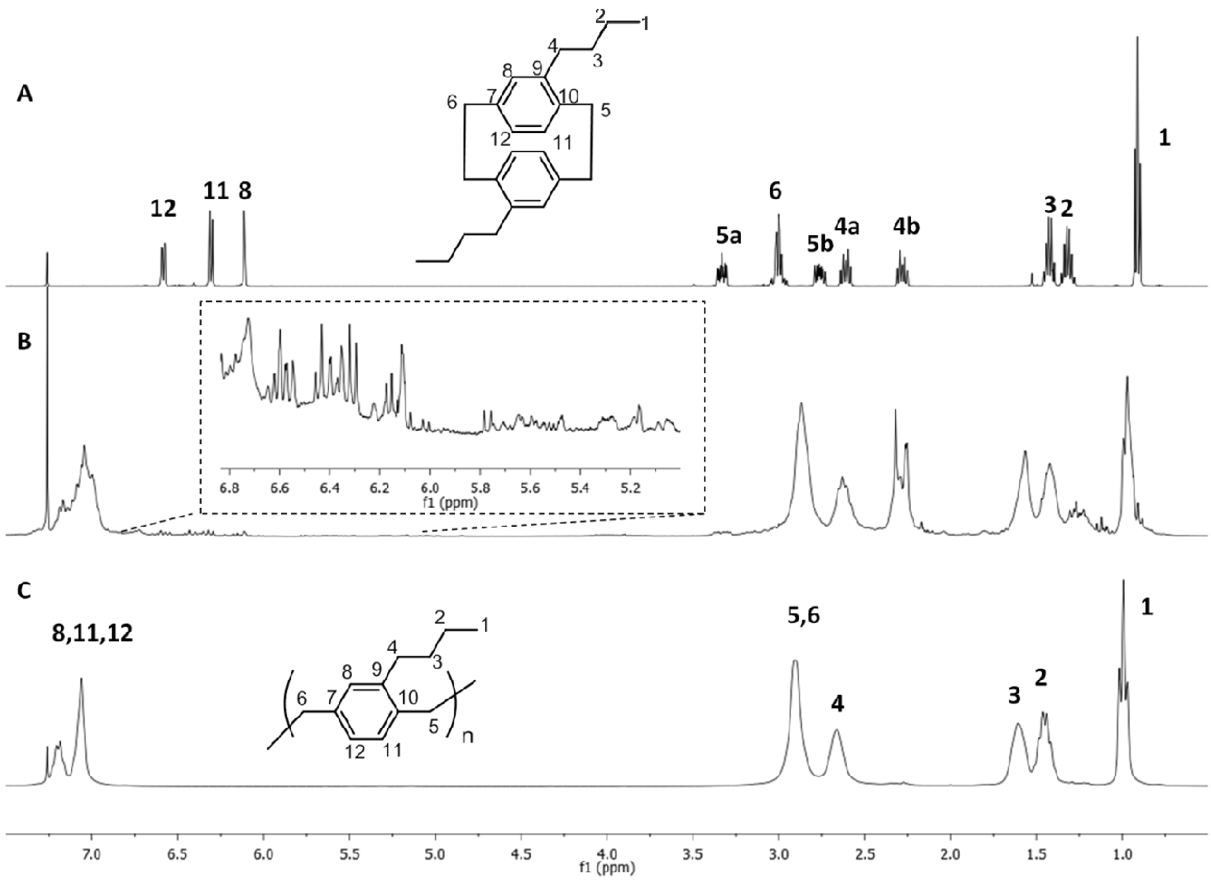

Figure 49 ^{1}H-NMR spectra of 4,12-di-*n*-butyl[2.2]paracyclophane (A), as deposited PPX-butyl (B) and PPX-butyl purified by precipitation from methanol (C). Especially in the region of 5-6.8 ppm and 2.4-2,2 ppm resonance signals of the oligomer impurities are present (spectrum B).

Thermogravimetric analysis of the non-purified samples provided quantitative information about the oligomer content. In contrast to the purified samples, in oligomer containing samples two degradation steps are present. The first, with maximum degradation temperatures around 230-310 °C for the oligomeric fraction and the second with maximum degradation temperature around 480 °C for the high molecular weight polymer (Figure 50 A, shown for PPX-butyl).

For PPX-propyl and PPX-butyl synthesized in the CVD reactor described in Section 5.3.1 a dependence of oligomer content with respect to the position in the deposition chamber was found for deposition parallel to the monomer flow. Here the oligomer content decreases to zero towards the end of the deposition chamber for PPX-propyl samples (Figure 50 B). Furthermore, PPX-pr was obtained with an overall less oligomer content compared to PPX-butyl samples synthesized under the same conditions (for detailed data see Section 5.5.7). Deposition perpendicular to the monomer flow resulted in comparable oligomer contents for samples recovered from different positions on the deposition target. The oligomer content did not depend on the deposition temperature or amount of precursor used for the synthesis.

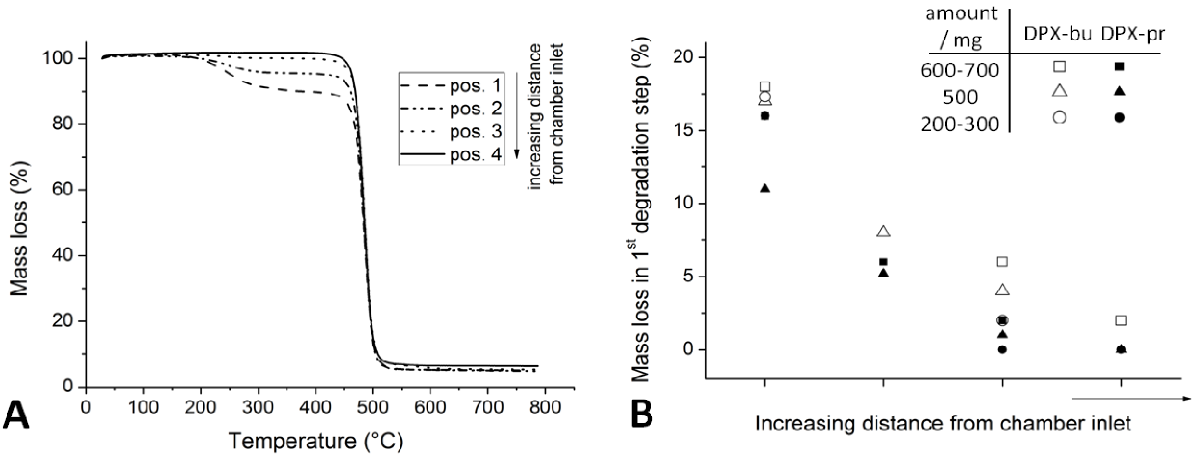

Figure 50 Thermal degradation of alkyl-PPX. Degradation curves for PPX-propyl (run 14) deposited parallel to monomer flow from different positions in the deposition chamber, polymer from pos. 4 does not contain oligomer (A). Dependence of oligomer content (measured by mass loss in first degradation step in TGA) in PPX-propyl and PPX-butyl in dependence of the position in the deposition chamber and amount of precursor (deposition parallel to monomer flow) (B).

Molecular weight analysis of PPX-propyl samples obtained from different positions of the deposition chambers supported the assumptions made on NMR and TGA results. The data showed larger polydispersity indices for samples collected from the entrance of the chamber (position 1) and tendentially lower molecular weights than at the back of the deposition chamber (Figure 51).

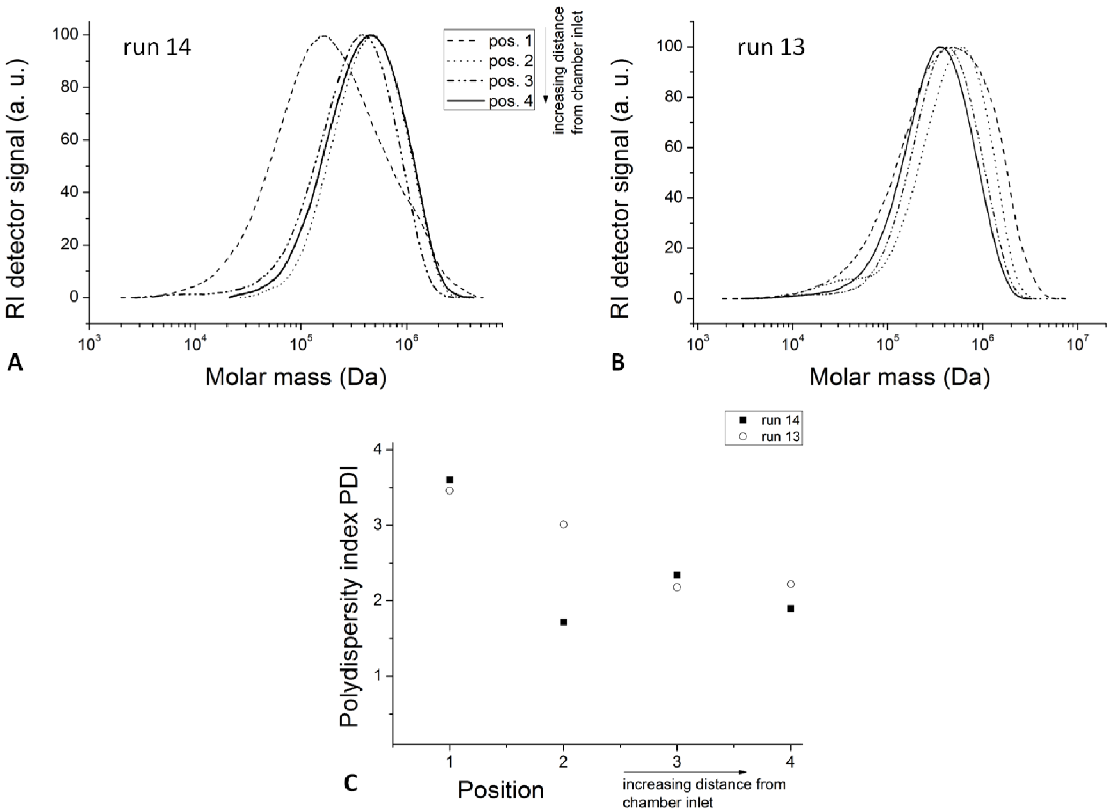

Figure 51 Molecular weights of PPX-propyl samples collected from different positions of the deposition chamber (A: run 14, B run 13) and plot of the respective polydispersity indices (C).

The isolation of the oligomers from PPX-butyl and PPX-propyl samples by either precipitation or extraction with methanol or ethanol and further analysis by THF GPC confirmed the low molecular weight. Figure 52 A and Figure 53 A show the molecular weight distributions of PPX-propyl and PPX-butyl before and after extraction for 1 week with ethanol. The molecular weight of the soluble fraction (red curve) is considerably less than the molecular weights of the insoluble fraction (black curve) and the untreated sample (blue curve) and was eluted in the exclusion volume. Analysis with olio-THF GPC showed the presence of two fractions for both PPX-propyl and PPX-butyl (Figure 52 B and Figure 53 B). The lower molecular weight fraction with masses < 1000 Da (compared to PS) showed several discrete peaks, while the fraction with M < 10,000 Da showed a broad distribution.

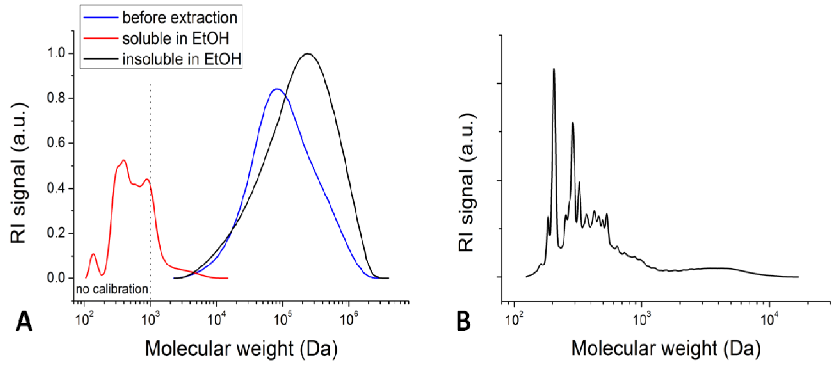

Figure 52 PPX-propyl was extracted with EtOH to remove the low molecular weight fraction. Molecular weights measured on THF-GPC as deposited (blue) compared to the insoluble fraction (black) and soluble fraction (red) (A). Analysis of the soluble fraction with oligo-THF GPC (B).

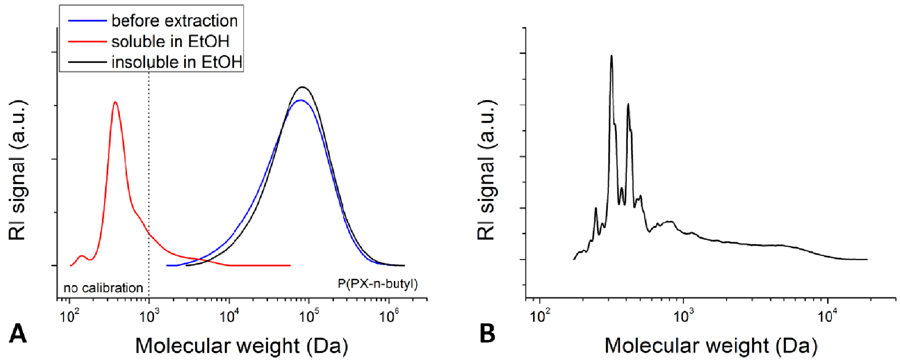

Figure 53 PPX-butyl was extracted with EtOH to remove the low molecular weight fraction. Molecular weights measured on THF-GPC as deposited (blue) compared to the insoluble fraction (black) and soluble fraction (red) (A). Analysis of the soluble fraction with oligo-THF GPC (B).

Thermogravimetric analysis of the samples before and after extraction was in accordance with the assumption that the oligomers show lower thermal stability. As shown in Figure 54 for PPX-butyl, before the extraction the polymer decomposed in two steps. After extraction of the soluble oligomer, a one step degradation was observed, while the oligomer fraction degrade at lower temperatures.

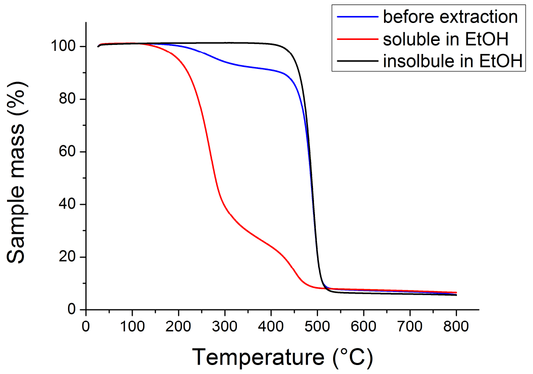

Figure 54 Thermal degradation of PPX-butyl directly after deposition shows two degradation steps (blue). The polymer extracted with ethanol degrades in one step (black), the fraction soluble in ethanol (red) is thermally less stable than the insoluble fraction.

To characterize the oligomeric fraction further, MALDI-TOF spectra were recorded with (*E*)-2-(3-(4-*tert*-butyl)phenyl)-2-methylallydiene)malononitrile (DCTB) and silver trifluoro acetat as matrix. By this means the presence of cyclic compounds in the oligomer fraction of PPX-propyl, PPX-butyl and PPX-heptyl obtained by precipitation in methanol was identified. For PPX-propyl and PPX-butyl the cyclic trimer was the predominant structure. For PPX-heptyl dimer and trimer were most abundant. The spectrum for PPX-butyl is shown in detail in Figure 55, additionally to the MALDI spectrum up to 1400 m/z an overlay of the spectrum region around 587 m/z (cyclic trimer) with the theoretical isotope distribution is given. For PPX-butyl cyclic structures with up to eight *p*X units were identified. Higher molecular weight oligomers or a second distribution, for example for linear structures, were not found.

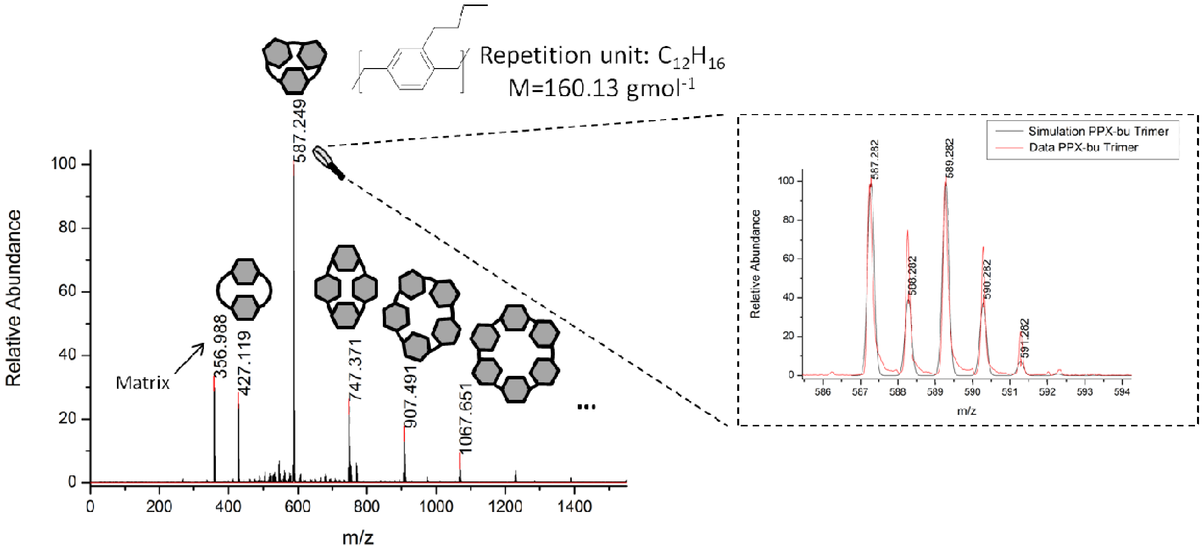

Figure 55 MALDI-TOF spectrum of PPX-butyl oligomer soluble in methanol. Cyclic compunds with up to eight *p*-xylylene units were identified. The magnification shows exemplarily the match of the experimentally obtained isotope distribution for the trimer in comparison with simulated data (Matrix: DCTB+Ag).

Figure 56 shows the MALDI spectra of PPX-propyl (A) and PPX-heptyl (B). For PPX-propyl cyclic species with up to nine *p*X units were identified, in case of PPX-heptyl the larges cylce was the pentamer. Same as for PPX-butyl no second distribution was identified. The unassigned peaks, especially present in PPX-heptyl spectrum, could not be identified as compounds composed of the *p*X repetition unit with alkyl substituent.

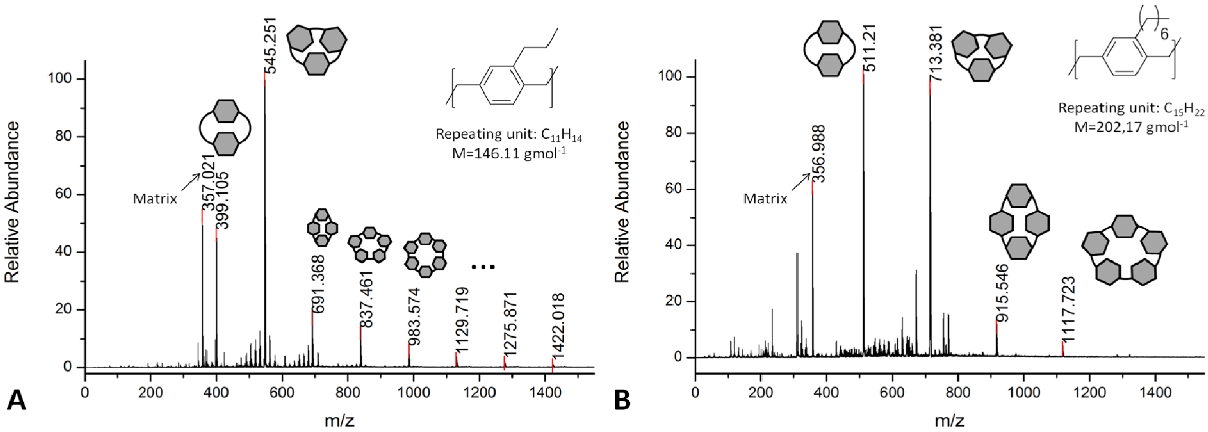

Figure 56 MALDI-TOF spectra of PPX-propyl (A) and PPX-heptyl (B) oligomer soluble in methanol. Cyclic compounds containing up to nine *p*-xylylene units were found for PPX-propyl. Cyclic PPX-heptyl compunds contained up to six *p*-xylyene units (Matrix: DCTB+Ag).

Table 8 shows the experimental masses in comparison to the theoretical masses for the most abundant isotope for each cyclic oligomer, the data are in good agreement.

Table 8 Experimental MALDI-TOF data (matrix DCTB+Ag) in comparison with simulated data for the most abundant isotope for PPX-propyl, PPX-butyl and PPX-heptyl up to the cyclic hexamer species.

Species	PPX-propyl		PPX-butyl		PPX-heptyl	
	Exact mass/g·mol^{-1}		Exact mass/g·mol^{-1}		Exact mass/g·mol^{-1}	
	Data	Simulation	Data	Simulation	Data	Simulation
Dimer + Ag	399.105	399.124	427.119	427.155	511.210	511.249
Trimer + Ag	545.251	545.234	587.249	587.281	713.381	713.422
Tetramer + Ag	691.368	691.343	747.371	747.405	915.546	915.593
Pentamer + Ag	837.461	873.453	907.491	907.531	1117.723	1117.766
Hexamer + Ag	983.574	983.562	1067.651	1067.656	-	1319.938

In addition to the observation of cyclic trimer as byproduct in alkyl-PPX synthesis via CVD,[16] cyclic tri- and tetramers as well as linear low molecular weight byproducts with an average degree of polymerization of 16 were reported by ERREDE for PPX-N obtained from *p*X polymerization in solution.[59] The amount of cyclic oligomers and byproducts was found to increase with increasing the reaction temperature from -78 °C to room temperature. In dilute solutions the intermolecular cyclization can compete with the addition of new monomers to the growing chain. However, in CVD the *p*X monomer adsorbes on the chamber walls and is, together with the growing chains, the only species present. The cyclization is relatively easy for the trimer, but less favored for the dimer due to the highly strained configuration for the [2.2]paracyclophane, though reported for PPX and PPV obtained via the GILCH route in solution.[142, 143] Since the dimer was most abundant in the PPX-heptyl sample, which was synthesized at the lowest pyrolysis temperature of the compared alkyl-PPX, it is assumed that the dimer found for PPX-heptyl was not formed in the deposition chamber but passed the pyrolysis zone unreacted. The longer a growing chain gets, the less mobile it is, therefore probability of cyclization reactions becomes less with increasing degree of polymerization, which is in accordance with the MALDI results.

Oligo-THF GPC measurements showed the presence of oligomers of higher molecular weight, that are assumed to be linear chains. This species could not be found in the recorded MALDI spectra what is supposed to be due to non ideal conditions for the larger molecules in this matrix-salt combination..

Attempts to reduce the oligomer content by doubling the length of the pyrolysis zone and placing quartz glass tubes in the pyrolysis zone to enhance contact surface were not successful.

A significant improvement in film quality was achieved by the synthesis of PPX-propyl in SCS Labcoater. As shown in the ^{1}H-NMR spectrum (Figure 57) no resonance signals in the regions of 7-5 ppm and 2.4-2.2 ppm are present. The thermal degradation curve (Figure 58) shows a one step degradation. The polymer therefore is free of oligomer impurities.

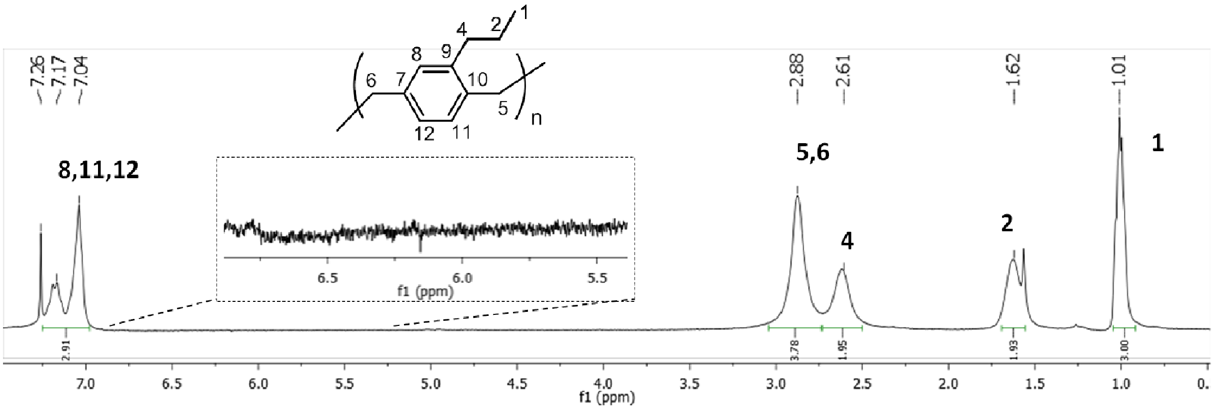

Figure 57 ^{1}H-NMR spectrum of as deposited PPX-propyl synthesized in Labcaoter. In the region of 7-5 ppm and 2.4-2.2 ppm no resonances are present, what accounts for oligomer free PPX-propyl.

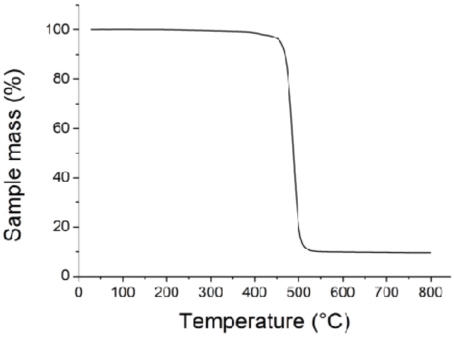

Figure 58 Thermogravimetric degradation curve of PPX-propyl synthesized in Labcoater.

The major difference between the homemade pyrolysis setup and the SCS Labcoater is the volume of the deposition chamber. The large volume difference (60-80 ml for homemade setup vs. ≈10 l for Labcoater) is related to a huge difference in available surface for *p*X deposition. Since the polymerization reaction of PPX starts with dimer formation on the substrate surface (see Section 3.2) the concentration of *p*X monomers on the surface is crucial for the initiation step. Though the initiation is energetically disfavored compared to the propagation reaction, with an increased number of monomer available on the surface the number of initiating chains is assumed to increase. Monomer availability is also related to faster film growth, that leaves growing chains buried in the film where they cannot be reached by monomer for further growth, which can explain the increased number of oligomers if PPX is deposited in small volume chambers. If the available monomers are distributed over a larger surface area, as in the case of the Labcoater deposition chamber, less chains are initiated per surface area, the overall filmthickness is less and individual chains grow longer. Molecular weights of PPX-propyl synthesized in the homemade setup were in the range of 150,000 to 300,000 Da, the polymer obtained in SCS Labcoater could not be measured by GPC because even in high dilutions the polymer does not pass the filtration prior to analysis. This is a strong hint for high molecular weights and supports, in combination with the above presented analysis, the assumptions that oligomer formation is related to availability of the monomer on the surface. Deposition temperatures certainly is another influence factor, but experiments in the homemade CVD setup with different T_{dep} showed no influence in the investigated range (-10 to 20 °C).

To verify this hypothesis, polymers synthesized at different process pressures, that (at T_{sub}= const.) is related to the amount of available monomer, and constant surface area (or vice versa) have to be analyzed regarding their oligomer content. Another possibility can be the detection of living radicals in the polymer films by EPR spectroscopy, as described by GAZIKI *et al.*[64]

4.1.5 Conclusion

Copolymers of 2-hydroxyethyl methacrylate (HEMA) with different [2.2]paracyclophanes were successfully obtained by chemical vapor deposition in different reactors. In case of the propyl and butyl substituted [2.2]paracyclophanes soluble copolymers were obtained. The solubility enabled for the first time NMR spectroscopic analysis of the copolymer composition and molecular weight analysis via GPC. 2D NMR techniques showed the connection of both monomer units, which proves the copolymer structures. Soluble P(PX-*co*-HEMA) copolymers with HEMA contents up to 35 % were synthesized, confirming reasonable reactivity of the HEMA comonomer with the highly reactive *p*X monomers. In order to determine reactivity ratios, similar to the work reported by GLEASON *et al.*[40] for iCVD copolymers, controlled flow of both monomers is needed. Such more detailed analysis will also give further insight into the copolymerization mechanism and will complement the theoretical studies of BOBROWSKI *et al.* who predict moderate reactivity of *p*X with vinylic monomers only if they comprise strong electronegative substituents.

Copolymer synthesis in the homemade CVD setup led to the presence of unreacted HEMA comonomer in the deposited copolymer films, that therefore require additional purification treatment. Polymer films free of unreacted comonomer were obtained for P(PX-N-*co*-HEMA) synthesized in the SCS Labcoater. For these copolymers a dependence in HEMA content and HEMA evaporation temperature was found. Consequently, with increasing HEMS content the water contact angle of copolymer films decreases down to 65°.

The copolymer coatings furthermore showed to be biocompatible, since in a first test no harm to mouse fibroblasts (L929) cells growing on the copolymer films could be detected. Biocompatibility is expected, because both PPX-N and PHEMA are well established in biomedical applications, but has to be proven for the copolymers before thinking of applications, like for example stent coatings.

Comparing the copolymerization results for the homemade setup with the Labcoater underlines the crucial importance of the CVD parameter. The influence of e.g. pressure, deposition temperature, reactor geometry and rotation of the sample holder, are well understood for PPX homopolymers, but resulted to be even more important for CVD copolymerization. Here homogeneous film composition, surface morphology and absence of unreacted starting material were achieved with the commercially available Labcoater equipped with a rotating sample holder. The use of this setup with a deposition chamber of large volume resulted also favorable for PPX-propyl synthesis, since films free of oligomeric byproducts were obtained. Detailed analysis of the low molecular weight byproducts in alkyl-PPX synthesis in the homemade setup showed the presence of cyclic oligomers with up to nine *p*X units for PPX-propyl.

Soluble alkyl-PPX peroxides were obtained by the use of gaseous oxygen as comonomer for alkyl-[2.2]paracyclophanes. By controlling the process pressure during deposition the peroxide content was regulated between 0 and 20 %. The cleavage of the peroxide bond was found to take place at temperatures above 100 °C. Peroxide bond cleavage in applications of alkyl-PPX as macronitiators will have to be achieved by other means, like for example amine assisted cleavage.[141] α,ω-hydroxy terminated alkyl-PPX peroxides obtained by reductive cleavage of the peroxide bonds are considered an alternative approach for block-copolymerization via e.g. polycondensations.

4.2 Surface Modification of PPX by *grafting to* and *grafting from*

4.2.1 Motivation, Hypothesis and Concept

Several methods for surface functionalization of PPX were presented in Section 3.3. Most of them involve several reaction steps, or need long reaction times. Especially the pre-deposition modification of [2.2]paracyclophanes to obtain functional and reactive surfaces can be time consuming and expensive.

Free radical polymerizations are known to proceed with many side reactions, that include chain transfer to monomer, to growing chains or to other species present in the reaction solution.[144] This side reactions are usually undesired because they affect the molecular architecture, the molecular weight and molecular weight distribution of the polymer and by this means the properties of the bulk material. In order to control radical polymerization several techniques have been established, which passivate the active radical reversibly, so that less side reactions occur, while the polymer chains are still able to grow by monomer addition. One of this techniques is atom transfer radical polymeriaztion (ATRP),[145] where the reactive radical on the polymer chain end is reversibly deactivated by the addition of a copper complex.

The working hypothesis was, that both, free radical polymerization and ATRP can be of use for the surface functionalization of PPX films in form of *grafting* reactions. In a *grafting to* approach, the radicals are generated by a conventional initiator, start the polymerization of a monomer and transfer radicals to a PPX film present in the reaction solution. This approach will be referred to as *grafting to*, though not completely in accordance with the common definition of *grafting to* reactions. On the other hand, controlled radical polymerization started from an initiator incorporated into the PPX film and is considered to lead to spatially controlled growth of polymer chains (*grafting from* approach).

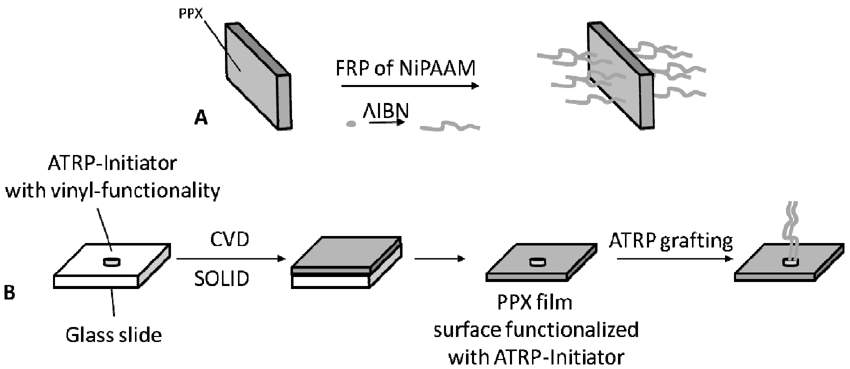

Figure 59 Illustration for the concept of easy surface functionalization of PPX-N films. *Grafting to* via chain transfer (A) and *grafting from* by SOLID (solid on liquid deposition) functionalization and ATRP.

The concepts for surface modification via *grafting to* and *grafting from* are illustrated in Figure 59. The double bond containing ATRP initiator was incorporated into the PPX-film during the CVD process by means of the SOLID method (see Section 3.3.3). Of particular interest were the grafting of *N*-isopropyl acrylamide (NiPAAm), because of its thermoresponsive behaviour, with a lower critical solution temperature (LCST) at 32 °C and glycidyl methacrylate (GMA) because of it epoxy group which is capable of further reactions.

4.2.2 Modification by Chain Transfer - *grafting to*

In order to modify the surface of PPX-N, free standing films were submerged into free radical polymerization (FRP) solutions of NiPAAm in ethanol and MMA in anisole. After the polymerization and intensive washing of the films by soxhlet extraction with a suitable solvent, the film surfaces were analyzed with ATR-IR spectroscopy (Figure 60). ATR-IR analysis showed the successful surface modification of the PPX-N films. The PPX-N film present in the FRP of NiPAAm showed absorption bands of the amide group at 1649 cm^{-1} and 1553 cm^{-1}, while the film present in FRP of MMA showed absorptions at 1729 cm^{-1} characteristic for carbonyl stretching vibrations.

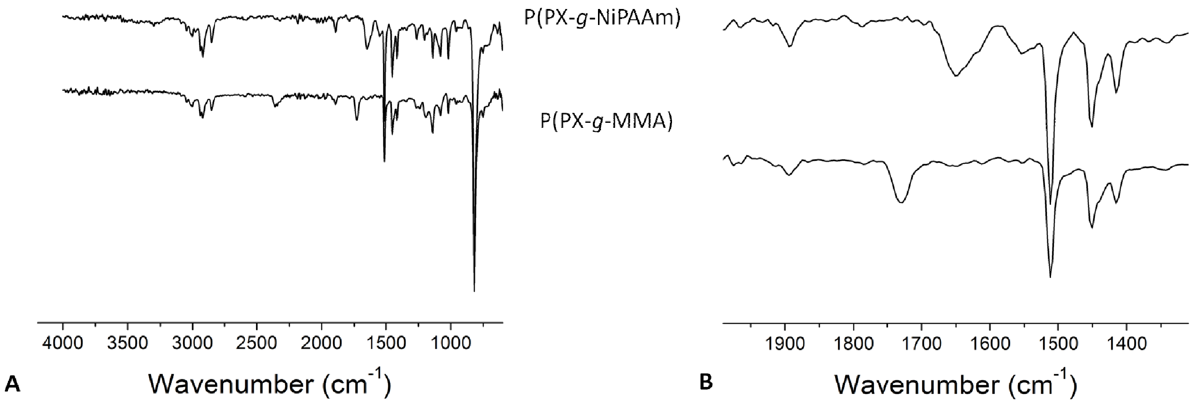

Figure 60 ATR-IR spectra of PPX-N films present in free radical polymerizations of NiPAAm and MMA (A: entire transmission spectrum, B: excerpt of relevant area with amide vibrations of NiPAAm at 1649 cm^{-1} and 1553 cm^{-1} and carbonyl vibration of MMA at 1729 cm^{-1}).

For contact angle measurements PPX-N films on glass slides were submerged to FRP solutions of NiPAAm. To ensure the adhesion of PPX-N onto the glass substrates, the glass slides were treated with adhesion promoter solution prior to PPX-N coating. Contact angle measurements after 3h reaction time for the FRP, the film on the glass slides were extracted for 2d with water prior to water contact angle determination. The NiPAAm modified PPX-N surfaces showed hydrophilic contact angles in the range of 40-55 °. A pronounced temperature dependence, as expected for PNiPAAm was not found, at 50 °C substrate temperature the contact angle was in the range of 55-60°. PPX-N that was surface modified for longer reaction times (5 h) showed contact angles in the same range.

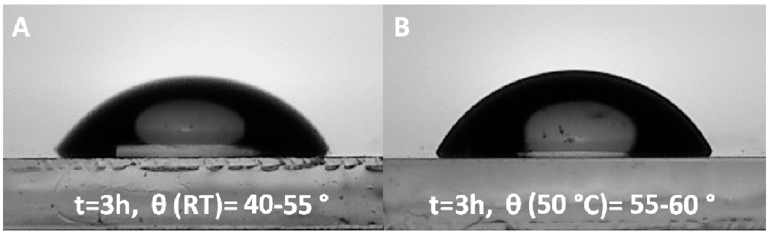

Figure 61 Photographs of water droplets on NiPAAm modified PPX-N surfaces (reaction times t= 3h) at room temperature (A) and 50 °C substrate temperature (B).

4.2.3 Modification by SOLID and ATRP - *grafting from*

For the SOLID (solid on liquid deposition) surface functionalization of PPX-N the double bond containing ATRP initiator 2-bromoisobytryloxy-oligo(ethylene glycol) methacrylate (OEGMA-Br) was synthesized from oligo(ethylene glycol) methacrylate (OEGMA) and α-bromoisobutyryl bromide (BiBB) (Figure 62).

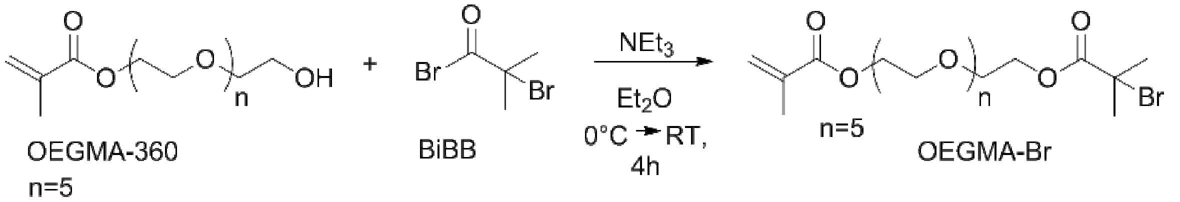

Figure 62 Synthesis of functional ATRP initiator 2-bromoisobutyryloxy-oligo(ethylene glycol) methacrylate (OEGMA-Br).

The successful conversion of the hydroxy group of OEGMA was confirmed by NMR analysis, Figure 63 shows the ^{1}H-NMR spectrum with the assigned resonance signals. Complete conversion is confirmed by comparing the resonance integral ratios of the double bound protons (H-3a or H-3b) at 6.13 ppm and 5.57 ppm to the methyl protons H-1 and H-12 (1.94 ppm), which for full conversion is 1:1:9.

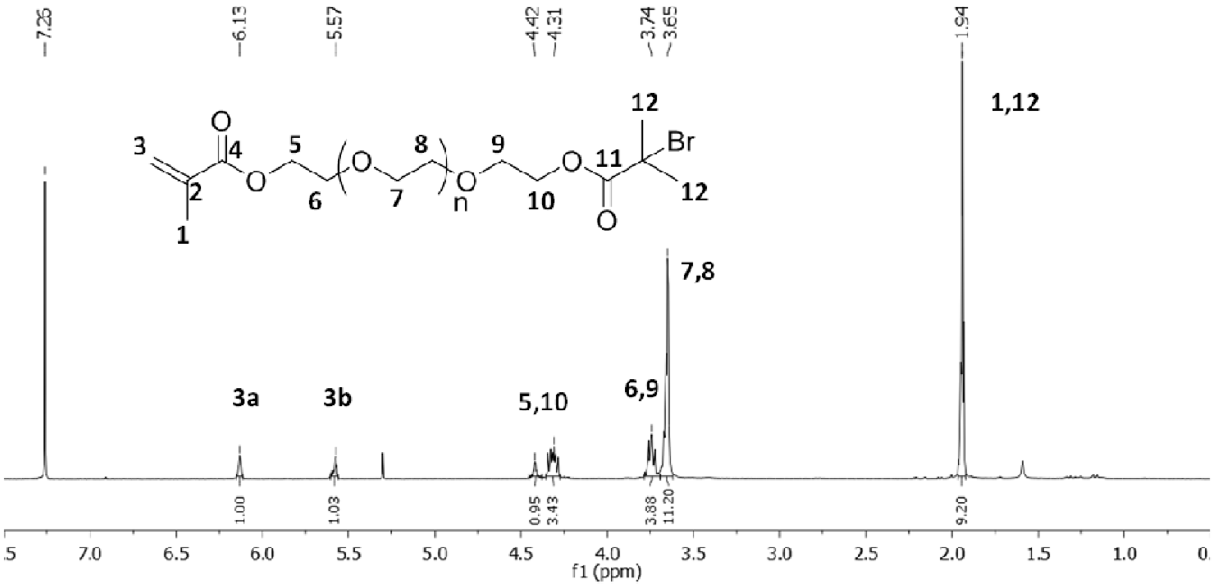

Figure 63 ^{1}H-NMR spectrum of OEGMA-Br in $CDCl_3$.

For the functionalization of PPX-N with ATRP initiator via the SOLID method, the liquid initiator was placed, either pure or diluted with diethyl ether, onto glass slide and coated via CVD. By varying the amount of precursor and the number of deposition runs, the film thickness was varied between 2 and 20 µm.

The incorporation of OEGMA-Br into the PPX-N film was confirmed by the presence of the carbonyl streching vibration of the two ester carbonyls at 1720 cm^{-1} by ATR-IR measurements. Figure 64 shows ATR-IR spectra of both, OEGMA-Br with unreacted double bond and OEGMA-Br incorporated into the surface of a PPX-N film (P(PX-N-*surf*-OEMGA-Br). The complete removal of unreacted OEMA-Br from the film by extraction is confirmed by the absence of the C=C stretching vibration at 1640 cm^{-1}.

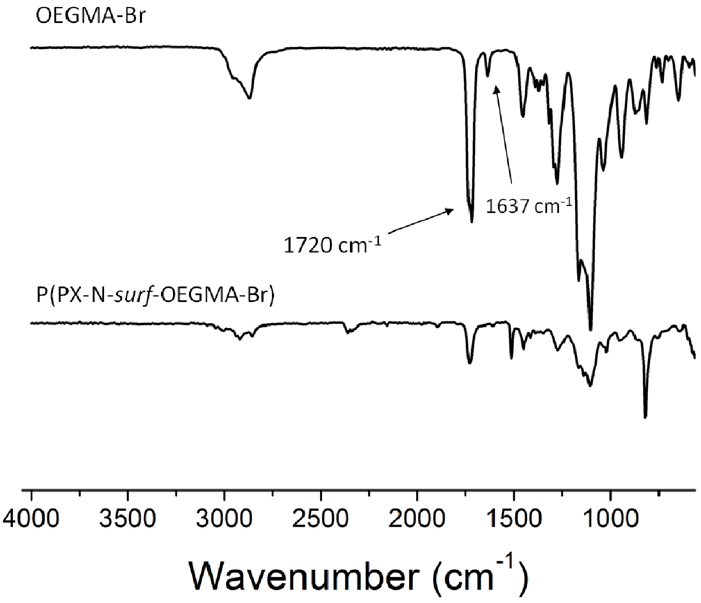

Figure 64 ATR-IR spectra of OEMGA-Br and P(PX-N-*surf*-OEMA-Br).

An OEGMA-Br pattern on the surface of PPX-N films was achieved by depositing the film onto isolated initiator droplets placed on a glass substrate (as illustrated in Figure 65). The incorporation of the initiator at the desired sites was controlled with ATR-IR and energy dispersive x-ray analysis (EDX).

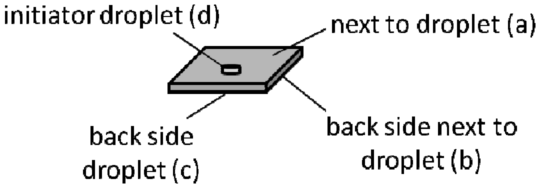

Figure 65 Schematic illustration of a P(PX-N-*surf*-OEGMA-Br) film with partially functionalized surface. The positions indicated with (a), (b), (c) and (d) are used later to describe the location of the recorded ATR-IR spectra.

Figure 66 shows the recorded EDX spectra and SEM micrographs of the repective location on the P(PX-N-*surf*-OEGMA-Br) film. The film was patterned with OEGMA-Br initiator as shown in Figure 65. The characteristic emission peaks for bromine of K_α= 11.90 keV, K_β= 13.36 keV and L_α= 1.48 keV were observed only on site (d) where the OEGMA-Br initiator droplet was intentionally incorporated into the PPX-N films. On all other spots, which are next to the droplet (a) and on the backside of the film (c) and (d) no bromine could be found. Same results were obtained by ATR-IR analysis as shown exemplarily in Figure 67 A and Figure 68 A.

Grafting from reactions were performed with Cu(I)Br and *N,N,N',N'',N''*-pentamethyl diethylene triamine (PMDETA) as ligand and different solvent/monomer combinations, among them NiPAAm in water, glycidyl methacrylate (GMA) in water/methanol 1:1, methyl methyacrylate (MMA) in anisole and 4-vinylpyridine (4-VP) in water. Figure 67 B shows the ATR-IR spectra of P(PX-N-*g*-GMA) for different positions on the film (as indicated in Figure 65). The presence of a strong absorption at 1720 cm^{-1} characteristic for carbonyl streching vibrations, showed, that poly glycidyl methacrylate (PGMA) was grafted on the entire film, despite the functionalization with OEGMA-Br.

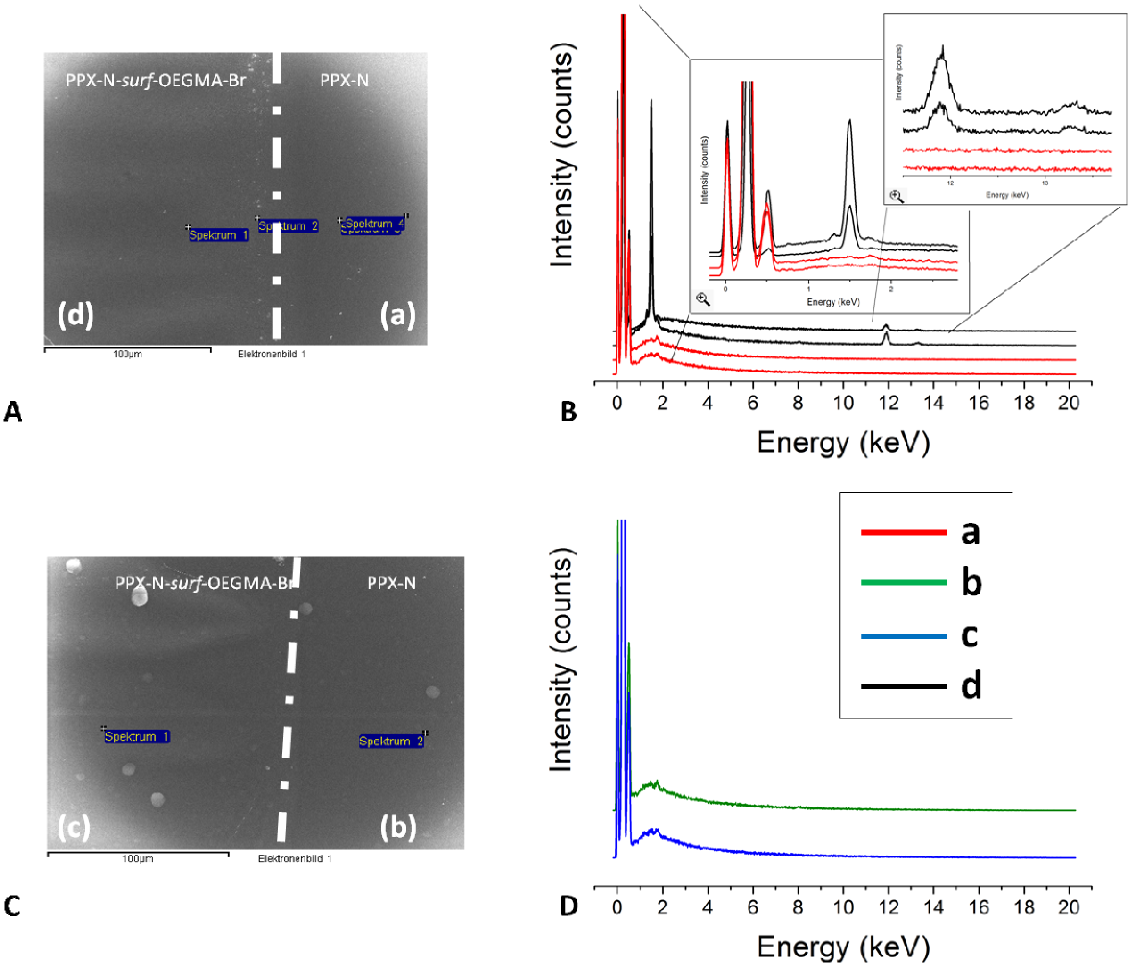

Figure 66 SEM micrographs (A,C) and results of EDX (B,D) analysis of PPX-N films surface functionalized with OEGMA-Br via the SOLID method. The small letters indicate the spots on the film as explained in Figure 67 A. The functionalized side (A,B) and the backside (C,D) of the film were analyzed with regard to their bromine content. Bromide was found only in spot (d).

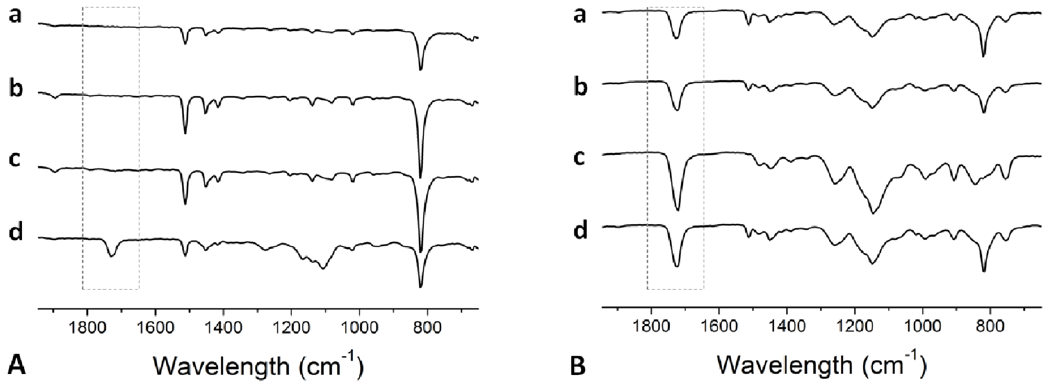

Figure 67 ATR-IR spectra of the OEGMA-Br surface functionalized PPX-N film at the four different spots described in Figure 65 (A). ATR-IR spectra of the same film after *grafting from* reaction via ATRP with glycidyl methacrylate (GMA) (B). Though the ATRP initiator OEGMA-Br can be detected only on the desired spot, GMA was grafted to the entire film.

Same results were obtained for all other monomer systems. As an example Figure 68 shows the ATR-IR spectra of P(PX-N-*surf*-OEMGA-Br) before and after the grafting with NiPAAm. Same as explained before, the grafted polymer is present all over the film, though in considerably less amounts on positions (a), (b) and (c) where no initiator was incorporated into the P(PX-N-*surf*-OEGMA-Br) film. However, the suface modification of the entire P(PX-N-*g*-NiPAAm) film was obvious due to low water contact angles as shown in Figure 68 C. PPX-N show contact angles around 90 °and is not temperature responsive. For the P(PX-N-*g*-NiPAAm) film the contact angle showed a temperature responsiveness, as expected for PNiPAAm, with a more hydrophobic contact angle, 70 ± 3 ° at position (a) and 69 ± 4° at position (d), at 50 °C and a more hydrophilic contact angle at room temperature (53 ± 2°, 57 ± 3°). Consequently there was no significant difference in the surface behavior of P(PX-N-*g*-NiPAAm) after the grafting reaction despite the initiator functionalization.

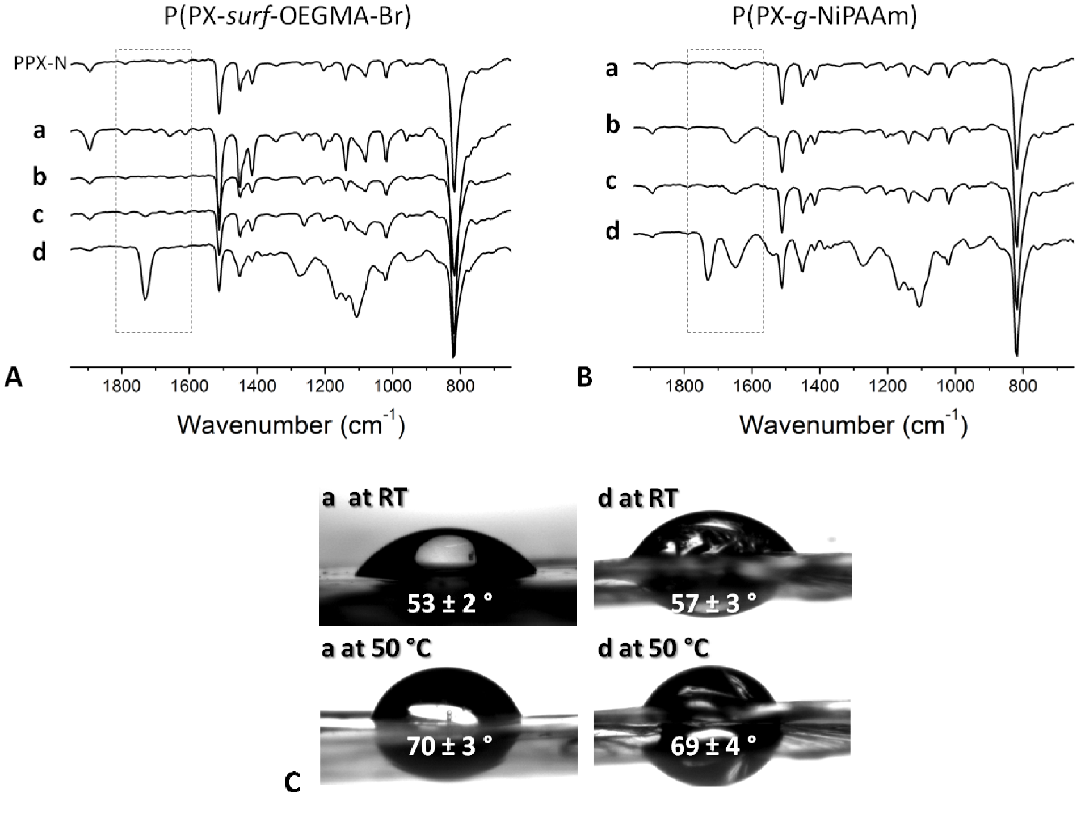

Figure 68 ATR-IR spectra of the OEGMA-Br surface functionalized PPX-N film at the four different spots as described in Figure 65 A (A). ATR-IR spectra of the same film after *grafting from* reaction via ATRP NiPAAm (B). Though the ATRP initiator OEGMA-Br can be detected only on the desired spot, NiPAAm was grafted to the entire film, as can be seen in the IR spectra and from water contact angle measurements (C).

Best hydrophilicitiy was achieved for PPX-N films that were functionalized with OEGMA-Br entirely on one side of the film. After *grafting* with NiPAAm water droplets spread on the surface of the film, and have a contact angle of 25° after 20 s (Figure 69 A). However, the same effect was observed on the backside of the film, were no initiator was incorporated. Here the initial contact angle after the impact was 80 ° and spreading led to a minimum contact angle of 50 ° after 30 s.

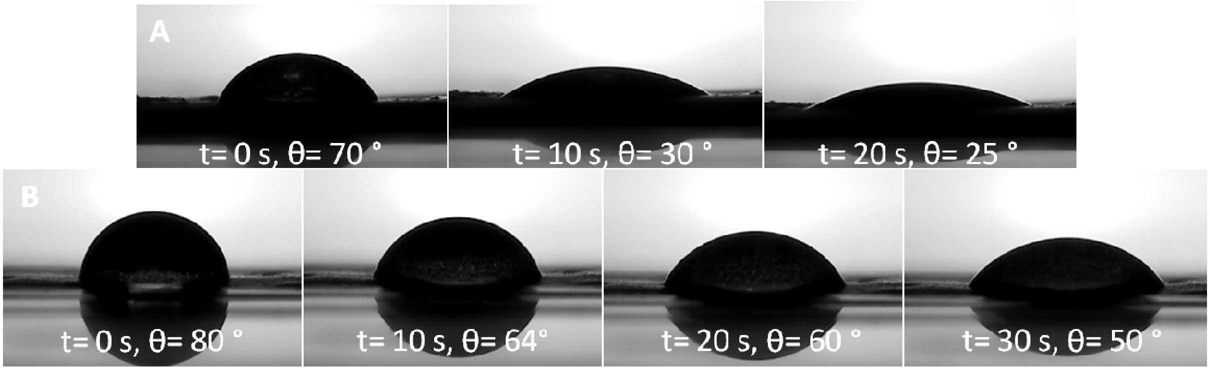

Figure 69 Water contact angle on a P(PX-N-*g*-NIPAM) film. The water droplet spreads faster on the side of the film that was functionalizes with OEGMA-Br prior to the grafting reaction with NiPAAm (A). On the backside of the film (B) the water droplet spreads, but the minimum contact angle is twice as on the other side.

4.2.4 Conclusion

Surface modification of PPX-N films with different polymers were achieved by two different *grafting* approaches.

The *grafting to* method by chain transfer is an easy tool for surface modification of free standing PPX films or PPX films on substrates. Surfaces modified by the attachment of PNiPAAm showed a water contact angle of about 50 ° and were therefore significantly more hydrophilic than PPX-N.

Via the SOLID process the vinyl functionalized ATRP initiator OEGMA-Br was successfully incorporated into PPX-N films. The surface initiated *grafting from* reactions, used in the second approach, showed too many side reactions for the chosen systems to surface patterning by the grafting reactions. Instead the entire film surface was functionalization, even on positions where no ATRP initiator was incorporated prior to the grafting. However, the *grafting* with PNiPAAm led to hydrophilic surfaces where water droplets spread and achieved contact angles down to 25 °. Since ATRP is a versatile polymerization method and offers great variety of solvent/metal/ligand systems, a change of solvent and ligand[145, 146] is expected to lead to more controlled ATRP polymerization. By this means PPX-N films with patterned surfaces will be available via surface initiated ATRP.

Both methods are applicable for common monomers suitable or FRP or ATRP and are not limited to the systems presented here.

4.3 Processing of Alkyl-PPX via Electrospinning

4.3.1 Motivation, Hypothesis and Concept

Alkyl-PPX polymers are a hydrophobic and flexible material,[16] which is available for surface coatings via the CVD process. The derivates with propyl substituents and longer are, due to their solubility, also available for solution processing methods. The polymer synthesis by CVD can be carried out either for direct coating purposes with deposition on the final substrate, or with a small collector chamber for further usage of the polymer (see Section 5.3 for CVD reactor details).

However, the water contact angle of as deposited and solvent cast films of alkyl-PPX lies between 95-100°, and does not increase significantly with the length of the alkyl substituent.[16] This value is comparable to conventional PPX-N and only moderately hydrophobic. To be applied as water repellent surface coatings, a higher water contact angle in combination with a low roll angle is needed. A more hydrophobic or even superhydrophobic surface of this material would be halogen free and is expected to be biocompatible and non toxic, same as PPX-N. The approach to obtain superhydrophobic and self-cleaning surfaces from alkyl-PPX synthesized via CVD without modification of the polymer itself is described in the following part of this thesis.

The hydrophobicity of a surface is, of course, governed by its chemical composition, but also by its surface structure in the micro and nanometer range. The hypothesis is, that there is no need to alter the alkyl-PPX polymers in their chemical composition, because structuring the material in adequate dimensions would lead to superhydrophobicity and self-cleaning ability. The structuring of surfaces in general can be achieved by different methods depending on the characteristics of the material. The approach chosen here is to process the hydrophobic alkyl-PPX by electrospinning into micro or nano fibers (Figure 70).

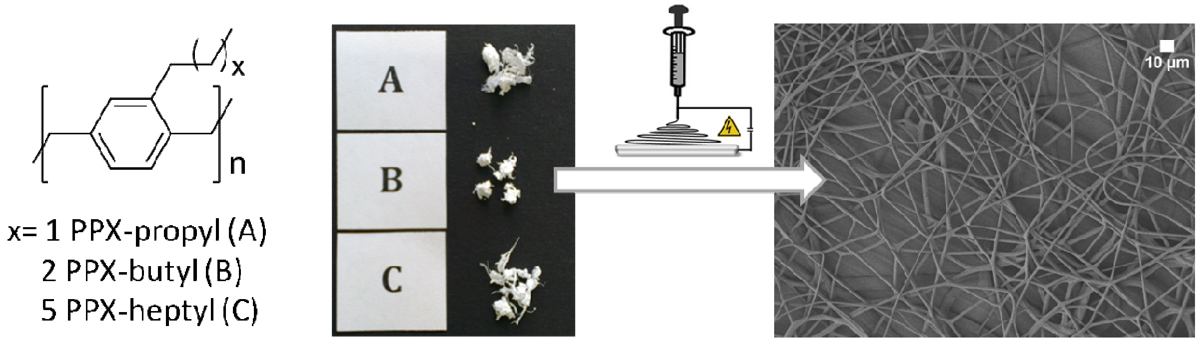

Figure 70 Concept for the processing of PPX. Alkyl-PPX obtained by CVD are solid polymers despite their low glass transition temperatures, and can be processed by electrospinning into stable micro and nano fibers.

During the electrospinning process fiber morphology can be influenced by several parameter providing additional structuring on different dimension scales (see Section 3.4). This can either be achieved by the production of beaded fibers (bead-on-string morphology) with e.g. beads in the dimension of several micrometer and significantly thinner fibers, or by providing the surface of microfibers with structures of smaller scale, like pores. Of course, the combination of both features is considered to be even more promising. To achieve beads and pores as structural features, low polymer concentrations and high relative humidity in the electrospinning environment were chosen.

Once the processability of alkyl-PPX is achieved further parameter can be varied in order to explore the possibilities of this new polymer class available for electrospinning.

4.3.2 Alkyl-PPX Nano Fibers: Towards Superhydrophobic Surfaces

Electrospinning was performed with three different alkyl-PPX derivates: PPX-propyl, PPX-butyl and PPX-heptyl, synthesized via chemical vapor deposition (Table 9). Though this PPX-alkyl derivates have glass transition temperatures of 20 to 40 °C below room temperature, they formed stable nano fibers in the electrospinning process (Figure 70). The polymers were spinnable from chloroform and THF solutions with 2-6 wt% polymer content. Above these concentrations rapid clogging of the electrospinning needle did not allow a continuous spinning process.

Table 9 CVD synthesis parameter and results of polymer analysis for alkyl-PPX.

Polymer	T_{sub}/ °C	T_{py}/ °C	$\cdot 10^5$ M_n/ Da	$\cdot 10^5$ M_w/ Da	PDI	T_g/ °C	E-modulus[16]/ GPa
PPX-propyl	120	550	1.12-2.7*	5.10-8.87*	≈3*	5	0.31-0.42
PPX-butyl	120	520	0.52-1.10*	1.49-4.52*	≈4*	-7	0.16
PPX-heptyl	150	500	0.85#	5.05#	6#	-27	0.06

* molecular weights varied in different batches, partially bimodal distrubutions; # bimodal; T_{sub}= precursor sublimation temperature; T_{py}= precursor pyrolysis temperature

By changing the solvent, the surface morphology of the electrospun alkyl-PPX fibers was varied from smooth fibers to bead-on-string structures. As a second influence factor the relative humidity (RH) was varied in the range of about 20% to 90% RH.

From chloroform solutions with 3 wt% polymer content smooth fibers were obtained at low RH (Figure 71 A,E,I). With increasing RH the fibers of all three alkyl-PPX showed a porous surface morphology. The threshold humidity for pore formation was found between 25% and 35% RH. When this border was exceeded, all observed fibers showed porous surfaces, regardless of their diameter. The pores obtained at 35% to 48% RH (Figure 71 B,F,J) were of circular or slightly oval shape. No differences for the alkyl-PPX derivatives could be observed.

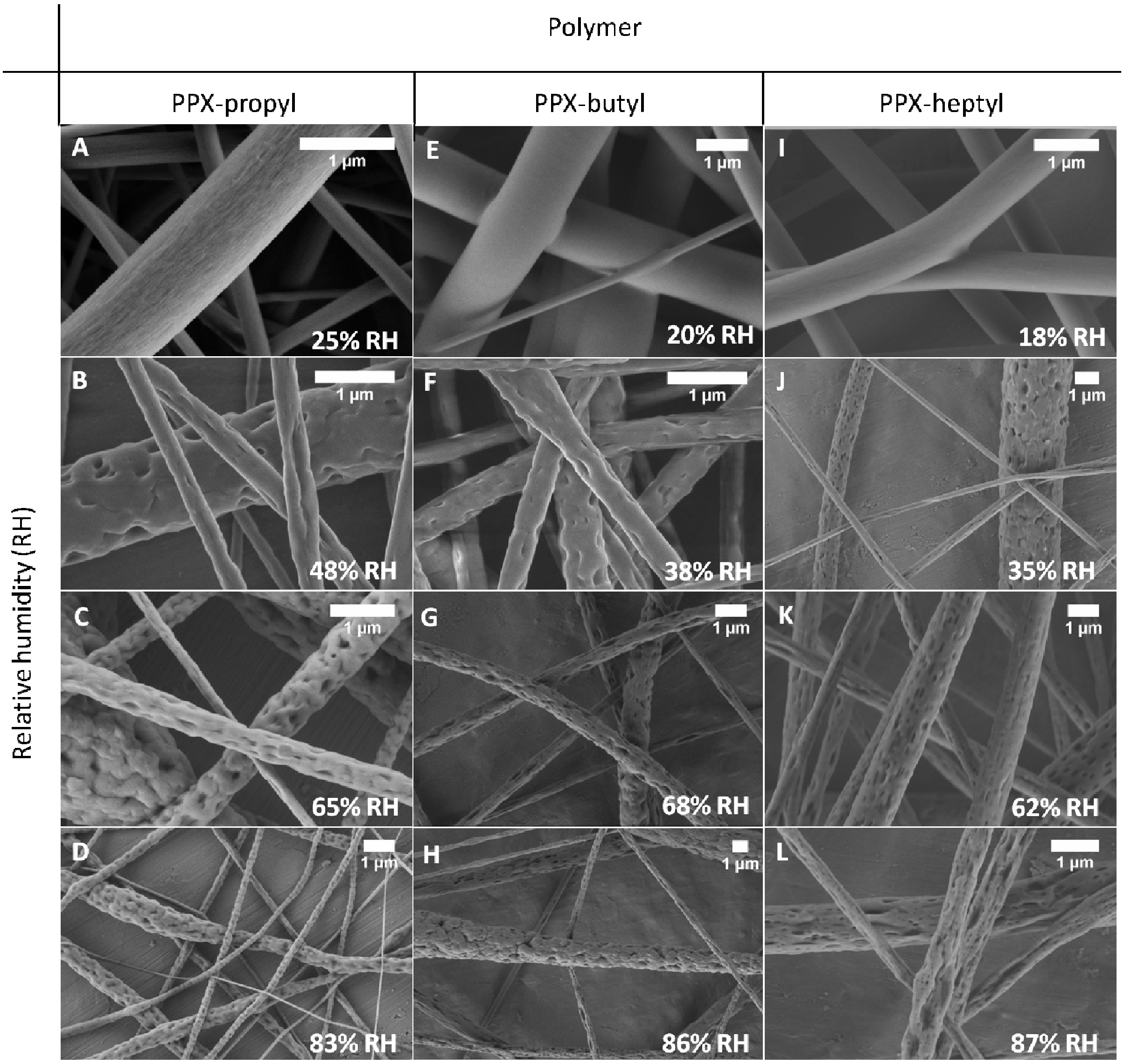

Figure 71 SEM micrographs of electrospun fibers of PPX-propyl (A-D), PPX-butyl (E-H) and PPX-heptyl (I-L) from 3 wt% solutions in chloroform at different relative humidity (RH) levels.

With increasing RH (>60%) the pore density on the fibers increased (Figure 71 C,G,K). Once the fiber surface was saturated with pores, they started to merge together forming larger structures of non-circular shape. Therefore the surface of PPX-propyl and PPX-butyl fibers were rough and uneven. At RH above 80% (Figure 71 D,H,L) the merging pores were of undefined structure for PPX-propyl and PPX-butyl, with increasing surface roughness. In contrast to this, PPX-heptyl fibers showed less surface roughness and still comprised stretched oval pores of 200-400 nm length in fiber direction together with a second distribution of smaller pores of 60-85 nm length.

The porous surface structure of a fiber, independent of its formation mechanism, is fixed after the solvent is evaporated. The difference in surface roughness and pore geometry of PPX-heptyl fibers compared to PPX-propyl and PPX-butyl fibers might be attributed to the difference in glass transition temperature (T_g). Due to the longer alkyl substituent on the aromatic ring, PPX-heptyl has a substantially lower T_g and E-modulus than PPX-propyl and PPX-butyl (Table 9). The T_g of a polymer influences its fiber morphology. The lower the T_g, the more flexible is the polymer fiber after solidification and the more susceptible to mechanical influence. The forces exerted on the fiber before deposition on the counter electrode stretch and elongate it. The pore deformation in fiber direction visible on PPX-heptyl fibers but not on fibers of PPX-propyl and PPX-butyl suggests, that only PPX-heptyl was in that way susceptible to the stretching forces. While dry PPX-propyl and PPX-butyl fibers maintain their pore geometry, PPX-heptyl fibers are, due to the low T_g of -27 °C and low E-modulus, ductile enough to be further stretched by the electric forces during electrospinning.

Polymers with T_g below room temperature can show macromolecular movement and/or relaxation even if the stretching forces of the charged polymer solution jet are no longer present. The consequence can be breakage or conglutination of the fibers directly after the spinning or upon storage. TIAN et al.[147] reported the morphological instability of polybutadien fibers upon storage for several hours at ambient conditions. In contrast to this alkyl-PPX fibers maintained their fiber shape and porous morphology for at least 30 days at room temperature and survived additional thermal treatment (14 h at 65 °C) (Figure 72), which accounts for high chain entanglement in the solid polymer preventing a shape loss.

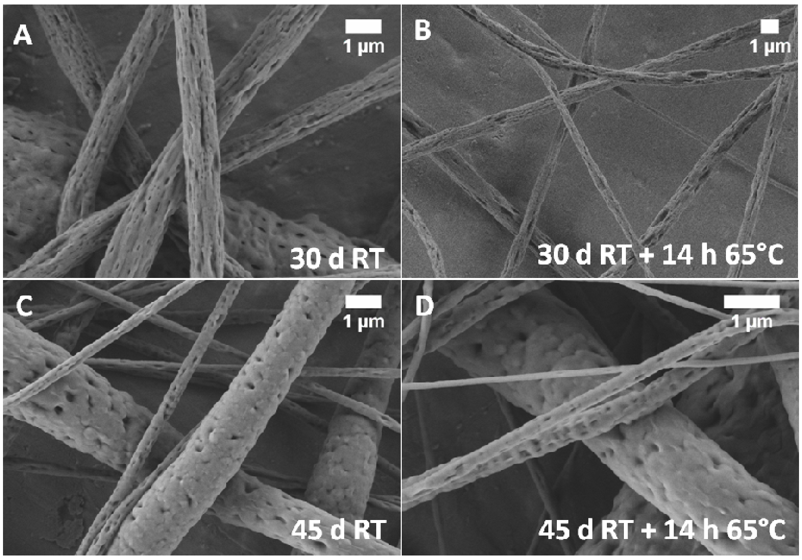

Figure 72 Stability of alkyl-PPX fibers. PPX-heptyl after 30 days storage at room temperature (A) and additional thermal treatment for 14 h at 65 °C (B), PPX-butyl after 45 days storage at room temperature (C) and additional thermal treatment for 14 h at 65 °C (D).

The mean fiber diameters of the fibers spun at different RH levels are given in Figure 73. As shown, spinning alkyl-PPX at higher RH tended to larger average fiber diameters and broader size distributions, occasional beads with length of more than 50 µm were present at all humidity levels and not taken into account. PPX-butyl fibers were spun with the same polymer batch at identical injection rates and voltages, and show the most pronounced increase at RH >70%. For

PPX-propyl and PPX-heptyl the injection rates were increased slightly at higher RH (>60%). This influence, same as slight changes in molecular weight distributions (see Table 9), did not affect the overall trend.

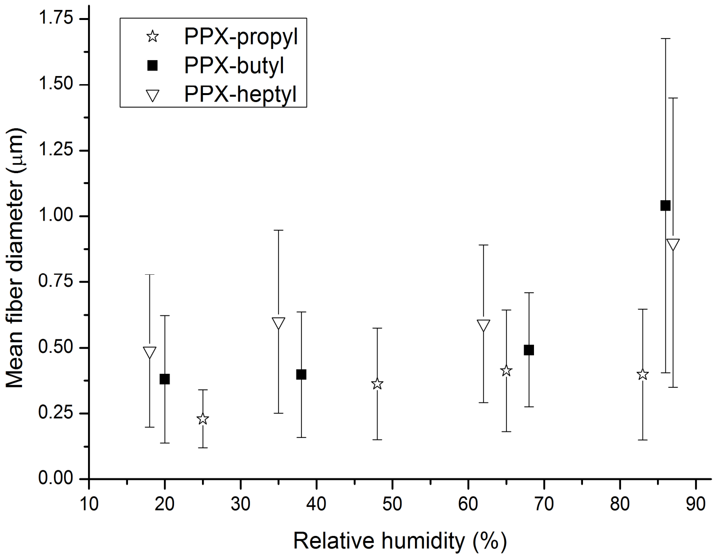

Figure 73 Evolution of fiber diameter of alkyl-PPX spun from 3wt% chloroform solution with increasing relative humidity.

For instance, the average fiber diameter for PPX-propyl increased from 230 ± 110 nm at 25% RH to 398 ± 249 nm at 83% RH. PPX-butyl and PPX-heptyl fiber diameter were 380 ± 242 nm and 488 ± 287 nm at RH ≤20% and showed the largest increase in RH between 62-86% RH, resulting in fibers of 1.04 ± 0.6 μm and 899 ± 552 nm thickness. For low RH levels the fiber size distribution followed a Gaussian-like distribution, which became broader and more undefined with increasing RH level (Figure 74). The increase in fiber diameter with increasing RH was reported for other polymers.[111, 148] This phenomenon is caused by water vapor which is known to discharge the jet, leading to lower charge density which results in less stretching of the jet and therefore thicker fibers.[111]

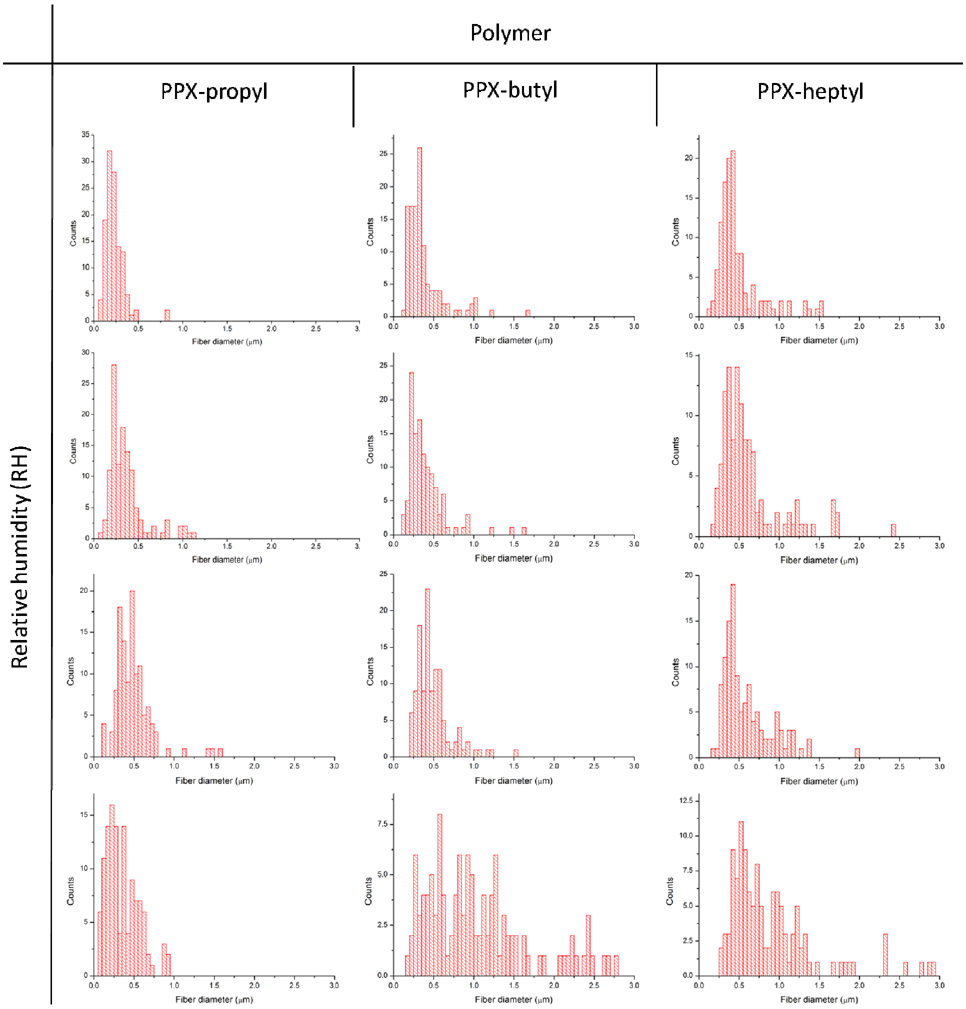

Figure 74 Histograms of fiber diameter distribution for alkyl-PPX spun from 3 wt% solutions in chloroform at different RH levels (up to diameters of 3 µm). For low RH the fiber diameter show Gaussian like distributions, which become broader and less pronounced with increasing RH.

An additional surface feature and change of the fiber morphology in the micrometer range, was obtained by the production of beaded fibers. The key factors in bead formation are viscosity of the solution, surface tension and net charge density, which is given by the applied electric field, and the conductivity of the solution. The use of THF as solvent and a reduction in polymer concentration to 2.5 wt% led to the desired fibers with bead-on-string morphology (Figure 75).

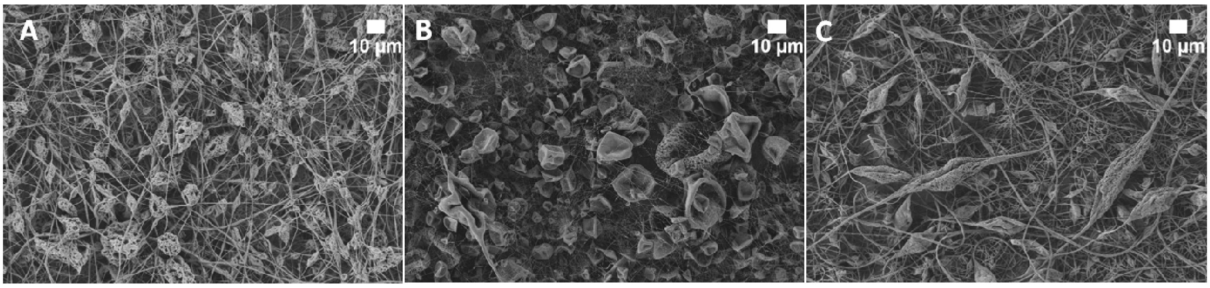

Figure 75 SEM micrographs of nonwovens of alkyl-PPX spun from 2.5 wt% solutions in THF. PPX-propyl, RH 50% (A), PPX-butyl, RH 25% (B) PPX-heptyl, 55% (C).

The beads were sensitive to the RH in the spinning environment, comprising a porous surface when the threshold value of RH was surpassed. Figure 76 shows SEM micrographs of the beads at different RH levels. At RH around 25% the beads are collapsed and comprise a smooth, slightly wrinkled surface (Figure 76 A,D,G). With increasing RH pores appeared on the beads' surfaces for all alkyl-PPX (Figure 76 B,C; E,F; H,I). In addition to the pores with diameters of 200-300 nm, the beads also showed substantially bigger holes with diameters in the range of 1-1.5 µm. As shown in Figure 76 B this holes reveal that, though partly collapsed, the beads have a hollow interior.

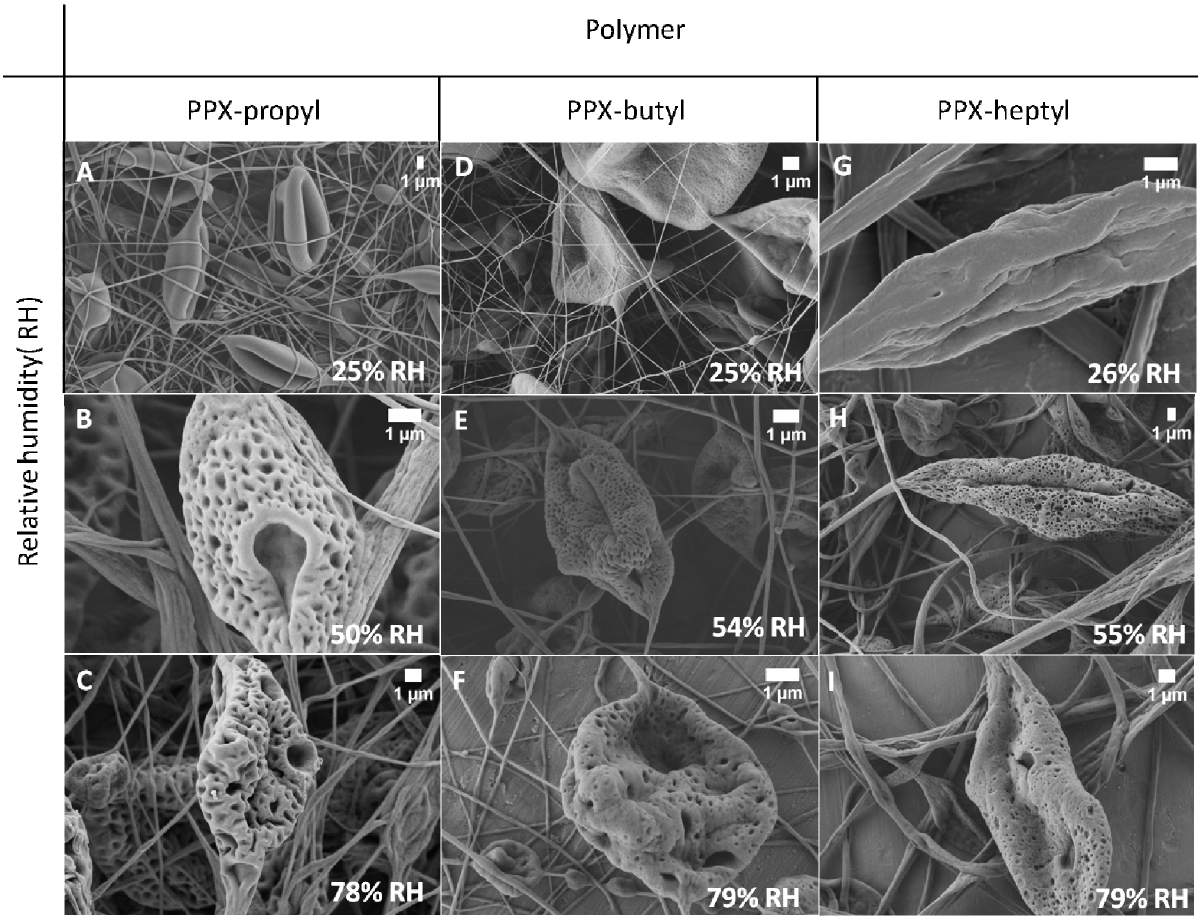

Figure 76 SEM micrographs of beads from the bead-on-string structures obtained by electrospinning of PPX-propyl (A, B, C), PPX-butyl (D, E, F) and PPX-heptyl (G, H, I) from 2.5 wt% solutions in THF at different relative humidity (RH).

In contrast to this, the morphology of the fiber segments of the bead-on-string structures was not affected significantly by increasing relative humidity (Figure 77) and do not show any pores. The fibers are of flat, ribbon like shape, often twisted and have a wrinkled surface. This surface wrinkles are caused by the rapid evaporation of the solvent while the jet is elongated by electrical forces. On the outside of the jet a solid polymer skin is formed meanwhile the inner core is still wet. The residue solvent diffuses to the outside causing a hollow structure in its interior. Ribbon-like fibers are formed when atmospheric pressure collapses this tubes as described by KOOMBHONGSE et al.[110] Surface wrinkles are also attributed to the formation of this "dry skin" and delayed solvent evaporation from the inner core.[149] PPX-heptyl (Figure 77 G, H, I) comprises flat disc like structures in the fiber segments, which are wrinkled same as the ribbon-fibers, but not porous as the beads described in Figure 76. This disks are formed by small beads which collapsed completely into flat structures.

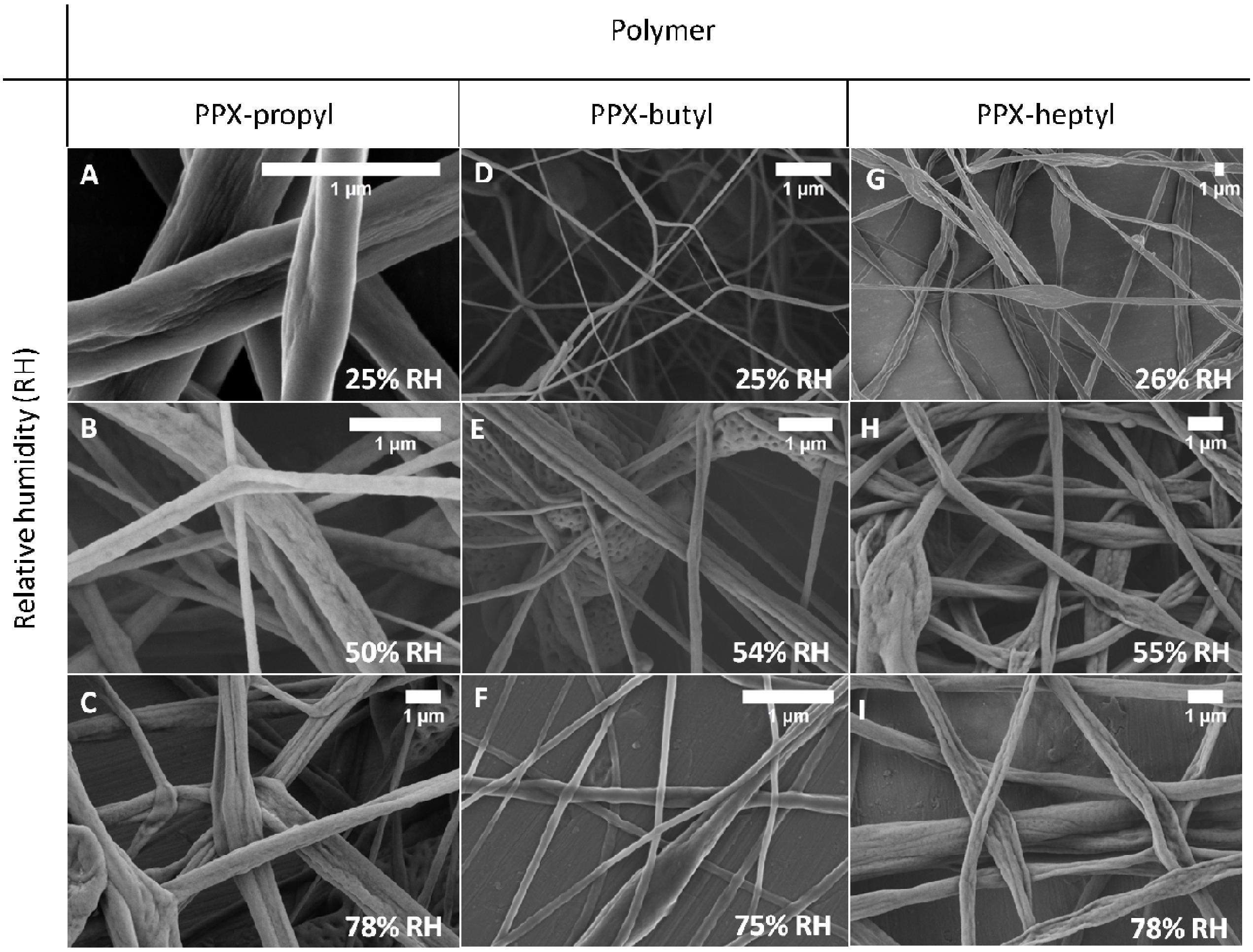

Figure 77 SEM micrographs of the fiber parts from the bead-on-string structures obtained by electrospinning of PPX-propyl (A, B, C), PPX-butyl (D, E, F) and PPX-heptyl (G, H, I) from 2.5 wt% solutions in THF at different relative humidity (RH).

Electrospinning from chloroform and THF solutions both led to fibers or bead-on-string fibers sensitive to the relative humidity in the electrospinning environment. This sensitivity is expressed by the formation of pores on the fiber surface (in case of chloroform) or on the bead surface (in case of THF). Same as in the electrospinning process, where several parameter interact in a complex manner, pore formation during electrospinning is subject to different influencing factors. The two concepts phase separation and breath figure formation explain their coactions. As MEGELSKI et al.[114] pointed out, phase separation can be induced by variation of different parameter of the spinning solution, causing thermodynamic instability of the system. Two often described mechanisms are TIPS (thermally induced phase separation) and VIPS[150] (vapor induced phase separation). In TIPS thermodynamic instability is caused by evaporation of the solvent from the polymer solution as the jet emerges from the needle. Solvent loss as well as consumption of evaporation heat can both lead to phase separation into polymer rich and polymer poor regions. Upon solidification of the jet by complete solvent evaporation the polymer rich regions form the continuous matrix and the polymer poor regions result in holes. Phase separation in solution is likely to occur via spinodal decomposition, since solvent evaporation takes place in split seconds.[113] TIPS mechanism possibly plays a role in pore formation in both systems presented here. For spinning from THF solutions the VIPS model has to be taken into account as well. The diffusion of water vapor into the jet requires a water miscible solvent, like THF. If the polymer is hydrophobic, like alkyl-PPX, water acts as non-solvent and phase separation is caused.

Nevertheless, phase separation alone can, if any, only be of minor importance for the pore formation observed on alkyl-PPX fibers spun from chloroform and THF solution, since the porosity is clearly dependent on the level of RH. The concept of breath figure formation[151] explains pore formation due to the condensation of moisture on the cooled fiber surface during the spinning process. When the fiber finally solidifies the water droplets leave an imprint on its surface.[111, 114, 150] The increase in pore formation with increasing RH of the electrospinning environment is in accordance with this model and can explain the observed porosity.

The processing into sub-micron fibers by electrospinning led to a different wetting behavior of the nonwovens compared to films obtained from the same alkyl-PPX polymers. Furthermore, since the wetting behavior of a surface greatly influenced by the size and geometry of its surface features, a difference in wetting behavior was expected for the different fiber morphologies.

Figure 78 shows the contact angle evolution in detail. For all alkyl-PPX derivates the water contact angle increased at least 30° by the processing into smooth fibers (chloroform) and smooth bead-on-string structures (THF). As an overall trend, fibermats comprising bead-on-string structures showed higher contact angles than fibermats consisting of fibers without this features. Furthermore the water contact angles increased for both fiber morphologies with increasing RH of the electrospinning environment. The additional structuring achieved by pores on the fibers and beads surface pushed the wetting behavior of the nonwovens into range of superhydrophobicity, marked by a water contact angle of 150°.

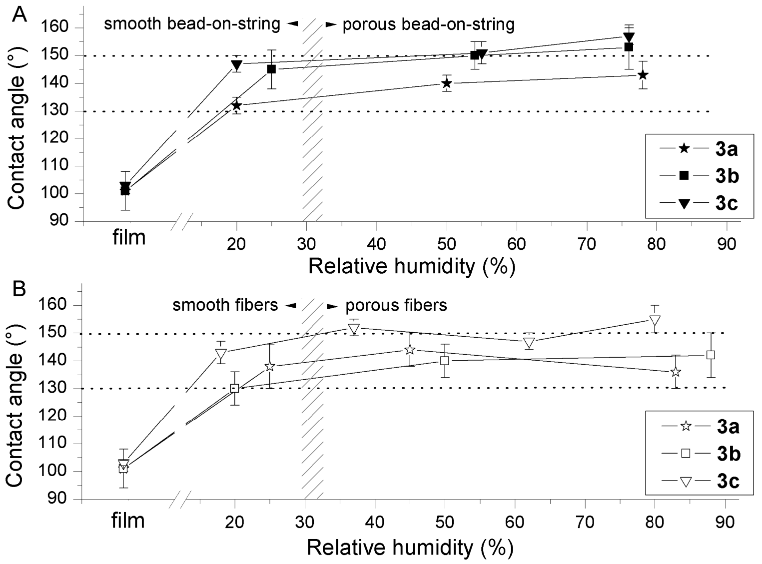

Figure 78 Water contact angle (CA) for electrospun fibermats of PPX-propyl (**3a**), PPX-butyl (**3b**) and PPX-heptyl (**3c**) at different relative humidity (RH) levels. (A) Bead-on-string structures from 2.5 wt% THF solution, (B) fibers from 3 wt% chloroform solution (dotted lines show 130° and 150° for better orientation). The dashed bars represent the area of border humidity for pore formation on beads (A) and fibers (B).

Best results were achieved for PPX-heptyl, which surpassed the value of 150°, for both electrospinning approaches. PPX-heptyl fibermats obtained from THF and chloroform solutions at high RH levels showed water contact angles of 157 ± 3° and 155 ± 5° respectively (Figure 79). Contact angles for PPX-propyl and PPX-butyl reached maximum values around 145°, except PPX-butyl spun from THF with a maximum contact angle of 153 ± 8° at 79% RH. Together with the superhydrophobic contact angle, the PPX-heptyl fiber mats comprised low roll-off angles for water droplets in the range of 10-15°.

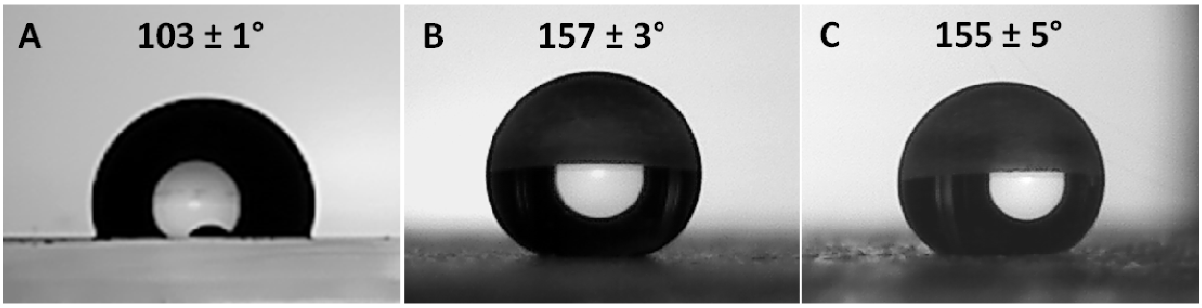

Figure 79 Water droplets on PPX-heptyl with differing surface structures: solvent cast smooth film (A) and electrospun fibermats with porous bead-on-string structures (2.5 wt% THF, 75% RH) (B), porous fiber structures (3 wt% chlorofrom, 88% RH) (C).

Another important characteristic of superhydrophobic and self-cleaning surfaces is the ability to repel an impacting water droplet. This ability can be visualized by observing the behavior of a water droplet falling on a surface, which can either bounce, stick or spread. The complex relation between surface structure and impacting velocity wich causes the droplet to stick or bounce[152, 153] is not taken into account here. As shown by high speed camera images in Figure 79, a water droplet with the volume of 7.5 µl falling from 1 cm height onto PPX-heptyl fiber mats with CA of 157 ± 3° and RA of 10-15° (B), and CA of 155 ± 5° and RA of 10-15° (C) bounced two times before remaining on the surface. In contrast to this, a droplet falling onto a solid PPX-heptyl film (A, CA 103 ± 1) sticked on the surface in a wobbling motion. A droplet falling onto a PPX-propyl fiber mat (D, CA 136 ± 6°, RA > 45°) bounced once off the surface once after the impact.

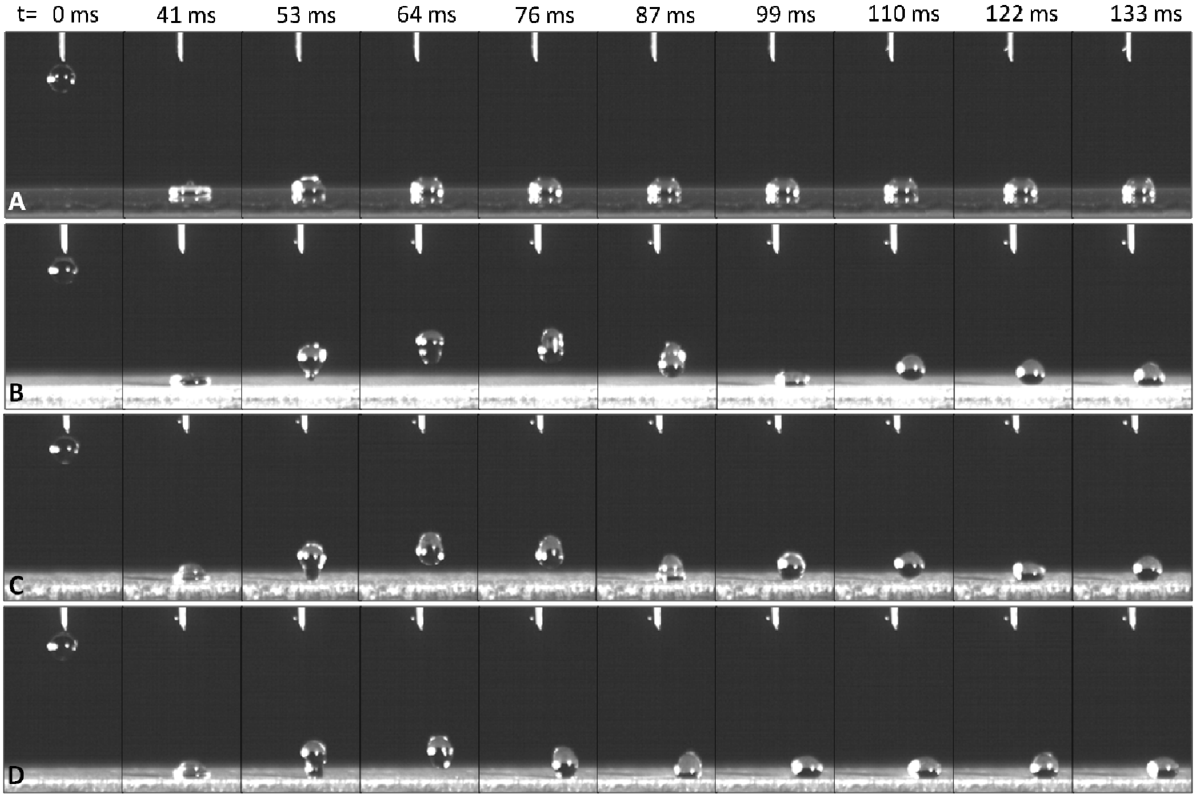

Figure 80 High speed camera snapshots of a water droplet (7.5 µl) falling from 1 cm height onto different PPX-alkyl surfaces at different time intervals. The exit of the droplet from the needle was chosen as starting point (0 ms). The droplet does not bounce off the surfaces of PPX-heptyl film (A), but from electrospun fiber mats (B: PPX-heptyl 2.5 wt% THF, 76% RH; C: PPX-heptyl 3 wt% chloroform 87% RH; D: PPX-propyl 3 wt% chloroform, 83% RH).

A surface is considered to be self-cleaning if a rolling water droplet is able to remove dirt form the surface in its motion.[124] Figure 81 shows high speed camera snapshots of a water droplet rolling down a carbon powder covered PPX-heptyl fiber mat. The fibermat was spun from 2.5 wt% THF solution at 20% RH showing a water contatc angle of 147 ± 3° and roll off angle of 10°-15°. Images A and B show individual droplets loaded with carbon powder leaving behind a clean surface, while images C-E show one droplet in its trajectory (marked by arrows).

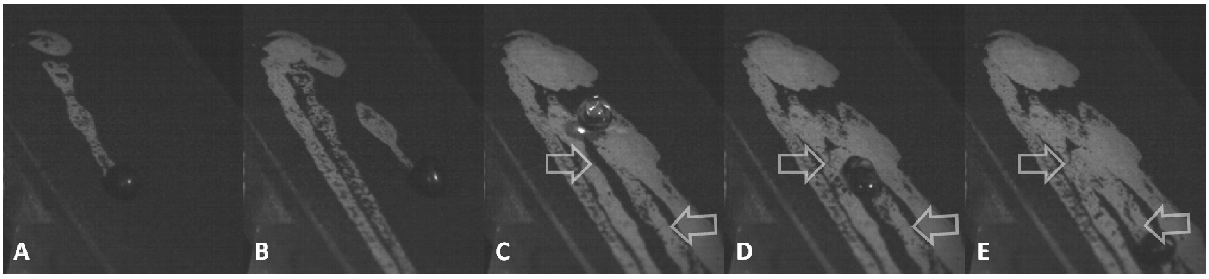

Figure 81 High speed camera snapshots of a water droplet rolling down a carbon powder covered PPX-heptyl fibermat (2.5 wt% THF, 20% RH, inclined 30°) show self cleaning abilities of such nonwovens. (A) and (B) individual droplets, already "loaded" with carbon powder. (C-E) a droplet at different points of its trajectory (marked by arrows), first the droplet is transparent (C), and after the uptake of carbon powder dark grey (D,E).

4.3.3 Alkyl-PPX Nano Nets: Alternative Formation Mechanism

The electrospinning of alkyl-PPX described in Sections 4.3.2 was performed without additives. The addition of cetyltrimethylammonium bromide (CTAB) to 3 wt% alkyl-PPX solutions in chloroform led to narrower size distributions of the obtained fibers and suppression of occasional beads. This is due to an increased conductivity of the solutions. For instance by addition of 0.5 wt% CTAB to a PPX-pr solution its conductivity increased from 0.2 µS cm^{-1} to 0.8 µS cm^{-1}. Furthermore the fibers were no longer sensitive to humidity, thus in the investigated range (17-55 % RH) no pore formation was observed. Instead the surface of fibers spun with CTAB comprised scales (Figure 82).

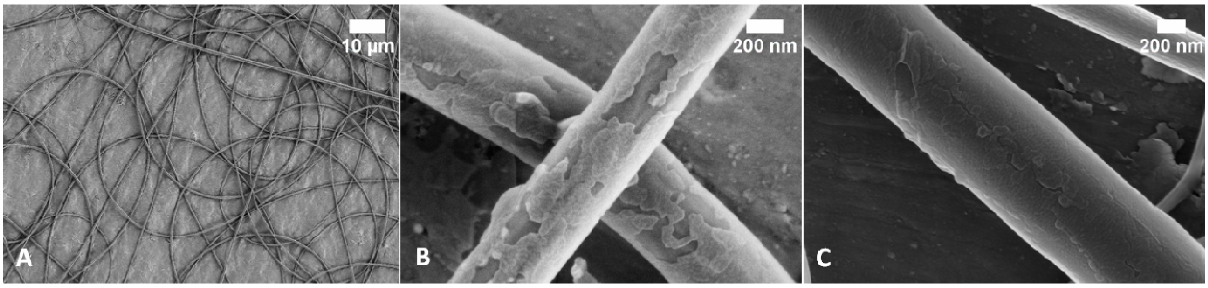

Figure 82 SEM micrographs of PPX-pr fibers obtained from chloroform solution with (A,B) 2 wt% polymer content and 0.5 wt% CTAB (22% RH) and (C) 3 wt% polymer, 0.5 wt% CTAB (38% RH). Bead free fibers with narrow size distributions were obtained (A), which have scales on their surface (B,C) but do not show pore formation (C).

In addition to the bead and pore free fibers, ribbons and nano nets were observed for PPX-propyl, PPX-butyl and PPX-heptyl spun from chloroform solution with CTAB. As shown in Figure 83 the area density of nets within a sample varied. For PPX-propyl and PPX-butyl small nets extending over only a few µm^2 (Figure 83 A,C) were found as well as nets expanding over larger areas and overlapping with others (Figure 83 B,D). In PPX-heptyl samples there were overall fewer, only isolated and often partially ruptured nets (Figure 83 E,F). The thickness of the wires and ribbons forming the nano nets were with 10-50 nm substantially less than the average fiber thickness of the nonwovens (250-400 nm). Furthermore the hole geometry of the nano nets was not uniform, round, triangular, rectangular and different polygonal holes were found.

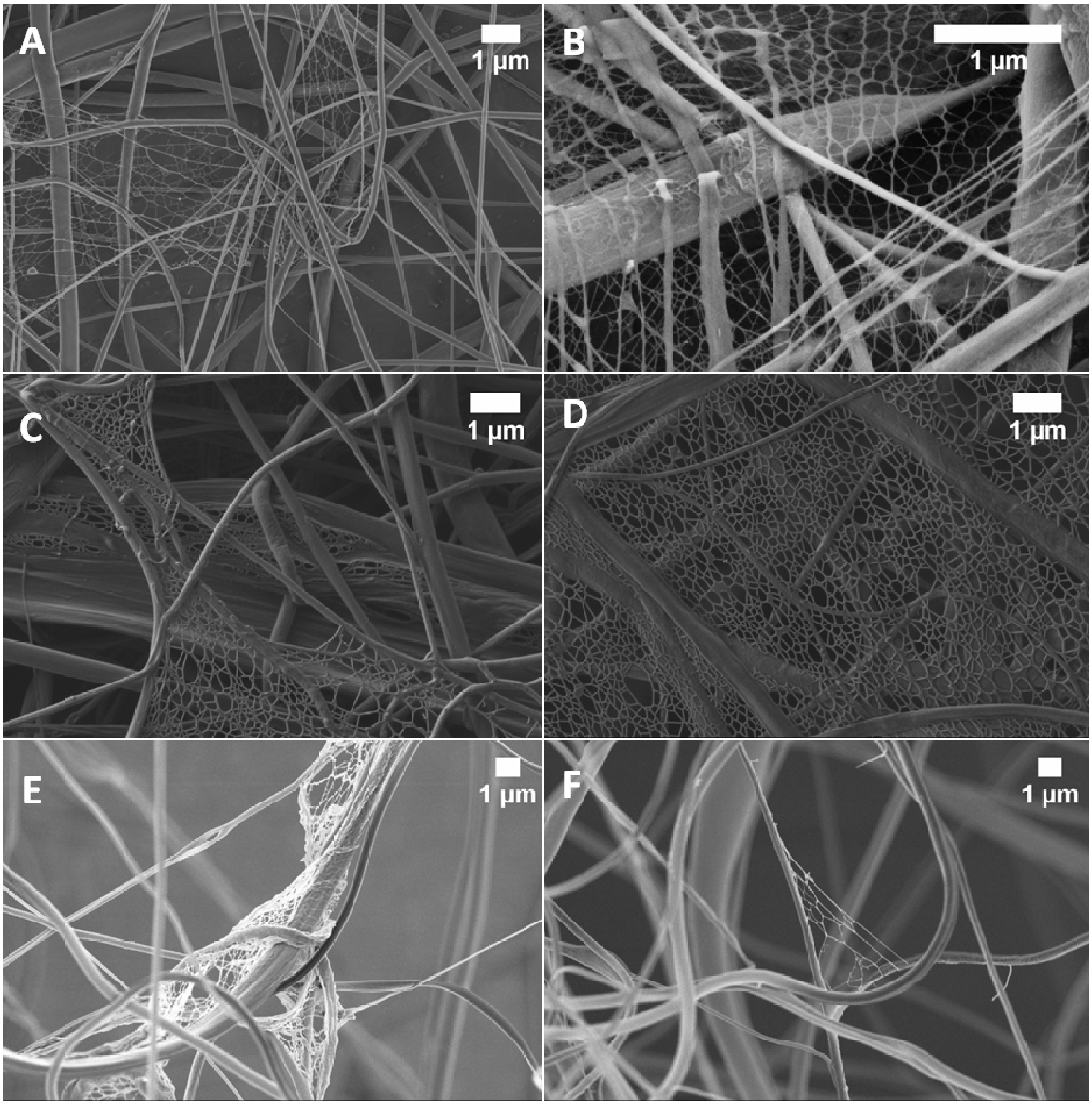

Figure 83 Alkyl-PPX nano nets obtained from 3 wt% chloroform solution with 0.5 wt% CTAB. (A, B) PPX-pr 15kV, 20% RH (C, D) PPX-bu 15 kV, 55% RH (E, F) PPX-heptyl 15 kV, 53% RH.

The formation of nano nets is known for different polymers, as explained in more detail in Section 3.4. According to DING et al.[118] and WANG et al.[120] instabilities during the electrospinning process cause the formation of charged droplets falling from the needle. This droplets travel towards the counter electrode, same as the continuous polymer jet. The droplets can either be deposited onto the counter electrode as small films, called defect films, or as nano nets. The net morphology is caused by phase separation as the solvent evaporates and the electric field stretches the droplet. The authors also reported that the connection between the nets and simultaneously electrospun fibers is due to residue solvent present in the nets upon deposition, which causes the net and the fibers to melt together.[118]

Within the alkyl-PPX nonwovens two different types of nano nets were found. Some, like the ones in Figure 83 C,E do not show distinct edges or beginnings/endings, but many other are of ribbon-like extension. The SEM micrographs of this type of nano nets show, that they are very unlikely formed of expanding droplets but instead of expanding ribbons.

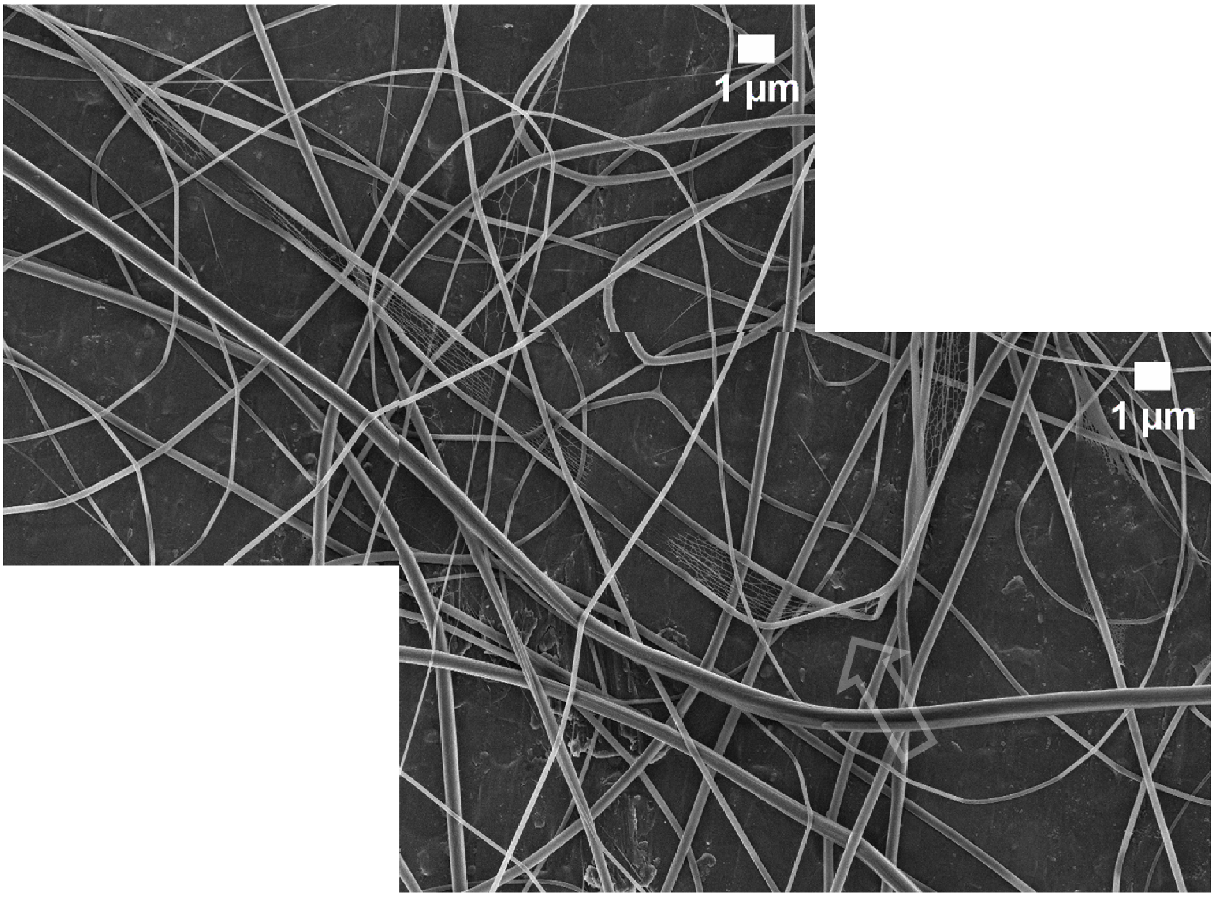

Figure 84 Two overlapping SEM micrographs of PPX-pr fibers and a long nano net, folding at the position marked with an arrow and continuing upwards.

As can be seen in Figure 84 nano nets in the shape of ribbons can extend over several tenth of microns and seem to be supported by two nearly parallel fibers. That this fibers are the origin of the net can be proven by the images shown in Figure 85. This ribbon-like nano nets often consist of broad, flat parts on the outer edges instead of fibers (Figure 85 A,B) or flat ribbons within the nano net (Figure 85 C, Figure 83 B). This nets did not completely expand before deposition onto the counter electrode. Beginning and ending of the ribbon nets cannot always be identified because they tend to disappear into the nonwoven. Figure 85 D-F shows beginnings (or endings) of small ribbon bands. Here it can be seen clearly, that a small fiber spreads into a net-like ribbons. This findings can hardly be explained by wet nano nets depositing onto fibers located on the collector electrode but rather by net formation from a fiber (or ribbon) during the deposition process.

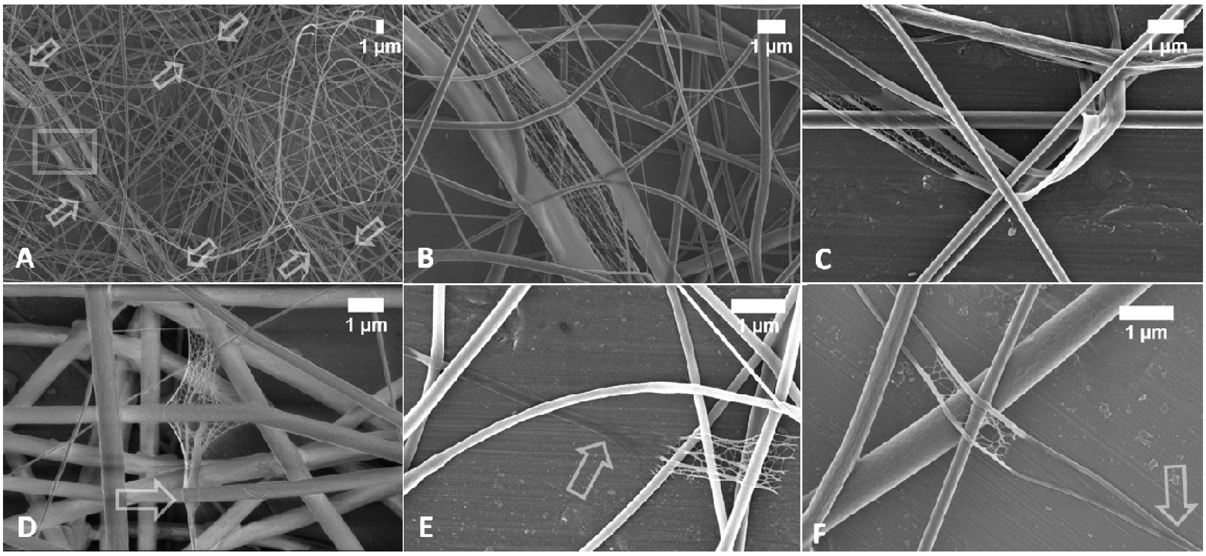

Figure 85 SEM micrographs of PPX-alkyl nano nets (3 wt% solution in chloroform, 0.5 wt% CTAB). Image A shows two ribbon nets (marked by arrows) of PPX-pr (magnification: B) which did not expand completely. C shows a folded PPX-propyl ribbon which has also only partially expanded into a net. The Images D-F show small fibers or ribbons splitting into nano nets, this is considered to be the beginnings/endings of the respective net (D,E: PPX-propyl; F: PPX-heptyl).

According to KOOMBHONGSE et al.[110] ribbons can form from fibers after a skin formed on the outside of the jet and the fibers collapse due to atmospheric pressure. The electrical charges on the jet surface cause a lateral force favoring the collapse. At the same time cohesive forces stick the thin polymer skin together and form a ribbon to increase the surface area for the repelling charges. The authors also reported that the charge repellence can cause a fiber/ribbon to split. Same as described by DING et al.[118] and WANG et al.[120] for the formation of nano nets from droplets, in the late state of ribbon formation the not yet dry jet is facing thermodynamic instabilities (for instance from evaporating solvent or the expansion), phase separation can occur and a net is forming from the ribbon. Charge repellence as described by KOOMBHONGSE et al.[110] might accelerate the further spreading of a ribbon or net.

As pointed out earlier, PPX-heptyl nets were less abundant and often partially ruptured when investigated by SEM only two day after electrospinning. Though “normal” electrospun fibers of the PPX-hetpyl were stable even at elevated temperatures (see Section 4.3.2) such thin wires of this low T_g, low E-modulus polymer did not withstand mechanical stress of sample preparation or even the bending forces during the electrospinning process. For this reason the stability of the nano nets was further investigated for PPX-propyl and PPX-butyl nets. PPX-butyl nets were found to be to partially ruptured after 30 days (Figure 86), while the PPX-propyl nets were found to be stable for at least 45 days stored at ambient conditions.

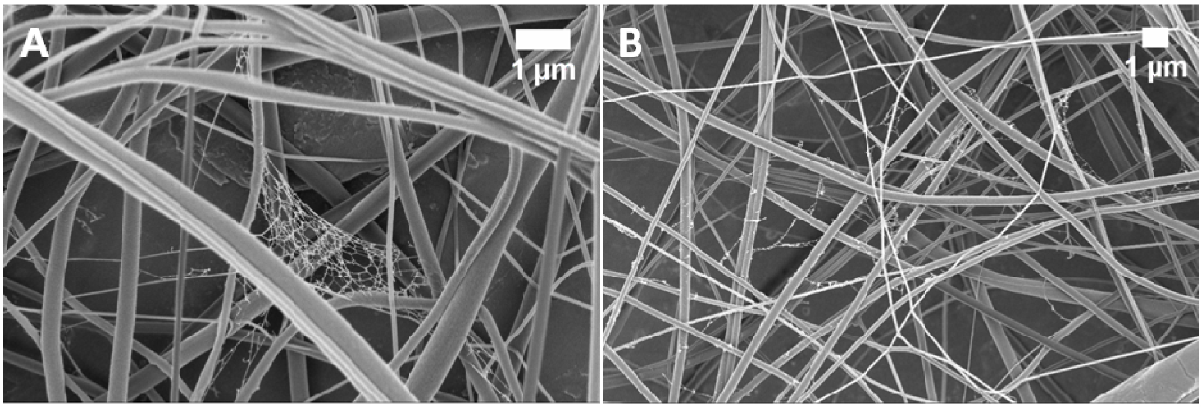

Figure 86 SEM micrographs of PPX-bu nano nets after 30 days storage at room temperature. The nano nets are partially (A) or completely destroyed (B).

4.3.4 Further Electrospinning of Alkyl-PPX

4.3.4.1 Interconnected Alkyl-PPX Fibers

As shown in Section 4.3.2 alkyl-PPX can be electrospun from THF and chloroform solutions without additives and form stable fibers despite their low glass transition temperatures (Table 9). As shown Figure 71 the fibers do not melt together at touching points, as might be expected, especially for PPX-heptyl with T_g -27 °C. The reason for stable fiber formation is, as mentioned before, high entanglement of the PPX chains which prevent the polymer fibers from losing their shape once they are formed. Even annealing treatment at temperatures up to 90 °C above the glass transition temperature (see Figure 72 B,D) did not cause the PPX-butyl and PPX-heptyl fibers to melt together. Therefore, in order to obtain interconnected fibers, the connection must be achieved during the electrospinning process.

By spinning PPX-propyl from a solvent mixture of chloroform and DMF (10/1 wt ratio) with 5 wt% polymer content bead free micro fibers with an average diameter of 2.31 ± 0.71 µm were obtained. SEM micrographs (Figure 87) show that the fibers are connected at the overlapping areas.

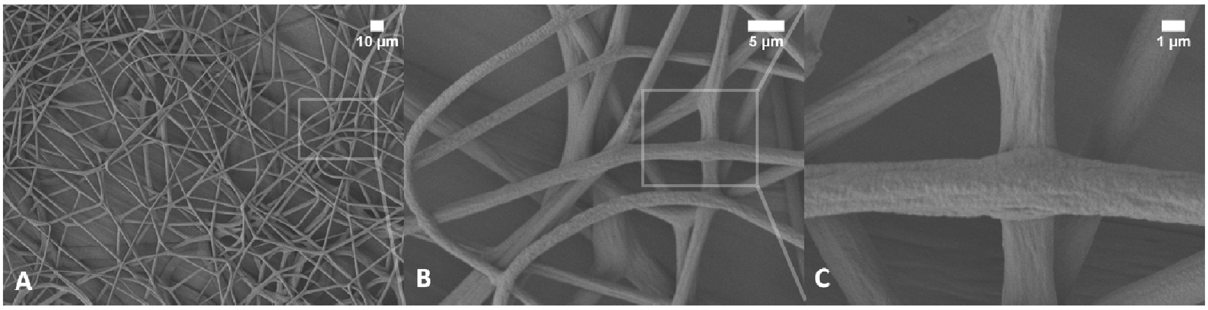

Figure 87 SEM micrographs of PPX-propyl microfibers electrospun from 5 wt% polymer solution chloroform/DMF (10:1 wt) in different magnifications.

When spinning from solutions with a highly volatile solvent, like chloroform, the fibers are completely dry when they deposit onto the counter electrode. Solvents with high boiling points, like DMF, need more time to evaporate and, at appropriate conditions, the fibers can still be "wet" when reaching the counter electrode. This residue solvent leads to a gluing of the fibers at the overlapping areas and facilitates the production of interconnected fiber networks.

4.3.4.2 Porous Fibers by Electrospinning of PPX Blends

The generation of porous alkyl-PPX fibers was achieved by electrospinning at high relative humidity levels, as described in Section 4.3.2. BOGNITZKI et al.[115] showed an alternative approach to porous fibers by spinning of an immiscible polymer blend and selectively removing on component. An ideal partner for alkyl-PPX in such a blend system is polyethylene oxide (PEO), since it is soluble in THF and chloroform, same as alkyl-PPX, but also water soluble. The combination of PEO and PPX is already widely used in the TUFT process (Tubes by Fiber Templates), where PEO fibers as templates are coated with PPX via CVD followed by extraction of the PEO to form hollow PPX tubes.[30]

Blend fibers of PPX-pr with PEO of different molecular weights (10,000 to 900,000 Da) were electrospun from chloroform solutions at different relative humidity. As shown in Figure 88 blend fibers obtained at 20% RH were smooth with occasional deformations on the surface, while fibers spun at RH >32% did show pores and therefore comprised a certain surface roughness. The surface roughness increased with increasing humidity (comparing images D, C and B), same as observed for pure alkyl-PPX fibers spun from chloroform solutions.

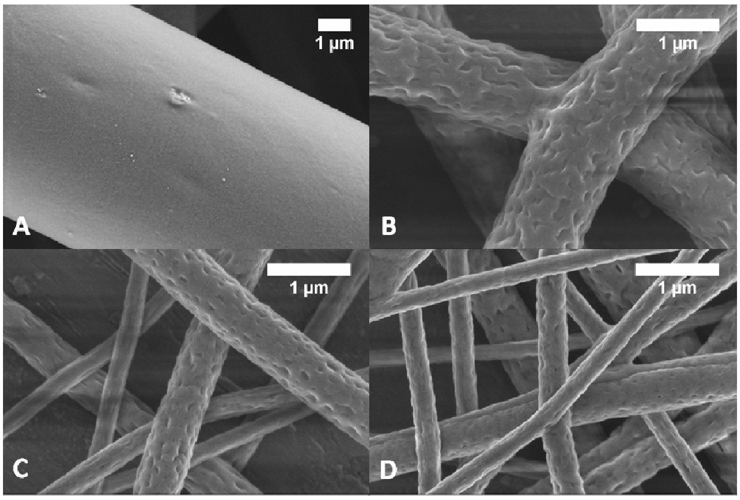

Figure 88 SEM micrographs of blend fibers before extraction. The blends consist of PPX-propyl with PEO of different molecular weights. Blend with PEO_{900k} spun at 20% RH (A) , with PEO_{300k} spun at 46% RH (B), with PEO_{35k} spun at 39% RH before (C) and PEO_{10k} spun at 32% RH.

The blend fibers were extracted with water for 2-3 days at room temperature or 40 °C. Though residue PEO was detected in the fibers via ATR-IR, surface analysis via SEM showed changes in the fibers surface morphology (Figure 89). The blend fibers spun at 20% RH showed oval pores with length of 200-300 nm on the surface (images A and B). The surface roughness and porosity of blend fibers spun at higher RH (e.g. PPX-pr/PEO_{35k}, Image C) is increased by the partial extraction of PEO.

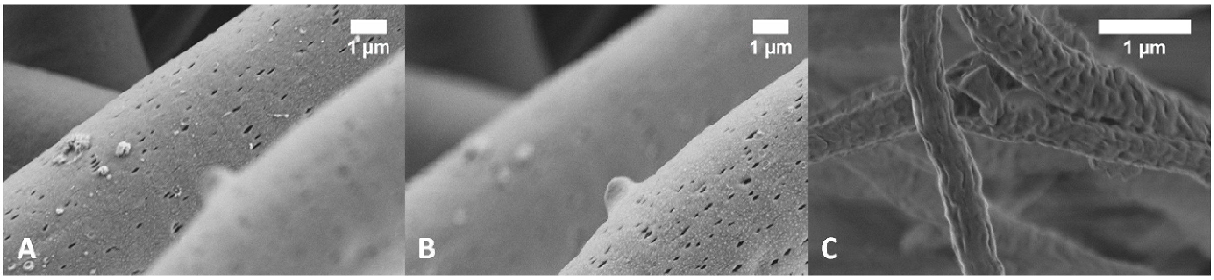

Figure 89 SEM micrographs of blend fibers after extraction. Blend PPX-pr/PEO_{900k} (A,B) and PPX-pr/PEO_{35k} (C). Blend fibers contained residue PEO.

4.3.5 Conclusion

PPX-propyl, PPX-butyl, and PPX-heptyl synthesized via CVD were successfully processed by electrospinning. The fiber morphology was influenced by choice of solvent or solvent mixture and altering the relative humidity (RH) in the electrospinning environment. By controlling the RH level while spinning from chloroform and THF solutions without further additives smooth fibers and bead-on-string structures as well as porous fiber and bead morphologies were obtained. The importance of the fiber morphology becomes visible by the dramatic change in the wetting behavior of such nonwovens compared to alky-PPX films. A water contact angle increase of at least 30° was achieved by simple electrospinning. The hydrophobicity of the fiber mats was further enhanced by the additional surface structures to the fiber through spinning at high RH. Best results were achieved for PPX-heptyl fiber mats spun from THF at RH 79%, where the double scale surface features of porous bead-on-string fibers led to a water contact angle of 157 ± 3° and therefore to superhydrophobicity. Fibermats from PPX-heptyl with contact angles in this range also comprise low roll off angles (10-15°) and show water repellence, i.e. water droplets falling onto the surface bounce off the surface. Furthermore the self-cleaning ability was shown by a water droplet cleaning the carbon powder covered fibermat.

The addition of cetyltrimethylammonium bromide (CTAB) to the chloroform electrospinning solution led to the formation of smooth fibers, which were not sensitive to humidity. Together with the fibers the formation of nano nets was observed for all three alkyl-PPX polymers. Though the nano nets are of different sizes and shapes, a ribbon-like extension of the nets was found to be predominant. SEM micrographs show that ribbon shaped fibers are the origin of such nets. This led to the extension of the formation mechanism reported in literature, where droplets are described as the origin of nano nets.

The feasibility of two more concepts for the processing of alkyl-PPX via electrospinning was shown by "proof of principle" experiments. Electrospinning of PPX-propyl from a solvent mixture with a high boiling component led to interconnected fibers. Blending of PPX-propyl with PEO of different molecular weights spun at different RH values showed another method to generate porous, rough fiber surfaces.

4.4 PPX in Blends, Foams and Composites

4.4.1 Motivation, Hypothesis and Concept

Polymers form a very important part of everyday life in both disposable and high performance products. However, the requirements are so diverse, that the commercially available polymers alone are not able to meet all demands. Therefore, application oriented research often is not the development of new polymers, but the modification of existing ones by the addition of other components.[154] Such "other components" can be other polymers, additives (plasticizers, pigments, antioxidants, UV stabilizers, flame retardants etc.) or fillers (carbon black, silica particles, optical fibers etc.) and serve to improve a polymer's performance for a special application and/or reduce cost. Important material classes resulting from these modifications are polymer blends, foams and composites. The purpose of this part of the present work is to explore the possibilities of PPX polymers to be applied in these polymer blends, foams, and composites.

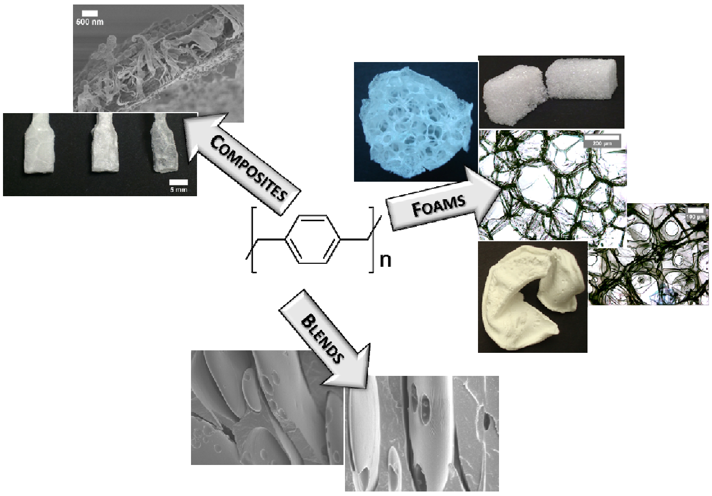

Figure 90 Exploring the possibilities for PPX-N in blends, foams and composites.

The solubility and tractability of alkyl-PPX permits the blending from solution with polymers soluble in THF and chloroform. The flexibility of the alkyl-PPX suggests adding them as a soft component to hard and brittle thermoplasts[154] like PMMA and PS or Poly(2,6-dimethyl-1,4-phenylether) (PPE). These three industrial thermoplasts are rigid materials and their blending and block-copolymerization with more flexible polymers is an established method to improve mechanical behavior. On the other hand, the addition of thermoplastic polymer to rubber-like material is equally interesting.[154-156] Though most polymer blends are immiscible for thermodynamic reasons, the structure resemblance of PS and PPE leads to a miscible blend, which is a commercial product.[154] The hypothesis for blending PPX-propyl with this thermoplasts was to modify the mechanical behavior and explore whether the structure similarity with PS and PPE might introduce miscibility.

The special synthesis approach via chemical vapor deposition (CVD) has established PPX polymers as protective coating materials for a great variety of substrates. In addition to their outstanding performances as gas barrier and electrical insulation material, PPX polymers are also temperature stable and show good mechanical properties.[1, 2] In combination with the ability to penetrate into small confinements, this characteristics suggest the investigation of PPX coatings that do not only act as an outer protection layer but rather serve as one component in a composite-like material. In order to combine PPX properties with another material in a CVD approach and to observe synergistic effects, the substrate component of the composite-like material needs to have a porous structure to allow the combination of both materials. An ideal substrate is provided by bead foams, since they comprise air channels that penetrate the whole structure. The hypothesis was that PX gas can penetrate the air channels of bead foams during the synthesis via CVD and by this means a composite like material is formed. The strategy was to apply PPX as reinforcement material in expanded polystyrene bead foams (EPS). By improving the junction of the beads equipping an EPS foam with a continuous PPX layer that penetrates the entire structure, the mechanical performance of EPS was expected to be enhanced. In addition to this, the PPX coating is expected to continue its performance as protective layer, same as in conventional applications.

Furthermore, if a continuous PPX structure is achieved by CVD coating of a foam, removing the original structure, e.g. by extraction, leads to new three dimensional PPX bodies. This bodies, same as in the TUFT process (see Section 2), are the negative image of the original template. By this means a production method for three dimensional, porous structures made of PPX derivates will be available. Foam generation by template coating would not be limited to bead foams, but be available for any porous structure composed of a template material that is soluble.

An alternative concept for the generation of foams from PPX is batch foaming of soluble PPX derivates. From this materials compact films of adequate geometry and thickness for the batch foaming process can be obtained by simple solvent casting.

Once the basic concepts of blending soluble PPX with other polymers, generating composite-like materials with PPX via CVD and PPX foams by template coating or batch foaming are proved to be generally feasible, more specific studies would lead the way to new fields of applications for PPX polymers.

4.4.2 PPX-propyl Blends

Polymer blends of PPX-propyl with PMMA, PS and PPE were obtained by solvent casting from chloroform. Criteria for the selection of these polymers for blending with PPX-propyl was not only solubility but also structure similarity in case of PS and PPE, which form a miscible blend with each other due optimum packing and aromatic interactions.[157] However, solution casting of the blend films of PPX-pr with all three polymers gave immiscible polymer blends for all tested weight ratios (1:3, 1:1, 3:1). Figure 91 shows SEM micrographs of cross sections of the blend films, where phase separation in the micrometer range was clearly visible for PPX-pr/PMMA and PPX-pr/PS blends. In each of the samples one continuous phase with disc-like or oval inclusions was observed. PPX-pr/PPE blends comprised a different phase morphology, where the different phases could not be observed that clearly by this method. However, the immiscibility was confirmed by DSC thermograms. Glass transitions in the region of both homopolymer components in first and second heating cycle indicated clearly the presence of separated phases in all blends for all the investigated compositions.

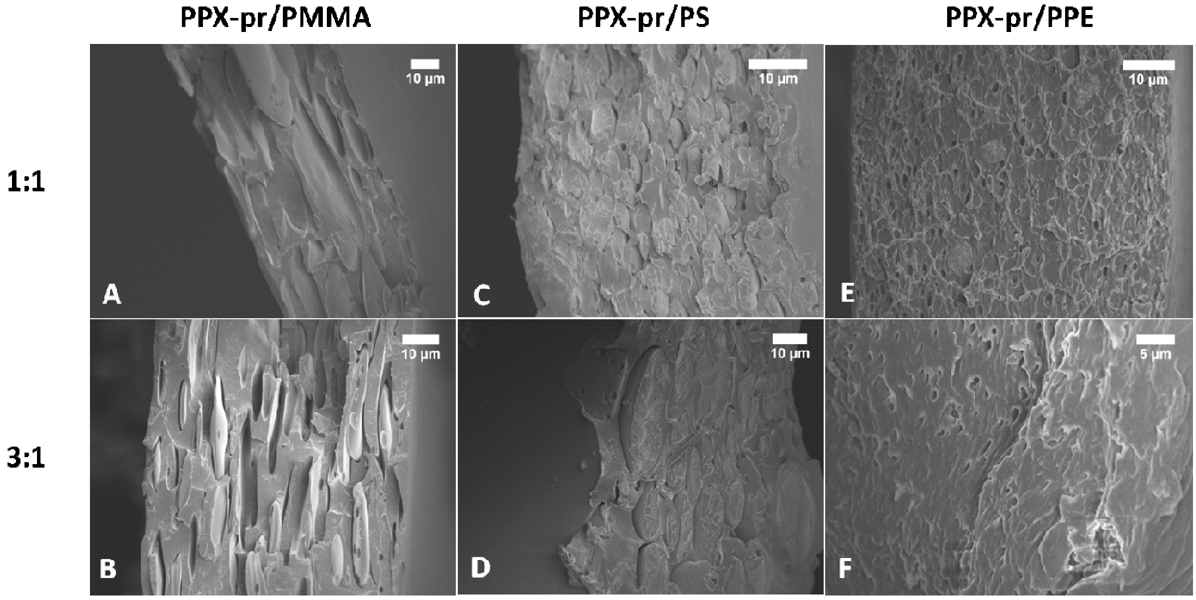

Figure 91 SEM micrographs of PPX-propyl blends with PMMA, PS and PPO for ratios 1:1 and 3:1. Phase separation with large disc-like and oval domains is clearly visible for PPX-pr/PMMA (A,B) and PPX-pr/PS (C,D)blends. PPX-pr/PPO blends show different phase morphology (E,F).

Stress-strain measurements of the blend films with bone-like test specimen (as shown in Figure 107 A) showed the effect of the PPX-propyl component on the thermoplasts and vice versa. The stess-strain curves of the respective blends compared to the homopolymers are given in Figure 92 and Table 10.

Table 10 Details for stress-strain analysis of PPX-pr blends with PMMA, PS, PPO and homopolymers.

Polymer	Blend ratio	Film thickness/ µm	E-Modulus /GPa	dL at break /%
PPX-propyl	homopolymer	37 ± 3	0.13 ± 0.03	250 ± 12
PMMA	homopolymer	69 ± 33	1.09 ± 0.22	4 ± 1
PS	homopolymer	83 ± 26	1.83 ± 0.40	2 ± 1
PPO	homopolymer	141 ± 28	1.19 ± 0.10	65 ± 8
PPX-pr : PMMA	1:1	61 ± 8	0.51 ± 0.04	193 ± 20
	3:1	72 ± 3	0.37 ± 0.03	265 ± 7
PPX-pr: PS	1:3	77 ± 9	0.42 ± 0.02	8 ± 2
	1:1	93 ± 3	0.29 ± 0.06	31 ± 6
	3:1	70 ± 3	0.23 ± 0.03	218 ± 32
PPX-pr : PPO	1:3	69 ± 7	0.75 ± 0.05	153 ± 6
	1:1	75 ± 7	0.51 ± 0.02	166 ± 7
	3:1	54 ± 8	0.27 ± 0.03	199 ± 10

The ductility of all thermoplasts blended with PPX-propyl increased with the blending. Best improvement upon the addition of 25 wt% of PPX-propyl was observed for PPE (Figure 92 C). Here the elongation at break was increased to 153 ± 6%, compared to 65 ± 8 % for the homopolymer. PPX-propyl/PPE blends showed an overall intermediate behavior compared to the respective homopolymers. These systems were considered to be of particular interest for testing their impact strength, since the area under the curve for all blends is larger than for the homopolymers, which is according to Koo *et al.* a good indicator for impact energy absorption.[156]

Considering the property change of PPX-propyl by the addition of a thermoplastic component, the addition of 25 wt% PMMA tripled the E-modulus of the material while maintaining the expansibility of the material (Figure 92 A). In case of the PPX-pr/PS blend the addition of 25 and 50 wt% PPX-pr to PS resulted in a considerable loss of toughness (lower E-modulus) and only little improvements considering elongation before break.

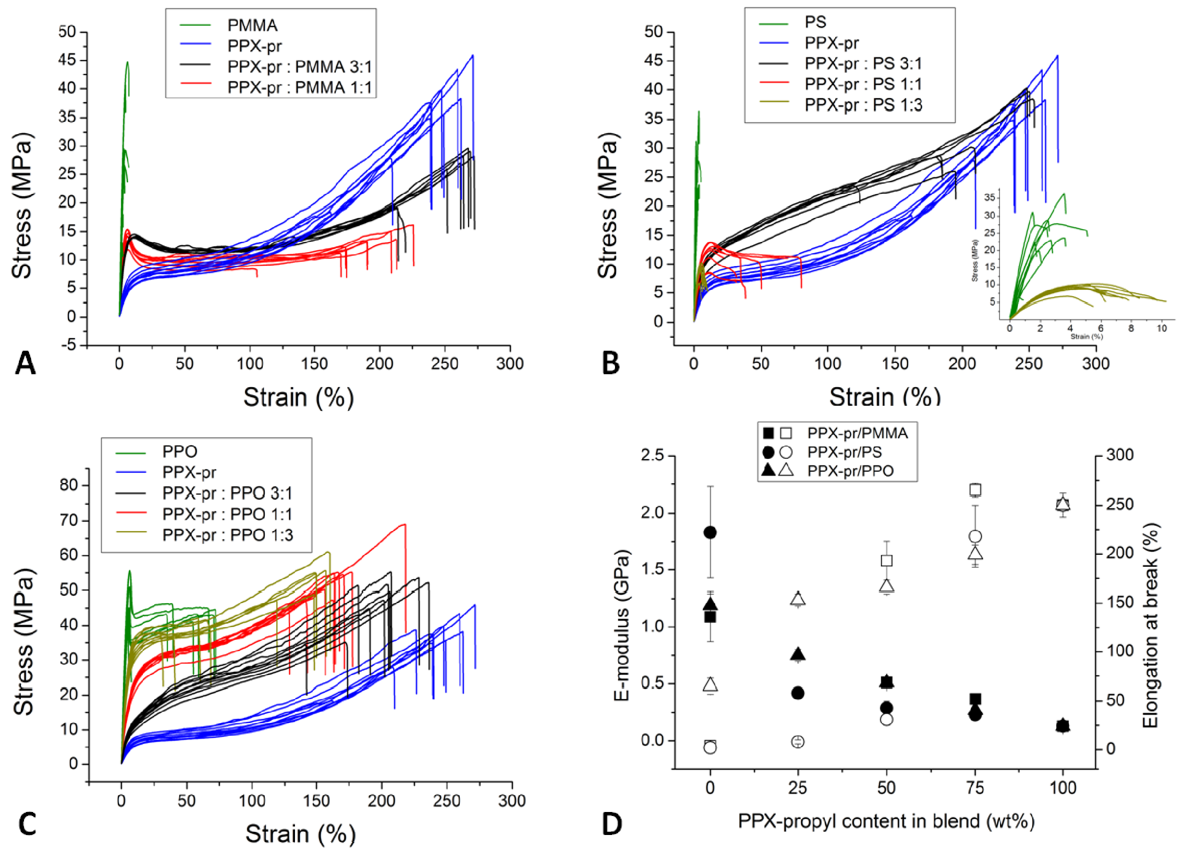

Figure 92 Stress-strain analysis of PPX-propyl blends with PMMA (A), PS (B) and PPE (C). The graphs show the stress strain curves of the blends in comparison with the respective homopolymers.

However, since the blends to not represent a thermodynamic equilibrium state, aging and thermal annealing influence the phase morphology. Changes in the phase morphology are known to affect the mechanical performance,[158] therefore it is required to add compatibilizers to the systems in order to stabilize the phase morphology.

4.4.3 Foams and Composites

As explained briefly in Section 3.6 expanded polystyrene bead foams (EPS) can have different densities, different bead sizes and quality of bead junctions. Specimen of three different EPS with varying density and bead sizes (Table 11) were coated with PPX-N. Specimen cut from EPS-1 were coated with different PPX derivates and used for mechanical analysis by stress-strain measurements (Section 4.4.3.3). For the analysis of the penetration of PX into cuboid EPS specimen (EPS-2 and EPS-3), the EPS was extracted with THF and the PPX-N structure was analyzed (Section 4.4.3.1).

Table 11 Density and bead size distribution of EPS used as template foams.

	Comment	Density/ g·cm^{-1}	Bead diameter*/ mm
EPS-1	sheet of 3 mm thickness, insulation material	0.018 ± 0.001	3.38 ± 0.86
EPS-2	sheet of 2 cm thickness, insulation material	0.023 ± 0.003	3.77 ± 0.89
EPS-3	molded piece, packing material	0.036 ± 0.002	1.36 ± 0.32

* spherical shape was assumed for diameter determination

4.4.3.1 Structure Mapping by Negative Images

Details of the different specimen cut from EPS-2 and EPS-3 raw material are given in Table 12. All specimen were coated with PPX-N at equal conditions in order to ensure comparability when analyzing the penetration depth of the PPX-N into the samples. On some specimen the faces were fused by pressing onto a hot plate to get rid of defect sites and give the specimen a denser skin, that was supposed to act as a barrier for the PX vapor to enter the structure.

As expected the density of the PPX-N-replica structures were less than the densities of the EPS template material (Table 12), specifically about 10% the original density for EPS-3, about 50% for EPS-2. Density variations for PPX-N structures obtained from specimen of different sizes but from the same EPS material are negligible, except when a thin EPS sheet was coated (specimen 3-5 and 2-5). Here the density of the PPX-N structure was nearly 6 times higher for EPS-3 and 2 times for EPS-2 compared to the density of a thick specimen. This can be explained by the surface to volume ratio of the different cuboids. Small volumes have a higher surface to volume ration than big volumes, the PX uptake of a specimen in the deposition chamber is limited by the surface it provides. The microstructure within the specimens surface has no influence on the absolute uptake of PX molecules, but only on the layer thickness of the final coating, since the absolute number of PX molecules is distributed over a larger surface area.

Table 12 Details of EPS specimen coated with PPX-N before and after the CVD process.

Specimen	EPS-type, comment	Specimen size/ cm	Weight before coating/mg	Weight after coating/mg	Density EPS specimen/ g·cm^{-1}	Density PPX-N structure/ g·cm^{-1}
3-1	EPS-3, fused	1.7x2.4x2.2	319.26	350.02	0.036	0.0034
3-2	EPS-3, fused	2.3x2x2.4	385.17	417.06	0.035	0.0029
3-3	EPS-3	2x2.1x2.2	345.37	377.1	0.037	0.0034
3-4	EPS-3	2.7x2.3x2.4*	474.63	519.42	0.032	0.0030
3-5	EPS-3, sheet	2.5x2x0.2*	37.92	54.71	0.038	0.0168
2-1	EPS-2, fused	1.3x1.5x2.7	138.46	176.67	0.026	0.0073
2-2	EPS-2, fused	1.5x1.5x1.5	89.87	113.84	0.027	0.0071
2-3	EPS-2	1.5x2x2	133.85	190.44	0.022	0.0094
2-4	EPS-2	2.6x1.5x1.8	160.18	217.14	0.023	0.0081
2-5	EPS-2, sheet	3x0.2x1.8*	20.46	37.17	0.019	0.0155

* slight deviation in height of the specimen, average value given

Photographs of the PPX-N sheet from specimen 3-5 and 2-5 (Figure 93 and Figure 94) show that more PPX material is accumulated at the bead borders. On the microscope images the bead borders were clearly identified and at higher magnification the closed-cell structure of EPS foams was found to be resembled by the PPX-N coating. The structures do not differ from EPS samples (compare to Figure 19 A,B).

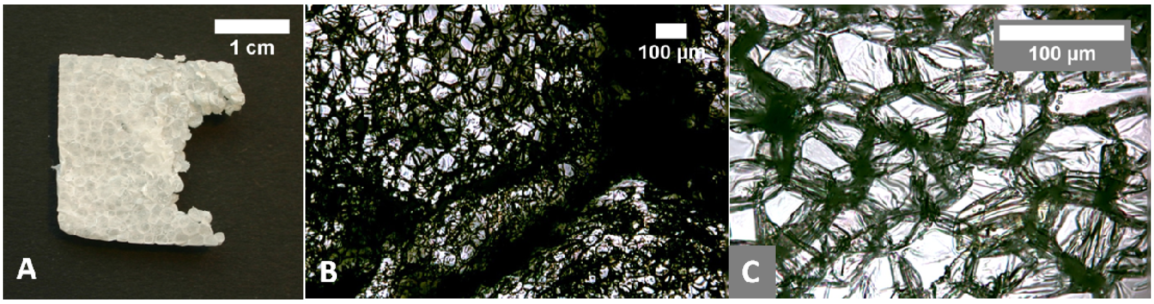

Figure 93 Specimen 3-5. Photograph of PPX-N foam obtained from a sheet of EPS-3 (A) and microscopic images# of the same (B,C).

The cross-section of specimen 2-5 (Figure 94 B) shows that only the outer layer of EPS foam cells were coated with PPX-N. In the interior of the sheet the PPX-N also reproduced only the foam cells of the bead borders, leaving what was formerly the interior of the beads open. Figure 94 C shows both outer layers of foam cells reproduced by PPX-N and a defect site (see also Figure 95) in the center.

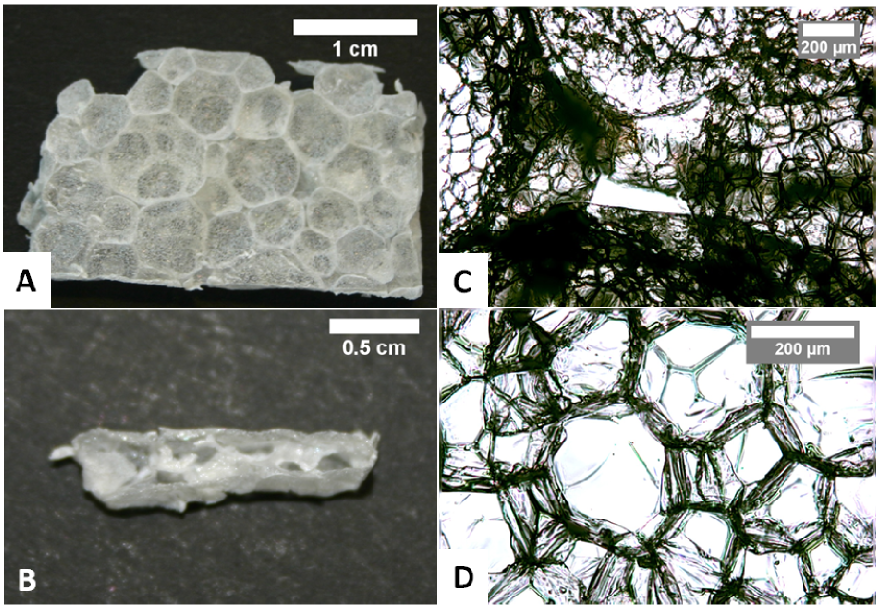

Figure 94 Specimen 2-5. Photograph (A,B) and microscope images# (C,D) of PPX-N foam sheet obtained from EPS-2. Image B shows the cross section of the foam sheet, image C shows both outer PPX-N layers and a defect site in the center.

The PPX-N cuboids obtained from specimen 3-1 to 3-4 and 2-1 to 2-4 did all comprise an outer skin of PPX-N, where, same as for the sheets, the original beads were still visible. The PPX-N coating conserved occasional defect sites, which originate from gaps between adjacent beads in the original EPS material (Figure 95). Fusing the faces of the EPS specimen resulted in destroyed foam cells and did not lead to a denser surface layer on the EPS. The PPX-N reproduces this damaged foam cells. The SEM micrograph in Figure 95 C shows that from the outer foam cell layer edges and vertices remained, but no closed surface was obtained. The microscope image

---

microscope images were stacked with picolay

(Figure 95 D) shows, that cell layers underneath the damaged surface were intact and coated with PPX-N.

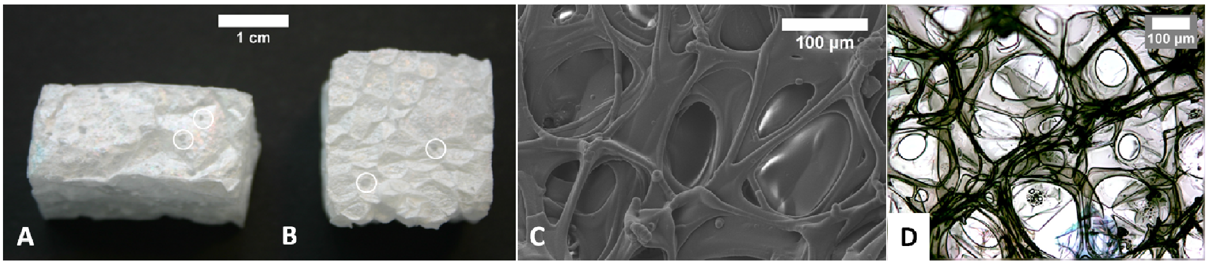

Figure 95 Outer skin of PPX-N structures from specimen 2-1 (fused, A) and 2-3 (non-fused, B). Both skins shows some defect sites (some discontinuities marked with circles), where the original EPS specimen had gaps between adjacent beads. The SEM micrograph (C) shows that fusing destroyed the outer foam cell layer, the microscope image (D) shows foam cell layers underneath the outer layer, which were intact.

PPX-N cuboids obtained from EPS-3 specimen all collapsed after EPS extraction, as shown in Figure 96 A. Cutting the cuboid (Figure 96 B) revealed that it was of hollow interior. The distance the PPX-N penetrated the cuboid was about 2 mm. This PPX-N “skin” (Figure 96 C) is comprised of a thin layer which shows planar circular structures, originated from the EPS beads, and some PPX-N beams reaching further inside (see schematic representation Figure 96 D).

In contrast to this, PPX-N cuboids obtained from EPS-2 specimen maintained their shape (Figure 97 A). Cutting this cuboid open showed an open-cell structure in the interior of the specimen (Figure 97 B). The removed open-cell PPX-N structure (Figure 97 C) was stable an sustained its own weight, leaving behind the outer PPX-N skin (Figure 97 D), which is of the same structure the skins obtained from EPS-3. These findings were independent from the investigated cuboid size range and pretreatment (fused or non-fused faces) for EPS-2 and EPS-3 specimen.

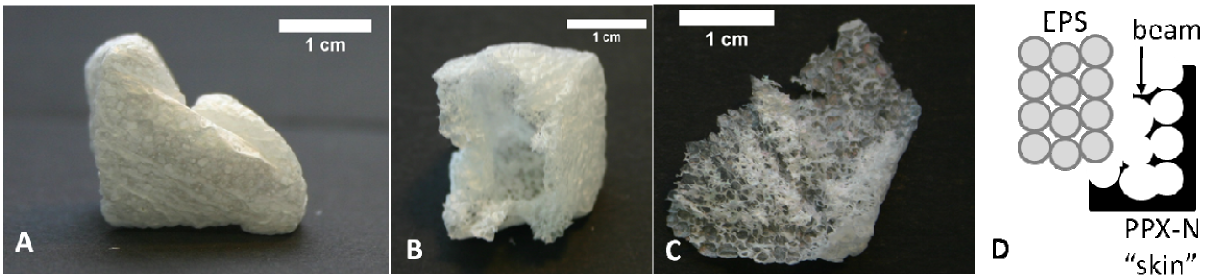

Figure 96 Specimen 3-1. Photographs of PPX-N foams obtained from a cube of EPS-3. Due to dense beads the PPX-N did not penetrate the entire EPS, thus after extraction the foam collapses (A) and is of hollow interior (B). The skin of the PPX-N structure on the interior is a negative image of the EPS foam (C,D).

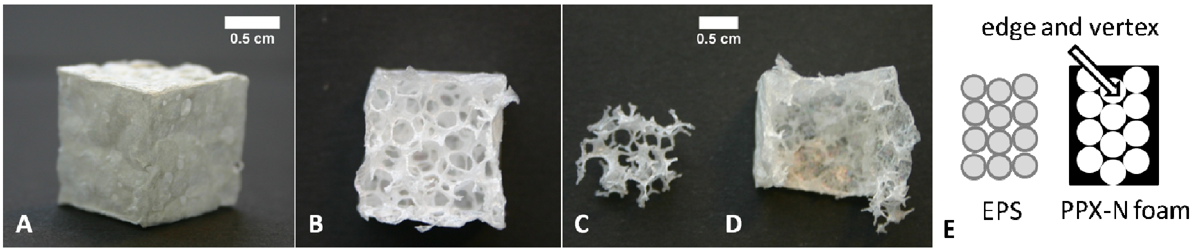

Figure 97 Specimen 2-2. Photographs of PPX-N foams obtained from a cube of EPS-2 with fused faces.

The higher density and better junction of the beads of EPS-3 inhibited the PX monomer to penetrate deep into the structure. In EPS-2 the air channels were of sufficient size to allow the PX monomer gas to penetrate the whole structure and deposit onto throughout the whole structure. Since the air channels in a bead foam have the same structure as an open-cell foam (see Section 3.6), the PPX-N resembles an open-cell foam structure in the interior, while forming a skin on the outside. This skin is comprised of at least one layer of foam cells reproduced by PPX-N as shown in Figure 98.

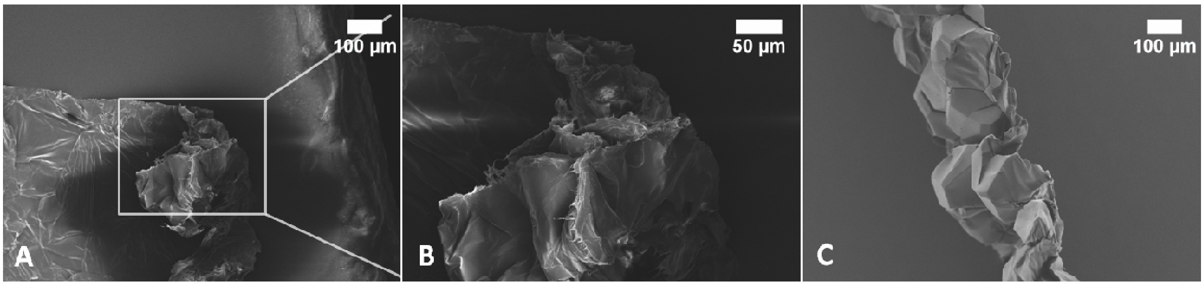

Figure 98 SEM micrographs of the skin of PPX-N foams obtained from EPS-2 template. The skins shown here are comprised of one layer of foam cells reproduced by the PPX-N coating.

The edges and vertices of the open-cell PPX-N foam were (see Figure 97 E), same as the outer skin of the cuboids, comprised of a continuous PPX-N layer and small closed-cells (Figure 99). Especially the SEM micrographs confirmed the reproduction of individual foam cells in the interior of the original template foam.

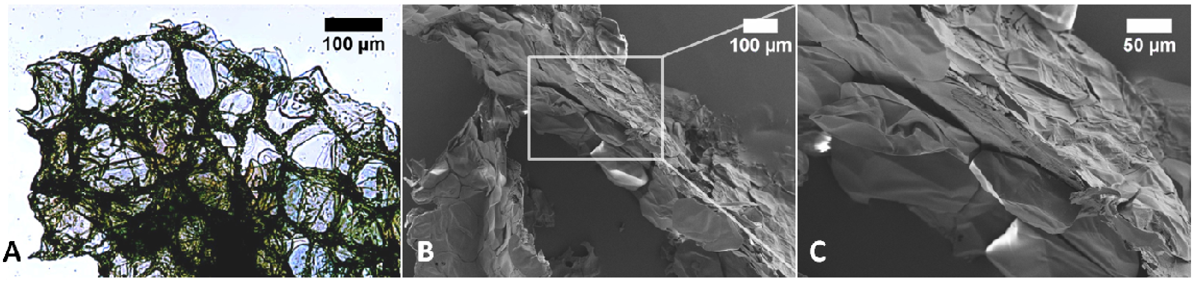

Figure 99 Microscope image[#] (A)and SEM micrographs (B,C) of the PPX-N forming edges and vertices of the open cell structure shown in Figure 97. The PPX-N reproduced the cell structure of the EPS template material for at least the outer cell layer of the beads.

All obtained microscope and SEM images showed, that wherever PPX-N deposited, the closed-cell structures of the outer EPS foam cells were reproduced. This applied to the outer skin of the specimen as well as for the edges and vertices of the inner open-cell foam. The outer layers of the foam cells had defect sites (e.g. due to rupture of cell walls from cutting or handling) which allowed the PX vapor to enter the first cell layer and reproduced this structure. Furthermore it was assumed that the foam cells forming a bead are not perfectly fused to each other. Therefore the PX vapor could penetrate a certain distance into the beads. Since the foam cells are much smaller and the fusion of the cells is better than the fusion of the beads, the air channels in a foamed bead are thinner and probably not continuous throughout the whole bead. This impeded the PX vapor to enter deeper into the individual bead and led to the reproduction of the outer cell layer only. Otherwise a thin network of PPX-N would have been found inside the EPS beads. However, the CVD coating of EPS foams with PPX-N can be used to map the air permeability. In case of good bead junction (as in case of EPS-3) no continuous structure of PPX-N was obtained in the interior of the coated specimen, in case of the presence of wide air channels (as in EPS-2) the PX gas penetrated the whole structure giving an in negative image of the entire foam.

As an alternative template material sugar cubes were coated with PPX-N and PPX-N foams obtained by template extraction (Figure 100 A-C). The density of this PPX-N foams was in the range of 10 mg·cm^{-3}, this is an enormous reduction compared to the original sugar cube with 1.2 g·cm^{-3}. In contrast to EPS, sugar cubes are porous, incompressible structures. The interior is composed of solid sugar crystals, glued together randomly. The PPX-N covered the entire structure of a sugar cube with a continuous layer. Film thickness gradients with samples of this dimension were negligible as structure imaging with micro computed tomography (µCT) showed. Especially the cross section analysis (Figure 100 E) gave an impression of the permeability of the PPX-N foams from sugar templates and revealed the labyrinth-like interior.

[#] microscope images were stacked with picolay

As demonstrated in Figure 100 D the µCT cross-sections can be combined to generate 3D images of the obtained foam structures.

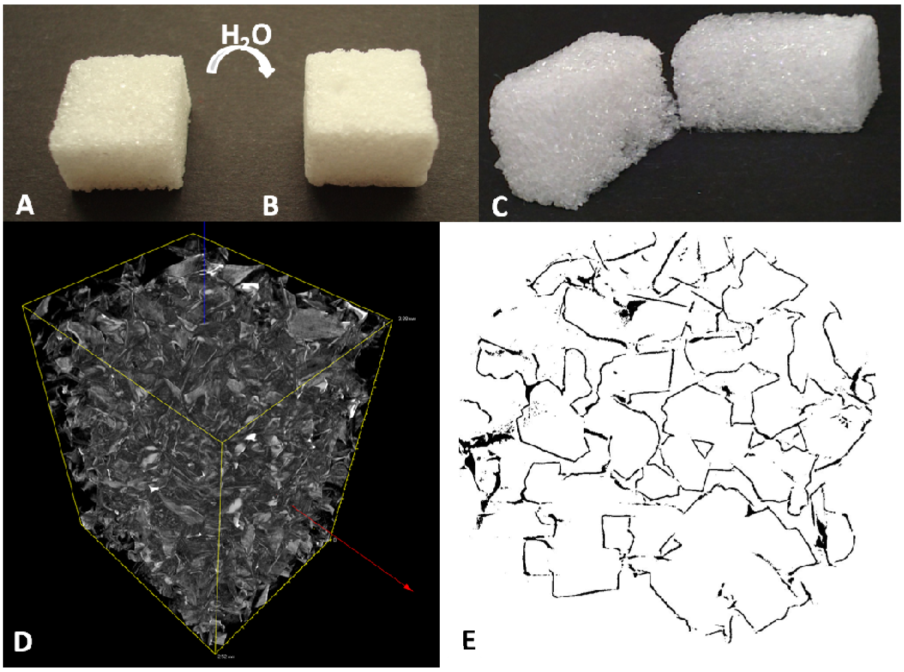

Figure 100 PPX-N coated sugar cube (A) turns into a PPX-N foam (B) after extraction of the template material with hot water. The cross section of the PPX-N foam (C) shows that PX penetrated the whole structure. Foam structure imaging by micro computed tomography is suitable for 3D reproduction (D) and cross section analysis (E) of the foams.

Figure 101 shows SEM micrographs of the surface of a sugar cube before (A,B) and after (C,D) the PPX-N coating. The PPX-N formed a conformal film on the rough surface of the sugar. As can be seen in Figure 101 E,F the PPX-N foam represented an intermediate of open and closed cell-structure.

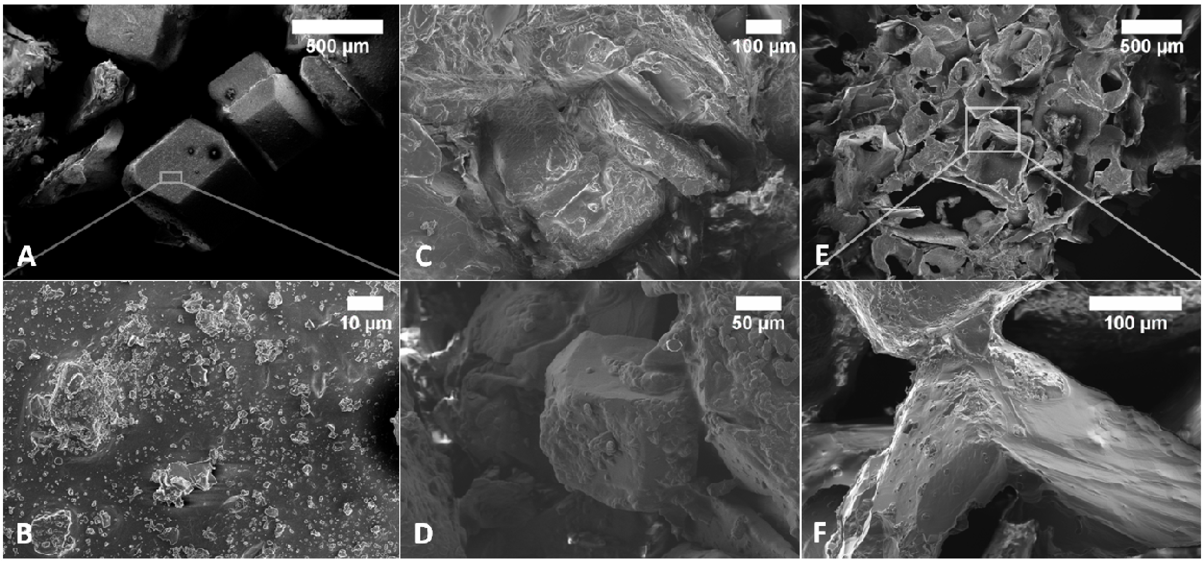

Figure 101 SEM micrographs of the surface of a sugar cube (A,B) and a PPX-N coated sugar cube (C,D) and the PPX-N structure (cross section) after extracting the sugar template (E,F).

Combining the results of both imaging techniques, the PPX-N foams obtained from sugar templates were identified as porous structures representing a three dimensional labyrinth. Furthermore, since the foam is porous, a high surface area is available inside the PPX-N cube.

4.4.3.2 PPX Foams for Further Applications

PPX-N coatings of porous structures is not only a method for structure mapping of the template foams but also generates PPX-N foams that can be of further use. As explained in 95, PPX foams obtained by CVD coating of a template produce the negative image of their template structures. In the following the conversion of the open-cell foam into a conductive material and the applicability of the labyrinth-like foam as host structure for living organisms will be shown briefly.

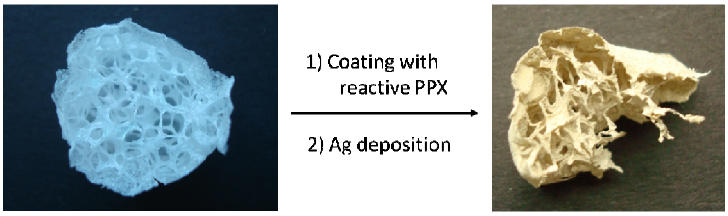

Figure 102 Images of PPX-N foam obtained by template coating of EPS a layer (left), and after deposition of a reactive PPX layer via CVD and a silver layer (right).

A conductive foam was obtained by deposition of silver via an electroless silver plating method described by Lili *et al.* from a $AgNO_3$ containing soltuion.[159] To promote the silver adhesion to the PPX structure, first a thin layer of poly(formyl-*p*-xylylene) (PPX-formyl) and poly(carbamido-*p*-xylylene-*co*-*p*-xlylene) (PPX-amid) were deposited onto different open-cell PPX-N foams. The presence of the functional groups was confirmed by the respective vibrations in ATR-IR spectra (Figure 103). The subsequent silver deposition resulted in a color change of the foam as shown in Figure 102.

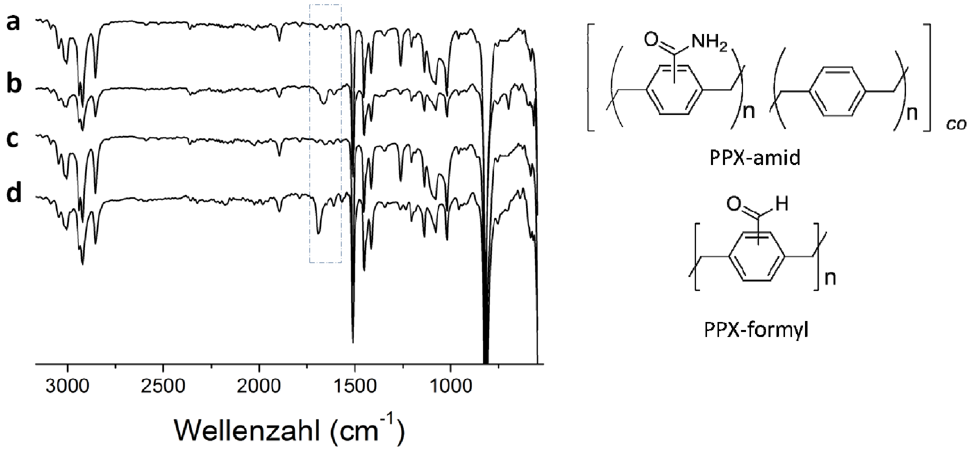

Figure 103 ATR-IR spectra of the PPX-N foams before (a,c) and after the coating with poly(carbamido-*p*-xylylene-*co*-*p*-xlylene) (c) and poly(formyl-*p*-xylylene) (d) and structures of the functional PPX derivates.

The SEM micrographs in Figure 104 show silver deposition on the entire foam structure and on both sides of the PPX layers. Though at high magnifications (image C) the silver layer seems to be discontinuous, the defect in the coating shown in image B reveals that the silver agglomerates are connected and hold together. Furthermore the foams were conductive as the current-voltage curves in Figure 105 show. Consequently there must be a non-interrupted pathways across the foam responsible for the conductivity. Optimizing the silver deposition process to achieve a continuous layer on top of the PPX will lead to an increased conductivity.

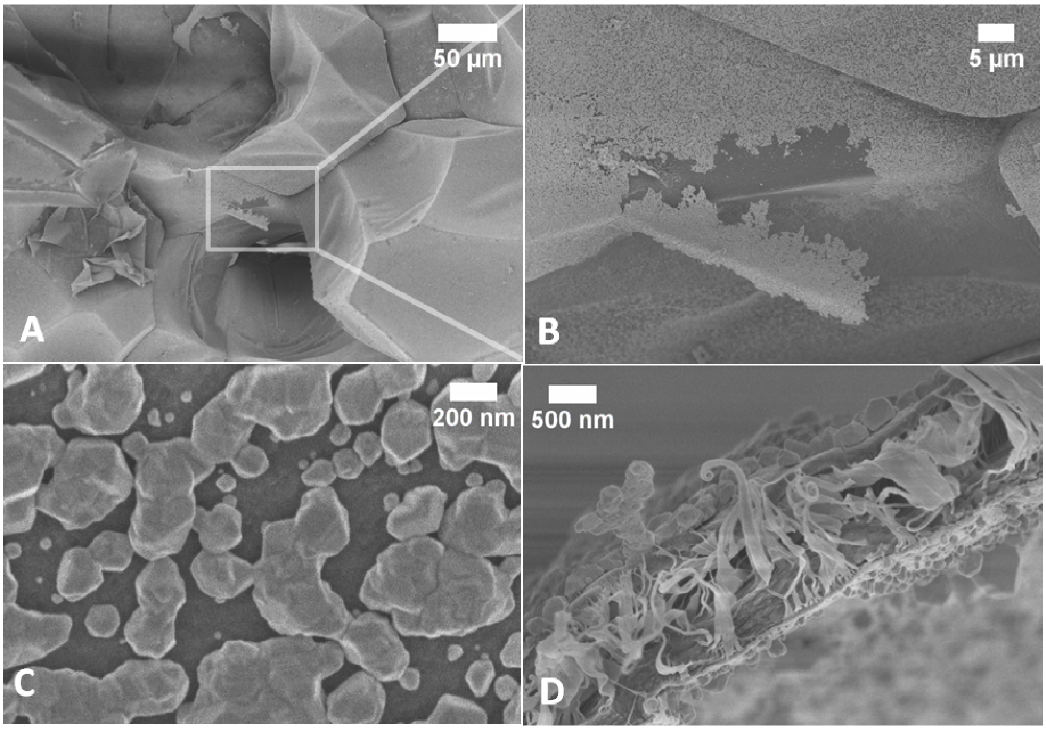

Figure 104 SEM micrographs of the silver coated PPX foam in different magnifications. Images A-C show Ag agglomerates on a PPX face. Images D shows the cross section of a PPX layer with silver agglomerates on both sides. The fringes result from cutting of the PPX and are observed often for cut or broken edges of PPX films.

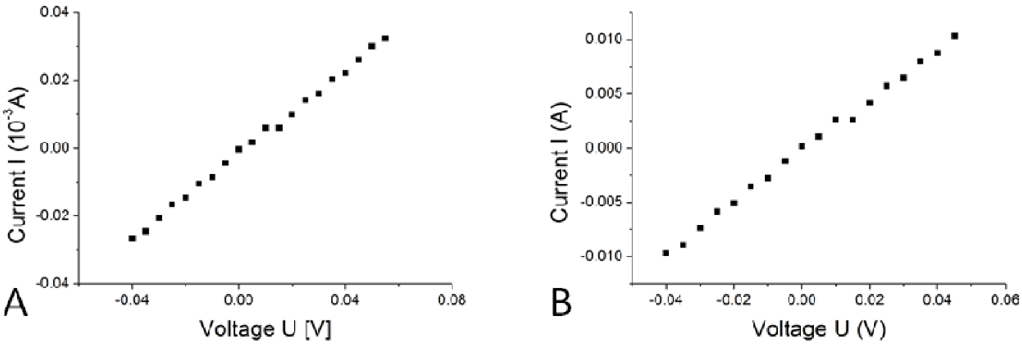

Figure 105 Current in dependence of applied voltage for Ag@PPX-N+NH_2 (A) and Ag@PPX-N+$CONH_2$ (B).

As could be seen from the analysis of PPX-N replica structures of different templates (Section 4.4.3.1), the foam obtained from sugar templates is denser, has a higher surface area and comprises a labyrinth-like interior. In a first experiment the usefulness of this PPX-N labyrinth structure as a host for living organisms was tested. For this reason PPX-N coated sugar cubes were extracted for different time periods (0, 17 and 48 h) with hot water in order to remove the template material completely (48 h) and partially (17 h). After loading the cubes with bacteria by submerging into an *Escherichia coli* (*E. coli*) containing nutritive solution, *E. coli* were found on and inside the extracted foams. The bacteria present in the 48 h extracted foam, outnumbered the bacteria found in the 17 h extracted foam. Figure 106 shows SEM micrographs of the 48 h extracted foam. As illustrated, the images were taken the center and close to the edge of the foam. *E.coli* were clearly identified by their characteristic oval structure and length of about 1-2 µm.

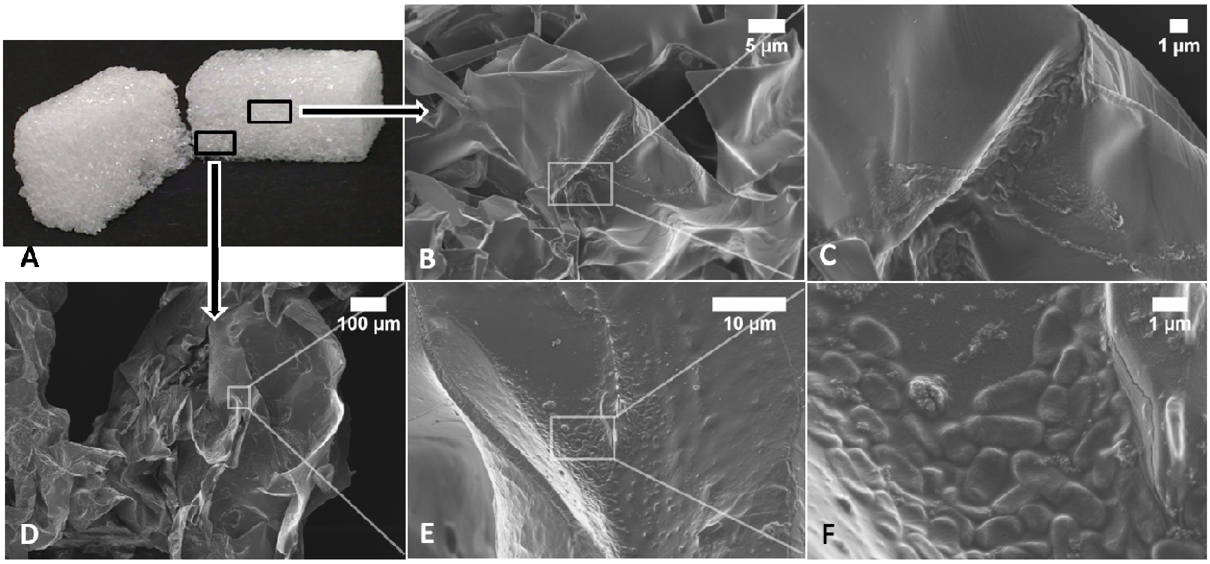

Figure 106 SEM micrographs (B-F) different positions from a PPX-N foam (template extraction time 48 h)loaded with *E. coli* bacteria. Before the bacteria loading the sugar template was extracted, the bacteria entered the whole PPX-N foam structure.

On and inside the non-extracted cube, no bacteria were found. The template sugar of the composite cube dissolved to some extend in the bacteria suspension, and the high concentration of sugar near the cube was considered responsible for the absence of bacteria. Since the number of bacteria in the partly extracted PPX-N foam was less than in the completely extracted, it was suspected that the high sugar concentration caused by the remaining sugar was equally lethal for the *E.coli* due to dehydration, [160] as in case of the non-extracted cube. As a conclusion from this first trail, PPX-N foams serve as host structures for *E.coli* and the provision of additional food in form of residue sugar in the foam is not only unnecessary but obstructive.

4.4.3.3 PPX as Mechanical Reinforcement and Protective Layer

The mechanical reinforcement of PS foams with different fillers like carbon nano tubes[161] or silicate[162], is reported in literature. Expanded polystyrene beads, however, are rather used as a component in light weight concrete,[163, 164] than being reinforced themselves.

In order to investigate the influence of the PPX coating on the mechanical performance EPS in tensile tests, test specimen for stress-stain measurements were coated with PPX-N, PPX-C and PPX-propyl. This PPX derivates differ in their mechanical properties, having E-moduli (for solid films) of 2.4,[76] 2.7[76] and 0.31-0.42[16] GPa and elongation at break up to 250[76], 200[76] and 380[16] % respectively (see also Table 1). Figure 107 shows the bone-like shape of the specimen. In the center the specimen were 3 mm wide, which is in the range of the bead size. Neat EPS specimen broke in stress-strain experiments preferentially on the bead junctions. Coating with PPX was supposed to fill possible gaps between the beads and give an additional continuous polymer layer on the outside of the specimen to improve their stress-strain performance.

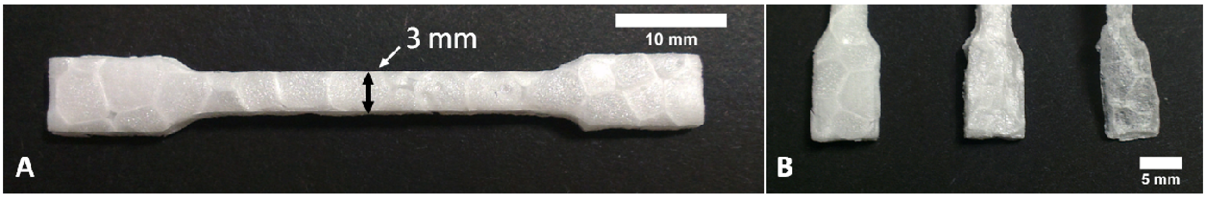

Figure 107 Test specimen for stress strain measurements. Pure EPS specimen in full size (A) and comparison (B) of EPS (left) PPX-N@EPS (center) and PPX-N (right).

Stress-strain measurements of the PPX@EPS specimen (Table 13) showed, that the E-moduli increased with increasing amount of PPX on the test specimen. Figure 108 shows detailed stress-strain curves for test specimen of run C3 and averaged curves of all PPX-C@EPS samples compared to neat EPS specimen and PPX-C foam, which was obtained from coating of EPS specimen and extraction of the template material.

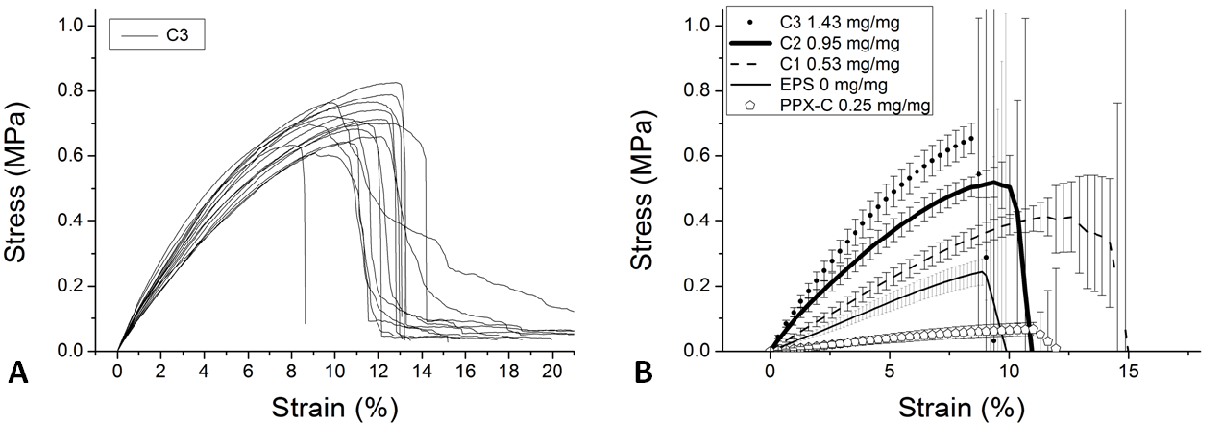

Figure 108 Stress-curves of PPX-C@EPS specimen show the deviation within one batch (A) and the averaged curves for all PPX-C@EPS batches in comparison with neat EPS and PPX-C foam (B).

The increase in E-modulus did not depend on the PPX derivate used for the reinforcement, but on the amount of PPX deposited onto the sample. The same trend was observed for the maximum force (F_{max}) the samples withstand (Figure 109). An influence of the PPX derivate could be found in the elongation at maximum force (Figure 110), where best results were obtained for specimen coated with thin PPX-propyl layers. Considering elongation at break no dependency could be observed.

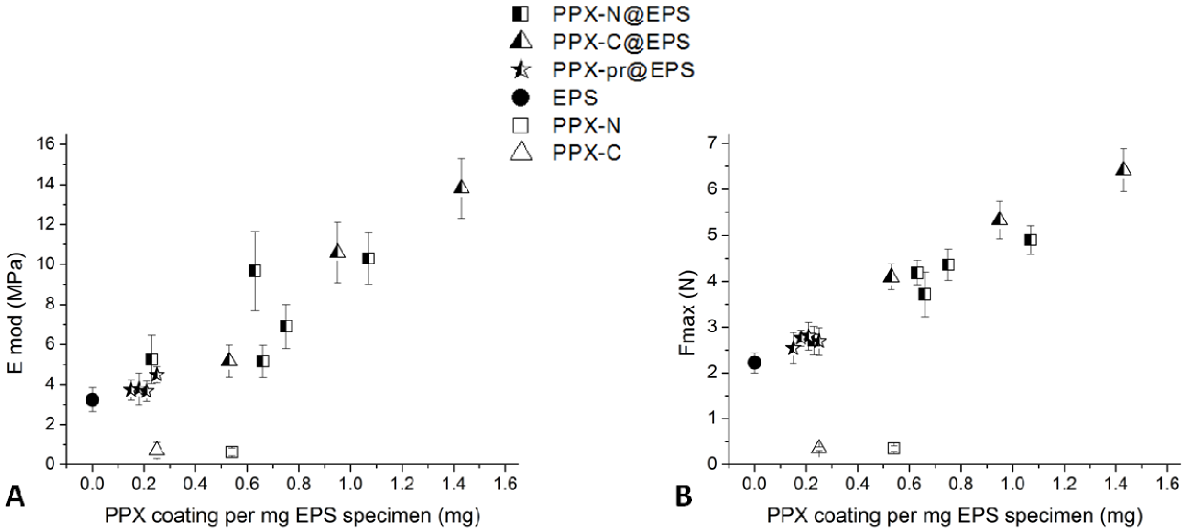

Figure 109 Results of mechanical analysis of PPX@EPS specimen from stress-strain tests. E-modulus (Emod) (A) and maximum force (F_{max}) (B) in dependence of the amount of PPX per mg EPS specimen.

Table 13 Details of PPX coated EPS specimens for stress-strain measurements.,

Run	Sample	Weight of EPS test specimen before coating/ mg	Amount of PPX coating per mg sample/ mg	E-modulus/MPa	F_{max} /N
N1	PPX-N@EPS	14.95 ± 0.86	0.23 ± 0.02	5.25 ± 1.2	2.71 ±.0.31
N2	PPX-N@EPS	14.21 ± 0.58	0.66 ± 0.04	5.16 ± 0.8	3.71 ± 0.49
N4	PPX-N@EPS	14.94 ± 0.33	0.63 ± 0.05	9.67 ± 2.0	4.18 ± 0.27
N5	PPX-N@EPS	15.22 ± 0.39	0.75 ± 0.07	6.91 ± 1.1	4.36 ± 0.34
N6	PPX-N@EPS	14.91 ± 0.41	1.07 ± 0.07	10.3 ± 1.3	4.9 ± 0.31
C1	PPX-C@EPS	15.02 ± 0.29	0.53 ± 0.02	5.17 ± 0.8	4.09 ± 0.28
C2	PPX-C@EPS	15.22 ± 0.39	0.95 ± 0.04	10.6 ± 1.5	5.33 ± 0.41
C3	PPX-C@EPS	14.80 ± 0.39	1.43 ± 0.08	13.8 ± 1.5	6.42 ± 0.47
P1	PPX-pr@EPS	15.30 ± 0.23	0.15 ± 0.01	3.73 ± 0.5	2.54 ± 0.33
P2	PPX-pr@EPS	15.32 ± 0.32	0.25 ± 0.04	4.49 ± 0.4	2.69 ± 0.30
P3	PPX-pr@EPS	15.31 ± 0.37	0.18 ± 0.01	3.78 ± 0.8	2.76 ± 0.18
P4	PPX-pr@EPS	15.07 ± 0.35	0.21 ± 0.01	3.67 ± 0.5	2.80 ± 0.30
PPX-N	PPX-N*	14.89 ± 0.33	0.54 ± 0.03	0.63 ± 0.2	0.35 ± 0.06
PPX-C	PPX-C*	15.11 ± 0.31	0.25 ± 0.01	0.70 ± 0.4	0.35 ± 0.04
EPS	EPS	n.d.	0.00	3.24 ± 0.6	2.22 ± 0.22

* EPS was dissolved before stress-strain testing, remaining PPX foams tested in stress-strain analysis; n.d.=not determined

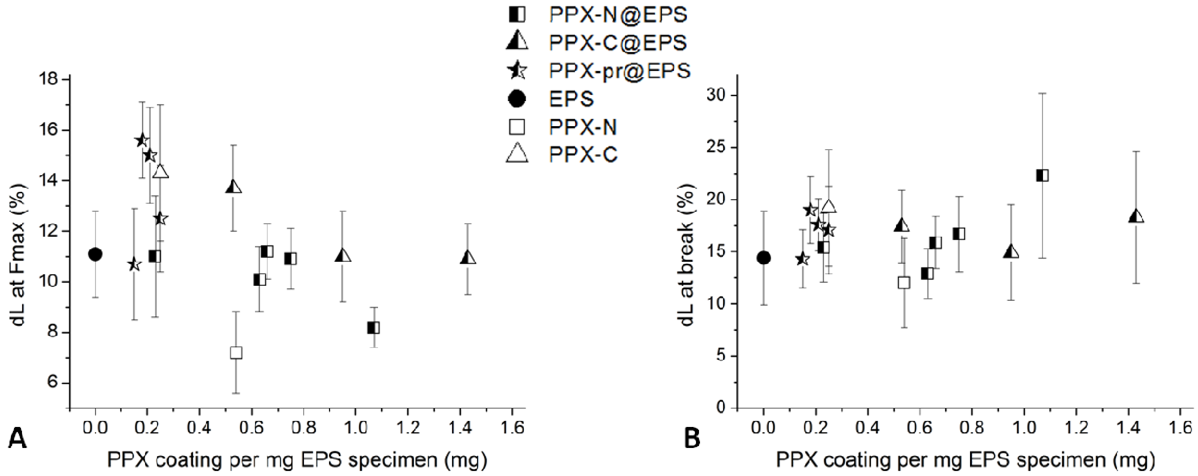

Figure 110 Results of mechanical analysis of PPX@EPS specimen from stress-strain tests. Elongation at maximum force (dL at F_{max}) (A) and elongation at break (dL at break) (B) in dependence of the amoung of PPX per mg EPS sepcimen.

The coating with PPX showed a considerable improvement in the E-modulus of the tested EPS, however, the weak points were still the junction sites of the individual beads. For further characterization and comparison with the mechanical behavior of other foamed materials compression tests are of mayor interest.

In addition to the mechanical reinforcement the PPX layer were acted as an effective gas barrier. Since the CVD is carried out under reduced pressure, the template EPS foams were evacuated together with the reactor. The structure of the EPS samples was not harmed by the evacuation but by fast ventilation after the coating process (Figure 111). The additional PPX layer hinders the diffusion of air back into the foam structure. The effect was dependent on ventilation speed and PPX coating thickness.

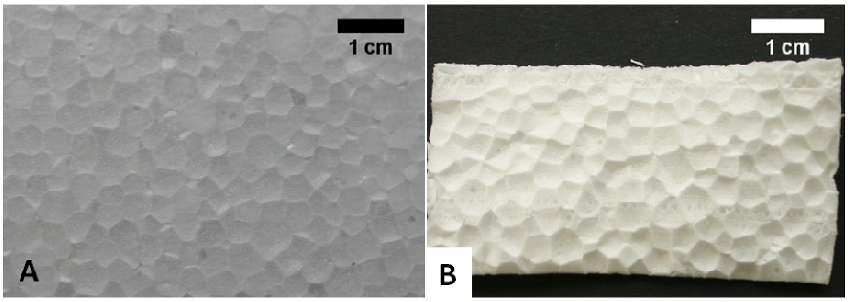

Figure 111 Photograph of an expanded polystyrene foam sheet (EPS-1) before (A) and after (B) CVD coating with fast ventilation of the deposition chamber, which led to a deformation of the bead structure.

PPX-is not only known to act as gas diffusion barrier but also to be temperature stable and solvent resistant. Both properties were true for PPX-N coated EPS specimen. As shown in Figure 112, the PPX-N coated specimen (PPX@EPS) was less susceptible to elevated temperatures than the neat EPS. Upon exposition to a lighter flame, the neat EPS melts instantly and starts dripping after 9 s. The PPX@EPS did neither melt nor burn in the first 5 seconds and dripping occurred after 18 seconds.

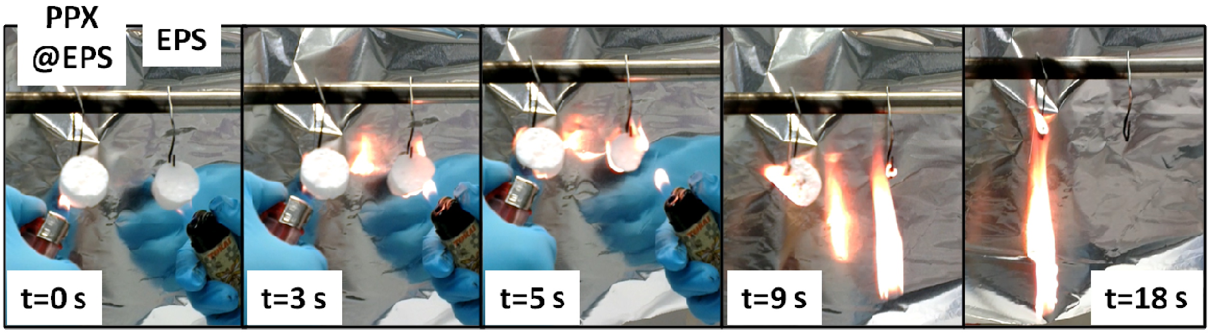

Figure 112 Temperature tolerability of neat EPS and PPX-N coated EPS (PPX@EPS). Cylindrical specimen were exposed to a lighter flame, the PPX-N layer makes the EPS specimen more stable at elevated temperatures.

4.4.3.4 Batch Foaming of PPX-propyl

For soluble PPX derivates the foam generation by batch foaming is an alternative to the template extraction method described above. In the batch foaming method a solid specimen of the desired polymer is saturated with an expansion agent (like CO_2), which upon its release form the solid material generates bubbles inside the polymer that form the foam cells.

As a proof of principle experiment a solid disco of PPX-propyl with 2.5 cm diameter (same as a 2 € coin) and 0.7 mm thickness was solvent cast from chloroform solution. The film was loaded with CO_2 for 1 day (at 50 bar) and expanded in a preheated oil bath at 120 °C. The foaming was done by Daniel Raps (Group Prof. Altstädt). The resulting PPX-propyl foam showed a density of 0.17 g·cm^{-1}, the increase in diameter was about 120 %.

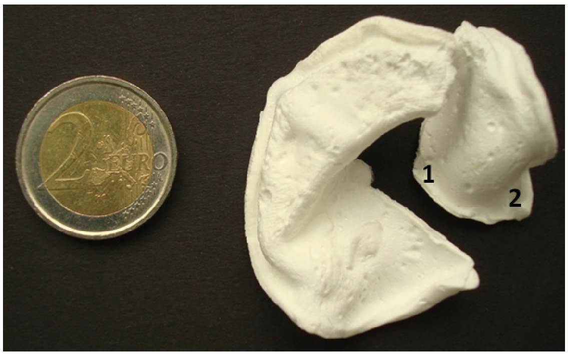

Figure 113 PPX-pr foam prepared by batch foaming. Before foaming the compact PPX-propyl film had the size of a 2 € coin (d=2.5 cm), thickness 0.7 mm.

The SEM micrographs in Figure 114 show a closed-cell structure with inhomogeneous cell size distribution. The vertical and horizontal extension of 167 cell visible in Figure 114 D was determined to be 13.73 ± 14.41 µm and 8.82 ± 6.57 µm. This values have to be taken with care, since some cells are deformed and the cross section analyzed does not represent the center of each cell. However this value reflects the inhomogentiy of the cell size. The face thickness was determined from Figure 114 C, giving 0.69 ± 0.35 µm.

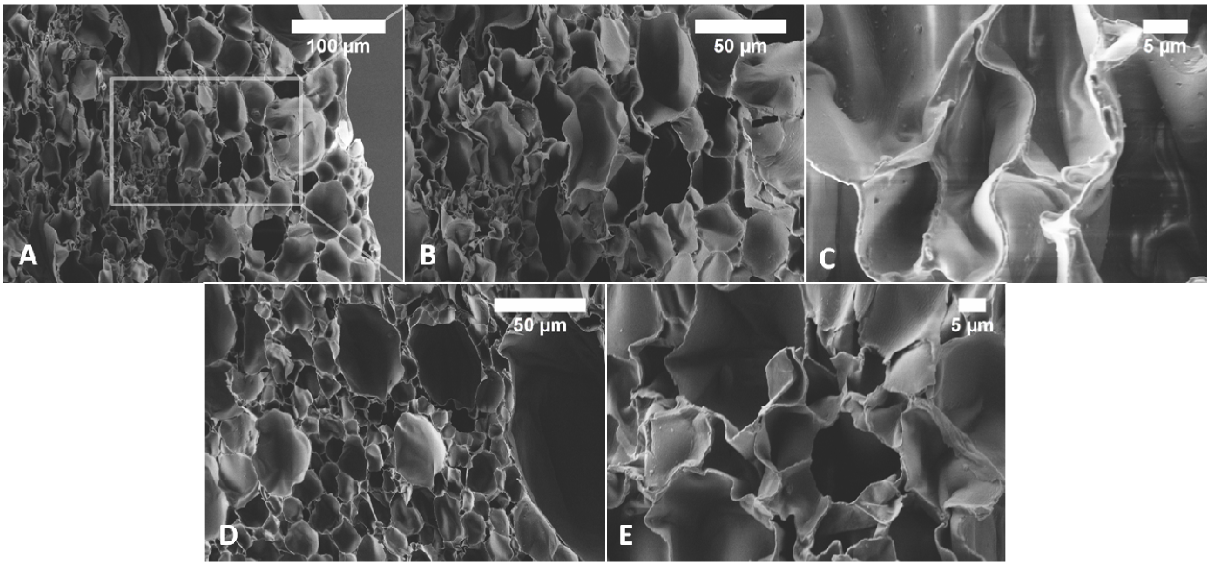

Figure 114 SEM micrographs of PPX-propyl foam at different positions (indicated in Figure 113) of the foam. The closed-cell structure is clearly visible, cell size distribution is broad. A,B,C from the center (position 1), D,E from the edge (position 2).

Cell size and size distribution can be influenced by foaming conditions and adding nucleation additives. Generally such experiments are carried out in form of a reaction design to find optimum parameter.

4.4.4 Conclusion

Different PPX derivates were successfully processed into polymer blends, foams and composite-like materials, and first studies in order to explore new fields of applications were realized.

Polymer blends of PPX-propyl with PMMA, PS and PPE were obtained by solvent casting. The immiscibility of the blends was detected by DSC and SEM analysis, and their mechanical behavior was investigated in stress-strain measurements. Especially in the case of PPX-pr/PPE blends, the mechanical performance of the blends showed intermediate behavior compared to both homopolymers. In addition to the analysis of the stress-strain behavior, the impact strength of the PPX-pr blends is an interesting issue. However, in order to investigate the materials properties further, there is a need for compatibilizers to stabilize the blend morphology, ensure reproducibility and provide interphasial adhesion of the two components, since this factors play key roles in the mechanical performance of polymer blends. A route to such compatibilizers can be the block-copolymerization of alkyl-PPX by the use of PPX-peroxide as building blocks (as described in Section 4.1.3), random-copolymers using the PPX-copolymerization via CVD as described in Section 4.1.2, or even grafted copolymers obtained by the method described in 4.2.

PPX coating of porous structures via CVD was found to be an excellent method for structure mapping of porous template materials. In case of continuous porosity of the template a three dimensional structure made of PPX, representing the negative image of the template, was obtained after extraction of the template material. In case of non-continuous air channels, e.g. EPS with tightly fused beads, only the outer shape of the template was reproduced. In addition to the structure mapping purpose, template coating is a method to obtain 3D-PPX structures, especially of insoluble and intractable derivates that can only be produced via CVD. With the possibility to design application tailored templates, it is a unique approach to model non-processable PPX polymers into desired structures directly during the CVD process. PPX foams were further modified to give conductive materials or used as host structure for *E. coli*. This experiments guide the way to further applications. As an example, conductive PPX foams that can host bacteria can be used as electrodes in microbial fuel cells, where good conductivity and high surface area of three dimensional structures are crucial parameter.[165] Three dimensional open-cell structure made of PPX might also be of interest in tissue engineering applications, where the scaffold does not have to be biodegradable or bioresorbable.

The PPX coating of EPS foams did furthermore improve their mechanical behavior in terms of a considerably higher E-modulus. Furthermore, this reinforcement was shown to be scalable with the amount of PPX deposited onto the EPS specimen. Experiments in larger scales, and further testing to determine more mechanical parameter (like E-modulus in compression, flexural modulus etc.) will show the quality of the reinforcements. In addition to the mechanical property modification the outer PPX layer served as protective coating, so that the substrate was less susceptible to elevated temperature and organic solvents, and showed to be an effective gas diffusion barrier for the otherwise permeable EPS material.

An alternative way to the generation of PPX foams was shown by batch foaming of PPX-propyl. This approach is suitable for soluble PPX derivates, because the specimen required for the batch foaming process need a certain thickness, which is difficult to obtain by CVD. Here PPX derivates obtained by Gilch polymerization are also promising materials, because the can be molded easily into the required shapes.

5 Experimental Part

5.1 Methods and Instrumentation

5.1.1 Contact Angle

Image recording for static contact angle determination was done with the contact angle measurement system G10 from Krüss with eScope USB-camera. Contact angle measurements were performed with DropSnake[166] plugin for ImageJ (Version 1.46r). If not mentioned otherwise, for each sample twelve images were evaluated, the highest and lowest value were discarded and the average calculated from the remaining ten.

In case of temperature dependent measuremtents of with PNiPAAm the films were placed on a heating table, set to 50 °C. Contact angles ranges reported in Section 4.2 were determines from 5-7 values each, exception are the time dependent measurements, where the angle was determined from the respective image.

5.1.2 Dektak Surface Profilometer

Thickness of PPX coatings performed in SCS Labcoater were analyzed be determining the film thickness deposited on standard glass slides, present during the respective CVD reaction. The film thickness was measured by analyzing the step height of incised lines in the film with Dektak Surface Profilometer models 3 ST and 3030 (Vecco). The average value was taken from three measurements at different positions on the glass slide.

5.1.3 Differential Scanning Calorimetry (DSC)

Thermal behavior of the polymers was studied with differential scanning calorimetry (DSC), with DSC 821^{e} module from Mettler Toledo calibrated with indium and zinc. Analysis were performed with 5-8 mg samples in 40 µl aluminum pans under nitrogen atmosphere (flow rate 50 $ml\cdot min^{-1}$) with heating and cooling rates of $20K\cdot min^{-1}$. The glass transition was determined from the second heating curve with Mellter Toledo STAR^{e} software (version 9.20).

5.1.4 Digital Microscope

Digital Microscope images were recorded with DMRX microscope from Leica, equipped with a DC 200 camera (Leica). Images were stacked with picolay[167] software (version 2013-05-12). Analysis of bead diameter of EPS samples was performed with ImageJ (Version 1.46r), if not mentioned otherwise, 100-120 measurements were executed to determine average values.

5.1.5 Elemental Analysis

For elemental analysis the carbon, hydrogen and nitrogen content of the polymer samples were determined by combustion analysis in vario-Micro cube instrument from Elementar (CHNS modus). Measurements were carried out by the routine analytics department of the University of Marburg.

5.1.6 Energy Dispersive X-ray Spectroscopy (EDX)

EDX measurements were performed with Zeiss 1530 scanning electron microscope equipped with Oxford INCA 400 EDX-detector.

5.1.7 Gas Chromatography (GC)

Gas chromatograms were recorded with GC-17A (Shimadzu) with a capillary column FS-SE-54-CB-0.25 (30 m), flame ionization detector and nitrogen carrier gas. [2.2]paracyclophanes were measured from 100 - 280 °C with heating rate of 10 $°C \cdot min^{-1}$, with injection and detection temperatures of 300 °C.

5.1.8 Gas Chromatorgraphy- Mass Sepctrometry (GC/MS)

GC/MS measurements were performed with a QP5050 A Instrument (Shimadzu) with a FS-SE-54-CB-0.25 column (30 m), with electron inionization detector and helium as carrier gas. [2.2]paracyclophanes were measured from 100-280 °C with heating rate of 10 $°C \cdot min^{-1}$, injection temperature 300 °C, interface temperature 230 °C. Measurements in Bayreuth were carried out in the university routine analytics laboratory.

5.1.9 Gel-Permeation Chromatography (GPC)

Analysis of molecular weights and distributions were done by gel permeation chromatorgraphy (GPC) with THF or chloroform as eluent and toluene as standard. For THF, flow rate was 0.8 $ml \cdot min^{-1}$, polymer concentration 1-2 $mg \cdot ml^{-1}$, and calibrated with linear polystyrene standards (purchased from PSS). The setup contained two SDV columns (10 µm, $60 \cdot 0.8$ mm^2) from PSS, refractive index and UV detector. PPX-alkyl homopolymers analyzed for electrospinning purpose were measured at 40 °C, other samples were measured at room temperature.For chloroform flow rate was 0.5 $ml \cdot min^{-1}$, with three PSS SDV columns (pore size: 1,000, 100,000 and 1,000,000 Å) and refractive index detector (Knauer RI2300), samples were measured at room temperature.

Data evaluation was performed with PSS WinGPC Unity software.

5.1.10 Infrared Spectroscopy (IR)

IR spectra were recorded on a Digilab IR-Spectrometer (Excalibur series) equipped with an ATR-unit containing a ZnSe crystal. Data evaluation was performed with WinIRPro software.

5.1.11 Matrix-assisted Laser Desportion/Ionization (MALDI-TOF)

MALDI-TOF spectra were recorded on a Bruker ReflexIII apparatus. Isotope distribution was simulated with Molecular Weight Calculator (version 4.69).[168]

5.1.12 Micro Computed Tomography (μ-CT)

Scans were performed with Bruker Skyscan microtomograph 1072. Image evaluation was done with MAVI software (version 14.1). Scan parameter were 60x, 29 kV, 172 μA and 180° rotation with a angular steps of 0.23°. The Scans were performed by Thomas Koeppl and Daniel Raps from the group of Prof. Altstädt.

5.1.13 Nuclear Magnetic Resonance Spectroscopy (NMR)

NMR measurements were performed with a Bruker ARX 300 NMR-spectrometer. Data evaluation was performed with MestReNova 6.1.0 software.

5.1.14 Roll Angle Measurements

Roll angles were determined with a tiltable plate with degree value scale. The sample (on a glass slide) was fixed on the table and a droplet with a volume of about 22.5 μl was dropet from approximately 3 cm distance onto the surface. The table was tilted until the droplet rolled off the surface, and the respective angle was determined from the scale.

5.1.15 Scanning Electron Microscopy (SEM)

Characterization of electrospun fibers was done by scanning electron microscopy (SEM) with Zeiss 1530 and Zeiss Ultra plus FE-SEM, at acceleration voltages of 2-3 kV. Samples were sputtered with 1.3-2 nm Pt prior to micrograph recording. Fiber diameters were measured with ImageJ (Version 1.46r), average was calculated from 100-120 measurements, occasional beads were not taken into account.

Characterization of the PPX-propyl blends was done with JSM-7500 F scanning electron microscope from JEOL. Samples were sputtered for 100 seconds with Pt prior to analysis.

5.1.16 Stress-strain Measurements

Stress-strain analysis was performed with a measuring device from Zwick/Roell model BT1-Fr0,5TN-D14 with force transducer KAT-TC (200 N). Measurements were performed without preload and test speed of 5mm/min for EPS specimen and 0.2 MPa preload and test speed of 50mm/min for bend specimen. Data evaluation was performed with *testXpert*® II V3.0 software, per batch 15 test specimen were measured in case of EPS specimen, 10 in case of blend specimen. Test specimen were obtained with a punching machine (Rayran) and stencil ISO 5272-1BB.

5.1.17 Thermogravimetrical Analysis (TGA)

The thermal decomposition of polymer samples was measured with a TG 851 thermobalance from Mettler Toledo. Analysis was performed under nitrogen atmosphere with a flow of 50 $ml \cdot min^{-1}$ in aluminum oxide crucibles. Samples of 3-15 mg were measured in a 70 µl aluminum oxide crucible with a heating rate of 10 $K \cdot min^{-1}$ in the temperature range of 25-800 °C. Data were evaluated with $STAR^e$ software (version 9.20).

5.2 Chemicals

[2.2]paracyclophane	Speciality Coatings Systems, used as received
1-bromobutane	Aldrich (99%), used as received
1-bromopropane	Aldrich (99%), used as received
2,2'-azoisobutyronitrile	Aldrich (≥98%), recrystallized from ethanol
2-hydroxyethyl methacrylate	Aldrich (97%), used as received
4,12-diethyl-[2.2]paracyclophane	provided by Anna K. Bier
4,12-di-formyl-[2.2]paracyclophane	provided by Michael Bognitzki
4,12-diheptyl-[2.2]paracyclophane	provided by Anna K. Bier
4,12-dimethyl-[2.2]paracyclophane	provided by Anna K. Bier
4-carbamido-[2.2]paracyclophane	provided by Michael Bognitzki
A174-silane	Speciality Coatings Systems, used as received
anisole	Fluka (p.a.), destilled over CaH_2
calciumhydride	Sigma-Aldrich (95%), used as received
chloroform	university supply (technical grade), distilled; Fischer Chemicals (p.a.) used as received
CTAB	ABCR Karlsruhe (98%), used as received
Cu(I)Br	Aldrich (99.99%), used as received
Cu(II)Br	Fluka (>99%), used as received
dichloro[2.2]paracyclophane	Speciality Coatings Systems, recrystallized from dioxane
diethyl ether	university supply, distilled or dried over P_2O_5
ethanol	university supply (technical grade), distilled
glycidyl methacrylate	Aldrich (97%), distilled
hydrchloric acid	Grüssing (37%), used as received
magnesium	university supply
methanol	university supply (technical grade), distilled
methyl methacrylate	Aldrich (99%), distilled over CaH_2
Ni(dppp)Cl_2	Aldrich, used as received
N-isopropyl acrylamide	Acros (99%), recrystallized from hexane
oligo(etylene glycol) methacrylate	Aldrich (M_n 360), used as received
phosphorus pentoxide	ACS reagent (≥98.0%), used as received
PMDETA	Alrich (99%), used as received
poly(ethylene oxide) 10,000	Fluka
poly(ethylene oxide) 300,000	Arcos Organics, used as received
poly(ethylene oxide) 35,000	Merck-Schuchard
poly(ethylene oxide) 900,000	
poly(methyl methacrylate)	Evonik Röhm
poly(oxy-2,6-methyl-1,4-phenyl)	General Electric
polystyrene	BASF
sodium hydroxide	Sigma-Aldrich(≥98%, pellets), used as received
tetrahydrofurane	university supply (technical grade), distilled
α-bromoisobutyryl bromide	Aldrich (98%), used as received

5.3 Chemical Vapor Deposition Reactors

5.3.1 Homemade Pyrolysis Reactor

The setup for PPX homopolymer synthesis consists of a glass apparatus subdivided in three compartments named sublimation chamber (borosilicate glass, length 5 cm), pyrolysis tube (fused quartz glass, length 90 cm, diameter 2.5 cm) and deposition chamber (borosilicate glass, see 5.3.2 for details), which is connected to a cryostat (Haake K40) (Figure 115). During the reaction pyrolysis tube and sublimation chamber are placed in a tubular three-zone furnace (Pyrolus AT) with independently adjustable temperatures for each zone (lenght 38 cm each). Sublimation, pyrolysis and deposition temperatures were adjusted for the respective precursor (Table 14). Reduced pressure was achieved with an Edwards S two-stage oil pump connected to the pyrolysis reactor. To protect the pump from pyrolysis product passing the deposition chamber three cooling traps with liquid nitrogen were placed between the pump and the reactor. The base pressure of around $2.1 \cdot 10^{-2}$ mbar was controlled with an Edwards Pirani gauge 1002 (PRL 10) behind the first cooling trap for the same reason.

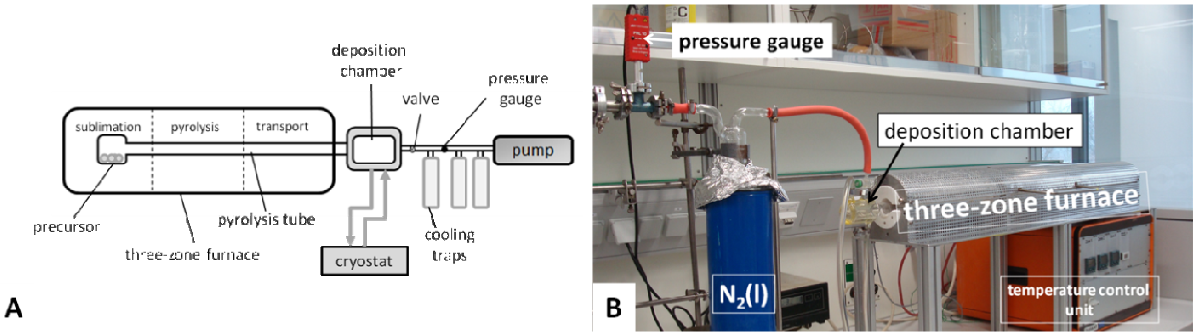

Figure 115 Schematic representation of the homemade CVD reactor for PPX homopolymerization (A) and photograph (B).

For PPX-peroxide synthesis a sublimation chamber with additional inlet for ambient air was used. The air flow was regulated with a HOKE Milli-mite 1335M4B valve connected to the sublimation chamber via a spirally metal capillary (Figure 116). To avoid the entrance of ambient moisture into the reactor the air passed through a short (10 cm) column filled with calcium chloride beforehand. Instead of three liquid nitrogen cooling traps, only one trap cooled with isoproanol to -20°C was used for PPX peroxide synthesis.

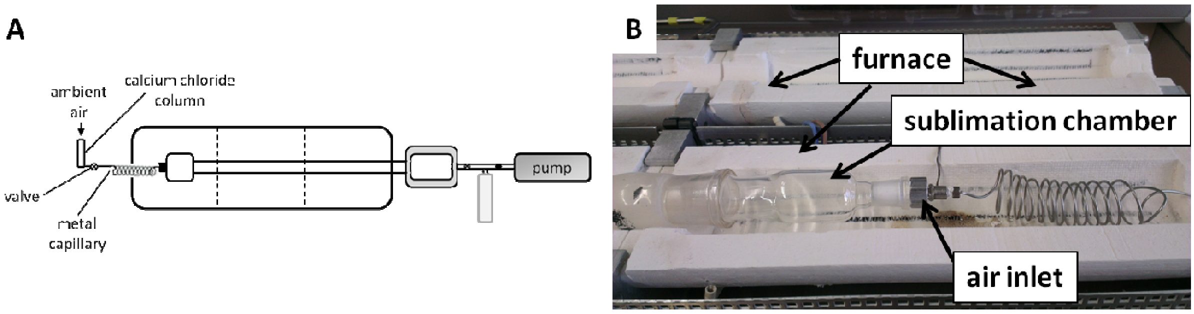

Figure 116 Schematic representation of the homemade CVD reactor for PPX peroxide synthesis (A) and photograph of the sublimation chamber with spirally metal capillary for ambient air inlet (B).

For copolymerization reactions an additional borosilicate glass piece in form of a "T" was added in between furnace and deposition chamber (Figure 117). The T-piece contained two glass valves to interrupt the monomer flow of *p*X and the comonomer independently. All glass tubing between furnace and deposition chamber was wrapped with heating tape (OMEGALUX, Stamford USA, Model FGH052-060L) and heated to 150 °C to prevent PPX from depositing. The temperature of the heating tape was monitored with NiCr-Ni temperature sensor (HORST, Model 070102) and a SIKA electronic TLK39 control unit.

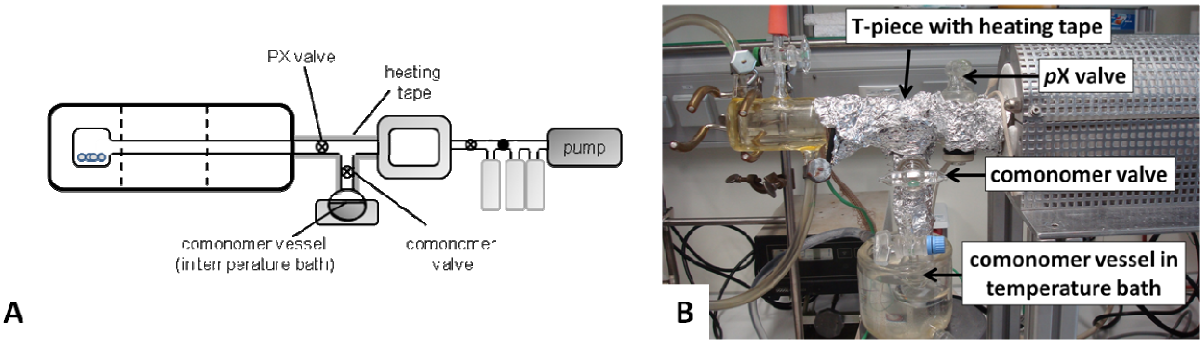

Figure 117 Schematic representation of the homemade CVD reactor with additional T-piece for copolymerization (A) and photograph of the additional T-piece (B).

5.3.2 Deposition Chamber Models

Two different deposition chamber models were used for polymer deposition. With model A (Figure 118 A) polymer was deposited parallel to the monomer flow, with model B (Figure 118) deposition was perpendicular to the monomer flow. Chambers of model A were 2.9-3.5 cm in diameter and 7-8 cm in length (volumes 60-70 ml). Chambers of model B had an inner diameter of 5 cm an a length of 13 cm.

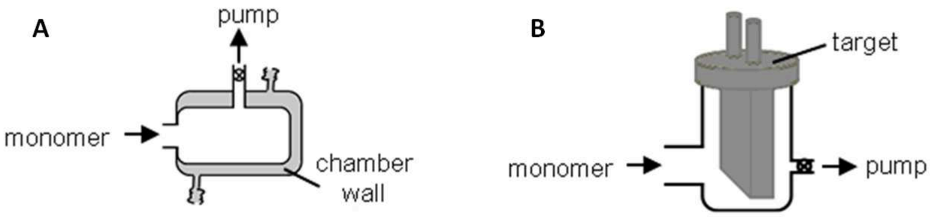

deposition chamber model A

deposition chamber model B

Figure 118 Deposition chamber models for homemade CVD reactor for deposition parallel (A) and perpendicular (B)to the monomer flow direction. Chamber A is also used as collector-chamber.

5.3.3 SCS Labcoater Modified for Copolymerization

For copolymerizations in SCS Labcoater PDS 2010 the commercially available setup was modified with a comonomer inlet in the deposition chamber (Figure 119). The additional components were attached to the Labcoater if needed for copolymerization, otherwise homopolymerzations were carried out as described in the handbook. In contrast to the homemade CVD reactor the Labcoater is equipped with a rotating sample holder.

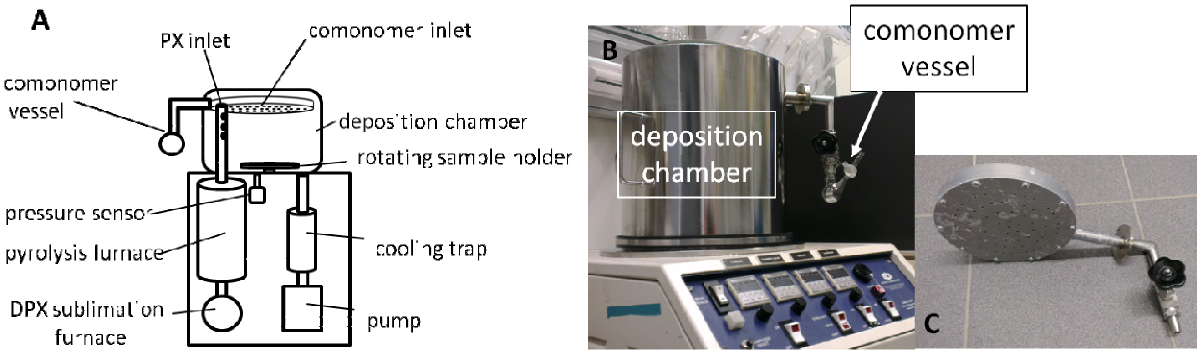

Figure 119 Schematic representation of the modified Labcoater with additional comonomer inlet for copolymer synthesis (A), photograph of the modified setup (B) and photograph of the comonomer inlet with valve (C).

5.4 General Procedures

5.4.1 PPX Homopolymer Synthesis in Homemade Reactor

In a typical synthesis run for PPX homopolymer, 2 g precursor were placed in the sublimation chamber and the glass apparatus was assembled. The deposition chamber was connected to the cryostat, which was set to the deposition temperature (T_{dep}). Then the reactor was evacuated for 1 h before the oven was preheated to the pyrolysis (T_p) and transportation (T_t) temperatures. Pyrolysis and deposition temperature varied with the respective precursor (Table 14), transportation temperature was kept at 300°C. After 0.5 h of temperature equilibration (pyrolysis and transportation zone) the sublimation zone was heated to the respective precursor sublimation temperature (T_{sub}). After complete precursor evaporation the apparatus was flooded with ambient air. The polymeric product was peeled off the chamber or removed with distilled water. For purification the alkyl-PPX and P(PX-alkyl-*co*-HEMA) polymers were dissolved in chloroform, precipitated in methanol and dried under reduced pressure

Table 14 Sublimation, pyrolysis and deposition temperatures used for PPX homopolymerization.

Precursor	T_{sub}/ °C	T_p/ °C	T_{dep}/ °C
[2.2]paracyclophane	80-110	650-660	0-25
4,12-di-methyl-[2.2]paracyclophane	87	600	0
4,12-di-ethyl-[2.2]paracyclophane	110	640	0
4,12-di-propyl-[2.2]paracyclophane	120	550	0
4,12-di-butyl-[2.2]paracyclophane	120	520	0
4,12-di-heptyl-[2.2]paracyclophane	155	500	0
4,12-di-formyl-[2.2]paracyclophane	90	650	RT
4-carbamido-[2.2]paracyclophane	100	650	RT

5.4.2 PPX Peroxide Synthesis in Homemade Reactor

In a typical synthesis run 500 mg DPX-propyl or DPX-butyl were placed in the sublimation chamber and the ambient air inlet (with closed valve) was connected. The glass apparatus was assembled and the deposition chamber was connected to the cryostat, which was set to the deposition temperature (5 °C or 10 °C). Then the reactor was evacuated for 1 h before the oven was preheated to the pyrolysis and transportation temperatures. Pyrolysis temperature varied with the respective precursor (Table 14), transportation temperature was kept at 300°C. After 0.5 h of temperature equilibration (pyrolysis and transportation zone), the air valve was opened until the desired pressure was reached, then the sublimation zone was heated to the respective precursor evaporation temperature. After complete precursor evaporation the apparatus was flooded with ambient air. The polymeric product was removed from the deposition chamber with distilled water or dissolved in chloroform.

5.4.3 PPX Copolymer Synthesis in Homemade Reactor

In a typical synthesis run, 300 mg precursor were placed in the sublimation chamber and 5 ml comonomer in the comonomer evaporation vessel and the glass apparatus was assembled. The comonomer vessel was evacuated shortly to remove air via the comonomer valve (without evaporation of the comonomer). The deposition chamber was connected to the cryostat, which was set to the respective deposition temperature and the heating tape was set to 150 °C. The reactor was then evacuated for 1 h before the furnace was preheated to the respective pyrolysis temperature (see Table 14), transportation temperature was kept at 300°C. At the same time the comonomer vessel was heated to the respective evaporation temperature in a preheated temperature bath. After 0.5 h of temperature equilibration, the *p*X valve behind the furnace was closed to prevent *p*X radicals from entering the deposition chamber and sublimation zone was heated to the respective temperature. After reaching the sublimation temperature, both, *p*X and comonomer valve were opened simultaneously. Polymerization was ended after about 2-5 h (depending on the amount of precursor and sublimation/vaporization temperatures). Copolymers with PPX-N, PPX-me or PPX-et were removed from the chamber with distilled water. Copolymers with PPX-pr or PPX-bu were dissolved in chloroform or peeled from the chamber.

5.4.4 Preparation of Electrospinning solutions and Electrospinning

Polymer solutions of different concentrations were prepared by weight % (wt%), if CTAB was added its concentration in wt% refers to the weight of the total polymer solution. Solutions were stirred over night in appropriate vessels prior to electrospinning. If a solvent mixture was used the ratio of the solvents is also given in wt%, considering only the weight of the solvents.

The polymer solution was placed in a 1 ml plastic syringe with a needle of 0.9 mm diameter and 25 mm length. In the homemade electrospinning setup aluminum sheets were connected to the ground collector. Samples for contact angle measurements and high speed camera images were spun onto a standard glass slide placed on the aluminum sheet. A syringe pump was used to control the injection rate of the polymer solution of 0.15 to 0.41 $ml \cdot h^{-1}$. The needle was connected to a high voltage source and voltages between 10-30 kV were applied. Electrospinning was performed at room temperature (20-26 °C). If not mentioned otherwise the tip to collector distance was 17 cm.

5.4.5 PPX Coating in SCS Labcoater

If not mentioned otherwise, the PPX coating of glass slide, EPS samples for stress-strain measurements and templates for PPX-N foam generation was performed in SCS Labcoater. Samples were placed in the deposition chamber, in case of EPS the samples were pinned on steel needles (to minimize the contact with any surface and facilitate homogeneous coating, see Figure 120). The coatings were performed as described in the Labcoater manual. The base pressures of about 50-70 mbar and process pressures of about 80-90 mbar. Precursor sublimation temperatures were 150 °C at the beginning of the coating process (for all types of precursor) and elevated up to 180 °C at the end of the coating process to ensure complete precursor sublimation. If EPS samples were coated, the Labcoater was not vented with the designated valve to avoid rapid pressure changes in the deposition chamber. Ventilation was performed "passively", letting the Labcoater first stand overnight and later opening the valve gradually. For thickness determination of the coatings via Dektak, at least on glass slide was put into the deposition chamber together with the samples.

The deposition of the reactive PPX (4.4.3.2) was performed in the homemade pyrolysis reactor.

Figure 120 EPS sample preparation for PPX coating, specimens were pinned on steel needles. Samples shown in this photograph were for stress-strain tests.

To prevent delamination of the PPX from glass slides, they were treated with adhesion promoter (A-174 silane) if needed (see Section 4.2.2). For a typical treatment, 400 ml solution of isopropanol/water (1:1) and 2 ml adhesion promoter was stirred at room temperature for 14-16 h. The clean glass slides were immersed in this solution for 30 minutes, air dried for 30 minutes, rinsed with isopropanol and finally dried at 80 °C at 100 mbar for 1 hour.

5.4.6 P(PX-N-*co*-HEMA) Copolymerization in SCS Labcoater

The SCS Labcaoter with modified with comonomer inlet was used. For copolymerizations 5 g [2.2]paracyclophane precursor and 5-8 ml HEMA monomer were used. After preheating of the pyrolysis furnace, evacuation to base pressure and preheating the HEMA comonomer to the respective temperature, the precursor sublimation furnace was heated set to 150 °C. When the oven reached 90 °C, the HEMA valve was opened. The synthesis was terminated before HEMA was evaporated completely form the comonomer vessel (in general 5-8 h), to ensure the availability of both monomer during the synthesis. After cooling down the excess precursor was removed from the sublimation furnace.

5.4.7 SOLID Porcess

For PPX surface functionalization via the SOLID process, standard glass slides were placed in the deposition chamber and covered completely or partially with OEGMA-Br or mixtures of OEGMA-Br and diethyl ether. The coating process was carried out as usual, that is pyrolysis furnace was heated to 650 °C and the reactor evacuated to base pressure, than the precursor sublimation furnace was heated to 150-180°C for complete precursor sublimation. After the coating was finished, the reactor was flooded with ambient air.

After the coating, the P(PX-*surf*-OEMGA-Br) films were immersed in water for delamination, and removed from the glass slides. The film were extracted with THF by Soxhlet extraction for minimum 48 h to ensure complete removal of unreacted OEGMA-Br form the films.

5.5 Synthesis and Electrospinning

5.5.1 Synthesis of 4,12-Dialkyl[2.2]paracyclophanes

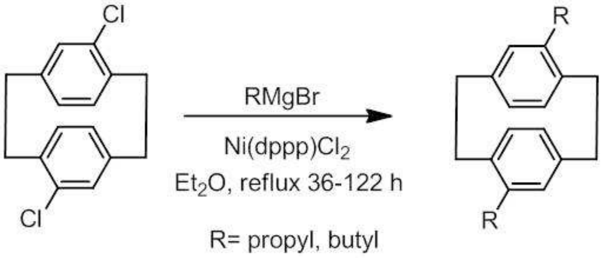

Figure 121 Synthesis of 4,12-dialkyl[2.2]paracyclophane.

The synthesis was carried out as described by BIER *et al.*[16] Reaction times varied with amount of starting material and catalyst quality. The conversion was monitored by GC measurements and stopped after full conversion was achieved. The product was recrystallized from ethanol (DPX-propyl) or methanol (DPX-butyl) until purity ≥99% (controlled by GC-MS).

5.5.2 Insoluble P(PX-*co*-HEMA) in Homemade Reactor

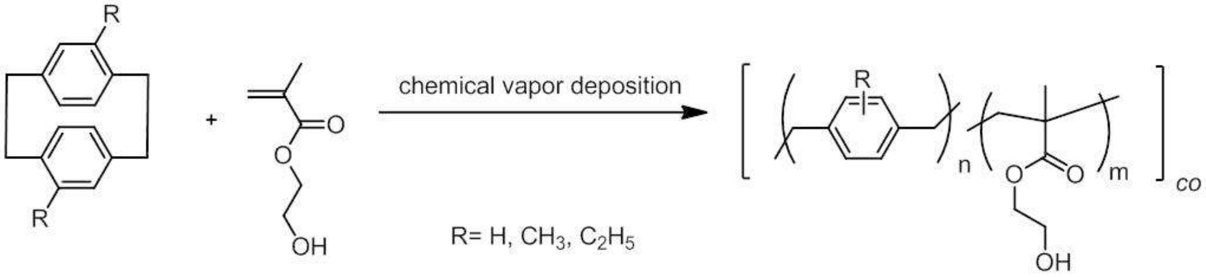

Figure 122 Synthesis of P(PX-N-*co*-HEMA), P(PX-methyl-*co*-HEMA) and P(PX-ethyl-*co*-HEMA) via CVD.

The synthesis was carried out as described in 5.4.3, for pyrolysis temperatures see Table 14, detailed screening parameter see Table 15.

Table 15 Parameter screening for P(PX-N-*co*-HEMA) synthesis, deposition parallel to monomer flow.

Run	DPX		T_{sub} DPX /°C	T_{vap} HEMA/°C	T_{dep}/°C
1	DPX-N	IEP20100323-1	120	70	20
2	DPX-N	IEP20100327-1	120	45	20
3	DPX-N	IEP20100328-1	120	55	20
4	DPX-N	IEP20100414-1	125	50	20
5	DPX-N	IEP20100415-1	125	50	20
6	DPX-N	IEP20120316-1	120	40	0
7	DPX-N	IEP20120319-1	120	20	0
8	DPX-N	IEP20120319-1	120	40	0
9	DPX-N	IEP20131011-1	105	35	20
10	DPX-N	IEP20131011-2	105	35	20
11	DPX-metyl	IEP20120509-1	90	30	5
12	DPX-ethyl	IEP20120429-1	110	30	5

Elemental analysis:

Table 16 Results of C,H,N-elemental analysis for different P(PX-*co*-HEMA) copolymers.

Run	comment	1st Analysis		2nd Analysis		average HEMA content/mol%[a]
		C/%	H/%	C/%	H/%	
3	sample 1	67.04	6.95	66.24	7.36	67
3	sample 2	66.81	7.06	66.97	7.18	66
4	-	67.33	6.81	66.57	7.09	66
5	-	66.92	7.78	67.93	7.70	63
6	sample from chamber beginning	71.26	7.73	71.38	7.22	52
6	sample from chamber end	73.41	7.66	73.47	7.71	46
7	-	79.97	7.74	80.19	7.79	29
8	-	66.64	7.78	65.44	7.73	66
11		68.10	8.04	69.86	8.03	60
12		73.41	7.66	73.47	7.71	50

[a] HEMA content calculated from oxygen content (100%-%C-%H=%O)

5.5.3 P(PX-pr-*co*-HEMA) in Homemade Reactor

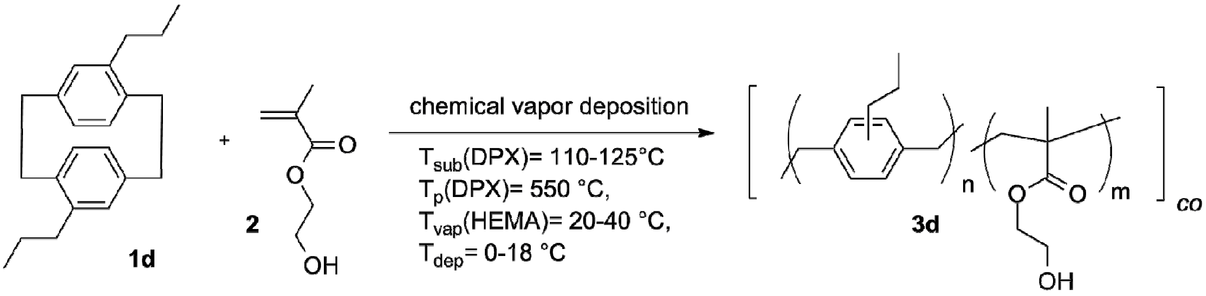

The synthesis was carried out as described in 5.4.3, detailed screening parameter see

Table 17 Details for P(PX-propyl-*co*-HEMA).

Run		T_{sub} DPX-N/ °C	T_{vap} HEMA/ °C	T_{dep}/ °C	Chamber	HEMA content[a]/mol%
1	IEP20110417-1	120	40	18	B	36.9*
2	IEP20110419-1	120	30	18	B	27.8*
3	IEP20110420-1	120	20 (RT)	18	B	2.5
4	IEP20110421-1	120	30	0	B	21.6
5	IEP20131023-1	120	20	0	B	0.8

5.5.4 P(PX-bu-*co*-HEMA) in Homemade Reactor

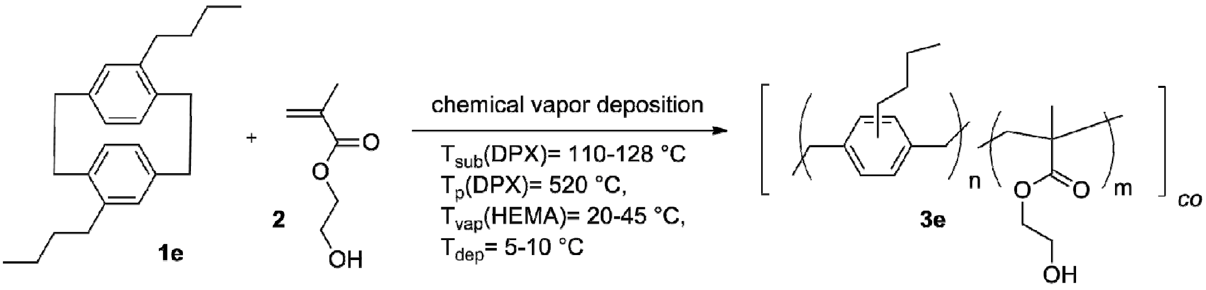

Figure 123 Synthesis of P(PX-bu-*co*-HEMA) via CVD.

The synthesis was carried out as described in 5.4.3, detailed screening parameter see Table 18.

Table 18 Parameter screening and resulting overall HEMA content for P(PX-*n*-butyl-*co*-HEMA).

Run		T_{sub} DPX-N/ °C	T_{vap} HEMA/ °C	T_{dep}/ °C	Chamber	HEMA content[a]/mol%
1	IEP20100928-1	128	30	5	B	6
2	IEP20100930-1	128	40	5	B	7
3	IEP20120428-1	120	30	5	A	8
4	IEP20101001-1	113	30	5	B	13
5	IEP20120502-2	120	45	5	A	13
6	IEP20120502-1	120	45	10	A	15
7	IEP20101005-1	110	40	5	B	24
8	IEP20100804-1	125	45	10	A	27
9	IEP20131003-1	120	40	10	A	29

[a] determined by ^{1}H-NMR, signal ration of -CH_2-CH$_2$-OH of HEMA (4.2 ppm) and -CH_3 (0.9 ppm)of the butyl substituent on PX

5.5.5 P(PX-N-*co*-HEMA) in Labcoater

Table 19 Assignment of P(PX-N-*co*-HEMA) samples prepared in SCS Labcoater.

Run	Labjournal No.	Run	Labjournal No.
1	IEP20121212-1	**7**	IEP20130326-2
2	IEP20130318-2	**8**	IEP20130402-1
3	IEP20130322-2	**9**	IEP20121217-2
4	IEP20120716-1	**10**	IEP20130212-2
5	IEP20130109-1	**11***	IEP20130131-1
6	IEP20130307-2		

* sample is not transparent but opaque

5.5.6 Cytotoxicity Tests

The cytotoxicity of PPX-N and P(PX-N-*ran*-HEMA) was determined by the MTT assay. Therefore microwell plates (NunclonTM, Nunc, Germany) were coated with the respective polymers (both prepared in SCS-Labcoater) and tempered 3 h at 50°C and 100 mbar. Tests were performed by Hui Wang (AK Prof. Agarwal).

After sterilization under UV-light for 1 h, L929 cells (mouse fibroblasts) were seeded into 96 well plates for each polymer and 48 well plates as blank control samples, at a density of $0.8 \cdot 10^4$ cells per well. After an incubation period of 24 h at 37.8 °C, 200 ml DMEM without serum and 20 ml MTT [2-(4,5-dimethylthazol-2-yl)-2,5-diphenyl tetrazolium; Sigma, Deisenhofen, Germany; 2 mg·ml^{-1} in PBS] were added. After incubation unreacted dye was removed by aspiration and formazan crystals were dissolved in 200 µl DMSO per microwell. Measurements were performed using an ELISA reader (Titerek Plus MS212, ICN, Eschwege, Germany) at wavelength of 580 and 690 nm. Results are given in Table 20. These results have to be taken with care, because the method applied is usually used for indirect contact tests, where the cells are in contact with polymer solution.

Table 20 Results of MTT tests.

Sample	**Polymer**	**Absorbance**
20120425-1b	PPX-N	1.68 ± 0.15
20120425-2a	P(PX-N-*ran*-HEMA)	1.83 ± 0.53
blank control	Polystyrene (microwell plate)	1.88 ± 0.19

5.5.7 PPX-butyl and PPX-propyl Homopolymers for Oligomer Analysis

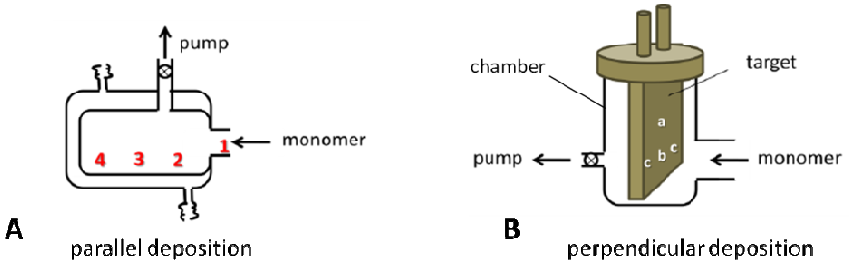

Figure 124 Schematic illustration of the deposition chambers for deposition parallel and perpendicular to the monomer flow with indicated positions (see following TGA data).

Table 21 Thermogravimetric degradation results of the first degradation step of PPX-butyl deposited perpendicular to monomer flow. Conditions: T_{py} 520 °C (length 60 cm), T_{vap}= 120°C (excpet run 6).

Run			T_{dep} /°C	Mass loss TGA 1^{st}/%	T (mass loss) TGA 1^{st}/ °C
1	target	IEP20110527-2	0	4	291
	chamber		RT=23	10	299
2	target	BP0606	0	35	319
3	target	IEP20110901-1	0	18	294
	chamber		RT=19	28	311
4	target	IEP20110902-1	20	37	267
5	target	IEP20110905-1	-10	17	275
6	target	IEP20110927-3	0	28	263

* T_{vap}= 110 °C

Table 22 Thermogravimetric degradation results of the first degradation step of PPX-butyl deposited parallel (runs 7-9) or perpendicular (run 10) to monomer flow. Conditions: T_{py} 520 °C, T_{transp}=300 °C, T_{vap}= 120°C.

Run			T_{dep} /°C	Mass loss TGA 1^{st}/%	T (mass loss) TGA 1^{st}/ °C
7*	pos. 1	IEP20111013-1	0	18	260
	pos. 3			6	278
8*	pos. 1	IEP20111020-2	0	17	261
	pos. 2			8	252
	pos. 3			4	252
9*	pos. 1	IEP20111026-1	0	17	252
	pos. 2			2	237
$10^{\#}$	pos. a	IEP20111028-2	0	20	219
	pos. b			18	231
	pos. c			17	241

* deposited parallel to monomer flow # deposited perpendicular to monomer flow

Table 23 Thermogravimetric degradation results of the first degradation step of PPX-propyl deposited parallel (run 11,13) or perpendicular (run 12) to monomer flow. Conditions: T_{py} 550 °C, T_{transp}=300 °C, T_{vap}= 120°C.

Run			**T_{dep} /°C**	**Mass loss TGA 1st/%**	**T (mass loss) TGA 1st/ °C**
11*	pos. 1	IEP20111201-4	0	16	251
	pos. 3			0	-
	pos. 4			0	-
12#	pos. a	IEP20111202-1	0	6	228
	pos. b			17	239
	pos. c			21	247
13*	pos. 1	IEP20111215-1	0	16	251
	pos. 2			6	248
	pos. 3			2	250
14	pos. 1	IEP20120105-1	0	11	249
	pos. 2			5	250
	pos. 3			1	251
	pos. 4			0	-

* deposited parallel to monomer flow # deposited perpendicular to monomer flow

Table 24 Analysis of samples extracted with ethanol.

	Mass loss first step / %	**THF-GPC (RI detector)**		
		Mn/ Da	**Mw/ Da**	**PDI**
PPX-butyl BP0306-1				
before extraction	10	39,000	95,300	2.45
insoluble in EtOH	0	48,200	105,400	2.19
soluble in EtOH	75			
PPX-propyl BP0305-1				
before extraction	10	55,700	187,000	3.36
insoluble in EtOH	-	72,500	313,000	4.32
soluble in EtOH	70			

5.5.8 Alkyl-PPX Peroxide Synthesis in Homemade Reactor

PPX-butyl peroxide synthesis was carried out as described in Section 5.4.2.

Table 25 Relation of process pressure and peroxide content for P(PX-butyl-peroxide)

Run		$p_{process}$/ mbar	O_2/%
1	IEP20130201-1	0.2	0
2	IEP20130203-1	1.0	3
3	IEP20130205-1	3.7	20
4	IEP20130227-1	3.0	20
5	IEP20130403-2	2.9	17
6	IEP20130509-1	2.0	8
7	IEP20130604-1	3.0	14

5.5.9 Surface Modification by *grafting to* - FRP

Free standing PPX films or PPX films on glass slides (treated with adhesion promoter) were prepared as described in 5.4.5. For functionalization via chain transfer the films were placed in 10 ml Schlenk tubes under argon atmosphere. The free radical polymerization solutions (FRP) were prepared as described below and added to the films in the Schlenk tubes.

5.5.9.1 FRP of Methyl methacrylate

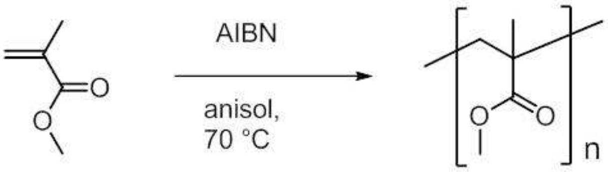

Figure 125 Free radical polymerization of MMA in anisol.

Table 26 Free radical polymerization of MMA in anisol

	M / g·mol^{-1}	ρ / g·ml^{-1}	n/ mmol	V/ ml	m/ mg	eq
methyl methacrylate	100.1	0.94	84	9	-	466
AIBN	164.2	-	0.18	-	30.6	1
anisole				15		

Under inert conditions the reaction mixture of 9 ml (84 mmol, 466 eq) methyl methacrylate, 5 ml anisole and 30.6 mg (0.18 mmol, 1 eq) AIBN was filled into a 50 ml Schlenk flask and degassed three times by a freeze-thaw-cycle. Afterwards the reaction mixture as distributed to Schlenk tubes equpiped with PPX-N films and placed in a preheated oils bath at 70 °C. Reaction mixtures were not stirred to prevent damage to the PPX films. After the reaction the film was removed from the mixture, rinsed with THF and extracted with chloroform or THF.

5.5.9.2 FRP of *N*-isoproypl acrylamide

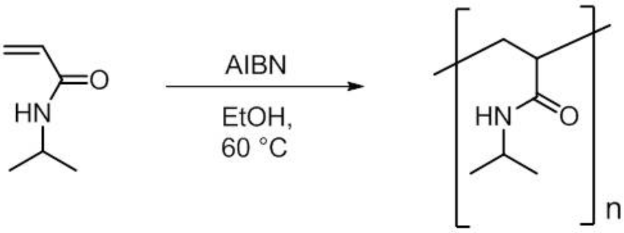

Figure 126 Free radical polymerization of *N*-isopropyl acrylamide.

Table 27 Free radical polymerization of *N*-isopropyl acrylamide.

	M / g·mol^{-1}	ρ / g·ml^{-1}	n/ mmol	V/ ml	m/ g	eq
***N*-isoproyl acrylamide**	113.2	-	20	-	2.25	333
AIBN	164.2	-	0.06	-	0.01	1
EtOH				15		

Under inert conditions the reaction mixture of 2.25 g (20 mmol, 333 eq) *N*-isopropyl acrylamide, 15 ml ethanol and 10 mg (0.06 mmol, 1 eq) AIBN was filled into a 50 ml Schlenk flask and degassed three times by a freeze-thaw-cycle. Afterwards the reaction mixture as distributed to Schlenk tubes equpiped with PPX-N films and placed in a preheated oils bath at 60 °C. Reaction mixtures were not stirred to prevent damage to the PPX films. After the reaction the film was removed from the mixture, rinsed with water and extracted with chloroform or water.

5.5.10 Synthesis of OEGMA-Br

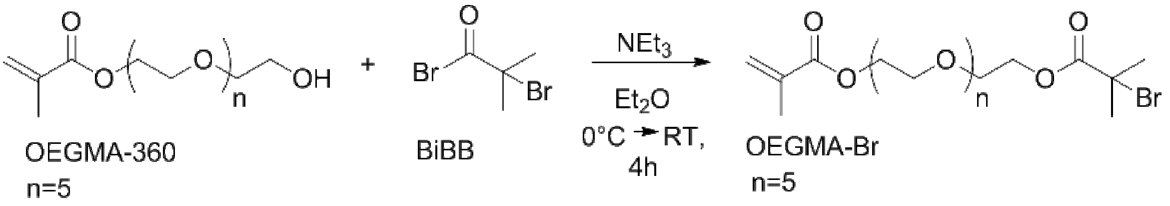

Figure 127 Synthesis of 2-bromoisobutyryloxy oligo(ethylene glycol) methacrylate (OEGMA-Br).

Table 28 Synthesis of 2-bromoisobutyryloxy oligo(ethylene glycol) methacrylate (OEGMA-Br).

	M / g·mol^{-1}	ρ / g·ml^{-1}	n/ mmol	V/ ml	eq
2-bromoisobutyryl bromide (BiBB)	229.9	1.86	56.0	6.92	2.00
OEGMA-360	360.0	1.11	28.0	9.05	1.00
triethylamine	101.2	0.73	56.0	7.81	2.00
diethyl ether (anhydrous)	74.12				200

Under inert conditions 9.05 ml (28 mmol, 1.oo eq) oligo(ethylene glycol) methacrylate (OEGMA) and 7.81 ml (56 mmol, 2.00 eq) triethylamine were dissolved in 200 ml diethyl ether and chilled to 0 °C in an ice bath and constantly agitated. 6.92 ml (56 mmol, 2.00 eq) BiBB was added dropwise, after complete addition the reaction was stirred for 4 h at room temperature. The reaction mixture was filtrated, the filtrate was washed 3 times with 100 ml distilled water each. The solvent was evaporated under reduced pressure and the residue dissolved in dichloromethane. After the addition of basic aluminum oxide the mixture was filtrated, the solvent was evaporated under reduced pressure. The reaction product was a slightly yellow liquid.

Yield: 8.63 g (67 %)

^{1}H-NMR: 300 MHz, $CDCl_3$: δ/ppm= 6.13 (m, 1H, H-3a), 5,57 (m, 1H, H3b), 4.42-4.31 (m, 4H, H-5, H-10), 3.74 (m, 4H, H-6, H-9), 3.65 (m, 12H, H-7, H-8), 1.94 (m, 9H, H-1, H-12). (for NMR resonance assignation see Figure 63)

IR: ν/cm^{-1}= 590 (w), 648 (w), 734 (w), 814 (m), 868 (m), 943 (m), 1037 (m), 1103 (s), 1161 (s), 1273 (s), 1371 (m), 1455 (m), 1637 (m), 1720 (s), 2871 (m), 2951 (w).

5.5.11 Surface Modification by SOLID and ATRP

The surface modified films P(PX-N-*surf*-OEGMA-Br) were prepared as describe in Section 5.4.7. After the removal of unreacted OEMGA-Br was confirmed by ATR-IR the films were placed under argon atmosphere in 10 ml Schlenk tubes.

5.5.11.1 ATRP of Methyl methacrylate

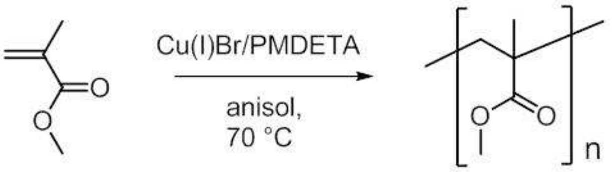

Figure 128 ATRP of methyl methacrylate.

Table 29 ATRP of methyl methacrylate.

	M / g·mol^{-1}	ρ / g·ml^{-1}	n/ mmol	V/ ml	m/ mg
methyl methacrylate	100.1	0.94	98	10.5	-
PMDETA	173.3	0.83	0.047	0.099	-
Cu(I)Br	143.5	-	0.47	-	67.8
anisole				11	

Under inert conditions the reaction mixture of 10.5 ml (98 mmol) *N*-isopropyl acrylamide, 11 ml anisol, 67.8 mg Cu(I)Br (0.47 mmol) and 99 µl (0.47 mmol) PMDETA was filled into a 50 ml Schlenk flask and degassed three times by a freeze-thaw-cycle. Afterwards the reaction mixture as distributed to Schlenk tubes equipiped with P(PX-N-*surf*-OEGMA-Br) films nd placed in a preheated oils bath at 70 °C. Reaction mixtures were not stirred to prevent damage to the PPX films. After the reaction the film was removed from the mixture, rinsed with THF and extracted with chloroform or THF.

5.5.11.2 ATRP of *N*-isoproypl acrylamide

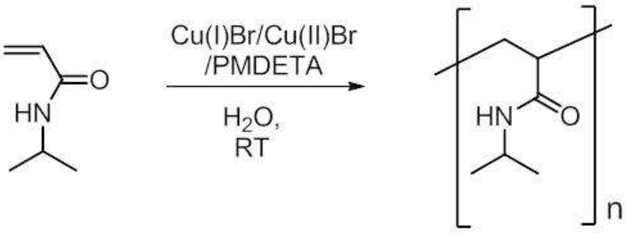

Figure 129 ATRP of *N*-isopropyl acrylamide.

Table 30 ATRP of *N*-isopropyl acrylamide.

	M / g·mol^{-1}	ρ / g·ml^{-1}	n/ mmol	V/ ml	m/ g
***N*-isopropyl acrylamide**	113.2	-	23	-	2.62
PMDETA	173.3	0.83	0.037	0.0782	-
Cu(I)Br	143.5	-	0.18	-	0.026
Cu(II)Br	223.4	-	0.076	-	0.017
H_2O				30	

The reaction mixture of 2.62 g (23 mmol) *N*-isopropyl acrylamide, 30 ml H_2O, 26 mg Cu(I)Br (0.18 mmol), 17 mg Cu(II)Br (0.076 mmol) and 78.2 µl (0.037 mmol) PMDETA was filled into a 50 ml Schlenk flask. To remove oxygen, argon was passed through the solution for 30 min. Afterwards the reaction mixture as distributed to Schlenk tubes equpiped with P(PX-N-*surf*-OEGMA-Br) films, the reaction took place at room temperature. Reaction mixtures were not stirred to prevent damage to the PPX films. After the reaction the film was removed from the mixture, rinsed with water and extracted with chloroform or water.

5.5.11.3 ATRP of Glycidyl methacrylate

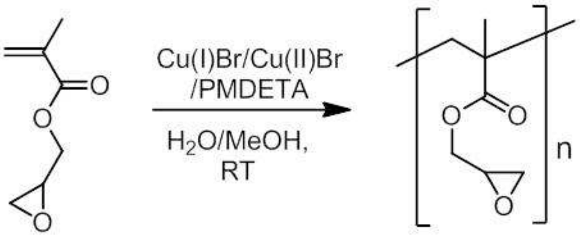

Figure 130 ATRP of glycidyl methacrylate.

Table 31 ATRP of glycidyl methacrylate.

	M / g·mol^{-1}	ρ / g·ml^{-1}	n/ mmol	V/ ml	m/ mg
glycidyl methacrylate	142.2	1.04	36.5	5	-
PMDETA	173.3	0.83	0.32	0.0687	-
Cu(I)Br	143.5	-	32.7	-	4.7
Cu(II)Br	223.4	-	0.003	-	0.7
H_2O				1.6	
methanol				8.4	

The reaction mixture of 5 ml g (36.5 mmol) glycidyl methacrylate, 1.6 ml H_2O, 8.4 ml methanol, 4.7 mg Cu(I)Br (32.7 mmol), 0.7 mg Cu(II)Br (0.076 mmol) and 68.7 µl (0.32 mmol) PMDETA was filled into a 50 ml Schlenk flask. To remove oxygen, argon was passed through the solution for 30 min. Afterwards the reaction mixture as distributed to Schlenk tubes equpiped with P(PX-N-*surf*-OEGMA-Br) films, the reaction took place at room temperature. Reaction mixtures were not stirred to prevent damage to the PPX films. After the reaction the film was removed from the mixture, rinsed and extracted with methanol.

5.5.12 Electrospinning of Porous Fibers

Electrospinning was carried out as described in Section 5.4.4. Specifically, 3wt% chloroform solutions were spun with 0.15-0.21 ml·h^{-1} and voltages of 15 kV at the needle and 0.5 kV at the counter electrode (exception: PPX-heptyl with 17 kV and 5 kV, at RH>50% with 0.41 ml h^{-1}), 2.5wt% THF solutions were spun with 0.15-0.25 ml·h^{-1}. and voltages of 15kV and 0.5 kV (exception: PPX-butyl at RH 75% with 17 kV at the needle and 2 kV at counter electrode). The needle to collector distance was kept at 17 cm. Due to the relatively high volatility of the solvents (chloroform, THF), the droplet on the needle rapidly formed a skin, which led to clogging of the needle. To enable continuous spinning an automatical remover was used to renew the droplet frequently. Humidity was controlled by introducing water vapor into the spinning chamber. For further details see the following tables.

Table 32 Details for PPX-propyl spun from 3 wt% chloroform, SEM images see Figure 71, diameter histograme see Figure 74 in Section 4.3.2.

	25% RH	**45% RH**	**65% RH**	**83% RH**
Sample name	SM010e	PH_19	IEP20130726-2-2	IEP20130726-2-1
Polymer from sample	SM0506	PH_07	IEP20130419-1	IEP20130419-1
Voltage needle/ kV	15	15	15	15
Voltage collector/ kV	2	0.5	1	1
Speed/ ml·h^{-1}	-0.10	-0.15	-0.21	-0.21
Fiber diameter/ nm	230 ± 110	363 ± 212	413 ± 231	398 ± 249

Table 33 Details for PPX-butyl spun from 3 wt% chloroform, SEM images see Figure 71, diameter histograme see Figure 74 in Section 4.3.2.

	20% RH	**38% RH**	**68% RH**	**86% RH**
Sample name	PH_23	PH_21	PH_30	PH_29
Polymer from sample	PH_11	PH_11	PH_11	PH_11
Voltage needle/ kV	15	15	15	15
Voltage collector/ kV	0.5	0.5	0.5	0.5
Speed/ ml·h^{-1}	-0.15	-0.15	-0.15	-0.15
Fiber diameter/ nm	380 ± 242	398 ± 238	492 ± 217	1040 ± 636

Table 34 Details for PPX-heptyl spun from 3 wt% chloroform, SEM images see Figure 71, diameter histograme see Figure 74 in Section 4.3.2.

	18% RH	**35% RH**	**62% RH**	**87% RH**
Sample name	IEP20130629-6	IEP20130629-5	IEP20130629-8	IEP20130629-7
Polymer sample	IEP20130618-1	IEP20130618-1	IEP20130618-1	IEP20130618-1
Voltage needle/ kV	17	17	17	17
Voltage collector/ kV	5	5	5	6
Speed/ ml·h^{-1}	-0.15	-0.15	-0.41	-0.41
Fiber diameter/ nm	488 ± 029	599 ± 348	591 ± 300	899 ± 550

Table 35 Details for PPX-propyl spun from 2.5 wt% THF, SEM images see Figure 75 and Figure 76.

	25% RH	**50% RH**	**78% RH**
Sample name	SM016a	IEP20130723-1-1	IEP20130723-1-2
Polymer sample	SM0506	IEP20130419-1	IEP20130419-1
Voltage needle/ kV	15	15	15
Voltage collector/ kV	-3	-0.5	-0.5
Speed/ ml·h^{-1}	0.26	0.15	0.15

Table 36 Details for PPX-butyl spun from 2.5 wt% THF, SEM images see Figure 75 and Figure 76.

	25% RH	**50% RH**	**78% RH**
Sample name	IEP20130723-3-1	PH_33	IEP20130725-3-2
Polymer sample	IEP20130709-1	PH_11	IEP20130709-1
Voltage needle/ kV	15	15	17
Voltage collector/ kV	-0.5	-0.5	-2
Speed/ ml·h^{-1}	0.15	0.15	0.15

Table 37 Details for PPX-heptyl spun from 2.5 wt% THF, SEM images see Figure 75 and Figure 76.

	2-5% RH	**50% RH**	**78% RH**
Sample name	IEP201300708-11	IEP20130723-5-1	IEP20130725-5-2
Polymer sample	IEP20130618-1	IEP20130618-1	IEP20130618-1
Voltage needle/ kV	15	15	15
Voltage collector/ kV	-0.5	-0.5	0.5
Speed/ ml·h^{-1}	0.25	0.15	0.15

Table 38 Water contact angles for fibermats spun from 3wt% solution in chloroform and 2.5 wt% solutions in THF.

Polymer	Spun from chloroform solution			Spun from THF soltuion		
		RH/ %	Contact Angle/ °		RH/ %	Contact Angle/ °
PPX-pr	SM	film	101 ± 1	SM	film	101 ± 1
	SM010e	25	138 ± 8	SM016	25	132 ± 3
	PH_20	45	144 ± 6	IEP20130723-1-1	50	140 ± 3
	IEP20130726-2-1	83	136 ± 6	IEP20130723-1-2	78	143 ± 5
PPX-bu	PH	film	101 ± 7	PH	film	101 ± 7
	PH_32	20	130 ± 6	IEP20130723-3-1	25	145 ± 7
	PH_22	50	140 ± 6	PH_33	54	150 ± 5
	PH_31	88	142 ± 8	IEP20130725-3-2	79	153 ± 8
PPX-he	IEP20130630-3	film	103 ± 1	IEP20130630-3	film	103 ± 1
	IEP20130629-6	18	143 ± 4	IEP20130726-5-3	20	147 ± 3
	IEP20130723-6-1	37	152 ± 3	IEP20130723-5-1	55	151 ± 4
	IEP20130629-8	62	147 ± 3	IEP20130723-5-2	76	157 ± 3
	IEP20130723-6-2	80	155 ± 5			

5.5.13 Electrospinning from Solvent Mixtures

Electrospinning was carried out as described in Section 5.4.4. A solution of PPX-propyl with 5 wt% polymer in DMF/$CHCl_3$ (wt ratio 1:10) was spun at 15 kV at the needle and -2 kV at the counter electrode, with an injection speed of 0.10-0.15 ml·h^{-1}, tip to collector distance was 20 cm, relative humidity was not determined. Sample name IEP20120611-2A.

5.5.14 Electrospinning of Blend Fibers

Electrospinning was carried out as described in Section 5.4.4., for details see Table 39.

Table 39 Details of PPX-pr/PEO blend solutions and electrospinning parameter.

Blend		M_n PEO/ 10^3 Da	PPX:PEO ratio	Polymer con. / wt%	Relative Humidity/ %	E-spin Voltage*/ kV	Injection rate/ ml·h^{-1}
PPX-propyl /PEO$_{900k}$	SM005	900	3:1	4	20	10, -0.5	0.05
PPX-propyl /PEO$_{300k}$	PH_08_2	300	2:1	3	46	15, -0.5	0.15
PPX-propyl /PEO$_{35k}$#	PH_09	35	2:1	3	39	10, -0.5	0.15
PPX-propyl /PEO$_{10k}$	PH_10_3	10	2:1	3	32	10, -0.5	0.15

* voltage needle, voltage counter electrode # spun at 10 cm tip to collector distance

5.5.15 Preparation of PPX-propyl Blends

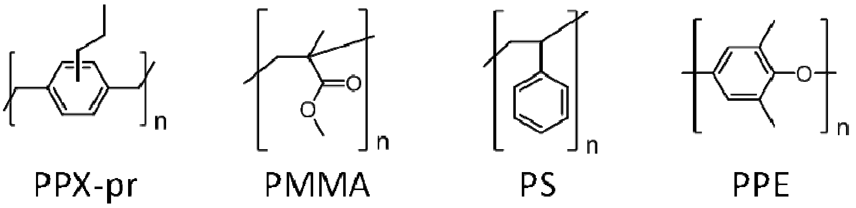

Figure 131 Structural formula of the polymers used for blend preparation: PPX-propyl, PMMA, PS and PPE.

PPX-propyl polymer blends were prepared by dissolving 0.5 g of 1:3, 1:1 and 3:1 wt% ratios with PMMA, PS and PPE in 25 ml chloroform respectively. The polymer solutions were solvent cast into glass petri dishes and the solvent was evaporated for 1 d at room temperature (at ambient pressure) and 2d at 60 °C (at 100 mbar).

Table 40 Glass transition temperatures T_g for PPX-pr, PMMA, PS and PPE homopolymers and blends.

	Blend ratio	T_g/ °C 2nd heating		
PPX-propyl	homopolymer	3		
PMMA	homopolymer	112		
PS	homopolymer	88		
PPO	homopolymer	214		
PPX-pr/PMMA	1:1	1	113	JS0605-1
	3:1	3	113	JS0605-2
PPX-pr/PS	1:3	-2	97	JS0604-2
	1:1	-3	100	JS0604-1
	3:1	-1	98	JS0604-3
PPX-pr/PPO	1:3	4	210	JS0618-3
	1:1	2	211	JS0618-1
	3:1	3	211	JS0618-2

5.5.16 PPX-N Coating of EPS Specimen

For determination of PPX-N penetration depth in EPS specimen, cuboids of EPS-2 and EPS-3 (see Table 11)were placed into the deposition chamber as described in Section 5.4.5. were coated with 3.5 DPX-N. After the PPX-N coating the cuboids were extracted with THF at room temperature.

Table 41 Assignment of EPS specimen coated with PPX-N for penetration depth analysis.

Specimen	Labjournal No.	Specimen	Labjornal No.
3-1	IEP20130510-2-A	**2-1**	IEP20130510-2-D
3-2	IEP20130510-2-H	**2-2**	IEP20130510-2-E
3-3	IEP20130510-2-G2	**2-3**	IEP20130510-2-C
3-4	IEP20130510-2-B	**2-4**	IEP20130510-2-F2
3-5	IEP20130510-2-G1	**2-5**	IEP20130510-2-F1

For all stress-strain specimen expanded polystyrene foam EPS-1 (see Table 11) were used. PPX coatings were carried out in SCS Labcoater as described in Section 5.4.5.

Table 42 Details of PPX coated EPS specimens for stress-strain measurements.

Run		Precursor amount/ g	Weight EPS specimen before coating/ mg	PPX coating per mg sample/ mg
N1	IEP20130204-1	1.5	14.95 ± 0.86	0.23 ± 0.02
N2	IEP20130322-1	2.2	14.21 ± 0.58	0.66 ± 0.04
N4	IEP20130125-2	3.0	14.94 ± 0.33	0.63 ± 0.05
N5	IEP20130307-1	4.0	15.22 ± 0.39	0.75 ± 0.07
N6	IEP20130208-1	5.0	14.91 ± 0.41	1.07 ± 0.07
C1	IEP20130403-1	2.0	15.02 ± 0.29	0.53 ± 0.02
C2	IEP20130404-1	4.0	15.22 ± 0.39	0.95 ± 0.04
C3	IEP20130405-1	6.0	14.80 ± 0.39	1.43 ± 0.08
P1	IEP20130512-1	2.0	15.30 ± 0.23	0.15 ± 0.01
P2	IEP20130718-1	3.0	15.32 ± 0.32	0.25 ± 0.04
P3	IEP20130518-1	4.0	15.31 ± 0.37	0.18 ± 0.01
P4	IEP20130520-1	6.0	15.07 ± 0.35	0.21 ± 0.01
PPX-N*	IEP20130301-1	3.0	14.89 ± 0.33	0.54 ± 0.03
PPX-C*	IEP20130419-1	2.0	15.11 ± 0.31	0.25 ± 0.01

* EPS was dissolved before stress-strain testing, remaining PPX foams tested in stress-strain analysis.

Table 43 Detailed results of stress-strain measurements.

Run	Amount of PPX coating per mg sample/ mg	E_{mod}/ MPa	F_{max}/ N	dL at F_{max}/ %	dL at break/ %
N1	0.23 ± 0.02	5.25 ± 1.2	2.71 ± 0.31	11.0 ± 2.4	15.4 ± 3.3
N2	0.66 ± 0.04	5.16 ± 0.8	3.71 ± 0.49	11.2 ± 1.1	15.9 ± 2.5
N3	0.63 ± 0.05	9.67± 2.0	4.18 ± 0.27	10.1 ± 1.3	12.9 ± 2.4
N4	0.75 ± 0.07	6.91 ± 1.1	4.36 ± 0.34	10.9 ± 1.2	16.7 ± 3.6
N5	1.07 ± 0.07	10.3 ± 1.3	4.90 ± 0.31	8.2 ± 0.8	22.3 ± 7.9
C1	0.53 ± 0.02	5.17 ± 0.8	4.09 ± 0.28	13.7 ± 1.7	17.4 ± 3.5
C2	0.95 ± 0.04	10.6 ± 1.5	5.33 ± 0.41	11.0 ± 1.8	14.9 ± 4.6
C3	1.43 ± 0.08	13.8 ± 1.5	6.42 ± 0.47	10.9 ± 1.4	18.3 ± 6.3
P1	0.15 ± 0.01	3.73 ± 0.5	2.54 ± 0.33	10.7 ± 2.2	14.3 ± 2.8
P2	0.25 ± 0.04	4.49 ± 0.4	2.69 ± 0.30	12.8 ± 2.1	17.1 ± 4.2
P3	0.18 ± 0.01	3.78 ± 0.8	2.76 ± 0.18	15.6 ± 1.5	19.0 ± 3.2
P4	0.21 ± 0.01	3.67 ± 0.5	2.80 ± 0.30	15.0 ± 1.9	17.6 ± 2.5
EPS-1#	0	3.24 ± 0.6	2.22 ± 0.22	11.1 ± 1.7	14.4 ± 4.5
PPX-N*	0.54 ± 0.03	0.63 ± 0.2	0.35 ± 0.06	7.2 ± 1.6	12.0 ± 4.3
PPX-C*	0.25 ± 0.01	0.70 ± 0.4	0.35 ± 0.04	14.3 ± 2.7	19.2 ± 5.6

* EPS was dissolved before stress-strain testing, remaining PPX foams tested in stress-strain analysis. # pure EPS-1

6 Summary

In the present work different methods and possibilities for the modification, functionalization, and structuring of poly(*p*-xylylene) (PPX) poylmeres were presented. The polymer was either changed in its molecular structure or processed on micro or macroscopic scale. Each approach is is summarized here independently.

The first part, molecular architecture, dealt with the copolymerization of [2.2]paracyclophane and its alkyl-substituted derivates with 2-hydroxymethyl methacrylate (HEMA) via chemical vapor deposition (CVD). Copolymers of propyl and butyl substituted [2.2]paracyclophane and HEMA showed, same as the PPX homopolymers, good solubility in THF and chloroform. The connection of both monomer species in the copolymer was proven by analysis of correlation resonances in 2D-NMR spectra of P(PX-butyl-*co*-HEMA). Furthermore the obtained copolymers showed higher glass transition temperatures and lower molecular weights than the PPX-alkyl homopolymers.

While copolymers obtained in a homemade CVD setup with static deposition chamber were inhomogeneous in composition and contained unreacted comonomer, the synthesis in the commercially available CVD reactor (Labcoater) led to homogeneous films free of unreacted HEMA comonomer. Furthermore, this copolymer film showed a dependence of HEMA evaporation temperature and HEMA content in the copolymers together with a decreasing water contact angle with increasing HEMA content. P(PX-N-*co*-HEMA) copolymers showed contact angles down to 65 ° (compared to about 90 ° for the PPX-N homopolymer).

The results of homo and copolymerization experiments in the homemade setup and the Labocater underlined the crucial importance of reactor geometry and process parameter of the CVD in order to obtain polymer films of good quality.

In addition to HEMA, oxygen from ambient air was copolymerized with PPX-butyl. The synthesis was carried out using the CVD process and soluble PPX-butyl peroxides were obtained. The peroxide content was influenced by the process pressure and NMR analysis confirmed the incorporation of peroxide moieties into the growing polymer chain. Molecular weights were significantly lower as for PPX-butyl homopolymers. The PPX-butyl peroxides are potential macroinitiators for block-copolymerization with e.g. vinyl, acryl or methyacryl monomer in solution. The relatively high temperatures (>100 °C) needed for thermal cleavage of the peroxide bond suggest alternative approaches for the cleavage.

In the second part of this work, surface modification, two approaches were presented to modifiy the surface of free standing PPX-N films by *grafting*. In the first method, named *grafting to*, radical polymerizations, of e.g. *N*-isopropyl acrylamide (NiPAAm), were carried out in the presence of PPX-N films. After the treatment the PPX-N films showed water contact angles of 55-60 ° at substrate temperatures above the lower critical solution temperature (LCST) of PNiPAAM (32 °C) and were a little lower at room temperature (40-55 °). The second approach, called *grafting from*, PPX-N films were functionalized with an ATRP (atrom transfer radical polymerization) initiator via the SOLID (solid on liquid deposition) method during the CVD synthesis. For this purpose the liquid initiator 2-bromosiobutyryloxy-oligo(ethylene glycol) methacrylate was given onto a glass substrate and coated with PPX-N. After removal from the substrate, the partially initiator functionalized film was submerged into a ATRP solution to perform the surface initiated *grafting from* reactions. Despite the spatially functionalization of the PPX-N film, the chosen systems (e.g. NiPAAm in water) led to functionalization of the entire film with the copolymer, which was proven by water contact angle and ATR-IR measurements.. Despite the controlled nature of ATRP polymerization reactions, the chosen systems showed side reactions that led to free growing chains in the ATRP solutions and chain transfer to the PPX-N films. However, hydrophilic surfaces with water contact angles down to 25 ° were achieved by grafting PNiPAAm onto the PPX-N films By the use of slower and more controlled systems[169] this side reactions are expected to be minimized and spatial surface modification via a combination of SOLID functionalization and surface initiated ATRP will be available.

The third part of the present work, polymer processing, dealt with electrospinning of propyl, butyl and heptyl substituted PPX in order to achieve high water contact angles in the superhydrophobic regime. The polymers were spun into sub-micron fibers and by choice of solvent and electrospinning conditions additional features were added to the fiber surface. Smooth fiber and bead-on-string structures were obtained by changing the solvent from chlorofrom to THF and a porous fiber or bead surface was achieved by fiber production at high relative humidity (RH) levels. The additional porosity led to a further increase in water contact angle compared to the smooth fibers and bead-on-string structures. Best results were achieved for PPX-heptyl fiber mats spun from 2.5 wt% THF at RH >75% with a contact angle of 157 ± 3°. This nonwovens also comprised low roll off angles (10-15°) and showed self-cleaning ability.

From alkyl-PPX solutions in chloroform containing cetyltrimethyammonium bromide nano net formation was observed in addition to the electrospun fibers. In literature, the formation of such nano nets is attributed to droplets that emerge from the needle during the electrospinning process. With the help of scanning electron microscopy (SEM) images it was shown, that nano nets can also originate from electrospun fibers and an additional mechanism was postulated.

In the fourth and last part (PPX blends, foams and composites), possibilities to modify PPX by combining with other polymers and macroscopic structuring were shown in order to amplify the application areas of PPX polymers. Due to the solubility of PPX-propyl blending with poly(methyl methacrylate) (PMMA), polystyrene (PS) and poly(phenylether) (PPE) was possible. The immiscible polymer blends showed changes in their mechanical behavior, which were particularly interesting for PPX-pr/PPE blends.

Furthermore a PS bead foam was coated with different PPX derivates for mechanical reinforcement purposes. Stress-strain measurements of test specimen coated with PPX-N, PPX-C and PPX-propyl showed an increase in E-modulus compared to the untreated PS foams. Interestingly the improvements did not depend on the mechanical properties of the PPX derivate used for reinforcement but rather on the thickness of the applied coatings. In addition to the reinforcement, PPX-N coatings also served as protection layer for the PS foams, hindering gas diffusion and retarding inflammability.

Macroscopic three dimensional structures were obtained by coating of porous template structure with PPX-N and subsequent removal of the template material by extraction. It was shown, that PPX-N can penetrate the air channels of bead foams and complicated inner geometries of sugar cubes and give negative image of such structures. In addition to the PPX foam generation by this template method, the coatings can help to visualize the porous structure of the template materials, or confirm the absence of continuous porous structure in the interior of a specimen, as shown for PS bead foams with different bead sizes and quality of bead fusion.

7 Outlook

The concepts and methods introduced in this work show the feasibility of easy bulk and surface modification of PPX by copolymerization, *grafting* reactions, blending and processing into micro and macroscopic structures.

The availability of soluble alkyl-PPX derivates enabled for the first time the structural analysis of PPX copolymers by solution NMR. Experiments with different CVD reactors underlined the importance of processing parameter for CVD copolymerization. Reactor design is a crucial influence factor in CVD and a constant possibility for improvements to ensure high quality coatings in good yields. By choice of adequate reaction conditions, like process pressure, controlled monomer flow and substrate temperature, the copolymerization mechanism of PPX with methacrylates and other double bound containing comonomer or reactive gases can be investigated and compared to actual theoretic studies. The copolymerization with commercially available comonomers is a powerful, versatile and cost effective tool for PPX modification. Therefore the combination of experimental results and theoretic investigations would be helpful in order to predict ideal copolymerization conditions for PPX with other monomers and help to reduce experimental parameter screening for new systems.

Further copolymer architectures are available by the use of soluble alkyl-PPX peroxides as macroinitiators or buildings blocks for polycondensations and polyadditions. Though the thermal decomposition of the PPX-butyl peroxide is not suitable for the initiation of common vinyl-, arcyl- or methacryl polymerizations due to high decomposition temperature, alternative ways like photoinduced decompositon or amine-assisted[141] decomposition are promising. The peroxides also enable access to PPX teleches by cleaving the peroxide bonds. As shown the cleavage products via the thermal route give a mixture of aldehyde and alcohol endgroups. By reductive cleavage of the peroxide bond, an *in situ* reduction of aldehyds is expected and α,ω-hydroxy terminated alkyl-PPX would be avialable for polycondensation or polyaddition reactions. Alkyl-PPX block-copolymer can be of particular interest in use as compatibilizers to stabilize the phase morphology of alkyl-PPX blends.

The surface modification by *grafting to* and *grafting from* methods represent mild and easy techniques to achieve surface modification of PPX-N films. The ATRP systems presented in this work showed side reactions that led to *grafting* without spatial resolution despite the controlled incorporation of ATRP initiator via the SOLID process. With the choice of more controlled ATRP systems *grafting* layers a great variety of ATRP polymers will be available for PPX surface modification.[145, 146] However, the surface modification with stimuli responsive polymers, and particularly PNiPAAm, is of special interest. Due to the hydrophobic-hydrophilic transition PNiPAAm functionalized surfaces find application as substrate in cell cultures, that detach the cells upon temperature stimuli.[80, 84] Another interesting monomer, capable of further reactions to immobilize e.g. biomolecules and enzymes is glycidyl methacrylate, since it contains an reactive epoxide group.[170, 171] Another interesting aspect is the incorporation of the ATRP initiator into PPX-propyl or PPX-butyl via the solid process. The resulting surface functionalized films are expected to be soluble and could give valuable information about the amount of initiator molecules attached to the PPX films. Furthermore, the *grafting from* reactions in solution will lead to brush-like graft copolymers of PPX, that represent another type of copolymer architectrue.

However modification via chain transfer is also an easy, though less controllable, method for rapid surface functionalization of PPX without the need to incorporate an ATRP initiator via the SOLID process or pre-deposition functionalization of the [2.2]paracyclophane precursor. The number of monomers suitable for free radical polymerization is vast, and this method can be of advantage, because in contrast to ATRP there is no need for metal catalysts.

The processing of soluble alkyl-PPX derivates by electrospinning into hydrophobic and superhydrophoic nonwovens with self cleaning ability showed one way to benefit of this new type of PPX polymers. Electrospinning is a multifaceted technique and by far not limited to the methods presented here.[30, 31] Due to their flexibility alkyl-PPX can be useful components in side by side electrospinning to for the production of core-shell fibers. In the present work electrospinning of alkyl-PPX polymers was so far carried out with solutions of relatively low polymer concentrations (up to 6 wt%) due to high viscosity of higher concentrated solutions. In order to optimize the efficiency of the electrospinning process and increase the polymer content dispersion spinning is a promising approach. The solubility of alkyl-PPX in the water miscible solvent THF is a prerequisite for dispersion generation by solvent displacement methods.

In first experiments alkyl-PPX were also electrospun from solvent mixture containing a high boiling solvent component. This fibers were found to be glued together at intersection points, which makes them interesting for two-dimensional cut fiber applications.

It was also shown that PPX and its derivates can be customized for further applications by combining them with other polymers. Soluble alkyl-PPX can used for the generation of polymer blends, as shown for PPX-propyl. For further investigations in this field and in order to improve the blend performance, the addition of compatibilizers to stabilize the phase morphology is needed. Such compatibilizers can be block-copolymers of the respective components, that might be available by block-copolymerization with the help of building blocks obtained from alkyl-PPX peroxides. By coating of PS bead foam specimen with different PPX derivates composit-like materials were obtained. The coating for reinforcement and protection purposes can be a powerful tool for high performance applications, where inertness upon short term exposure to chemicals and high temperature is needed.

A powerful tool for three dimensional structure generation and structure imaging is the coating of porous templates with PPX. Similar to the TUFT (tubes by fiber templates) approach, the ability of PPX to penetrate porous structures was exploited not for substrate coating purposes but for three dimensional structure generation. In the case of sugar cubes as templates, high surface area structures are obtained, that were tested in first experiments for their applicability as structure elements in electrodes for microbial fuel cells. The template approach offers countless possibilities to model PPX into different geometries. Thus the method is not limited to the examples presented in this work but expandable to all kind of porous templates of different geometries as long as they comprise continuous air channels or pores in adequate dimensions.

8 Zusammenfassung

Im Rahmen dieser Arbeit wurden verschiedene Möglichkeiten aufgezeigt Poly(*p*-xylylen) (PPX) zu modifizieren und zu strukturieren. Im ersten Teil, Molekulare Architekturen, wurden [2.2]Paracyclophan und verschiedene alkyl-substituierte Derivate mit 2-Hydroxymethylmethacrylat (HEMA) über das Gasphasenabscheidungsverfahren (*engl.* chemical vapor deposition, CVD) copolymerisiert. Copolymere, bei denen propyl- und butyl-substituierte [2.2]Paracylophane als Präkursoren verwendet wurden, zeigten wie ihre PPX-Homopolymere, Löslichkeit in THF und Chloroform. Anhand von P(PX-butyl-*co*-HEMA) wurde die Copolymerisation über 2D-NMR Spektroskopie durch Kopplungssignale zwischen beiden Monomereinheiten nachgewiesen. Die Copolymere zeigten außerdem höhere Glasübergangstemperaturen und geringere Molekulargewichte als ihre PPX-Homopolymere. Die Durchführung der Synthese in einem kommerziell erhältlichen Gasphasenabscheidungsreaktor (Labcoater) führte, im Gegensatz zu den Copoylmerfilmen aus dem selbst konzipierten CVD-Reaktor, zu homogenen P(PX-N-*co*-HEMA) Filmen frei von unreagiertem Comonomer. Bei den im Labcoater hergestellten Copolymerfilmen war ein Zusammenhang zwischen Reaktionsbedingungen und HEMA-Anteil im Copolymer zu beobachten. Des Weiteren wurde eine Reduktion des Wasserkontaktwinkels von ca 90 ° für PPX-N auf 65 ° für P(PX-N-*co*-HEMA) erreicht. Durch Homo- und Copolymerisationsexperimente im selbst konzipierten CVD Reaktor und dem Labcoater wurde gezeigt, dass Reaktorgeometrie und Prozessbedingungen währen der Gasphasenabscheidung von entscheidender Bedeutung für die Filmbeschaffenheit und -qualität sind. Dies gilt insbesondere, aber nicht ausschließlich, für die Herstellung von Copolymeren.

Neben HEMA wurde außerdem Luftsauerstoff als Comonomer in PPX-butyl eingebaut. Die Synthese erfolgte ebenfalls über das CVD-Verfahren und ermöglichte den Zugang zu löslichen PPX-butyl Peroxiden. Der Peroxid Gehalt im Copolymer konnte über den Prozessdruck gesteuert und der Einbau von Sauerstoff in die wachsende Polymerkette durch NMR Spektroskopie bestätigt werden. Die Molekulargewichte lagen deutlich unter denen der PPX-butyl Homopolymere. Die PPX-butyl Peroxide sind potenzielle Makroinitiatoren für Blockcopolymerisationen mit z.B. Vinyl,- Acryl- oder Methacryl-Comonomeren. Aufgrund der zur Spaltung der Peroxidbindung nötigen Temperaturen (>100 °C), erwies sich die thermische Initiierungsmöglichkeit als problematisch.

Im zweiten Teil der Arbeit, Oberflächenmodifikation von PPX, wurden zwei einfache Methoden angewandt um die Oberfläche von PPX-N Filmen durch *„graften“* anderer Polymer zu modifizieren. Hierbei wurden die Konzepte, beschrieben als *grafting to* und *grafting from*, eingesetzt. Bei der ersten Methode wurden radikalische Polymerisationen, von zum Beispiel *N*-isoproyplacrylamid (NiPAAm) in Anwesenheit von PPX-N Filmen durchgeführt, was vermutlich zu Übertragungsreaktionen und damit zur Anbindung von Poly(*N*-isopropylacrylamid) (PNiPAAm) an die PPX-N Oberfläche führte. Die Oberfläche der so behandelten PPX-N Filme zeigte Wasserkontaktwinkel von 55-60 ° bei Substrattemperaturen oberhalb der unteren kritischen Lösungstemperatur (*engl.* lower critical solution temperature, LCST) von PNiPAAm von 32 °C und leicht hydrophilere Kontaktwinkel bei Raumtempeature (40-55 °). Bei der *grafting from* Methode wurden die PPX-N Filme zunächst während der Synthese im CVD-Verfahren über den SOLID (*engl.* solid on liquid deposition, fest-auf-flüssig-Abscheidung) Prozess mit einem ATRP-Initiator (*engl.* atom transfer radical polymerization, radikalische Atomtranfer-Polymerisation) funktionalisiert. Dazu wurde der flüssige ATRP-Initiator 2-Bromoisobutyryl-oligo(ethylenglycol)methacrylat auf ein flaches Glassubstrat gegeben und mit PPX-N beschichtet. An die vom Substrat gelösten, teilweise funktionalisierten PPX Filme wurde dann über oberflächeninitiierte ATRP ein Comonomer anpolymersiert. Bei den gewählten ATRP Systemen (z.B. NiPAAm in Wasser) wurde entgegen der Erwartung der Film vollständig mit PNiPAAm modifiziert, was wie bei der *grafting to* Methode über den Wasserkontaktwinkel oder ATR-IR nachgewiesen werden konnte. Dennoch wurden die PPX-N Oberlfächen durch die oberflächeninitierte polymerisation von PNiPAAm hydrophil modifiziert und Kontaktwinkel von 25 ° erreicht.

Im dritten Teil der vorliegenden Arbeit, Polymer Verarbeitung, wurden propyl-, butyl- und heptyl- substituierte PPX über Elektrospinnen zu Fasern im sub-Mikrometer Bereich verarbeitet. Ziel war es, durch gezielte Strukturierung der Oberfläche einen möglichst hohen, im superhydrophoben Bereich liegenden Wasserkontaktwinkel zu erreichen. Durch die Wahl des Lösungsmittels, Chloroform und THF, wurden glatte Fasern bzw. Fasern mit spindelförmigen Verdickungen (beads) erhalten. Das Verspinnen bei hoher relativer Luftfeuchtigkeit führte außerdem zu einer porösen Oberfläche, was sich positiv auf die Erhöhung des Kontaktwinkels auswirkte. Die besten Ergebnisse mit einem Kontaktwinkel von 157 ± 3 ° wurden für PPX-heptyl, versponnen aus 2.5 gew% THF Lösung bei relativer Luftfeuchtigkeit von > 75% erhalten. Diese Faservlise zeigten außerdem niedrige Rollwinkel (10-15°) und Tendenzen zur Selbstreinigung.

Durch den Zusatz von Cetyltrimethylammoniumbromid zu den Spinnlösungen der alkyl-PPX in Chloroform wurden zusätzlich zu Nanofasern so genannte Nanonetze erhalten. Die Entstehung dieser Netze wird in der Literatur einer Tropfenbildung während des Elektrospinnprozesses zugeschrieben. Anhand von Rasterelektronenmikroskopischen Aufnahmen konnte gezeigt werden, dass sich die Netze auch aus Fasern bilden können und ein ergänzender Mechanismus postuliert.

Im vierten und letzten Teil dieser Arbeit, PPX Blends, Schäume und Komposite, wurden verschiedene Möglichkeiten dargestellt, wie PPX durch Kombination mit anderen Polymeren und Polymermaterialien modifiziert werden kann bzw. neue Anwendungsbereiche erschlossen werden können. Dank der Löslichkeit der alkyl-PPX Derivate gelang die Verblendung mit Polymethylmethacrylat (PMMA), Polystyrol (PS) und Polyphenylenether (PPE). Dies führte, besonders im Fall der PPX-propyl/PPE Blends, zu interessanten Veränderung der mechanischen Eigenschaften.

Des Weiteren wurden unterschiedliche PPX Derivate zur mechanischen Verstärkung von Polystyrol Schäumen verwendet. Hierzu wurden Probenkörper für Zug-Dehnungsmessungen mit PPX-N, PPX-C und PPX-propyl im CVD Verfahren beschichtet. Die Beschichtung führte zu einer beachtlichen Erhöhung des E-Modul, wobei die Verbesserung im untersuchten Bereich nicht von den mechanischen Eigenschaften des PPX-Derivates sondern vielmehr von der Dicke der Beschichtung abhing.

Makroskopische dreidimensionale Strukturen aus PPX wurden durch die Beschichtung von porösen Templatstrukturen erhalten. Hierzu wurden Körper aus Polystyrol Partikelschaum und Zucker mit unlöslichem PPX-N im CVD Verfahren beschichtet und anschließend das Templatmaterial extrahiert. Hierbei zeigte sich, das PPX die kontinuierlichen Strukturen innerhalb der Template vollständig abbilden kann. Diese Methode eignet sich daher nicht nur zur Herstellung von PPX Schäumen sondern auch zur Untersuchung der Zwischenräumen in Porösen Strukturen wie z.B. der Luftkanäle in Partikelschäumen. In ersten Vorversuchen wurde die Verwendbarkeit der Schäume z.B. als strukturgebendes Elemente für Elektrodenmaterialien in mikrobiellen Brennstoffzellen untersucht.

9 Acknowledgements/Danksagung

Meinem Doktorvater, Prof. Dr. Andreas Greiner, danke ich für die Bereitstellung dieses interessanten und vielseitigen Forschungsthemas sowie für die umfangreiche Betreuung und Unterstützung während meiner Promotion. Besonders bedanken möchte ich mich für die Möglichkeit, meine Arbeit nach dem Umzug nach Bayreuth in der Arbeitsgruppe fortgesetzt haben zu können.

Prof. Dr. Joachim H. Wendorff danke ich für die Übernahme des Zweitgutachtens und dem damit, vor allem in Anbetracht des engen Zeitplans, verbundenen Aufwand.

Prof. Dr. Anreas Seubert danke ich, für die Bereitschaft der Prüfungskommission als drittes Mitglied beizuwohnen.

Bei Prof. Dr. Seema Agarwal möchte ich mich für die gute Zusammenarbeit und zahlreiche Anregungen im Gruppenseminar bedanken.

Bei Prof. Volker Altstädt (Lehrstuhl für Polymere Werkstoffe), Thomas Koeppl und besonders Daniel Raps bedanke ich mich für die gute Zusammenarbeit im Projekt der PPX-Schäume.

Dr. Rakesh Kumar und der Firma SCS Speciality Coatings Systems danke ich für die Bereitstellung der Paracyclophane.

Dr. Gunther Brunklaus (MPI Mainz/Uni Münster) danke ich für die Festkörper-NMR Aufnahmen.

Edith Schmidt (MR), Rigobert Donner (MR) und Gaby Oliver (BT) danke ich herzlich für Ihre unermüdliche Hilfe und Unterstützung bei jeglichen administrativen Angelegenheiten.

Dr. Roland Dersch danke ich für zahlreiche Ratschläge rund um Elektrospinnen, Lichtmikroskope, High Speed Kamera und Antworten auf die Frage des Tages.

Dr Anna Katharina Bier und Dr. Michael Bognitzki danke ich für ihre, besonders in der Anfangsphase unentbehrliche Hilfe zum Thema PPX und Paracyclophane.

Dr. Christian Brandl danke ich für die Zusammenarbeit Projekt zur Oberflächenfunktionalisierung von PPX-Filmen via ATRP-*grafting*.

Michael Hellwig (MR), Martina Haider, Miriam Mauer und besonders Melanie Müller (alle BT) danke ich für Unterstützung und Hilfe am Rasterelektronenmikroskop und bei der Bild-Aufnahme. Sowie Martina Haider für die EDX-Messungen.

Besonderer Dank gilt meinen Vertiefungsstudenten Hui Wand, Fangyao Liu und Amanda Pineda (MR, alkyl-PPX), Tobias Moss (MR, Oberflächenfunktionalisierung), Judith Schöbel (MR, PPX Blends), sowie Svenja Marl und Patrick Hummel (BT, Elektrospinnen), die trotz gelegentlichen wissenschaftlichen Rückschlägen immer motiviert und engagiert mit mir zusammengearbeitet und so einen wertvollen Beitrag zu dieser Arbeit geleistet haben.

Besonderer Dank gilt außerdem den Mitarbeitern der Glas-, Feinmechanik und Elektronik Werkstätten der Uni Marburg, ohne deren Hilfe die Instandhaltung und Umgestaltung der CVD Apparaturen nicht möglich gewesen wäre!

Dank gebührt allen Korrekturlesern dieser Arbeit: Roland Dersch, Markus Langener, Viola Buchholz, Tobias Moss, Fabian Mitschang, Peter Ohlendorf, Oliver Hauenstein, Holger Pletsch, Paul Ksionsko und Amanda Pineda.

Ein ganz besonderer Dank für die immer angenehme Arbeitsatmosphäre gilt meinen, durch den Umzug zahlreichen, Labor- und Bürokollegen: Dr. Marco Gensheimer, Dr. Thorsten Röcker, Hui Wang, Tobias Moss, Lisa Hamel und Fabian Mitschang.

Ich bedanke mich besonders bei dem weltbesten Laborkollegen Dr. Christian Knierim für seine immer guten Laune und Hilfsbereitschaft vor allem bei chemischen Fragen, aber auch bei anderweitigen handwerklichen und technischen Schwierigkeiten. Die jahrelange Zusammenarbeit, auf zum Teil auf engstem Raum in 4415, wird immer in guter Erinnerung bleiben!

Ich danke meinem Kommilitonen Andreas Haedler für die unverzichtbare Start- und Eingewöhnungshilfe in Bayreuth.

Auch allen ehemaligen und aktuellen Mitarbeitern und Doktoranden der Arbeitskreise Greiner und Agarwal danke ich für das gute Arbeitsklima, die Hilfe bei Bedienung verschiedenster Geräte und vor allem der Durchführung vieler GPC-Messungen (besonders Uwe Justus, Katrin Bubel und Marietta Böhm) und MALDI-Messungen (Annika Pfaffenberger). Besonderer Dank gilt außerdem Hui Wang für die Durchführung der Cytotoxizitäts-Test und Bakterien-Versuche und Markus Langner für die Durchführung der Silber Abscheidung an PPX-Schäumen.

Schließlich bedanke ich mich herzlich bei Familie und Freunden, besonders bei meinen Eltern Monika und Horst-Dieter Paulus, für die jahrelange moralische Unterstützung, ohne die die Entstehung und Fertigstellung dieser Arbeit um einiges schwerer gefallen wäre.

10 Literature

[1] L. Alexandrova, R. Vera-Graziano, *Polymeric Materials Encyclopedia* **1996**, *9*, 7180-7189.

[2] M. Gazicki-Lipman, *Journal of the Vacuum Society of Japan* **2007**, *50*, 601-608.

[3] A. Greiner, *The Polymeric Materials Encyclopedia* **1996**, *9*, 7171-7180.

[4] W. F. Gorham, *Journal of Polymer Science: Part A-1* **1966**, *4*, 3027-3039.

[5] E. Meng, C. Po-Jui, D. Rodger, T. Yu-Chong, M. Humayun, in *Microtechnology in Medicine and Biology, 2005. 3rd IEEE/EMBS Special Topic Conference on*, **2005**, pp. 116-119.

[6] E. Meng, T. Yu-Chong, in *TRANSDUCERS, Solid-State Sensors, Actuators and Microsystems, 12th International Conference on, 2003, Vol. 1*, **2003**, pp. 686-689 vol.681.

[7] L. Po-Ying, T. K. Givrad, D. P. Holschneider, J. M. I. Maarek, E. Meng, *Microelectromechanical Systems, Journal of* **2009**, *18*, 1184-1197.

[8] L. Wolgemuth, *Business Briefing: Medical Device Manufacturing & Technology* **2002**.

[9] T. Y. Chang, V. G. Yadav, S. De Leo, A. Mohedas, B. Rajalingam, C.-L. Chen, S. Selvarasah, M. R. Dokmeci, A. Khademhosseini, *Langmuir* **2007**, *23*, 11718-11725.

[10] M. Kaminska, W. Okroj, W. Szymanski, W. Jakubowski, P. Komorowski, A. Nosal, H. Szymanowski, M. Gazicki-Lipman, H. Jerczynsk, Z. Pawlowska, B. Walkowiak, *Acta of Bioengineering and Biomechanics* **2009**, *11*, 19-25.

[11] P. Hanefeld, U. Westedt, R. Wombacer, T. Kissel, A. Schaper, J. H. Wendorff, A. Greiner, *Biomacromolecules* **2006**, *7*, 2086-2090.

[12] E. M. Schmidt, J. S. McIntosh, M. J. Bak, *Medical & Biological Engineering & Computing* **1988**, *26*, 96-101.

[13] R. Kumar, Y. Ke, D. England, US 2013/0011456 A1, **2013**.

[14] X. Deng, C. Friedmann, J. Lahann, *Angewandte Chemie International Edition* **2011**, *50*, 6522-6526.

[15] C. P. Tan, H. G. Craighead, *Materials* **2010**, *3*, 1803.

[16] A. K. Bier, M. Bognitzki, J. Mogk, A. Greiner, *Macromolecules* **2012**, *45*, 1151-1157.

[17] A. K. Bier, M. Bognitzki, A. Schmidt, A. Greiner, E. Gallo, P. Klack, B. Schartel, *Macromolecules* **2012**, *45*, 633-639.

[18] A. M. Coclite, R. M. Howden, D. C. Borrelli, C. D. Petruczok, R. Yang, J. L. Yagüe, A. Ugur, N. Chen, S. Lee, W. J. Jo, A. Liu, X. Wang, K. K. Gleason, *Advanced Materials* **2013**, n/a-n/a.

[19] L. A. Auspos, L. A. R. Hall, J. K. Hubbard, W. M. Kirk, J. R. Schaefgen, S. B. Spek, *Journal of Polymer Science* **1955**, *15*, 9-17.

[20] J. R. Schaefgen, *Journal of Polymer Science* **1955**, *15*, 203-219.

[21] V. Sochilin, K. Mailyan, L. Aleksandrova, A. Nikolaev, A. Pebalk, I. Kardash, *Doklady Akademii Nauk SSSR (Doklady Chemistry)* **1991**, *319*, 173-176.

[22] J. F. Gaynor, Polymeric THin Films by Chemical Vapor Deposition for the Microelectronics Industry, **1995**.

[23] J. F. Gaynor, S. B. Desu, *Journal of Materials Research* **1994**, *9*, 3125-3130.

[24] J. F. Gaynor, S. B. Desu, *Journal of Materials Research* **1995**, *11*, 236-241.

[25] J. F. Gaynor, S. B. Desu, S. S. Senkevich, *Macromolecules* **1995**, *28*, 7343-7348.

[26] J. F. Gaynor, J. J. Senkevich, S. B. Desu, *Journal of Materials Research* **1996**, *11*, 1842-1850.

[27] H. Hou, Z. Jun, A. Reuning, A. Scharper, J. H. Wendorff, A. Greiner, *Macromolecules* **2002**, *35*, 2429-2431

[28] F. Mitschang, B. K. Dettlaff, J.-P. Lindner, A. Studer, A. Greiner, *Macromolecules* **2013**, *46*, 8784-8789.

[29] C. Knierim, Immobilisierung von Bakterien in Hydrogelen und chemische Weiterverarbeitung zu wasserstabilen lebenden Biohybridsystemen, Philipps Universität Marburg (Marburg), **2013**.

[30] A. Greiner, J. H. Wendorff, *Angewandte Chemie International Edition* **2007**, *46*, 5670-5703.

[31] S. Agarwal, A. Greiner, J. H. Wendorff, *Progress in Polymer Science* **2013**, *38*, 963-991.

[32] J. M. Jasinski, B. S. Meyerson, B. A. Scott, *Annual Review of Physical Chemistry* **1987**, *38*, 109-140.
[33] M. J. Hampden-Smith, T. T. Kodas, *Chemical Vapor Deposition* **1995**, *1*, 8-23.
[34] J. R. Creighton, J. E. Parmeter, *Critical Reviews in Solid State and Materials Sciences* **1993**, *18*, 175-237.
[35] A. C. Jones, M. L. Hitchma, Chemical Vapor Deposition - Precursors, Porcess and Applications, RSC Publishing, Cambridge, **2009**
[36] R. Sreenivasan, K. K. Gleason, *Chemical Vapor Deposition* **2009**, *15*, 77-90.
[37] S. P. Krumdieck, (Eds.: A. C. Jones, M. L. Hitchman), Royal Society of Chemistry, **2009**.
[38] M. E. Alf, A. Asatekin, M. C. Barr, S. H. Baxamusa, H. Chelawat, G. Ozaydin-Ince, C. D. Petruczok, R. Sreenivasan, W. E. Tenhaeff, N. J. Trujillo, S. Vaddiraju, J. Xu, K. K. Gleason, *Advanced Materials* **2010**, *22*, 1993-2027.
[39] K. K. S. Lau, K. K. Gleason, *Thin Solid Films* **2008**, *516*, 678-680.
[40] W. E. Tenhaeff, K. K. Gleason, *Langmuir* **2007**, *23*, 6624-6630.
[41] K. K. S. Lau, K. K. Gleason, *Macromolecules* **2006**, *39*, 3688-3694.
[42] K. Chan, K. K. Gleason, *Langmuir* **2005**, *21*, 8930-8939.
[43] K. Chan, K. K. Gleason, *Chemical Vapor Deposition* **2005**, *11*, 437-443.
[44] Y. Mao, K. K. Gleason, *Langmuir* **2004**, *20*, 2484-2488.
[45] S. K. Murthy, K. K. Gleason, *Macromolecules* **2002**, *35*, 1967-1972.
[46] Y. Mao, K. K. Gleason, *Macromolecules* **2006**, *39*, 3895-3900.
[47] J. P. Lock, S. G. Im, K. K. Gleason, *Macromolecules* **2006**, *39*, 5326-5329.
[48] M. Szwarc, *Discussions of the Faraday Society* **1947**, 46-49.
[49] C.-M. Chou, K.-C. Hsieh, C.-J. Chung, J.-L. He, *Surface and Coatings Technology* **2010**, *204*, 1631-1636.
[50] B. Mitu, S. Bauer-Gogonea, H. Leonhartsberger, M. Lindner, S. Bauer, G. Dinescu, *Surface and Coatings Technology* **2003**, *174–175*, 124-130.
[51] A. Greiner, S. Mang, O. Schäfer, P. Simon, *Acta Polymer* **1997**, *48*, 1-18.
[52] H. G. Gilch, W. L. Wheelwright, *Journal of Polymer Science Part A-1: Polymer Chemistry* **1966**, *4*, 1337-1349
[53] W. R. Roth, H. Hopf, A. d. Meijere, F. Hunold, S. Börner, M. Neumann, T. Wasser, J. Szurowski, C. Milynek, *Liebigs Annalen* **1996**, 2141-2154.
[54] J. B. Fortin, T. M. Lu, *Journal of Vacuum Science and Technology A* **2000**, *18*, 2459-2465.
[55] K. Smalara, A. Gieldón, M. Bobrowski, J. Rybicki, C. Czaplewski, *Journal of Physical Chemistry A* **2010**, *114*, 4296-4303.
[56] C. J. Brown, A. C. Farthing, *nature* **1949**, *26*, 915-916.
[57] W. F. Beach, *Macromolecules* **1978**, *11*, 72-76.
[58] M. Szwarc, *Polymer Engingeering and Science* **1976**, *16*, 473-479.
[59] L. A. Errede, R. S. H. J. M. Gregorian, *Journal of the American Chemical Society* **1960**, *82*, 5218-5223.
[60] S. Kubo, B. Wunderlich, *Journal of Polymer Science* **1972**, *10*, 1949-1966.
[61] H. Y. Chen, Y. Elkasabi, J. Lahann, *Journal of the American Chemical Society* **2006**, *128*, 374-380.
[62] J. B. Fortin, T. M. Lu, *Chemical Materials* **2002**, *14*, 1945-1949.
[63] D. E. Kirkpatrick, B. Wunderlich, *Makromolekulare Chemie* **1985**, *186*, 2595-2607.
[64] M. Gazicki, W. J. James, H. Yasuda, *Journal of Polymer Science: Polymer Letters Edition* **1985**, *23*, 639-645.
[65] H. Hopf, F. T. Lenich, *Chemische Berichte* **1974**, *107*, 1891-1902.
[66] H. J. Reich, D. J. Cram, *Journal of the American Chemical Society* **1969**, *91*, 3505-3516.
[67] S. E. Gibson, J. D. Knight, *Organic and Biomolecular Chemistry* **2003**, *1*, 1256-1269.
[68] Y. L. Yeh, W. F. Gorham, *The Journal of Organic Chemistry* **1969**, *34*, 2366-2370.
[69] A. K. Bier, Erzeugung substituierter Poly(*p*-xylylen)e durch Gasphasenabscheidung, Philipps Universität Marburg (Marburg), **2011**.
[70] J. Lahann, D. Klee, W. Pluester, H. Hoecker, *Biomaterials* **2001**, *22*, 817-826.
[71] J. C. Palmaz, *AJR* **1993**, *160*, 613-618.
[72] Y. M. Elkasabi, J. Lahann, P. H. Krebsbach, *Biomaterials* **2011**, *32*, 1809-1815.

[73] Y. Elkasabi, J. Lahann, *Macromolecular Rapid Communications* **2009**, *30*, 57-63.
[74] X. Jiang, H. Y. Chen, G. Galvan, M. Yoshida, J. Lahann, *Advanced Functional Materials* **2008**, *18*, 27-35.
[75] H. Y. Chen, J. Lahann, *Analytical Chemistry* **2005**, *77*, 6909-6914.
[76] S. S. C. Systems, www.scscoatings.com{corporate/library.aspx, November 24, 2013
[77] M. Herrera-Alonso, T. J. McCarthy, *Langmuir* **2004**, *20*, 9184-9189.
[78] M. Bera, A. Rivaton, C. Gandon, J. L. Gardette, *European Polymer Journal* **2000**, *36*, 1753-1764.
[79] J. J. Senkevich, G. R. Yang, T. M. Lu, *Colloids and Surfaces A* **2003**, *216*, 167.
[80] P. N. Wahjudi, J. H. Oh, S. O. Salman, J. A. Seabold, D. C. Rodger, Y. C. Tai, M. E. Thompson, *Jorunal of Biomedical Materials Research Part A* **2009**, *89A*, 206-214.
[81] T. Takezawa, Y. Mori, K. Yoshizato, *Nat Biotech* **1990**, *8*, 854-856.
[82] C. de las Heras Alarcón, T. Farhan, V. L. Osborne, W. T. S. Huck, C. Alexander, *Journal of Materials Chemistry* **2005**, *15*, 2089-2094.
[83] J. Zeng, Meso- and Nano-scaled Polymer Fibers and Tubes, Philipps-Universität (Marburg), **2003**.
[84] C. Zhang, P. T. Vernier, Y.-H. Wu, W. Yang, *Journal of Biomedical Materials Research Part B: Applied Biomaterials* **2012**, *100B*, 217-229.
[85] L. A. Errede, J. M. Hoyt, *Journal of the American Chemical Society* **1960**, *82*, 436.
[86] S. Iwatsuki, H. Kamiya, *Macromolecules* **1974**, *7*, 732.
[87] L. A. Errede, W. A. Pearson, *Journal of the American Chemical Society* **1961**, *83*, 954-960.
[88] L. A. Errede, S. L. Hopwood, Jr., *Journal of the American Chemical Society* **1957**, *79*, 6507-6510.
[89] L. A. Errede, M. Szwarc, *Quarterly Reviews* **1958**, 301-322.
[90] R. S. Corley, H. C. Haas, M. W. Kane, D. I. Livingston, *Journal of Polymer Science* **1954**, *8*, 137-156.
[91] K. Stumpe, Copolymerisation von Paracyclophanen mit vinylischen Estern aus der Gasphase, **2003**.
[92] A. Bolognesi, C. Botta, A. Andiscova, U. Giovanella, S. Arnautov, J. Charmet, E. Laux, H. Keppner, *Macromolecular Chemistry and Physics* **2009**, *210*, 2052-2057.
[93] M. Naddaka, F. Asen, S. Ferea, M. Bobrowski, P. Skurski, E. Laux, J. Charmet, H. Keppner, J. P. Lellouche, *Journal of Polymer Science A: Polymer Chemistry* **2011**, *517*, 4583-4586.
[94] M. Bobrowski, P. Skurski, S. Freza, *Chemical Physics* **2011**, *382*, 2026.
[95] S. Freza, P. Skurski, M. Bobrowski, *Chemical Physics* **2010**, *368*, 126-132.
[96] M. Bobrowski, S. Freza, P. Skurski, *Macromolecules* **2012**.
[97] M. C. Demirel, *Colloids and Surfaces A: Physicochemical and Engineering Aspects* **2008**, *321*, 121-124.
[98] G. Demirel, N. Malvadkar, M. C. Demirel, *Thin Solid Films* **2010**, *518*, 4252-4255.
[99] M. Cetinkaya, M. C. Demirel, *Chemical Vapor Deposition* **2009**, *15*, 101-105.
[100] M. Bognitzki, H. Hou, M. Ishaque, T. Frese, M. Hellwig, C. Schwarte, A. Schaper, J. H. Wendorff, A. Greiner, *Advanced Materials* **2000**, *12*, 637-640.
[101] J. A. M. Hepperle, F. Mitschang, A. K. Bier, B. K. Dettlaff, A. Greiner, A. Studer, *RSC Advances* **2013**, *3*, 25976-25981.
[102] P.-J. Chen, *Lab on a Chip* **2006**, *6*, 803-810.
[103] B. Ilic, D. Czaplewski, M. Zalalutdinov, B. Schmidt, H. G. Craighead, *Journal of Vacuum Science & Technology B: Microelectronics and Nanometer Structures* **2002**, *20*, 2459-2465.
[104] A. Formhals, US 1,975,504, **1934**.
[105] G. Taylor, *Proceedings of the Royal Society A* **1969**, *313*, 453-475.
[106] D. H. Reneker, A. L. Yarin, *Polymer* **2008**, *49*, 2387-2425.
[107] A. L. Yarin, S. Koombhongse, D. H. Reneker, *Journal of Applied Physics* **2001**, *89*, 3018-3026.
[108] F. R. S. Rayleigh, *London, Edinburgh and Dublin Philosophical Magazine and Journal* **1882**, *14*, 184-186.
[109] H. Fong, I. Chun, D. H. Reneker, *Polymer* **1999**, *40*, 4585-4592.

[110] S. Koombhongse, W. Liu, D. H. Reneker, *Journal of Polymer Science Part B: Polymer Physics* **2001**, *39*, 2598-2606.
[111] E. S. Medeiros, L. H. C. Mattoso, R. D. Offeman, D. F. Wood, W. J. Orts, *Can. J. Chem.* **2008**, *86*, 590-599.
[112] R. M. Nezarati, M. B. Eifert, E. Cosgriff-Hernandez, *Tissue Engineering: Part C* **2013**, *19*, 1-10.
[113] M. Bognitzki, W. Czado, T. Frese, A. Schaper, M. Hellwig, M. Steinhart, A. Greiner, J. H. Wendorff, *Advanced Materials* **2001**, *13*, 70-72.
[114] S. Megelski, J. S. Stephens, D. B. Chase, J. F. Rabolt, *Macromlecules* **2002**, *35*, 8456-8466.
[115] M. Bognitzki, T. Frese, M. Steinhart, A. Greiner, J. H. Wendorff, A. Scharper, M. Hellwig, *Polymer Engineering & Science* **2001**, *41*, 982-989.
[116] A. Holzmeister, M. Rudisile, A. Greiner, J. H. Wendorff, *European Polymer Journal* **2007**, *43*, 4859-4867.
[117] B. Ding, Y. Si, X. Wang, J. Yu, L. Feng, G. Sun, *Journal of Materials Chemistry* **2011**, *21*, 13345-13353.
[118] B. Ding, C. Li, Y. Miyauchi, O. Kuwaki, S. Shiratori, *Nanotechnology* **2006**, *17*, 3685-3691.
[119] X. Wang, B. Ding, J. Yu, J. Yang, *Colloids and Surfaces B: Biointerfaces* **2011**, *86*, 345-352.
[120] X. Wang, B. Ding, J. Yu, Y. Si, S. Yang, G. Sun, *Nanoscale* **2011**, *3*, 911-915.
[121] W. Barthlott, C. Neinhuis, *Planta* **1997**, *202*, 1-8.
[122] P. Roach, N. J. Shirtcliffe, M. I. Newton, *Soft Matter* **2008**, *4*, 224-240.
[123] T. Young, *Philosophical Transactions of the Royal Society A* **1805**, *95*, 65-87.
[124] I. Sas, R. E. Gorga, J. A. Joines, K. A. Thoney, *Journal of Polymer Science Part B: Polymer Physics* **2012**, n/a-n/a.
[125] R. N. Wenzel, *Industrial & Engineering Chemistry* **1936**, *28*, 988-994.
[126] A. B. D. Cassie, S. Baxter, *Transactions of the Faraday Society* **1944**, *40*, 546-551.
[127] M. F. Ashby, R. F. Mehl Medalist, *Metallurgical Transactions A* **1983**, *14*, 1755-1769.
[128] S. Doroudiani, M. T. Kortschot, *Jurnal of Applied Polymer Science* **2003**, *90*, 1421-1426.
[129] A. H. Landrock, Handbook of Plastic Foams - Types, Properties, Manufacture and Application, Noyes Publications, Park Ridge, New Jersey **1995**
[130] L. A. Errede, B. F. Landrum, *Journal of the American Chemical Society* **1957**, *79*, 4952-4955.
[131] M. C. Demirel, S. Boduroglu, M. Cetinkaya, A. Lakhtakia, *Langmuir* **2007**, *23*, 5861-5863.
[132] G. P. Spellman, J. F. Carley, L. A. Lopez, *Journal of Plastic Film & Sheeting* **1999**, *15*, 308-328.
[133] J. P. Montheard, M. Chatzopoulos, D. Chappard, *Polymer Reviews* **1992**, *32*, 1-34.
[134] T. V. Chirila, I. J. Constable, G. J. Crawford, S. Vijayasekaran, D. E. Thompson, Y.-C. Chen, W. A. Fletcher, B. J. Griffin, *Biomaterials* **1993**, *14*, 26-38.
[135] C. Schmidt, V. Stümpflen, J. H. Wendorff, A. Hasenhindl, W. Gronski, M. Ishaque, A. Greiner, *Acta Polymerica* **1998**, *49*, 232-235.
[136] D. A. Loy, R. A. Assink, G. M. Jamison, W. F. McNamara, S. Prabakar, D. A. Schneider, *Macromolecules* **1995**, *28*, 5799-5803.
[137] U. Göschel, H. Walter, *Langmuir* **2000**, *16*, 2887-2892.
[138] R. Tao, M. Anthamatten, *Langmuir* **2012**, *28*, 16580-16587.
[139] P. Nising, T. Meyer, R. Carloff, M. Wicker, *Macromolecular Materials and Engineering* **2005**, *290*, 311-318.
[140] M. Stickler, G. Meyerhoff, *Die Makromolekulare Chemie* **1978**, *179*, 2729-2745.
[141] T. Mukundan, V. A. Bhanu, K. Kishore, *Journal of the Chemical Society, Chemical Communications* **1989**, 780-781.
[142] J. Wiesecke, M. Rehahn, *Angewandte Chemie International Edition* **2003**, *42*, 567-570.
[143] J. Wiesecke, M. Rehahn, *Macromolecular Rapid Communications* **2007**, *28*, 78-83.
[144] M. D. Lechner, K. Gehrke, E. H. Normeier, *Makromoleukulare Chemie*, Birkhäuser, **2003**.
[145] K. Matyjaszewski, J. Xia, *Chemical Reviews* **2001**, *101*, 2921-2990.
[146] J. Ye, R. Narain, *The Journal of Physical Chemistry B* **2008**, *113*, 676-681.
[147] M. Tian, Q. Hu, H. Wu, L. Zhang, H. Fong, L. Zhang, *Materials Letters* **2011**, *65*, 3076-3079.

[148] L. Huang, N.-N. Bui, S. S. Manickam, J. R. McCutcheon, *Journal of Polymer Science Part B: Polymer Physics* **2011**, *49*, 1734-1744.

[149] R. V. N. Krishnappa, K. Desai, C. Sing, *Journal of Materials Science* **2003**, *38*, 2357-2365.

[150] C. L. Casper, J. S. Stephens, N. G. Tassi, D. B. Chase, J. F. Rabolt, *Macromolecules* **2003**, *37*, 573-578.

[151] M. Srinivasarao, D. Collings, A. Philips, S. Patel, *Science* **2001**, *292*, 79-83.

[152] C. R. Crick, I. P. Parkin, *Chemical Communications* **2011**, *47*, 12059-12061.

[153] Y. C. Jung, B. Bhushan, *Langmuir* **2008**, *24*, 6262-6269.

[154] H. Domininghaus, *Die Kunststoffe und ihre Eigenschaften*, Springer, Berlin, **2005**.

[155] J. A. Schmitt, *Journal of Applied Polymer Science* **1968**, *12*, 533-546.

[156] K.-K. Koo, T. Inoue, K. Miyasaka, *Polymer Engineering & Science* **1985**, *25*, 741-746.

[157] K. Nakashima, Y. Ren, T. Nishioka, N. Tsubahara, I. Noda, Y. Ozaki, *The Journal of Physical Chemistry B* **1999**, *103*, 6704-6712.

[158] C. F. Lee, *Polymer* **2000**, *41*, 1337-1344.

[159] L. Lili, Y. Dan, W. Le, W. Wei, *Journal of Applied Polymer Science* **2012**, *124*, 1912-1918.

[160] J. Chirife, L. Herszage, A. Joseph, E. S. Kohn, *Antimicrobial Agents and Chemotherapy* **1983**, *23*, 766-776.

[161] J. Shen, X. Han, L. J. Lee, *Journal of Cellular Plastics* **2006**, *42*.

[162] W. Strauss, N. A. D'Souza, *Journal of Cellular Plastics* **2004**, *40*, 229-241.

[163] K. Miled, K. Sab, R. Le Roy, *Mechanics of Materials* **2007**, *39*, 222-240.

[164] A. Kan, R. Demirboğa, *Cement and Concrete Composites* **2009**, *31*, 489-495.

[165] S. Chen, H. Hou, F. Harnisch, S. A. Patil, A. A. Carmona-Martinez, S. Agarwal, Y. Zhang, S. Sinha-Ray, A. L. Yarin, A. Greiner, U. Schröder, *Energy and Environmental Science* **2011**, *4*, 1417-1421.

[166] A. F. Stalder, G. Kulik, D. Sage, L. Barbieri, P. Hoffmann, *Colloids and Surfaces A* **2006**, *286*, 92-103.

[167] H. Cypionka, www.picolay.de, 14 May 2013

[168] M. Monroe, www.alchemistmatt.com, 17 July 2013

[169] Y. S. Yeh, W. J. James, H. Yasuda, *Journal of Polymer Science Part B: Polymer Physics* **1990**, *28*, 545-568.

[170] P. F. Cañamero, J. L. de la Fuente, E. L. Madruga, M. Fernández-García, *Macromolecular Chemistry and Physics* **2004**, *205*, 2221-2228.

[171] F. J. Xu, Q. J. Cai, Y. L. Li, E. T. Kang, K. G. Neoh, *Biomacromolecules* **2005**, *6*, 1012-1020.

Lebenslauf

wurde aus der elektronischen Version entfernt.